

Discretization techniques and efficient algorithms for contact problems

Von der Fakultät Mathematik und Physik der Universität Stuttgart
zur Erlangung der Würde eines Doktors der
Naturwissenschaften (Dr. rer. nat.) genehmigte Abhandlung

Vorgelegt von
Stefan Hüeber
aus Vaihingen an der Enz

Hauptberichter: Prof. Dr. B. Wohlmuth
Mitberichter: Prof. Dr. R. Krause
Prof. Dr. P. Le Tallec

Tag der mündlichen Prüfung: 24. Juli 2008

Institut für Angewandte Analysis und Numerische Simulation
Universität Stuttgart
2008

Acknowledgments

This thesis summarizes the results of my research activities during the years 2002 to 2008 at the chair "Numerische Mathematik für Höchstleistungsrechner" of the Institut für Angewandte Analysis und Numerische Simulation at the Universität Stuttgart.

First of all and all-over, I would like to express my outstanding gratitude to my supervisor Prof. Dr. Barbara Wohlmuth for her excellent mentoring, guidance and encouragement during the past years. Although she is involved in many activities she has always been available to offer her advice and assistance both in professional and more personal issues. Her outstanding motivation for excellent research activities for the whole group has been impressing and inspiring me a lot. In particular, I highly appreciate the countless stimulating discussions on research topics together with her.

My special thanks go to Prof. Dr. Rolf Krause and Prof. Dr. Patrick Le Tallec for their effort to provide the referee reports for this thesis. I also would like to thank Prof. Dr. Barbara Kaltenbacher for participating in the oral defense. Many thanks also to the other scientists which whom I had the pleasure to work with and co-author several contributions: Dr. Andaluzia Matei and Dr. Georg Stadler.

I would especially like to thank my colleagues Stephan Brunßen, Bernd Flemish, Corinna Hager, Andreas Klimke, Bishnu Lamichhane, Michael Mair, Brit Steiner and Alexander Weiß during my employment at the Institut für Angewandte Analysis und Numerische Simulation for working with me, for always being available and for their advice and help in various topics connected with this thesis. I always admire the friendly and cooperative atmosphere at the institute.

I also would like to thank my parents and my whole family for their support and understanding, and for providing me with the chance to pursuit an academic career.

Stuttgart, July 2008

Stefan Hieber

Contents

Abstract	vii
Zusammenfassung	ix
I. Introduction and problem formulation	1
1. Contact mechanics	3
1.1. Continuum mechanics	3
1.2. Contact constraints	6
1.3. Constitutive equations	10
II. Discretization techniques	15
2. Hybrid variational formulation and space discretization	17
2.1. Mortar formulation in terms of inequalities	18
2.2. Space discretization	23
2.3. Algebraic representation	28
3. Optimal a priori error estimates	35
3.1. Theoretical results	36
3.2. Numerical examples	43
3.3. Visualization of discontinuous Lagrange multiplier	49
3.4. Extension to quadratic finite elements	52
3.5. Extension to simplified frictional problem	56
3.6. Numerical convergence studies for a frictional contact problem	60
III. Numerical algorithms	63
4. Semi-smooth Newton method for normal constraints	65
4.1. Semi-smooth Newton methods	66
4.2. Nonlinear complementarity function	67
4.3. Elimination of the Lagrange multiplier	69
4.4. Inexact semi-smooth Newton method	71
4.5. Numerical studies	73

5. Semi-smooth Newton method for frictional constraints	81
5.1. Nonlinear complementarity function	82
5.2. Elimination of the Lagrange multiplier	88
5.3. Inexact semi-smooth Newton method	90
5.4. Numerical studies for Tresca friction	91
5.5. Fixed point based algorithm for Coulomb friction	95
5.6. Full semi-smooth Newton approach for Coulomb friction	104
IV. More general applications	111
6. Large deformations	113
6.1. Algorithmic aspects for nonlinear materials	114
6.2. Numerical examples for nonlinear materials	116
6.3. Contact dynamics with large deformations	121
6.4. Numerical examples	126
7. Thermo-mechanical contact problems	135
7.1. Problem formulation for linear thermo-elasticity	135
7.2. Discretization in time	138
7.3. Space discretization and mortar formulation	139
7.4. Algebraic representation	143
7.5. Numerical algorithm	146
7.6. Numerical examples	146
8. Concluding remarks	155
Bibliography	157

Abstract

This thesis is concerned with the development of efficient numerical solution algorithms for nonlinear contact problems with friction. Such type of problems play an important role in many technical and engineering applications. Thus, the design of discretization techniques and efficient solution strategies is still a challenging task both from the engineering and the mathematical point of view.

Domain decomposition techniques based on finite element methods are a powerful tool to approximate the solution of partial differential equations as they occur in the framework of structural mechanics. Here, we focus on discretization techniques based on the mortar method by introducing an additional unknown named Lagrange multiplier or dual variable in order to formulate the interface constraints between the involved bodies. In the framework of contact problems, where the weak formulation consists of a variational inequality, this additional variable models the contact stresses at the common contact interface. Using standard finite elements for the discretization of the Lagrange multiplier, the contact conditions result in a segment-to-segment approach, where the mechanical inequality constraints can only be resolved by some global optimization procedure on the contact boundary. This can be avoided by working with locally defined dual or biorthogonal basis functions for the Lagrange multiplier space. Then, the segment-to-segment approach is algebraically equivalent to a node-to-segment approach, and the inequality constraints decouple point-wise. Additionally, we are able to transform a two-body contact problem into a one-body problem by a local preprocess, and hence apply the same nonlinear solver. Mathematically, the preprocess is equivalent to a basis transformation; physically, master and slave side are glued together such that the two bodies form a composite material and the displacement on the slave side reflects the relative displacement between the two bodies. In this thesis, we analyze the discretization error of the proposed mortar formulation and give optimal a priori error estimates. A various set of numerical examples are given to confirm the achieved theoretical results.

The decoupled contact constraints provide a basis for the construction of efficient solution algorithms. The presented numerical approaches are semi-smooth Newton methods which are equivalent to a primal-dual active set strategy in the case without friction. The point-wise inequality constraints between the primal variable, i.e., the displacement, and the dual variable, i.e., the Lagrange multiplier, are written as an equality constraint by the use of a semi-smooth nonlinear complementarity function. Even for the case of contact problems including friction with Coulomb's friction law we are able to construct a full semi-smooth Newton algorithm. Due to the use of the dual basis functions for the Lagrange multiplier, we are able to locally eliminate the degrees of freedom for the dual variable. Thus, in each iteration step, we have to solve a linear system with respect to the primal variable, where, the contact constraints enter as boundary conditions of

Dirichlet-, Neumann-, or Robin-type. Therefore, existing finite elements codes for structural mechanics can be easily extended to the case of contact problems by using the proposed methods. Using iterative solvers like optimal multigrid methods to solve the arising linear system in each step, we are able to construct inexact strategies, where the linear system is not completely solved in each Newton step. By this, we get an efficient algorithm for solving a fully nonlinear contact problem whose additional cost is negligible compared to solving a linear system. Several numerical examples are provided to investigate the performance and efficiency of the introduced algorithms.

In the last part of this thesis, we extend the proposed formulation and the efficient solution algorithms to more general applications. Firstly, we adapt our solution strategies to the case of dynamical contact problems in combination with nonlinear material laws. Especially, we focus on energy-conserving algorithms. Secondly, we treat thermo-mechanical contact problems, where, the temperature is introduced as an additional unknown. This extension is quite natural since heat is generated due to the mechanical frictional work. Similar as the mechanical Lagrange multiplier takes care on the mechanical contact constraints, a thermal Lagrange multiplier modeling the heat flux across the contact interface is added to enforce the thermal flux conditions over the contact interface. We propose a mortar formulation for this Robin-type thermal interface conditions and extend our contact algorithms to solve the resulting nonlinear problem.

This thesis is organized as follows. In the first part we introduce in Chapter 1 the mathematical formulation of contact problems. The second part introduces the variational formulation and its discretization in terms of the mortar method in Chapter 2. In Chapter 3 the optimal a priori error estimates for the discretization errors are derived. The numerical solution algorithms based on semi-smooth Newton methods are presented in the third part. Chapter 4 contains the algorithm for the contact problem without friction while Chapter 5 deals with the numerical solution of frictional contact problems. In the last part we extend the proposed discretization techniques and the numerical algorithms to more general contact problems. In Chapter 6 we consider dynamical contact problems with large deformations and in Chapter 7 thermo-mechanical contact problems are studied. For a detailed description of the content of the several chapters and the literature overview we refer to the introductions at the beginning of each chapter.

Finally, we mention that our implementation for all numerical examples presented in this thesis is based on the finite element toolbox UG, [5], and the fast optimized direct solver package PARDISO, [123, 124]. The visualization in the three-dimensional case has been performed with NETGEN, [125].

Zusammenfassung

Die numerische Simulation von Vorgängen in Natur und Technik nimmt in heutiger Zeit eine stetig zunehmende Rolle in der Entwicklung neuer Produkte in der Industrie aber auch im Verständnis von Naturphänomenen ein. Selbst in der Medizin werden mittlerweile numerische Simulationsmethoden beispielsweise zur Planung von komplizierten Operationen eingesetzt. Mathematisch werden alle diese Vorgänge mit Hilfe von partiellen Differentialgleichungen beschrieben, deren analytische Lösungen im Allgemeinen nicht bekannt sind. Geeignete Diskretisierungsmethoden, wie beispielsweise Finite Element Methoden in Kombination mit effizienten Lösungsverfahren, stellen daher ein mächtiges Werkzeug dar, um näherungsweise Lösungen dieser Systeme zu erhalten.

Diese Arbeit befasst sich mit der Diskretisierung und der Entwicklung effizienter Lösungsverfahren für Kontaktprobleme in der nichtlinearen Strukturmechanik. Kontaktprobleme spielen nicht nur im Alltag, sondern auch in vielen ingenieurwissenschaftlichen Fragestellungen eine große Rolle. Beispielsweise stellt jede Art der Fortbewegung, sei es das Gehen oder der rollende Reifen eines Autos einen reibungsbehafteten Kontaktvorgang dar. In der Technik findet man derartige Vorgänge zum Beispiel in der Blechumformung oder beim Crash zweier Fahrzeuge. Gerade hier ist man an einer effizienten Simulation bereits im Entwicklungsstadium eines Fahrzeuges sehr interessiert.

Da bei der Simulation solcher Vorgänge meist mehrere Objekte beteiligt sind und diskretisiert werden müssen, stellen moderne Gebietszerlegungsmethoden einen hervorragenden Ausgangspunkt für die Entwicklung effizienter Lösungsalgorithmen dar. Insbesondere eignet sich hierfür die Mortar-Methode, welche einen mathematisch analysierbaren Zugang liefert, der ein nichtkonformes Vernetzen der beteiligten Objekte an ihren Schnittstellen, den Kontaktflächen, erlaubt. Somit können die Rechengitter den Eigenschaften der einzelnen Objekte separat erzeugt und deren Gestalt optimal angepasst werden. Der Informationsaustausch zwischen den einzelnen Teilgebieten geschieht bei der Mortar-Methode mit Hilfe einer zusätzlichen Variablen, dem Lagrange-Multiplikator. Im Falle eines Kontaktvorgangs beschreibt dieser gerade die Kontaktkräfte, die zwischen den beteiligten Objekten ausgetauscht werden. Für die diskrete Beschreibung des Lagrange-Multiplikators werden in dieser Arbeit duale Basisfunktionen verwendet. Die Verwendung dieser Basisfunktionen führt zu einer Entkopplung der Kontaktnebenbedingungen an den einzelnen Diskretisierungspunkten an der Kontaktfläche, welche dann einen hervorragenden Ausgangspunkt für die Entwicklung effizienter iterativer Lösungsalgorithmen für das entstehende nichtlineare Gleichungssystem basierend auf nichtglatten Newton-Verfahren darstellt. Somit ist der Zugang mit Mortar-Techniken, der in seiner Grundform eine Segment-to-Segment-Formulierung darstellt, in seiner algebraischen Form äquivalent zu einer Node-to-Segment-Formulierung. Weiter lassen sich aufgrund der Wahl dieser speziellen Basisfunktionen im resultierenden algebraischen Gleichungssystem die

zusätzlichen Freiheitsgrade für den Lagrange-Multiplikator auf effiziente Weise lokal eliminieren, so dass am Ende nur noch ein auskondensiertes System bezüglich der primalen Variable gelöst werden muss. Nichtglatte Newton-Verfahren gewinnen in modernen Simulationstechniken stetig an Bedeutung. Im Rahmen dieser Arbeit soll ihre Anwendung auf Kontaktprobleme in Kombination mit der Mortar-Methode vorgestellt und untersucht werden. Im Folgenden sind die Inhalte der einzelnen Abschnitte und Kapitel dieser Arbeit beschrieben.

Der erste Teil mit Kapitel 1 ist der mathematischen Beschreibung eines Kontaktproblems gewidmet. Neben einer kurzen Übersicht über die kontinuumsmechanischen Grundlagen zur Beschreibung der Strukturmechanik wird die detaillierte mathematische Beschreibung der nichtlinearen Kontaktvorgänge eingeführt. Diese Kontaktvorgänge sind einerseits die Nichtdurchdringungsbedingung der beteiligten Objekte und andererseits die Reibungsbedingungen, welche über Haften oder Gleiten entscheiden. Abschließend werden die gebräuchlichsten konstitutiven Materialgesetze, welche die Beziehung zwischen den Verzerrungen und den Spannungen mathematisch beschreiben, vorgestellt.

Im zweiten Teil wird in den Kapiteln 2 und 3 die Ortsdiskretisierung des Kontaktproblems mit Hilfe der Mortar-Methode vorgestellt und mathematisch untersucht. Kapitel 2 beschäftigt sich zunächst mit der Herleitung der schwachen Formulierung und der daraus resultierenden Variationsungleichungen. Anschließend wird deren diskrete Formulierung unter Verwendung von dualen Basisfunktionen für den Lagrange-Multiplikator dargestellt. Die Verwendung dieser speziellen Wahl von Basisfunktionen führt dazu, dass die Kontaktbedingungen an den einzelnen Knoten auf dem Kontaktrand entkoppeln. In Kapitel 3 wird diese Ortsdiskretisierung hinsichtlich ihrer Konvergenz untersucht. Unter geeigneten Regularitätsanforderungen an die Lösung werden optimale a priori Fehlerabschätzungen hergeleitet. Diese werden zunächst für den reibungsfreien Fall für Finite Elemente erster und zweiter Ordnung bewiesen. Der Fall mit Reibung wird anhand eines vereinfachten Reibungsproblems untersucht. Die theoretisch gewonnenen Resultate werden anhand zahlreichen numerischen Beispielen untermauert.

Der dritte Teil dieser Arbeit ist der Konstruktion von effizienten numerischen Algorithmen zur Lösung der resultierenden nichtlinearen algebraischen Gleichungen gewidmet. Zunächst wird in Kapitel 4 ein nichtglatte Newton-Verfahren zur Lösung des Kontaktproblems ohne Reibung vorgestellt und numerisch analysiert. Die Konstruktion dieses Verfahrens basiert darauf, dass sich die nichtlineare Ungleichungsnebenbedingung der Nichtdurchdringungsbedingung mit Hilfe einer nichtglatte nichtlinearen Komplementaritätsfunktion in eine äquivalente Gleichungsnebenbedingung bezüglich den Verschiebungen, den primalen Variablen, und den Kontaktspannungen, den dualen Variablen, umschreiben lässt. Dieser Zugang kann im reibungsfreien Fall auch als eine primal-duale Aktive-Mengen-Strategie aufgefasst werden. Weiter wird die lokal effizient durchführbare Elimination der zusätzlichen Freiheitsgrade für den Lagrange-Multiplikator aus den resultierenden algebraischen Gleichungssystemen, welches in jedem iterativen Newton-Schritt zu lösen gilt, vorgestellt. Folglich muss in jedem Iterationsschritt nur noch die Lösung eines linearen Gleichungssystem bezüglich der primalen Variablen gefunden werden. Kombiniert man nun effiziente iterative Löser für lineare Gleichungssysteme, wie beispielsweise optimale Mehrgitterverfahren, so erlaubt uns dies die Verwen-

dung von inexakten Methoden. In diesem Fall entspricht der Lösungsaufwand zur Lösung des gesamten nichtlinearen Kontaktproblems ungefähr dem Lösungsaufwand eines linearen Problems. Das zweite Kapitel 5 ist der Konstruktion von effizienten nichtglatten Newton-Verfahren für den Fall mit Reibung gewidmet. Im ersten Schritt wird ein nichtglattes Newton-Verfahren für den Fall mit Tresca-Reibung vorgestellt. Insbesondere werden hier numerische Modifikationen der linearen Gleichungen in jedem Iterationsschritt vorgestellt, welche sich für die numerische Konvergenz der Verfahren als äußerst relevant herausstellen. Dieser Zugang wird auf den Fall der physikalisch relevanten Coulomb-Reibung mit Hilfe einer Anpassung der Reibungsschranke in einer Fixpunktstrategie erweitert. Da diese Vorgehensweise kein volles Newton-Verfahren darstellt und damit erwartungsgemäß kein superlineares Konvergenzverhalten zeigt, wird weiter ein volles nicht-glattes Newtonverfahren für den Fall mit Coulomb-Reibung konstruiert, welches auf einer Modifikation der nichtlinearen Komplementaritätsfunktion basiert. Ein wesentlicher Vorteil aller dieser vorgestellten Zugänge ist, dass sich die zusätzlichen Kontakt-Nichtlinearitäten als Dirichlet-, Neumann-, oder Robin-Randbedingungen für die Strukturgleichung interpretieren lassen. Diese Tatsache stellt einen hervorragenden Ausgangspunkt für den Einbau der betrachteten Kontaktalgorithmen in bereits existierende Finite-Element-Software dar.

Der letzte Teil dieser Arbeit befasst sich mit der Erweiterung der vorgestellten Algorithmen auf allgemeinere Kontaktprobleme. In Kapitel 6 wird die Erweiterung auf dynamische Kontaktprobleme mit großen Deformationen und nichtlinearem Materialverhalten aufgezeigt. Ein besonderes Augenmerk liegt hierbei auf der Konstruktion von energieerhaltenden Zeitinterationsverfahren, sowohl für den Strukturanteil als auch den Kontaktanteil. Weiter wird eine modifizierte Massenmatrix verwendet, welche dazu führt, dass die unphysikalischen Oszillationen in den Kontaktspannungen, welche bei der Verwendung von Zeitintegratoren basierend auf der Mittelpunktsregel auftreten, verschwinden. Im letzten Kapitel 7 wird die Erweiterung auf ein thermo-mechanisches Kontaktproblem vorgestellt. Die aufgrund der Reibung entstehende Energie wird in Wärme umgewandelt und somit stellt die Einbeziehung der Temperatur als weitere Unbekannte in die Modellierung eine logische Erweiterung dar. Andererseits beeinflusst die Temperatur am Kontaktrand auch die Größe des Reibungskoeffizienten. Ausgehend von der starken Formulierung für linearisierte Thermo-Elastizität wird die schwache Variationsformulierung für das Verschiebungsfeld und das Temperaturfeld hergeleitet. Hierzu wird analog zum mechanischen Lagrange-Multiplikator, der die Kontaktspannungen beschreibt, ein weiterer Lagrange-Multiplikator für den Temperaturfluss über den Kontaktrand eingeführt. Die Kopplungsbedingungen des Temperaturfeldes über den Kontaktrand stellen Robin-Interfacebedingungen dar. Ein wesentlicher Teil dieses Kapitels ist die Behandlung dieser Kopplungsbedingungen mit Rahmen der Mortar-Methode in Kombination mit dualen Basisfunktionen. Schließlich werden in Kapitel 8 die Schlussfolgerungen dieser Arbeit zusammengefasst.

Part I.

Introduction and problem formulation

1. Contact mechanics

In the first chapter, we formulate the dynamical contact problem of two bodies and give the governing field equations and the restrictions for the displacement due to the detection of the two bodies. A schematic plot of a two-dimensional two-body contact problem is given in Figure 1.1. Caused by external volume forces and surface tractions and the initial motion the two bodies are deformed and assumed to come into contact. We start with a short introduction to continuum mechanics in Section 1.1, In Section 1.2 we focus on the non-penetration condition of the two bodies and the frictional condition using Coulomb's law. The formulation of contact problems is also treated in the textbooks [42, 91, 106, 135, 143]. Finally, we provide a brief overview about the basic material laws in hyper-elasticity in Section 1.2.1. For details about the material behavior, we refer to the classical textbooks [31, 117, 131, 142].

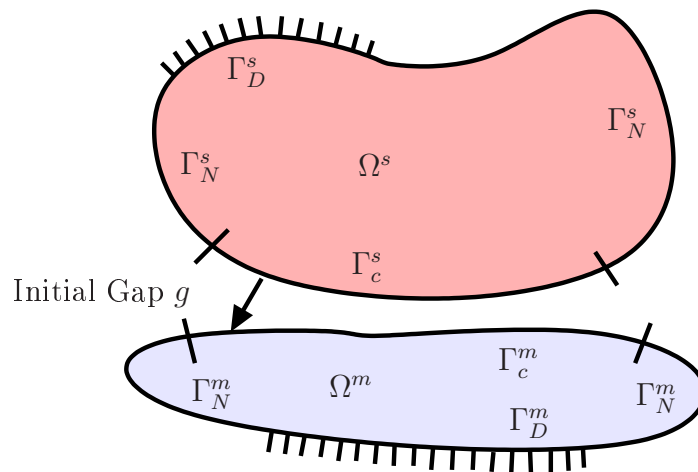


Figure 1.1.: Two body contact problem.

1.1. Continuum mechanics

We consider two bounded bodies given in the reference configuration by the polygonal bounded open sets $\Omega^s, \Omega^m \subset \mathbb{R}^d$, $d = 2, 3$. The superscript s stands for the slave body and m for the master body; the choice is arbitrary but should be fixed and plays only a role for the discretization in space. The boundary of the body Ω^i is denoted by $\partial\Omega^i$, $i = s, m$. By $\Omega := \Omega^s \cup \Omega^m$ we define the union of the two subdomains and by $\partial\Omega := \Gamma^s \cup \Gamma^m$ its boundary. Each of the boundaries Γ^i is assumed to be divided into three open disjoint

subsets Γ_D^i , Γ_N^i and Γ_c^i such that $\Gamma^i = \overline{\Gamma}_D^i \cup \overline{\Gamma}_N^i \cup \overline{\Gamma}_c^i$ holds. Furthermore, we assume that Γ_D^s is compactly embedded in $\Gamma^s \setminus \overline{\Gamma}_c^s$. Our calculations are performed within the time interval $(0, T)$, where $T > 0$ denotes the final time. To describe the motion under external loading given by volume and traction forces we introduce the deformation φ^i , $i = s, m$,

$$\varphi^i : \Omega^i \times (0, T) \rightarrow \mathbb{R}^d, \quad \Omega^i \times (0, T) \ni (\mathbf{x}, t) \mapsto \varphi^i(\mathbf{x}, t) \in \mathbb{R}^d.$$

We remark that $\varphi^i(\mathbf{x}, t)$ denotes the current position at time t of the point $\mathbf{x} \in \Omega^i$ in the reference configuration. To simplify the notation we neglect the domain index i in the reference position \mathbf{x} . The affiliation of \mathbf{x} to the correct subdomain Ω^i , $i = s, m$, is still clear in the context of its usage. In addition to the deformation the displacement \mathbf{u}^i is given by

$$\mathbf{u}^i(\mathbf{x}, t) := \varphi^i(\mathbf{x}, t) - \mathbf{x}. \quad (1.1)$$

For the current position of $\mathbf{x} \in \Omega^i$ we also use the notation $\mathbf{x}^\varphi(t) := \varphi^i(\mathbf{x}, t)$. Next, we introduce the deformation gradient \mathbf{F}^i by

$$\mathbf{F}^i := \nabla \varphi^i = (\varphi_{k,l}^i)_{1 \leq k, l \leq d}, \quad \varphi_{k,l}^i := \frac{\partial \varphi_k^i}{\partial x_l}, \quad (1.2)$$

where x_l denotes the l -th component of the vector \mathbf{x} and φ_k^i the k -th component of the deformation φ^i . For its determinant we write

$$J^i := \det(\mathbf{F}^i).$$

With the use of the deformation gradient we are able to define the right Cauchy strain tensor \mathbf{C}^i by

$$\mathbf{C}^i := (\mathbf{F}^i)^\top \mathbf{F}^i = (\nabla \varphi^i)^\top \nabla \varphi^i$$

and the Green–Saint Venant strain tensor \mathbf{E}^i by

$$\mathbf{E}^i := \frac{1}{2}(\mathbf{C}^i - \text{Id}_d) = \frac{1}{2}(\nabla \mathbf{u}^i + (\nabla \mathbf{u}^i)^\top + (\nabla \mathbf{u}^i)^\top \nabla \mathbf{u}^i), \quad (1.3)$$

where Id_d denotes the identity matrix in $\mathbb{R}^{d,d}$. We remark that for a rigid deformation, which is obtained by a superposition of a rotation and a translation, we have $\mathbf{C}^i = \text{Id}_d$ and $\mathbf{E}^i = \mathbf{0}$. Therefore \mathbf{E}^i can be interpreted as the measure of the true deformation of the body Ω^i .

After defining the kinematic quantities \mathbf{C} and \mathbf{E} we focus on the balance equation. In continuum mechanics, one assumes that there are only two kinds of forces the body might be subjected to: volume forces and surface forces. We consider arbitrary subdomains $A^i \subset \Omega^i$, $i = s, m$. Let $\mathbf{f}^{i,\varphi}$ be the density of the volume forces acting on the current subdomain $\varphi^i(A^i, t) \subset \varphi^i(\Omega^i, t)$. Then the volume force at time $t \in (0, T)$ acting on the current subdomain $\varphi^i(A^i, t)$ is given by

$$\mathcal{F}_{\varphi(A)}(t) = \sum_{i=s,m} \int_{\varphi^i(A^i, t)} \mathbf{f}^{i,\varphi}(\mathbf{x}^\varphi) \, d\mathbf{x}^\varphi. \quad (1.4)$$

Furthermore, let $\mathbf{p}^{i,\varphi}$ be the density of the surface forces acting on $\varphi^i(\Gamma_N^i, t)$, then the surface force acting on $\varphi^i(\partial A^i, t) \cap \varphi^i(\Gamma_N^i, t)$ is given by

$$\mathcal{P}_{\varphi(\partial A)}(t) = \sum_{i=s,m} \int_{\varphi^i(\partial A^i, t) \cap \varphi^i(\Gamma_N^i, t)} \mathbf{p}^{i,\varphi}(\mathbf{x}^\varphi, \mathbf{n}^\varphi) \, ds^\varphi, \quad (1.5)$$

where \mathbf{n}^φ denotes the current outward unit normal vector on $\varphi^i(A^i, t)$. In addition to the volume force (1.4) and the surface force (1.5) we have to consider in the dynamical case the inertia force

$$\mathcal{I}_{\varphi(A)}(t) := \sum_{i=s,m} \int_{\varphi^i(A^i, t)} \varrho^{i,\varphi} \ddot{\mathbf{x}}^\varphi \, d\mathbf{x}^\varphi,$$

where $\varrho^{i,\varphi}(\mathbf{x}^\varphi)$ is the current mass density at the position \mathbf{x}^φ . Following the stress principle of Euler and Cauchy, [31], there exists a vector $\mathbf{t}^{i,\varphi}$, called the Cauchy stress vector, such that the balance equation on the subdomains A^i reads as

$$\int_{\varphi^i(A^i, t)} \varrho^{i,\varphi} \ddot{\mathbf{x}}^\varphi \, d\mathbf{x}^\varphi + \int_{\varphi^i(A^i, t)} \mathbf{f}^{i,\varphi}(\mathbf{x}^\varphi) \, d\mathbf{x}^\varphi + \int_{\varphi^i(\partial A^i, t)} \mathbf{t}^{i,\varphi}(\mathbf{x}^\varphi, \mathbf{n}^\varphi) \, ds^\varphi = \mathbf{0}. \quad (1.6)$$

Cauchy's theorem states that there exists a symmetric tensor $\mathbf{T}^{i,\varphi}$, called the Cauchy stress tensor, such that

$$\mathbf{t}^{i,\varphi}(\mathbf{x}^\varphi, \mathbf{n}^\varphi) = \mathbf{T}^{i,\varphi}(\mathbf{x}^\varphi) \mathbf{n}^\varphi, \quad \mathbf{x}^\varphi \in \varphi^i(\Omega^i, t)$$

and

$$\mathbf{t}^{i,\varphi}(\mathbf{x}^\varphi, \mathbf{n}^\varphi) = \mathbf{p}^{i,\varphi}(\mathbf{x}^\varphi), \quad \mathbf{x}^\varphi \in \varphi^i(\Omega^i, t).$$

Applying now partial integration to (1.6) we get due to the fact that the subsets A^i are arbitrary the local form of the balance equation in the current configuration $\varphi^i(\Omega^i, t)$

$$\varrho^{i,\varphi} \ddot{\mathbf{x}}^\varphi - \operatorname{div}^\varphi \mathbf{T}^{i,\varphi}(\mathbf{x}^\varphi) = \mathbf{f}^{i,\varphi}(\mathbf{x}^\varphi), \quad \mathbf{x}^\varphi \in \varphi^i(\Omega^i, t), \quad (1.7a)$$

$$\mathbf{T}^{i,\varphi}(\mathbf{x}^\varphi) \mathbf{n}^\varphi = \mathbf{p}^{i,\varphi}(\mathbf{x}^\varphi), \quad \mathbf{x}^\varphi \in \varphi^i(\Gamma_N^i, t), \quad (1.7b)$$

where $\operatorname{div}^\varphi$ is the divergence operator with respect to the current position \mathbf{x}^φ .

To formulate the balance equation (1.7) with respect to the reference configuration, we define the first Piola–Kirchhoff stress tensor by

$$\mathbf{P}^i(\mathbf{x}, t) := J^i(\mathbf{x}, t) \mathbf{T}^i(\mathbf{x}, t) \mathbf{F}^i(\mathbf{x}, t)^{-\top},$$

where we used the relation

$$\mathbf{T}^i(\mathbf{x}, t) := \mathbf{T}^{i,\varphi}(\mathbf{x}^\varphi) = \mathbf{T}^{i,\varphi}(\varphi^i(\mathbf{x}, t)).$$

Furthermore, the second Piola–Kirchhoff stress tensor is given by

$$\mathbf{S}^i(\mathbf{x}, t) := (\mathbf{F}^i(\mathbf{x}, t))^{-1} \mathbf{P}^i(\mathbf{x}, t). \quad (1.8)$$

Due to the symmetry of \mathbf{T}^i the tensor \mathbf{S}^i is also symmetric. Additionally, the density of the applied volume force \mathbf{f}^i and the density of the applied surface force \mathbf{p}^i with respect to the reference configuration is defined by

$$\mathbf{f}^i(\mathbf{x}, t) := J^i(\mathbf{x}, t)\mathbf{f}^{i,\varphi}(\boldsymbol{\varphi}^i(\mathbf{x}, t)), \quad (1.9)$$

$$\mathbf{p}^i(\mathbf{x}, t) := J^i(\mathbf{x}, t)\|\mathbf{F}^i(\mathbf{x}, t)^{-\top}\mathbf{n}_0(\mathbf{x}, t)\|\mathbf{p}^{i,\varphi}(\boldsymbol{\varphi}^i(\mathbf{x}, t)), \quad (1.10)$$

where $\mathbf{n}_0(\mathbf{x})$ is the outward unit normal vector in the reference configuration Ω^i at the point \mathbf{x} , and $\|\cdot\|$ denotes the standard Euclidean norm in \mathbb{R}^d . The balance equation (1.7) in the reference configuration reads as

$$\varrho^i(\mathbf{x})\ddot{\boldsymbol{\varphi}}^i(\mathbf{x}, t) - \operatorname{div} \mathbf{P}^i(\mathbf{x}, t) = \mathbf{f}^i(\mathbf{x}, t), \quad (\mathbf{x}, t) \in \Omega^i \times (0, T), \quad (1.11a)$$

$$\mathbf{P}^i(\mathbf{x}, t)\mathbf{n}_0(\mathbf{x}) = \mathbf{p}^i(\mathbf{x}, t), \quad (\mathbf{x}, t) \in \Gamma_N^i \times (0, T) \quad (1.11b)$$

with the reference mass density $\varrho^i(\mathbf{x})$. Due to (1.1) we can also use $\ddot{\mathbf{u}}^i$ instead of $\ddot{\boldsymbol{\varphi}}^i$ in (1.11a). Now, we can formulate the initial boundary value problem as

$$\varrho^i(\mathbf{x})\ddot{\mathbf{u}}^i(\mathbf{x}, t) - \operatorname{div} \mathbf{P}^i(\mathbf{x}, t) = \mathbf{f}^i(\mathbf{x}, t), \quad (\mathbf{x}, t) \in \Omega^i \times (0, T), \quad (1.12a)$$

$$\mathbf{P}^i(\mathbf{x}, t)\mathbf{n}_0(\mathbf{x}) = \mathbf{p}^i(\mathbf{x}, t), \quad (\mathbf{x}, t) \in \Gamma_N^i \times (0, T), \quad (1.12b)$$

$$\mathbf{u}^i(\mathbf{x}, t) = \mathbf{u}_D^i(\mathbf{x}, t), \quad (\mathbf{x}, t) \in \Gamma_D^i \times (0, T), \quad (1.12c)$$

$$\mathbf{u}^i(\mathbf{x}, 0) = \mathbf{0}, \quad \mathbf{x} \in \Omega^i, \quad (1.12d)$$

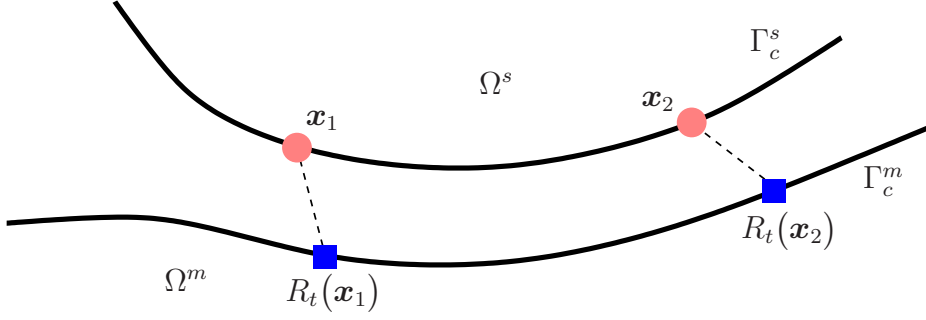
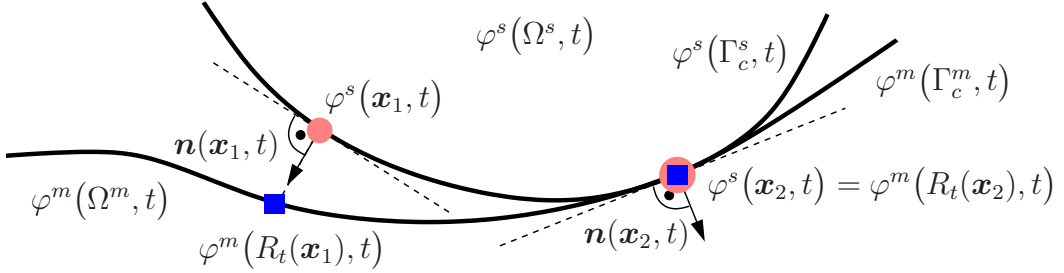
$$\dot{\mathbf{u}}^i(\mathbf{x}, 0) = \mathbf{v}_0^i, \quad \mathbf{x} \in \Omega^i. \quad (1.12e)$$

Equation (1.12c) states the Dirichlet condition with the prescribed displacements $\mathbf{u}_D^i(\mathbf{x}, t)$. The last two equations (1.12d) and (1.12e) are the initial conditions, where \mathbf{v}_0^i denotes the initial velocity. The contact boundary conditions on the possible contact boundary segments Γ_c^i are introduced in Subsection 1.2. Possible stress-strain relations between the second Piola–Kirchhoff stress tensor \mathbf{S} , see (1.8), and the deformation gradient \mathbf{F} , see (1.2), are given in Subsection 1.3.

1.2. Contact constraints

In this subsection we give the frictional contact constraints on the possible contact segments Γ_c^i on which the bodies may come into contact. These conditions consist of the non-penetration condition enforcing that the two bodies cannot penetrate each other, and the friction condition separating the zone, at which the bodies are in contact, into a sliding and a sticking one. The decision whether a contact point is a sliding or a sticking point is made on the value of the so called friction bound. We consider the well known Coulomb’s friction law. Here, the friction bound depends on the contact pressure at the corresponding contact point. A simpler model is expressed by Tresca’s law, where the friction bound is assumed to be a priori given, see, e.g., [40, 58].

To state these conditions, we use for the normal vector on the slave side of the current configuration for each point $\mathbf{x} \in \Gamma_c^s$ the notation $\mathbf{n}(\mathbf{x}, t) := \mathbf{n}^s(\mathbf{x}, t) := \mathbf{n}^\varphi(\mathbf{x}, t)$. In


 Figure 1.2.: Illustration of the mapping $R_t(\cdot)$: reference configuration.

 Figure 1.3.: Illustration of the mapping $R_t(\cdot)$: current configuration.

order to formulate the non-penetration condition of the two bodies, we use a predefined relation between the points of the possible contact zones Γ_c^i constructed by a smooth mapping

$$\begin{aligned} R_t : \Gamma_c^s &\rightarrow \Gamma_c^m \\ \mathbf{x} &\mapsto R_t(\mathbf{x}) \end{aligned}$$

for all $t \in (0, T)$. The current position $\varphi^s(\mathbf{x}, t) := \mathbf{x} + \mathbf{u}^s(\mathbf{x}, t) \in \varphi^s(\Gamma_c^s, t)$ of the reference point $\mathbf{x} \in \Gamma_c^s$ is projected onto the current master boundary $\varphi^m(\Gamma_c^m, t)$ in the direction of the current normal $\mathbf{n}(\mathbf{x}, t)$; the reference point corresponding to the projection $\varphi^m(R_t(\mathbf{x}), t) \in \varphi^m(\Gamma_c^m, t)$ defines $R_t(\mathbf{x})$. We assume that this mapping is well defined. The definition of the mapping $R_t(\mathbf{x})$ is illustrated in the Figures 1.2-1.3. Two points $\mathbf{x}_1^s, \mathbf{x}_2^s \in \Gamma_c^s$ are shown in their reference configuration in Figure 1.2 whereas Figure 1.3 shows the configuration at the current time t . Point \mathbf{x}_2^s is assumed to come into contact, whereas \mathbf{x}_1^s is a free node at time t . Now, the current gap at a point $\mathbf{x} \in \Gamma_c^s$ is defined by

$$g(\mathbf{x}, t) := \left(\varphi^s(\mathbf{x}, t) - \varphi^m(R_t(\mathbf{x}), t) \right) \mathbf{n}(\mathbf{x}, t). \quad (1.13)$$

Furthermore, we denote the current contact pressure of the two bodies by \mathbf{p}_c^i , $i = s, m$, where we have due to Newton's law

$$\mathbf{p}_c^s(\mathbf{x}, t) = -\mathbf{p}_c^m(R_t(\mathbf{x}, t)), \quad (\mathbf{x}, t) \in \Gamma_c^s \times (0, T). \quad (1.14)$$

In the following, we use

$$\mathbf{p}_c(\mathbf{x}, t) := \mathbf{p}_c^s(\mathbf{x}, t), \quad (\mathbf{x}, t) \in \Gamma_c^s \times (0, T). \quad (1.15)$$

Defining the normal component and the tangential vector of the contact pressure via

$$p_n(\mathbf{x}, t) := \mathbf{p}_c(\mathbf{x}, t)\mathbf{n}(\mathbf{x}, t), \quad \mathbf{p}_\tau(\mathbf{x}, t) := \mathbf{p}_c(\mathbf{x}, t) - p_n(\mathbf{x}, t)\mathbf{n}(\mathbf{x}, t) \quad (1.16)$$

respectively, we now are able to formulate the non-penetration condition on Γ_c^s as

$$g(\mathbf{x}, t) \leq 0, \quad p_n(\mathbf{x}, t) \geq 0, \quad g(\mathbf{x}, t)p_n(\mathbf{x}, t) = 0, \quad (\mathbf{x}, t) \in \Gamma_c^s \times (0, T). \quad (1.17)$$

Next, we introduce the jump of the displacement by

$$[\mathbf{u}(\mathbf{x}, t)] := \mathbf{u}^s(\mathbf{x}, t) - \mathbf{u}^m(R_t(\mathbf{x}), t), \quad (\mathbf{x}, t) \in \Gamma_c^s \times (0, T) \quad (1.18)$$

and define according to (1.16) its normal component and its tangential vector via

$$[\mathbf{u}(\mathbf{x}, t)]_n := [\mathbf{u}(\mathbf{x}, t)]\mathbf{n}(\mathbf{x}, t), \quad [\mathbf{u}(\mathbf{x}, t)]_\tau := [\mathbf{u}(\mathbf{x}, t)] - [\mathbf{u}(\mathbf{x}, t)]_n\mathbf{n}(\mathbf{x}, t),$$

respectively. With a given coefficient of friction $\mathfrak{F} \geq 0$, Coulomb's friction law reads as

$$\begin{cases} \|\mathbf{p}_\tau(\mathbf{x}, t)\| \leq \mathfrak{F}|p_n(\mathbf{x}, t)|, \\ \|\mathbf{p}_\tau(\mathbf{x}, t)\| < \mathfrak{F}|p_n(\mathbf{x}, t)| \Rightarrow [\dot{\mathbf{u}}(\mathbf{x}, t)]_\tau = \mathbf{0}, \\ \|\mathbf{p}_\tau(\mathbf{x}, t)\| = \mathfrak{F}|p_n(\mathbf{x}, t)| \Rightarrow \exists \alpha \in \mathbb{R} : \mathbf{p}_\tau(\mathbf{x}, t) = \alpha^2[\dot{\mathbf{u}}(\mathbf{x}, t)]_\tau \end{cases} \quad (1.19)$$

for $(\mathbf{x}, t) \in \Gamma_c^s \times (0, T)$. Equivalently to (1.19) one can write Coulomb's law as

$$\|\mathbf{p}_\tau\| \leq \mathfrak{F}|p_n|, \quad \mathbf{p}_\tau = \alpha^2[\dot{\mathbf{u}}]_\tau, \quad \|[\dot{\mathbf{u}}]_\tau\|(\|\mathbf{p}_\tau\| - \mathfrak{F}|p_n|) = 0. \quad (1.20)$$

Friction models with a coefficient of friction depending on the sliding velocity $\dot{\mathbf{u}}_\tau$ can be found in [106] and the references therein. In the case of Tresca's friction law the friction bound $\mathfrak{F}|p_n(\mathbf{x}, t)|$ has to be replaced by $g_f(\mathbf{x})$, where the non-negative function $g_f(\cdot) : \Gamma_c^s \rightarrow \mathbb{R}$ is a priori given.

1.2.1. Linearized contact conditions

In the case of small deformations, the non-penetration condition (1.17) formulated in the current configuration is often replaced by its linearized version. Here, one does not take care on the change of the normal vector and the predefined time-dependent mapping R_t during the contact process over time. Defining the initial gap $g_0(\mathbf{x})$ in the reference configuration by

$$g_0(\mathbf{x}) := \|\mathbf{x} - R_0(\mathbf{x})\|, \quad \mathbf{x} \in \Gamma_c^s$$

and the jump $[\mathbf{u}]_{n_0}$ with respect to the reference normal \mathbf{n}_0 on Γ_c^s at the point \mathbf{x} and the mapping R_0 , which now maps any point $\mathbf{x} \in \Gamma_c^s$ onto a point $R_0(\mathbf{x}) \in \Gamma_c^m$, by

$$[\mathbf{u}(\mathbf{x}, t)]_{n_0} := (\mathbf{u}^s(\mathbf{x}, t) - \mathbf{u}^m(R_0(\mathbf{x}), t))\mathbf{n}_0(\mathbf{x}), \quad (\mathbf{x}, t) \in \Gamma_c^s \times (0, T),$$

the linearized version of the non-penetration condition (1.17) states that

$$[\mathbf{u}(\mathbf{x}, t)]_{n_0} \leq g_0(\mathbf{x}), \quad (\mathbf{x}, t) \in \Gamma_c^s \times (0, T).$$

When using the linearized version of the non-penetration condition, one can replace the current contact pressure \mathbf{p}_c by the reference contact pressure \mathbf{p}_{0c} . Due to the transformation rule (1.10), the relation between these quantities is given by

$$\mathbf{p}_c(\mathbf{x}, t) = J^s(\mathbf{x}, t) \|\mathbf{F}^s(\mathbf{x}, t)^{-\top} \mathbf{n}_0(\mathbf{x}, t)\| \mathbf{p}_{0c}(\mathbf{x}, t), \quad (\mathbf{x}, t) \in \Gamma_c^s \times (0, T). \quad (1.21)$$

Furthermore, taking into account (1.15) the relation

$$\mathbf{p}_{0c}(\mathbf{x}, t) = -\mathbf{P}^i(\mathbf{x}, t) \mathbf{n}_0(\mathbf{x}), \quad (\mathbf{x}, t) \in \Gamma_c^s \times (0, T),$$

holds and Newton's law (1.14) can be formulated with respect to the reference configuration as

$$\mathbf{p}_{0c}(\mathbf{x}, t) = \mathbf{p}_{0c}^s(\mathbf{x}, t) = -\mathbf{p}_{0c}^m(R_0(\mathbf{x}), t), \quad (\mathbf{x}, t) \in \Gamma_c^s \times (0, T). \quad (1.22)$$

The linearized version of the contact constraints (1.17) now states that

$$[\mathbf{u}(\mathbf{x}, t)]_{n_0} \leq g_0(\mathbf{x}), \quad p_{0n}(\mathbf{x}, t) \geq 0, \quad p_{0n}(\mathbf{x}, t) \left([\mathbf{u}(\mathbf{x}, t)]_{n_0} - g_0(\mathbf{x}) \right) = 0, \quad (1.23)$$

and Coulomb's friction model using the reference pressure reads as

$$\begin{cases} \|\mathbf{p}_{0\tau}(\mathbf{x}, t)\| \leq \mathfrak{F} |p_{0n}(\mathbf{x}, t)|, \\ \|\mathbf{p}_{0\tau}(\mathbf{x}, t)\| < \mathfrak{F} |p_{0n}(\mathbf{x}, t)| \Rightarrow [\dot{\mathbf{u}}(\mathbf{x}, t)]_{\tau_0} = \mathbf{0}, \\ \|\mathbf{p}_{0\tau}(\mathbf{x}, t)\| = \mathfrak{F} |p_{0n}(\mathbf{x}, t)| \Rightarrow \exists \alpha \in \mathbb{R} : \mathbf{p}_{0\tau}(\mathbf{x}, t) = \alpha^2 [\dot{\mathbf{u}}(\mathbf{x}, t)]_{\tau_0}, \end{cases} \quad (1.24)$$

for $(\mathbf{x}, t) \in \Gamma_c^s \times (0, T)$, where the normal component \mathbf{p}_{0n} and the tangential vector and $\mathbf{p}_{0\tau}$ of the reference contact pressure \mathbf{p}_{0c} are defined according to (1.16). A rigorous mathematical derivation of the linearized version (1.23) can be found in the textbook [91].

1.2.2. Static contact constraints

In the static case the time derivative in the friction model (1.19) does not exist and friction does not make any sense from the physical point of view. Although, for, e.g., testing algorithms, often the relative sliding velocity $[\dot{\mathbf{u}}]_{\tau}$ is replaced by the tangential part of the displacement $[\mathbf{u}]_{\tau}$ in (1.19). Furthermore, we define the mapping $\widehat{R} : \Gamma_c^s \rightarrow \Gamma_c^m$ to map any final point $\boldsymbol{\varphi}^s(\mathbf{x})$ of the final contact boundary $\boldsymbol{\varphi}^s(\Gamma_c^s)$ to the intersection of the final normal $\mathbf{n}(\mathbf{x})$ on $\boldsymbol{\varphi}(\Gamma_c^s)$ at the point $\boldsymbol{\varphi}(\mathbf{x})$ with the final boundary $\boldsymbol{\varphi}^s(\Gamma_c^m)$ of the master body. With the help of \widehat{R} we can introduce the final gap

$$g(\mathbf{x}) := \|\boldsymbol{\varphi}(\mathbf{x}) - \widehat{R}(\mathbf{x})\|, \quad \mathbf{x} \in \Gamma_c^s,$$

the static form of the contact conditions is given by the non-penetration condition

$$g(\mathbf{x}) \leq 0, \quad p_n(\mathbf{x}) \geq 0, \quad g(\mathbf{x}) p_n(\mathbf{x}) = 0, \quad \mathbf{x} \in \Gamma_c^s. \quad (1.25)$$

Then, the static form of Newton's law (1.14) by

$$\mathbf{p}_c^s(\mathbf{x}) = -\mathbf{p}_c^m(\widehat{R}(\mathbf{x})), \quad \mathbf{x} \in \Gamma_c^s, \quad (1.26)$$

and the static form of Coulomb's friction model (1.19) by

$$\begin{cases} \|\mathbf{p}_\tau(\mathbf{x})\| \leq \mathfrak{F}|p_n(\mathbf{x})|, \\ \|\mathbf{p}_\tau(\mathbf{x})\| < \mathfrak{F}|p_n(\mathbf{x})| \Rightarrow [\mathbf{u}(\mathbf{x})]_\tau = \mathbf{0}, \\ \|\mathbf{p}_\tau(\mathbf{x})\| = \mathfrak{F}|p_n(\mathbf{x})| \Rightarrow \exists \alpha \in \mathbb{R} : \mathbf{p}_\tau(\mathbf{x}) = \alpha^2[\mathbf{u}(\mathbf{x})]_\tau, \end{cases} \quad \mathbf{x} \in \Gamma_c^s. \quad (1.27)$$

In the case of small deformations one can also use the linearized version of the contact conditions as in the previous section. The linearized version of the non-penetration condition (1.25) is exactly the same as (1.23),

$$[\mathbf{u}(\mathbf{x})]_{n_0} \leq g_0(\mathbf{x}), \quad p_{0n}(\mathbf{x}) \geq 0, \quad p_{0n}(\mathbf{x})([\mathbf{u}(\mathbf{x})]_{n_0} - g_0(\mathbf{x})) = 0, \quad \mathbf{x} \in \Gamma_c^s, \quad (1.28)$$

Newton's law (1.26) is replaced by

$$\mathbf{p}_{0c}^s(\mathbf{x}) = -\mathbf{p}_{0c}^m(R_0(\mathbf{x})), \quad \mathbf{x} \in \Gamma_c^s. \quad (1.29)$$

The static version of Coulomb's friction model with the reference contact pressure (1.24) reads

$$\begin{cases} \|\mathbf{p}_{0\tau}(\mathbf{x})\| \leq \mathfrak{F}|p_{0n}(\mathbf{x})|, \\ \|\mathbf{p}_{0\tau}(\mathbf{x})\| < \mathfrak{F}|p_{0n}(\mathbf{x})| \Rightarrow [\mathbf{u}(\mathbf{x})]_{\tau_0} = \mathbf{0}, \\ \|\mathbf{p}_{0\tau}(\mathbf{x})\| = \mathfrak{F}|p_{0n}(\mathbf{x})| \Rightarrow \exists \alpha \in \mathbb{R} : \mathbf{p}_{0\tau}(\mathbf{x}) = \alpha^2[\mathbf{u}(\mathbf{x})]_{\tau_0}, \end{cases} \quad \mathbf{x} \in \Gamma_c^s. \quad (1.30)$$

1.3. Constitutive equations

In this section, we present some possible material laws defining the stress-strain relation between the second Piola–Kirchhoff stress tensor \mathbf{S} , see (1.8), and the deformation gradient \mathbf{F} , see (1.2). To simplify the notation, we neglect the index $i = s, m$ which refers to the slave or the master side in the rest of this section. We restrict ourselves to hyper-elastic materials. A material is called hyper-elastic, if there exists a stored energy function $W(\mathbf{C})$ or $\widehat{W}(\mathbf{E})$ such that

$$\mathbf{S} = 2 \frac{\partial W}{\partial \mathbf{C}} \quad \text{or} \quad \mathbf{S} = \frac{\partial \widehat{W}}{\partial \mathbf{E}}, \quad (1.31)$$

respectively. In the literature this function is also called the response function. For an overview of elastic material laws we refer to [117, 131, 142]. For an isotropic material the energy function depends on the three invariants of the right Cauchy–Green strain tensor

$$I_C := \text{tr}(\mathbf{C}), \quad II_C := \frac{1}{2}((\text{tr}(\mathbf{C}))^2 - \text{tr}(\mathbf{C}^2)), \quad III_C := \det(\mathbf{C}) = J^2.$$

For the derivatives with respect to \mathbf{C} we find the relations, see, e.g., [142],

$$\begin{aligned}\frac{\partial}{\partial \mathbf{C}} J &= \frac{1}{2} J \mathbf{C}^{-1}, \\ \frac{\partial}{\partial \mathbf{C}} I_C &= \text{Id}_d, \\ \frac{\partial}{\partial \mathbf{C}} II_C &= I_C \text{Id}_d - \mathbf{C}, \\ \frac{\partial}{\partial \mathbf{C}} III_C &= III_C \mathbf{C}^{-1}.\end{aligned}\tag{1.32}$$

Next, we introduce the Lamé parameters λ and μ of the considered material. These constants are defined in terms of Young's modulus $E > 0$ and the Poisson ratio $\nu \in (0, 0.5)$ of the corresponding material by

$$\lambda := \frac{E\nu}{(1+\nu)(1-2\nu)}, \quad \mu := \frac{E}{2(1+\nu)}.\tag{1.33}$$

We remark that in the two-dimensional case ($d = 2$), the relations (1.33) refers to the situation of plain strain, whereas in the situation of plain stress one has to work with

$$\lambda := \frac{E\nu}{(1-\nu^2)}, \quad \mu := \frac{E}{2(1+\nu)}.$$

1.3.1. Saint Venant–Kirchhoff material

We consider a Saint Venant–Kirchhoff material. This material can be used to model large displacements and small strains. The energy function is given by

$$\widehat{W}(\mathbf{E}) := \frac{\lambda}{2} (\text{tr}(\mathbf{E}))^2 + \mu \text{tr}(\mathbf{E}^2).\tag{1.34}$$

The Green–Saint Venant strain tensor \mathbf{E} is given in (1.3). It depends nonlinearly on the displacement field \mathbf{u} . Using relation (1.31), we derive the second Piola–Kirchhoff stress tensor as

$$\mathbf{S} = \lambda \text{tr}(\mathbf{E}) \text{Id}_d + 2\mu \mathbf{E},\tag{1.35}$$

It is common to write (1.35) as

$$\mathbf{S}_{ij} = \mathcal{C}_{ijkl} \mathbf{E}_{kl}\tag{1.36}$$

with the symmetric fourth order material tensor \mathcal{C} given by

$$\mathcal{C}_{ijkl} := \lambda \delta_{ij} \delta_{kl} + \mu (\delta_{ik} \delta_{jl} + \delta_{il} \delta_{jk}),$$

where δ_{ij} denotes the well-known Kronecker symbol defined by

$$\delta_{ik} := \begin{cases} 1 & \text{if } i = k, \\ 0 & \text{if } i \neq k. \end{cases}\tag{1.37}$$

Equation (1.36) is also known as Hooke's law. In the literature it is common to denote this law as linear elasticity, since the relation between the strain \mathbf{E} and the stress \mathbf{S} is linear.

In the case of small deformations and small strains often the geometric linearization of (1.35) is used. The linearized version of the first Piola–Kirchhoff stress tensor $\mathbf{P} = \mathbf{F}\mathbf{S}$ with the second Piola–Kirchhoff stress tensor (1.35) is used. Therefore \mathbf{P} is replaced by the linearized stress tensor

$$\boldsymbol{\sigma} := \lambda \operatorname{tr}(\boldsymbol{\varepsilon}) \operatorname{Id}_d + 2\mu \boldsymbol{\varepsilon}, \quad (1.38)$$

where the linearized strain tensor $\boldsymbol{\varepsilon}$ is the linearized version of the Green–Saint Venant strain tensor \mathbf{E} , see (1.3), given by

$$\boldsymbol{\varepsilon} := \frac{1}{2}(\nabla \mathbf{u} + (\nabla \mathbf{u})^\top). \quad (1.39)$$

This linearized law is also named as linearized elasticity.

1.3.2. Mooney–Rivlin material

The Mooney–Rivlin material law describes the situation of large displacements and large strains. For this material law, the energy function depends on the first and the second invariant I_C and II_C , respectively. In the most general form it is given by

$$W(\mathbf{C}) := \lambda g_i(J) - \mu \ln(J) + \frac{\mu}{2} \left((1 - c_m)(I_C - d) + c_m(II_C - d) \right), \quad (1.40)$$

where c_m is an additional parameter. The additional function $g_i(J)$ can be defined in different ways as

$$\text{case 1: } \quad g_1(J) := \frac{1}{4}(J^2 - 1 - 2\ln(J)), \quad (1.41a)$$

$$\text{case 2: } \quad g_2(J) := \frac{1}{4}(J - 1)^2, \quad (1.41b)$$

$$\text{case 3: } \quad g_3(J) := \frac{1}{2}(\ln(J))^2. \quad (1.41c)$$

We remark that we get (1.41b) by using the Taylor expansion $\ln(J) \approx J - 1$ in (1.41a). Differentiating equation (1.40) with respect to right Cauchy tensor \mathbf{C} leads with (1.32) to

$$\frac{\partial W}{\partial \mathbf{C}} = \lambda \frac{\partial g_i}{\partial \mathbf{C}} - \frac{\mu}{2} \mathbf{C}^{-1} + \frac{\mu}{2} \left((1 - c_m) \operatorname{Id}_d + c_m(I_C \operatorname{Id}_d - \mathbf{C}) \right),$$

where the terms $\frac{\partial g_i}{\partial \mathbf{C}}$ for the three different cases are given by

$$\frac{\partial g_1}{\partial \mathbf{C}} = \frac{1}{4}(J^2 - 1) \mathbf{C}^{-1},$$

$$\frac{\partial g_2}{\partial \mathbf{C}} = \frac{1}{4}J(J - 1) \mathbf{C}^{-1},$$

$$\frac{\partial g_3}{\partial \mathbf{C}} = \frac{1}{2} \ln(J) \mathbf{C}^{-1}.$$

Therefore, we get for the second Piola-Kirchhoff stress tensor due to (1.31)

$$\mathbf{S} = 2\lambda \frac{\partial g_i}{\partial \mathbf{C}} - \mu \mathbf{C}^{-1} + \mu \left((1 - c_m) \text{Id}_d + c_m (I_C \text{Id}_d - \mathbf{C}) \right).$$

Consequently, the first Piola-Kirchhoff stress tensor $\mathbf{P} = \mathbf{F}\mathbf{S}$ can be written as

$$\mathbf{P} = G_i(J, \mathbf{F}) - \mu \mathbf{F}^{-\top} + \mu \left((1 - c_m) \mathbf{F} + c_m (I_C \mathbf{F} - \mathbf{F}\mathbf{C}) \right),$$

where we used the abbreviation $G_i(J, \mathbf{F}) := 2\lambda \mathbf{F} \frac{\partial g_i}{\partial \mathbf{C}}$. For the three cases, these terms are given by the expressions

$$G_1(J, \mathbf{F}) = \frac{\lambda}{2} (J^2 - 1) \mathbf{F}^{-\top}, \quad (1.42a)$$

$$G_2(J, \mathbf{F}) = \frac{\lambda}{2} J(J - 1) \mathbf{F}^{-\top}, \quad (1.42b)$$

$$G_3(J, \mathbf{F}) = \lambda \ln(J) \mathbf{F}^{-\top}. \quad (1.42c)$$

1.3.3. Neo-Hookean material

The neo-Hookean material law is a special case of the Mooney-Rivlin material law presented in the last subsection. Using the parameter $c_m = 0$ in (1.40), we get the energy function (1.31) as

$$W(\mathbf{C}) := \lambda g_i(J) - \mu \ln(J) + \frac{\mu}{2} (I_C - d). \quad (1.43)$$

The energy function of the neo-Hookean material depends only on the first invariant I_C of \mathbf{C} and its determinant J . Following Subsection 1.3.2 one ends up with the first Piola-Kirchhoff stress tensor

$$\mathbf{P} = G_i(J, \mathbf{F}) + \mu (\mathbf{F} - \mathbf{F}^{-\top}),$$

where the expressions for the three cases of the terms $G_i(J, \mathbf{F})$ are given in (1.42).

Part II.

Discretization techniques

2. Hybrid variational formulation and space discretization

In this chapter, we introduce the hybrid variational formulation and the discretization of the dynamical contact problem with the linearized contact conditions (1.23), (1.24) introduced in Subsection 1.2.1. In contrast to the widely used penalty approach, see, e.g., [92], for variational inequalities in contact mechanics, we apply mortar techniques. Since we have to deal with nonmatching meshes, mortar discretization techniques are a promising tool to handle such type of problems.

To compare the mortar approach with other possible contact formulations, we like to mention that both the node-to-segment approach and the segment-to-segment approach can be used in the case of a nonconforming situation, whereas the node-to-node formulation can only be used for a conforming mesh. In contrast to the node-to-segment approach, where the non-penetration condition holds in a strong point-wise sense only at the nodes of the finite element mesh, the mortar method allows us to fulfill the inequalities for the non-penetration condition and the friction bound in a weak integral sense. Thus, in some situations the mortar formulation can lead to a more better fulfillment of the non-penetration condition. In the widely used penalty approach, we have a non-physical violation of these inequalities even in the weak integral sense depending on the penalty parameter. Furthermore, by using mortar techniques, we avoid the difficulties with the large condition number of the stiffness matrix occurring in the penalty approach. A further advantage of the mortar method is the fact, that the so called patch test is fulfilled, i.e., constant contact forces are transmitted correctly to the other body. This is not the case for the node-to-segment formulation, see [45, 118]. Furthermore, [50] shows that a point-wise coupling approach may lead to suboptimal error decay. For details concerning all these approaches, we refer to [91, 92, 106, 135, 143] and the references therein. The combination of the penalty and the mortar-approach leads to the augmented Lagrangian formulation, see, e.g., [25, 110, 128]. Formulations based on an additional stabilization term are given in [68].

This chapter introduces the hybrid variational formulation also referred to as mortar formulation or mixed formulation and considers a discretization technique based on dual basis functions for the additional unknown referred to as Lagrange multiplier. The mortar method was originally introduced in [11, 12]. Since mortar techniques are a promising tool to handle non-matching meshes, there is a highly active research on their application to contact problems. Mortar techniques with standard Lagrange multiplier spaces for contact problems have been considered and analyzed in, e.g., [9, 10, 33, 48, 49, 72, 73, 113, 119, 120, 145]. Due to the wide range of activities in this field, we remark that this list cannot be exhaustive. In this thesis, we apply these techniques to Lagrange multiplier

spaces with dual basis functions introduced in [136] and used in the context of contact problems already in [98, 141]. The main advantage of using dual basis functions for the Lagrange multiplier is that the resulting coupling matrix is diagonal and thus the contact constraints decouple into a local condition for each node on the contact boundary after applying locally a suitable basis transformation of the finite element basis, see [84, 140]. This allows the construction of efficient numerical algorithms for the arising nonlinear equations. Due to the use of dual basis functions for the Lagrange multiplier, these additional unknowns can be eliminated in a local efficient way. Thus, in each step of the iterative solution algorithm only a linear system with the same complexity as in the penalty approach but with a good condition number has to be solved.

2.1. Mortar formulation in terms of inequalities

In the following we obtain the weak variational formulation based on mortar techniques for contact problems. In Subsection 2.1.1 we introduce the Lagrange multiplier. The variational formulation is stated in Subsection 2.1.2. In Subsection 2.1.3 we show that the variational inequality fulfills the strong point-wise contact constraints in a weak sense. Finally, we give further possible variational formulations in Subsection 2.1.4.

2.1.1. Lagrange multiplier

The hybrid or mortar formulation is based on the introduction of the so called Lagrange multiplier or dual variable $\boldsymbol{\lambda}$ as an additional unknown modeling the contact stress

$$\boldsymbol{\lambda}(\mathbf{x}, t) := \mathbf{p}_{0c}^s(\mathbf{x}, t), \quad \mathbf{x} \in \Gamma_c^s \times (0, T).$$

This additional variable is necessary to enforce the contact constraints in our weak integral variational formulation. With this notation, the linearized contact constraints (1.23) and (1.24) can be rewritten as

$$[\mathbf{u}(\mathbf{x}, t)]_n \leq g(\mathbf{x}), \quad \lambda_n(\mathbf{x}, t) \geq 0, \quad \lambda_n(\mathbf{x}, t)([\mathbf{u}(\mathbf{x}, t)]_n - g(\mathbf{x})) = 0 \quad (2.1)$$

and

$$\begin{cases} \|\boldsymbol{\lambda}_\tau(\mathbf{x}, t)\| \leq \mathfrak{F}|\lambda_n(\mathbf{x}, t)|, \\ \|\boldsymbol{\lambda}_\tau(\mathbf{x}, t)\| < \mathfrak{F}|\lambda_n(\mathbf{x}, t)| \Rightarrow [\dot{\mathbf{u}}(\mathbf{x}, t)]_\tau = \mathbf{0}, \\ \|\boldsymbol{\lambda}_\tau(\mathbf{x}, t)\| = \mathfrak{F}|\lambda_n(\mathbf{x}, t)| \Rightarrow \exists \alpha \in \mathbb{R} : \boldsymbol{\lambda}_\tau(\mathbf{x}, t) = \alpha^2[\dot{\mathbf{u}}(\mathbf{x}, t)]_\tau. \end{cases} \quad (2.2)$$

Here, the normal component λ_n and the tangential part $\boldsymbol{\lambda}_\tau$ are given according to (1.16) with respect to the reference normal \mathbf{n}_0 . To simplify the notation, we write from now on \mathbf{n} and $(\cdot)_\tau$ instead of \mathbf{n}_0 and $(\cdot)_{\tau_0}$, respectively, and g instead of g_0 .

2.1.2. Variational formulation

We start with the introduction of the necessary functional spaces for the primal variable \mathbf{u}^i and for the dual variable $\boldsymbol{\lambda}$. These functions spaces are the well-known Sobolev

spaces on the domain or the boundary. For the definition of these spaces we refer, e.g., to [1, 17, 114]. The vector valued spaces \mathbf{V}^i , $i = s, m$, contain the admissible displacement fields \mathbf{u}^i for each subdomain Ω^i ,

$$\mathbf{V}^i := \left\{ \mathbf{u}^i \in [H^1(\Omega^i)]^d : \mathbf{u}^i|_{\Gamma_D^i} = \mathbf{u}_D^i \right\},$$

while the corresponding product space is given by $\mathbf{V} := \mathbf{V}^s \times \mathbf{V}^m$. For the test space, we have to use functions satisfying zero Dirichlet boundary conditions on Γ_D^i , denoted by $\mathbf{V}_0 := \mathbf{V}_0^s \times \mathbf{V}_0^m$. We define the space \mathbf{M} as the dual space of the trace space \mathbf{W} of \mathbf{V}_0^s restricted to Γ_c^s . If $\bar{\Gamma}_c^s$ is a compact subset of $\partial\Omega^s \setminus \bar{\Gamma}_D^s$, we have $\mathbf{W} = [H^{1/2}(\Gamma_c^s)]^d$ and $\mathbf{M} = [H_{00}^{-1/2}(\Gamma_c^s)]^d$, otherwise we have $\mathbf{W} = [H_{00}^{1/2}(\Gamma_c^s)]^d$ and $\mathbf{M} = [H^{-1/2}(\Gamma_c^s)]^d$. Introducing $\mathbf{v} = (\mathbf{v}^s, \mathbf{v}^m)$ and $\langle \cdot, \cdot \rangle$ as the duality pairing between the spaces \mathbf{M} and \mathbf{V} on Γ_c^s given by

$$\langle \boldsymbol{\lambda}, \mathbf{v} \rangle := \int_{\Gamma_c^s} \boldsymbol{\lambda} \mathbf{v} \, ds,$$

the admissible space for the Lagrange multiplier $\boldsymbol{\lambda}$ is the convex subset $\mathbf{M}(\boldsymbol{\lambda}) \subset \mathbf{M}$ given by

$$\mathbf{M}(\boldsymbol{\lambda}) := \left\{ \boldsymbol{\mu} \in \mathbf{M} : \langle \boldsymbol{\mu}, \boldsymbol{\eta} \rangle \leq \langle \boldsymbol{\lambda}, \boldsymbol{\eta} \rangle, \boldsymbol{\eta} \in \mathbf{W} \text{ with } \eta_n \leq 0 \right\}. \quad (2.3)$$

Multiplying equation (1.12a) with a test function $\mathbf{v}^i \in \mathbf{V}_0^i$, integration over Ω^i , applying partial integration and summation over $i = s, m$, together with the boundary conditions (1.12b) and Newton's law (1.22) leads to

$$m(\ddot{\mathbf{u}}, \mathbf{v}) + a(\mathbf{u}, \mathbf{v}) + \langle \boldsymbol{\lambda}, [\mathbf{v}] \rangle = f(\mathbf{v}), \quad (2.4)$$

where the bilinear form $m(\cdot, \cdot)$ and the form $a(\cdot, \cdot)$ are given by

$$\begin{aligned} m(\mathbf{u}, \mathbf{v}) &:= \sum_{i=s,m} \int_{\Omega^i} \varrho^i \mathbf{u}^i \mathbf{v}^i \, dx, \\ a(\mathbf{u}, \mathbf{v}) &:= \sum_{i=s,m} \int_{\Omega^i} \mathbf{P}^i(\mathbf{u}^i) : \nabla \mathbf{v}^i \, dx. \end{aligned}$$

We remark that in the case of linearized elasticity, see (1.38), the form $a(\cdot, \cdot)$ is bilinear. For general nonlinear material laws as introduced in Section 1.3, $a(\cdot, \cdot)$ is only linear in the second argument. The linear form $f(\cdot)$ is defined by

$$f(\mathbf{v}) := \sum_{i=s,m} \int_{\Omega^i} \mathbf{f}^i \mathbf{v}^i \, dx + \sum_{i=s,m} \int_{\Gamma_N^i} \mathbf{p}^i \mathbf{v}^i \, ds.$$

The weak form of the linearized mechanical contact conditions (2.1) and (2.2) amounts to [56, 81, 84],

$$\boldsymbol{\lambda} \in \mathbf{M}(\boldsymbol{\lambda}) : \quad \langle [\mathbf{u}]_n, \mu_n - \lambda_n \rangle + \langle [\dot{\mathbf{u}}]_\tau, \boldsymbol{\mu}_\tau - \boldsymbol{\lambda}_\tau \rangle \leq \langle g, \mu_n - \lambda_n \rangle, \quad \boldsymbol{\mu} \in \mathbf{M}(\boldsymbol{\lambda}). \quad (2.5)$$

A detailed discussion of this variational inequality is given in Subsection 2.1.3.

Summarizing (2.4) and (2.5), we end up with the variational formulation of the dynamical contact problem: find $(\mathbf{u}, \boldsymbol{\lambda}) \in \mathbf{V} \times \mathbf{M}(\boldsymbol{\lambda})$ such that for all $t \in (0, T)$

$$m(\ddot{\mathbf{u}}, \mathbf{v}) + a(\mathbf{u}, \mathbf{v}) + \langle [\mathbf{v}], \boldsymbol{\lambda} \rangle = f(\mathbf{v}), \quad \mathbf{v} \in \mathbf{V}_0, \quad (2.6a)$$

$$\langle [\mathbf{u}]_n, \mu_n - \lambda_n \rangle + \langle [\dot{\mathbf{u}}]_\tau, \boldsymbol{\mu}_\tau - \boldsymbol{\lambda}_\tau \rangle \leq \langle g, \mu_n - \lambda_n \rangle, \quad \boldsymbol{\mu} \in \mathbf{M}(\boldsymbol{\lambda}), \quad (2.6b)$$

together with the weak form of the initial conditions (1.12d) and (1.12e), namely

$$(\mathbf{u}(\cdot, 0), \mathbf{v}) = 0, \quad (\dot{\mathbf{u}}(\cdot, 0), \mathbf{v}) = (\mathbf{v}_0, \mathbf{v}), \quad \mathbf{v} \in \mathbf{V}_0, \quad (2.7)$$

where (\cdot, \cdot) denotes the standard L^2 -scalar product on $\Omega := \Omega^s \cup \Omega^m$.

2.1.3. Variational inequalities

In this subsection we want to show that the weak form (2.5) fulfills the strong contact constraints in a weak sense. Therefore we prove that the strong point-wise non-penetration condition (2.1) is equivalent to the variational inequality

$$\lambda_n \in \mathbb{R}_0^+ : \quad ([\mathbf{u}]_n - g)(\mu_n - \lambda_n) \leq 0, \quad \mu_n \in \mathbb{R}_0^+, \quad (2.8)$$

at each point $\mathbf{x} \in \Gamma_c^s$ and each time $t \in (0, T)$, where \mathbb{R}_0^+ denotes the semi-positive real half-space. The corresponding variational inequality for the strong point-wise friction condition (2.2) reads as

$$\boldsymbol{\lambda}_\tau \in \mathcal{B}(\mathfrak{F}\lambda_n) : \quad [\dot{\mathbf{u}}]_\tau(\boldsymbol{\mu}_\tau - \boldsymbol{\lambda}_\tau) \leq 0, \quad \boldsymbol{\mu}_\tau \in \mathcal{B}(\mathfrak{F}\lambda_n), \quad (2.9)$$

for $(\mathbf{x}, t) \in \Gamma_c^s \times (0, T)$, where $\mathcal{B}(\mathfrak{F}\lambda_n)$ denotes the $(d-1)$ -dimensional sphere with center $\mathbf{0}$ and radius $\mathfrak{F}\lambda_n$. The variational inequality (2.5) states the weak form of the conditions (2.8) and (2.9), and the subset $\mathbf{M}(\boldsymbol{\lambda})$ of the weak analogue the semi-positive half-space \mathbb{R}_0^+ for the normal part and the sphere $\mathcal{B}(\mathfrak{F}\lambda_n)$ for the tangential part. To show this we start from the definition of $\mathbf{M}(\boldsymbol{\lambda})$ introduced in (2.3) and deduce for any $\boldsymbol{\mu} \in \mathbf{M}(\boldsymbol{\lambda})$ for $\boldsymbol{\eta} = \eta_n \mathbf{n} \in \mathbf{W}$ with $\eta_n \leq 0$ the relation

$$\langle \boldsymbol{\mu}, \boldsymbol{\eta} \rangle = \langle \mu_n, \eta_n \rangle \leq 0, \quad \eta_n \leq 0.$$

Therefore, each function $\boldsymbol{\mu} \in \mathbf{M}(\boldsymbol{\lambda})$ satisfies $\mu_n \geq 0$ in a weak integral sense. Choosing $\boldsymbol{\eta} = (\|\boldsymbol{\eta}_\tau\|/\|\boldsymbol{\mu}_\tau\|)\boldsymbol{\mu}_\tau$ in the definition of $\mathbf{M}(\boldsymbol{\lambda})$, where we assume $\boldsymbol{\lambda}$ to be smooth enough, we get

$$\langle \boldsymbol{\mu}, \boldsymbol{\eta} \rangle = \langle \|\boldsymbol{\mu}_\tau\|, \|\boldsymbol{\eta}_\tau\| \rangle \leq \langle \mathfrak{F}\lambda_n, \|\boldsymbol{\eta}_\tau\| \rangle.$$

Obviously each function $\boldsymbol{\mu} \in \mathbf{M}(\boldsymbol{\lambda})$ fulfills the strong point-wise condition $\|\boldsymbol{\mu}_\tau\| \leq \mathfrak{F}\lambda_n$ in the weak form. Therefore the subset $\mathbf{M}(\boldsymbol{\lambda})$ is the weak analogue to the strong point-wise subset $\mathbb{R}_0^+ \cap \mathcal{B}(\mathfrak{F}\lambda_n)$.

To show that (2.1) results from (2.8) we use in (2.8) the function $\lambda_n + \mu_n \geq 0$, with $\mu_n \geq 0$. Then, we observe

$$([\mathbf{u}]_n - g)\mu_n \leq 0, \quad \mu_n \in \mathbb{R}_0^+,$$

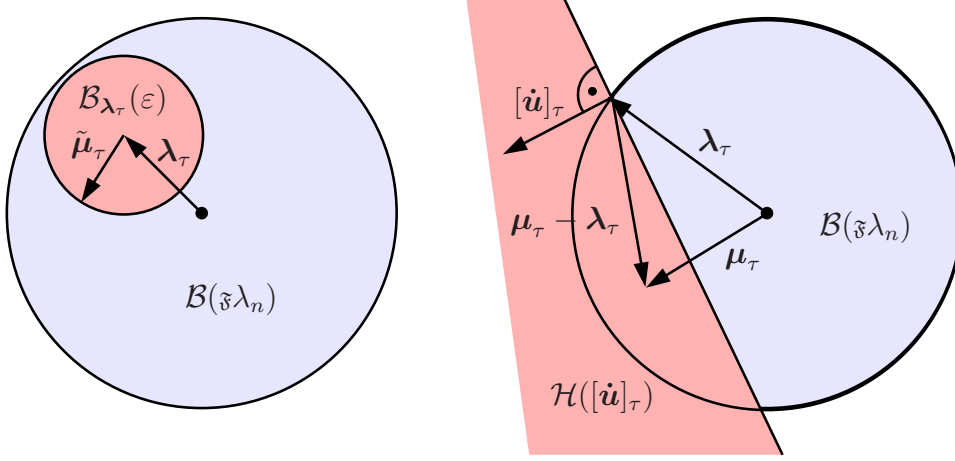


Figure 2.1.: Illustration of variational inequality (2.9).

and therefore the non-penetration condition $[\mathbf{u}]_n \leq g$ in (2.1) holds. To deduce the condition $\lambda_n([\mathbf{u}]_n - g) = 0$ from (2.8), we obtain by choosing $\mu_n = 0 \in \mathbb{R}_0^+$ that

$$-([\mathbf{u}]_n - g)\lambda_n \leq 0,$$

and by choosing $\mu_n = 2\lambda_n \in \mathbb{R}_0^+$ that

$$([\mathbf{u}]_n - g)\lambda_n \leq 0.$$

Combining both inequalities leads to the desired relation

$$([\mathbf{u}]_n - g)\lambda_n = 0.$$

Next, we prove by means of the illustrations of Figure 2.1 that the frictional conditions (2.2) can be deduced from the variational inequality (2.9). In the case $\|\boldsymbol{\lambda}_\tau\| < \xi\lambda_n$, we can find a $(d-1)$ -dimensional sphere $\mathcal{B}_{\boldsymbol{\lambda}_\tau}(\varepsilon)$ with center $\boldsymbol{\lambda}_\tau$ and radius $\varepsilon > 0$, such that $\mathcal{B}_{\boldsymbol{\lambda}_\tau}(\varepsilon) \subset \mathcal{B}(\xi\lambda_n)$ holds as indicated in the left picture in Figure 2.1. For any $\tilde{\boldsymbol{\mu}}_\tau$ with $\|\tilde{\boldsymbol{\mu}}_\tau\| = \varepsilon$ we get for $\boldsymbol{\mu}_\tau := \boldsymbol{\lambda}_\tau + \tilde{\boldsymbol{\mu}}_\tau \in \mathcal{B}(\xi\lambda_n)$. Inserting this $\boldsymbol{\mu}_\tau$ into (2.9) leads to the relation

$$[\dot{\mathbf{u}}]_\tau \tilde{\boldsymbol{\mu}}_\tau \leq 0.$$

Since the vector $\tilde{\boldsymbol{\mu}}_\tau$ with $\|\tilde{\boldsymbol{\mu}}_\tau\| = \varepsilon$ was arbitrary we conclude $[\dot{\mathbf{u}}]_\tau = 0$. For the case $\|\boldsymbol{\lambda}_\tau\| = \xi\lambda_n$, we consider the hyper-plane $\mathcal{H}([\dot{\mathbf{u}}]_\tau)$

$$\mathcal{H}([\dot{\mathbf{u}}]_\tau) := \{\boldsymbol{\eta}_\tau \in \mathbb{R}^{d-1} : [\dot{\mathbf{u}}]_\tau(\boldsymbol{\eta}_\tau - \boldsymbol{\lambda}_\tau) > 0\}.$$

For the definition of this hyper-plane, we refer to the right picture in Figure 2.1. If we cannot find any $\alpha \in \mathbb{R}$, such that $\boldsymbol{\lambda}_\tau = \alpha^2[\dot{\mathbf{u}}]_\tau$, we observe that the intersection between the half-plane $\mathcal{H}([\dot{\mathbf{u}}]_\tau)$ and the sphere $\mathcal{B}(\xi\lambda_n)$ is not empty. Then, for each vector $\boldsymbol{\mu}_\tau \in \mathcal{H}([\dot{\mathbf{u}}]_\tau) \cap \mathcal{B}(\xi\lambda_n)$, we find

$$[\dot{\mathbf{u}}]_\tau(\boldsymbol{\mu}_\tau - \boldsymbol{\lambda}_\tau) > 0,$$

see Figure 2.1. Therefore the variational inequality (2.9) is not fulfilled and thus condition $\boldsymbol{\lambda}_\tau = \alpha^2[\dot{\mathbf{u}}]_\tau$ is a direct consequence from the variational inequality (2.9) for the case $\|\boldsymbol{\lambda}_\tau\| = \mathfrak{F}\lambda_n$. Moreover, we mention that the variational inequalities (2.8) and (2.9) are an immediate consequence of the strong point-wise contact constraints (2.1) and (2.2), respectively. Thus, both formulations are equivalent.

Before we provide an overview over further possible variational formulations in Subsection 2.1.4, we give the following remark concerning the equivalence between the variational inequalities (2.8) and (2.9) and appropriate projection operators:

Remark 2.1. The variational inequality (2.8) can be rewritten for any $c > 0$ as

$$((\lambda_n + c([\mathbf{u}]_n - g)) - \lambda_n)(\mu_n - \lambda_n) \leq 0, \quad \mu_n \in \mathbb{R}_0^+.$$

Since this relation can be interpreted as the definition of the projection operator $\text{Proj}_{\mathbb{R}_0^+}(\cdot)$ onto \mathbb{R}_0^+ we can rewrite (2.1) as

$$\lambda_n = \text{Proj}_{\mathbb{R}_0^+}(\lambda_n + c([\mathbf{u}]_n - g)), \quad (2.10)$$

see, e.g., [44, 52, 53]. Furthermore, we get from the variational inequality (2.9) the relation

$$((\boldsymbol{\lambda}_\tau + c[\dot{\mathbf{u}}]_\tau) - \boldsymbol{\lambda}_\tau)(\boldsymbol{\mu}_\tau - \boldsymbol{\lambda}_\tau) \leq 0, \quad \boldsymbol{\mu}_\tau \in \mathcal{B}(\mathfrak{F}\lambda_n).$$

From this we deduce the equivalence of the friction condition (2.2) to

$$\boldsymbol{\lambda}_\tau = \text{Proj}_{\mathcal{B}(\mathfrak{F}\lambda_n)}(\boldsymbol{\lambda}_\tau + c[\dot{\mathbf{u}}]_\tau), \quad (2.11)$$

where $\text{Proj}_{\mathcal{B}(\mathfrak{F}\lambda_n)}(\cdot)$ is the projection operator onto $\mathcal{B}(\mathfrak{F}\lambda_n)$.

2.1.4. Alternative formulations

In this subsection we shortly present variational formulations working without Lagrange multipliers, an equivalent minimization approach and the characterization of the solution as a saddle point for the static case. The static version can be obtained from (2.6) by neglecting the mass term $m(\cdot, \cdot)$ and by replacing $[\dot{\mathbf{u}}]_\tau$ by $[\mathbf{u}]_\tau$. For details and an overview about the wide field of theoretical aspects of variational inequalities we refer to [14, 40, 53, 54, 60, 63, 91].

Introducing the convex subset \mathbf{K} of \mathbf{V} by

$$\mathbf{K} := \{\mathbf{v} \in \mathbf{V} : [v]_n \leq g\}$$

and the friction functional $j(\cdot, \cdot) : \mathbf{V} \times \mathbf{V} \rightarrow \mathbb{R}$ via

$$j(\mathbf{u}, \mathbf{v}) := \int_{\Gamma_c^s} \mathfrak{F}|p_n(\mathbf{u})| \|[\mathbf{v}]_\tau\| \, ds$$

with the normal part of the contact stress $p_n(\mathbf{u}) = \mathbf{p}_{0c}^s((\mathbf{u}(\mathbf{x}, t)))$, an equivalent variational formulation is given by: find $\mathbf{u} \in \mathbf{K}$ such that

$$a(\mathbf{u}, \mathbf{v} - \mathbf{u}) + j(\mathbf{u}, \mathbf{v}) - j(\mathbf{u}, \mathbf{u}) \geq f(\mathbf{v} - \mathbf{u}), \quad \mathbf{v} \in \mathbf{K}.$$

In the case of a constant friction bound g_f instead of $\mathfrak{F}|p_n(\mathbf{u})|$, the solution can alternatively be obtained by a minimization process. Defining the energy functional $\mathcal{J}(\cdot) : \mathbf{V} \rightarrow \mathbb{R}$ via

$$\mathcal{J}(\mathbf{v}) := \frac{1}{2}a(\mathbf{v}, \mathbf{v}) + j(\mathbf{v}) - f(\mathbf{v}),$$

where now the functional $j(\cdot)$ is given by

$$j(\mathbf{v}) := \int_{\Gamma_c^s} g_f \|[\mathbf{v}]_\tau\| \, ds,$$

the solution can be characterized by the minimum

$$\mathcal{J}(\mathbf{u}) = \min_{\mathbf{v} \in \mathbf{K}} \mathcal{J}(\mathbf{v}).$$

Finally, we characterize for the case without friction, i.e., $g_f = 0$ or $\mathfrak{F} = 0$ in (2.6), the solution $(\mathbf{u}, \boldsymbol{\lambda})$ of the static version of (2.6) as a saddle point. In this case, the space $\mathbf{M}(\boldsymbol{\lambda})$ defined in (2.3) is independent of $\boldsymbol{\lambda}$, since $\boldsymbol{\lambda}_\tau = \mathbf{0}$, and we write \mathbf{M}_+ instead of $\mathbf{M}(\boldsymbol{\lambda})$. The subscript $+$ is motivated due to the fact that the normal part of the functions in \mathbf{M}_+ are positive. Introducing the Lagrange functional $\mathcal{L}(\cdot, \cdot) : \mathbf{V} \times \mathbf{M}_+ \rightarrow \mathbb{R}$ by

$$\mathcal{L}(\mathbf{v}, \boldsymbol{\mu}) := \frac{1}{2}a(\mathbf{v}, \mathbf{v}) - f(\mathbf{v}) + \langle [\mathbf{u}]_n - g, \boldsymbol{\mu}_n \rangle,$$

the solution $(\mathbf{u}, \boldsymbol{\lambda}) \in \mathbf{V} \times \mathbf{M}_+$ can be characterized as the saddle point

$$\mathcal{L}(\mathbf{u}, \boldsymbol{\mu}) \leq \mathcal{L}(\mathbf{u}, \boldsymbol{\lambda}) \leq \mathcal{L}(\mathbf{v}, \boldsymbol{\lambda}), \quad \mathbf{v} \in \mathbf{V}, \quad \boldsymbol{\mu} \in \mathbf{M}_+.$$

2.2. Space discretization

In this section, we derive the discrete form of the hybrid variational formulation (2.6). To approximate the continuous spaces \mathbf{V} and \mathbf{V}_0 , we use standard conforming finite elements of lowest order on simplicial and quadrilateral ($d = 2$) or tetrahedral and hexahedral ($d = 3$) meshes. The triangulation of the body Ω^i is denoted by \mathcal{T}_{h,Ω^i} and we define $\mathcal{T}_{h,\Omega} := \mathcal{T}_{h,\Omega^s} \cup \mathcal{T}_{h,\Omega^m}$. Let h_T be the diameter of the element $T \in \mathcal{T}_{h,\Omega}$. Then the meshsize h is defined by the maximum diameter of all elements

$$h := \max_{T \in \mathcal{T}_{h,\Omega}} h_T.$$

The triangulation $\mathcal{T}_{h,\Omega}$ is called shape-regular if and only if there exists a constant $c > 0$, such that

$$\rho_T \geq ch_T, \quad T \in \mathcal{T}_{h,\Omega},$$

where ρ_T denotes the diameter of a inscribed ball of the element T . Furthermore, we assume the triangulation to be quasi-uniform, i.e., there exists a constant $c > 0$, such that

$$h_T \geq ch, \quad T \in \mathcal{T}_{h,\Omega}.$$

The triangulations on the higher level of the family $\{\mathcal{T}_{h,\Omega}\}_h$ of triangulations are obtained by uniform refinement techniques from the initial triangulation.

The finite element space associated with the triangulation \mathcal{T}_{h,Ω^i} is denoted by $\mathcal{S}_1^i := S_1(\Omega^i, \mathcal{T}_{h,\Omega^i})$. To introduce the discrete function spaces, we define the vector valued space $\mathbf{V}^{i,h} \subset [H^1(\Omega^i)]^d$ as the discrete counterpart of the continuous space $\mathbf{V}^i = [H^1(\Omega^i)]^d$ on each subdomain $i = s, m$ by

$$\mathbf{V}^{i,h} := \left\{ \mathbf{u}^i \in [\mathcal{S}_1^i]^d : \mathbf{u}^i|_{\Gamma_D^i} = \mathbf{u}_D^i \right\}.$$

We remark that if the Dirichlet data \mathbf{u}_D^i not resolved by the discrete space $\mathbf{V}^{i,h}$, we have to work with an appropriate approximation for \mathbf{u}_D^i . The corresponding product space is given by $\mathbf{V}^h := \mathbf{V}^{s,h} \times \mathbf{V}^{m,h}$. As test spaces, we have to use spaces satisfying zero Dirichlet boundary conditions given by $\mathbf{V}_0^h := \mathbf{V}_0^{s,h} \times \mathbf{V}_0^{m,h}$ with

$$\mathbf{V}_0^{i,h} := \left\{ \mathbf{v}^i \in [\mathcal{S}_1^i]^d : \mathbf{v}^i|_{\Gamma_D^i} = \mathbf{0} \right\}.$$

As common, we write any function $\boldsymbol{\xi} \in \mathbf{V}^h$ or $\boldsymbol{\xi} \in \mathbf{V}_0^h$ as $\boldsymbol{\xi} = (\boldsymbol{\xi}^s, \boldsymbol{\xi}^m)$. We remark that the space \mathbf{V}^h depends on time, if the Dirichlet data \mathbf{u}_D^i are not constant over time. But to simplify the notation, we neglect this time index. The space \mathbf{V}^h can be spanned by the standard nodal basis $\{\phi_p \mathbf{e}_k, p = 1, \dots, N_V, k = 1, \dots, d\}$, where \mathbf{e}_k denotes the k -th unit vector and ϕ_p the scalar standard nodal basis function associated with the node p . The number N_V is the total number of the nodes of the finite element mesh.

2.2.1. Dual basis functions

As it is standard in the mortar context, the Lagrange multiplier space inherits its $(d-1)$ -dimensional mesh from the d -dimensional triangulation on the slave side. We assume that Γ_c^s can be written as union of element faces on the slave side. Here, we use discontinuous piecewise linear or bilinear nodal dual basis functions for the Lagrange multiplier as introduced in [136] for the two-dimensional case. The dual or biorthogonal basis functions ψ_p with $\text{supp}(\psi_p) = \text{supp}(\phi_p)$ for the Lagrange multipliers satisfy the orthogonality relation

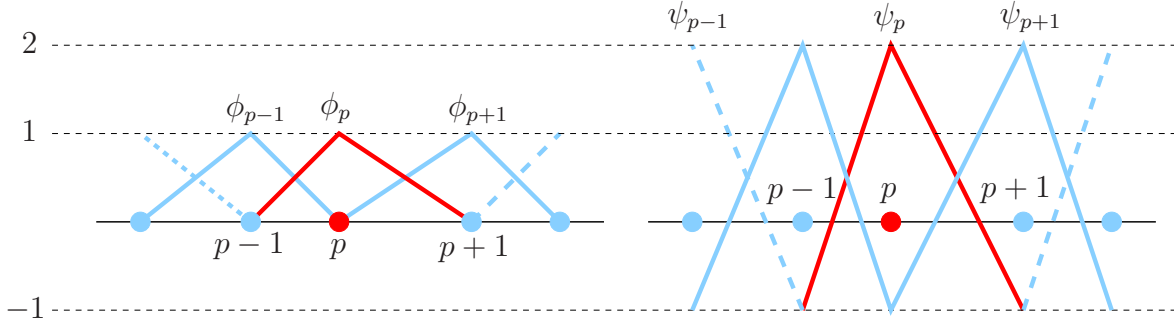
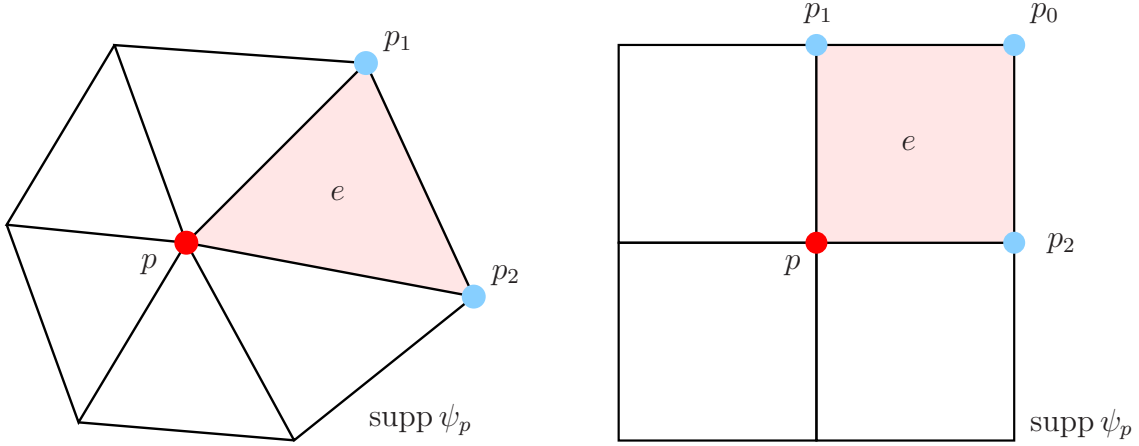
$$\int_{\Gamma_c^s} \phi_p \psi_q \, d\mathbf{s} = \delta_{pq} \int_{\Gamma_c^s} \phi_p \, d\mathbf{s}, \quad (2.12)$$

where δ_{pq} denotes the Kronecker symbol introduced in (1.37). Furthermore, we assume that the dual basis functions ψ_p can be written as a linear combination of the standard basis functions ϕ_p inside its own support. Thus, we get in the two-dimensional case

$$\psi_p := 2\phi_p - \phi_{p-1} - \phi_{p+1}, \quad (2.13)$$

where $p-1$ and $p+1$ are the two neighboring nodes of p . The standard and the dual basis functions are illustrated in Figure 2.2. For a tetrahedral mesh in the three-dimensional case the boundary surfaces are planar triangles and the dual basis function restricted to the face $e \subset \text{supp}(\phi_p) = \text{supp}(\psi_p)$ at the node $p \in \partial e$ is given by

$$\psi_p|_e := 3\phi_p - \phi_{p_1} - \phi_{p_2},$$


 Figure 2.2.: Standard (left) and dual (right) basis functions for $d = 2$.

 Figure 2.3.: Surface triangle (left) and surface quadrilateral (right) for $d = 3$.

where now p_1 and p_2 are the two other points of ∂e as indicated in the left picture in Figure 2.3. If the surface of a hexahedral mesh is planar and has a tensor-product structure, the dual basis function restricted to the face e is obtained via the formula

$$\psi_p|_e := 4\phi_p - 2\phi_{p_1} - 2\phi_{p_2} - \phi_{p_0},$$

where for the arrangement of the other boundary nodes p_i , $i = 0, 1, 2$, of the face e we refer to the right picture in Figure 2.3. These explicit formulas for the dual basis functions in the three-dimensional case are introduced in [140]. In these cases, the determinant of the transformation matrix between the face e and the reference face \hat{e} is constant over e . If this does not hold, one has to take into account the determinant of the transformation in the definition of the biorthogonality relation (2.12), see [51].

In the following, the discrete Lagrange multiplier space is denoted by \mathbf{M}^h and can be spanned by $\{\psi_p \mathbf{e}_k, p = 1, \dots, N_M, k = 1, \dots, d\}$, where ψ_p denotes the p -th scalar dual basis function associated with the node p , and N_M is the total number of nodes on the slave side of $\bar{\Gamma}_c^s$. In contrast to the general mortar setting, we do not have to remove the degrees of freedom of \mathbf{M}^h on $\partial\Gamma_c^s$. We note that this has to be done if $\bar{\Gamma}_D^s \cap \bar{\Gamma}_c^s \neq \emptyset$ but not in our case.

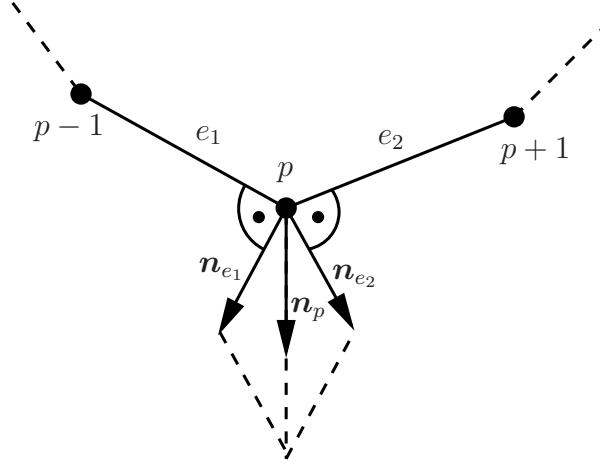


Figure 2.4.: Definition of the normal vector \mathbf{n}_p , see (2.14).

2.2.2. Discrete variational formulation

Before introducing the discrete admissible set $\mathbf{M}^h(\boldsymbol{\lambda}^h)$ for the Lagrange multiplier, we have to clarify the definition of the normal and the tangential part of a discrete function. To do so, we denote by \mathcal{S} the set of all nodes on the discrete counterpart of Γ_c^s . First we define the normal vector \mathbf{n}_p at the node $p \in \mathcal{S}$. Let us define by $\mathcal{E}(p)$ for $p \in \mathcal{S}$ all surface edges of the mesh having the node p as boundary node

$$\mathcal{E}(p) := \{e \text{ surface element of } \mathcal{T}_{h,\Omega^s} : e \subset \Gamma_c^s, p \in \partial e\}.$$

Then the normal \mathbf{n}_p at the node p can be defined via

$$\mathbf{n}_p := \frac{1}{\|\sum_{e \in \mathcal{E}(p)} \mathbf{n}_e\|} \sum_{e \in \mathcal{E}(p)} \mathbf{n}_e, \quad p \in \mathcal{S}, \quad (2.14)$$

where \mathbf{n}_e is the unit normal vector of the surface edge e , see Figure 2.4. We remark that the normal vector \mathbf{n}_e is constant over e in the two-dimensional case and for a planar face e in the three-dimensional case which is always the case for a tetrahedral mesh. For hexahedral meshes, we do not necessarily have planar surface element. Thus, we use here as \mathbf{n}_e the normal vector at the midpoint of the face e . We remark that one can also use the size $|e|$ of the face e as weighting factor in (2.14) and replace the summation formulas by $\sum_{e \in \mathcal{E}(p)} |e| \mathbf{n}_e$. A further possibility using a continuous normal field on Γ_c^s can be found in [145]. Now, the normal and the tangential part of the nodal value $\mathbf{v}_p \in \mathbb{R}^d$ are given by $v_{pn} := \mathbf{v}_p \mathbf{n}_p$ and $\mathbf{v}_{p\tau} := \mathbf{v}_p - v_{pn} \mathbf{n}_p$, respectively. We then can express the normal and the tangential part of the discrete function $\mathbf{v}^h \in \mathbf{V}^h$ on the contact interface Γ_c^s by

$$v_n^h := \sum_{p \in \mathcal{S}} v_{pn} \phi_p, \quad \mathbf{v}_\tau^h := \sum_{p \in \mathcal{S}} \mathbf{v}_{p\tau} \phi_p, \quad p \in \mathcal{S}. \quad (2.15)$$

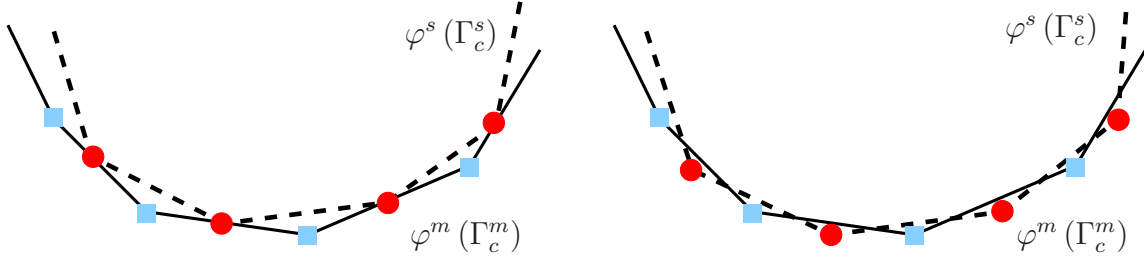


Figure 2.5.: Node-to-segment formulation (left) and weak formulation (right).

Similar we write for the normal and the tangential part of a function $\boldsymbol{\mu}^h = \sum_{p \in \mathcal{S}} \boldsymbol{\mu}_p \psi_p \in \mathbf{M}^h$ with $\boldsymbol{\mu}_p \in \mathbb{R}^d$ for $p \in \mathcal{S}$

$$\mu_n^h := \sum_{p \in \mathcal{S}} \mu_{pn} \psi_p, \quad \boldsymbol{\mu}_\tau^h := \sum_{p \in \mathcal{S}} \boldsymbol{\mu}_{p\tau} \psi_p, \quad p \in \mathcal{S}, \quad (2.16)$$

where the normal component μ_{pn} and the tangential part $\boldsymbol{\mu}_{p\tau}$ of the coefficient $\boldsymbol{\mu}_p \in \mathbb{R}^d$ are defined in the same way as v_{pn} and $\mathbf{v}_{p\tau}$. Denoting by \mathbf{W}^h the discrete trace space of $\mathbf{V}^{s,h}$ restricted to Γ_c^s , and introducing the subset

$$\mathbf{W}_-^h := \{\mathbf{v}^h \in \mathbf{W}^h : v_n^h \leq 0\}, \quad (2.17)$$

the discrete analogue $\mathbf{M}^h(\boldsymbol{\lambda}^h)$ of the admissible Lagrange multiplier space $\mathbf{M}(\boldsymbol{\lambda})$ given in (2.3) can be defined as

$$\mathbf{M}^h(\boldsymbol{\lambda}^h) := \{\boldsymbol{\mu}^h \in \mathbf{M}^h : \langle \boldsymbol{\mu}^h, \mathbf{v}^h \rangle \leq \langle \mathfrak{F} \lambda_n^h, \|\mathbf{v}_\tau^h\|_h \rangle, \mathbf{v}^h \in \mathbf{W}_-^h\}. \quad (2.18)$$

In this definition we use the mesh dependent absolute value $\|\mathbf{v}_\tau^h\|_h$ of the function $\mathbf{v}_\tau^h = \sum_{p \in \mathcal{S}} \mathbf{v}_{p\tau} \phi_p$ is given by

$$\|\mathbf{v}_\tau^h\|_h := \sum_{p \in \mathcal{S}} \|\mathbf{v}_{p\tau}\| \phi_p.$$

The discrete version of the hybrid variational formulation (2.6) reads as: find $(\mathbf{u}^h, \boldsymbol{\lambda}^h) \in \mathbf{V}^h \times \mathbf{M}^h(\boldsymbol{\lambda}^h)$ such that for all $t \in (0, T)$

$$m(\ddot{\mathbf{u}}^h, \mathbf{v}^h) + a(\mathbf{u}^h, \mathbf{v}^h) + \langle [\mathbf{v}^h], \boldsymbol{\lambda}^h \rangle = f(\mathbf{v}^h), \quad \mathbf{v}^h \in \mathbf{V}_0^h, \quad (2.19a)$$

$$\langle [\mathbf{u}^h]_n, \mu_n^h - \lambda_n^h \rangle + \langle [\dot{\mathbf{u}}^h]_\tau, \boldsymbol{\mu}_\tau^h - \boldsymbol{\lambda}_\tau^h \rangle \leq \langle g, \mu_n^h - \lambda_n^h \rangle, \quad \boldsymbol{\mu}^h \in \mathbf{M}^h(\boldsymbol{\lambda}^h). \quad (2.19b)$$

Furthermore, the discrete version of the weak form of the initial conditions (2.7) states

$$(\mathbf{u}^h(\cdot, 0), \mathbf{v}^h) = 0, \quad (\dot{\mathbf{u}}^h(\cdot, 0), \mathbf{v}^h) = (\mathbf{v}_0, \mathbf{v}^h), \quad \mathbf{v}^h \in \mathbf{V}_0^h. \quad (2.20)$$

Remark 2.2. We remark that the weak formulation of contact constraints (2.19b) in some situations leads to a more reliable physical enforcement of the non-penetration condition than the node-to-segment formulation. This effect is illustrated in Figure 2.5

2.3. Algebraic representation

To state the algebraic formulation of (2.19), we first introduce a new constrained basis of \mathbf{V}^h which can be obtained by an efficient local transformation from the standard nodal finite element basis, due to the dual basis functions. In this constrained basis, the weak form of the contact constraints (2.19b) gives rise to decoupled point-wise conditions, which is an optimal starting point for the construction of efficient iterative solvers.

2.3.1. Constrained basis

To introduce the new basis of the space \mathbf{V}^h , we partition the nodes $1 \leq p \leq N_V$ of the finite element mesh into three disjoint sets $\mathcal{S} \cup \mathcal{M} \cup \mathcal{N}$. As introduced before, the set \mathcal{S} contains all nodes on the discrete counterpart of Γ_c^s , \mathcal{M} all nodes on the discrete counterpart of Γ_c^m and \mathcal{N} all remaining nodes. The new or constrained basis $\hat{\phi} = \{\hat{\phi}_p\}_p$ can be obtained in terms of the standard finite element basis $\phi = \{\phi_p\}_p$ for $p \in \mathcal{S} \cup \mathcal{M} \cup \mathcal{N}$. A linear combination of the nodal basis functions on the slave side is attached to the nodal basis functions of the master side in such a way, that the basis functions in $\hat{\phi}$ on the slave side describe the relative displacement between the two bodies, i.e., the jump in the displacement. To introduce this transformation, we define the entries of the coupling matrices \mathbf{D}_d and \mathbf{B}_d between the finite element basis functions ϕ_q , $q \in \mathcal{S}, \mathcal{M}$, and the dual basis functions for the Lagrange multiplier ψ_p , $p \in \mathcal{S}$, by

$$\begin{aligned} \mathbf{D}_d[p, q] &:= \langle [\phi_q], \psi_p \rangle \text{Id}_d = \langle \phi_q, \psi_p \rangle \text{Id}_d =: \delta_{pq} D_p \text{Id}_d, & p, q \in \mathcal{S}, \quad D_p \in \mathbb{R}, \\ \mathbf{B}_d[p, q] &:= \langle [\phi_q], \psi_p \rangle \text{Id}_d = -\langle \phi_q, \psi_p \rangle \text{Id}_d, & p \in \mathcal{S}, \quad q \in \mathcal{M}, \end{aligned} \quad (2.21)$$

see [136]. Due to the biorthogonality (2.12), the matrix \mathbf{D}_d is diagonal. Defining $\tilde{\mathbf{B}}_d := -\mathbf{D}_d^{-1} \mathbf{B}_d$, the constrained basis $\hat{\phi}$ of V^h is obtained from ϕ by the transformation

$$\hat{\phi} := \begin{pmatrix} \hat{\phi}_{\mathcal{N}} \\ \hat{\phi}_{\mathcal{M}} \\ \hat{\phi}_{\mathcal{S}} \end{pmatrix} := \begin{pmatrix} \text{Id} & \mathbf{0} & \mathbf{0} \\ \mathbf{0} & \text{Id} & \tilde{\mathbf{B}}_1^\top \\ \mathbf{0} & \mathbf{0} & \text{Id} \end{pmatrix} \begin{pmatrix} \phi_{\mathcal{N}} \\ \phi_{\mathcal{M}} \\ \phi_{\mathcal{S}} \end{pmatrix} =: \mathbf{Q}_1 \phi. \quad (2.22)$$

Here, for example, the vector $\phi_{\mathcal{N}}$ contains all basis functions associated with the nodes $p \in \mathcal{N}$ and so on. We remark that this transformation can be carried out efficiently in a local way and is of lower complexity, since $\tilde{\mathbf{B}}_1^\top$ is sparse and since only basis functions on the master side associated with a node $p \in \mathcal{M}$ are modified. The definition (2.22) yields for a node $q \in \mathcal{M}$ the relation

$$\hat{\phi}_q = \phi_q - \sum_{\tilde{p} \in \mathcal{S}} \tilde{\mathbf{B}}_1[\tilde{p}, q] \phi_{\tilde{p}} = \phi_q - \sum_{\tilde{p} \in \mathcal{S}} \frac{\mathbf{B}_1[\tilde{p}, q]}{\mathbf{D}_1[\tilde{p}, \tilde{p}]} \phi_{\tilde{p}} = \phi_q + \sum_{\tilde{p} \in \mathcal{S}} \frac{\langle \phi_q, \psi_{\tilde{p}} \rangle}{\langle \phi_{\tilde{p}}, \psi_{\tilde{p}} \rangle} \phi_{\tilde{p}}.$$

In this relation we build the sum between the basis function ϕ_q with $\text{supp}(\phi_q) \subset \Omega^m$ and a linear combination of the basis functions $\phi_{\tilde{p}}$ with $\text{supp}(\phi_{\tilde{p}}) \subset \Omega^s$. Thus, we get for the jump of a constrained basis function associated with a node $q \in \mathcal{M}$ on the master side

$$[\hat{\phi}_q] = \sum_{\tilde{p} \in \mathcal{S}} \frac{\langle \phi_q, \psi_{\tilde{p}} \rangle}{\langle \phi_{\tilde{p}}, \psi_{\tilde{p}} \rangle} \phi_{\tilde{p}} - \phi_q.$$

By multiplying this relation with the function ψ_p , $p \in \mathcal{S}$, we observe after integration over Γ_c^s in terms of the biorthogonality relation (2.12)

$$\langle [\hat{\phi}_q], \psi_p \rangle = 0, \quad p \in \mathcal{S}, \quad q \in \mathcal{M}. \quad (2.23)$$

This equation states that the jump of the finite element basis functions on the master side vanishes in a weak sense.

Next, we give the transformation of the coefficients associated with a discrete function in \mathbf{V}^h with respect to the standard basis ϕ and the new constrained basis $\hat{\phi}$. Each function $\mathbf{v}^h \in \mathbf{V}^h$ can be equivalently written with respect to the standard basis or the constrained basis as

$$\mathbf{v}^h = \sum_p \mathbf{v}_p \phi_p = \sum_p \hat{\mathbf{v}}_p \hat{\phi}_p \in \mathbf{V}^h,$$

where the \mathbf{v}_p are the coefficients with respect to the standard basis ϕ and the $\hat{\mathbf{v}}_p$ are the coefficients with respect to the constrained basis $\hat{\phi}$. We get the coefficient vector $\mathbf{v} = \{\mathbf{v}_p\}_p$ in the standard basis from the coefficient vector $\hat{\mathbf{v}} = \{\hat{\mathbf{v}}_p\}_p$ in the constrained basis via the relation

$$\mathbf{v} = \mathbf{Q}_d^\top \hat{\mathbf{v}}, \quad (2.24)$$

where the matrix \mathbf{Q}_d is defined according to \mathbf{Q}_1 in (2.22) but with the matrix $\tilde{\mathbf{B}}_d$ instead of $\tilde{\mathbf{B}}_1$. It acts on a vector having d components in each node, whereas the finite element basis functions in the transformation formula (2.22) have only one component at each node. We mention that for the nodes $p \in \mathcal{N} \cup \mathcal{M}$, we have $\mathbf{v}_p = \hat{\mathbf{v}}_p$, and for the nodes $p \in \mathcal{S}$, we find

$$\mathbf{v}_S = \tilde{\mathbf{B}}_d \hat{\mathbf{v}}_M + \hat{\mathbf{v}}_S \quad \Leftrightarrow \quad \hat{\mathbf{v}}_S = \mathbf{v}_S - \tilde{\mathbf{B}}_d \mathbf{v}_M. \quad (2.25)$$

The second relation shows that the values $\hat{\mathbf{v}}_S$ on the slave side reflect the relative displacement. The matrix $\tilde{\mathbf{B}}_d$ comes into play since the jump is considered in a weak integral sense and we have, in general, non-matching meshes. Due to the non-conforming situation of the meshes, a strong point-wise approach is not possible. In the case of a conforming situation, the matrix $\tilde{\mathbf{B}}_d$ is the identity.

2.3.2. Point-wise decoupled constraints

By means of the biorthogonality relation (2.12), the spaces \mathbf{W}_-^h and $\mathbf{M}^h(\boldsymbol{\lambda}^h)$ can be expressed via restrictions onto the coefficients of the discrete functions as follows:

Lemma 2.3. *The space \mathbf{W}_-^h introduced in (2.17) can be equivalently expressed by*

$$\mathbf{W}_-^h = \left\{ \mathbf{v}^h = \sum_{p \in \mathcal{S}} \mathbf{v}_p \phi_p \in \mathbf{W}^h : v_{pn} \leq 0, \quad p \in \mathcal{S} \right\} \quad (2.26)$$

and the space $\mathbf{M}^h(\boldsymbol{\lambda}^h)$ in (2.18) is equivalent to

$$\mathbf{M}^h(\boldsymbol{\lambda}^h) = \left\{ \boldsymbol{\mu}^h = \sum_{p \in \mathcal{S}} \boldsymbol{\mu}_p \psi_p \in \mathbf{M}^h : \mu_{pn} \geq 0, \quad \|\boldsymbol{\mu}_{p\tau}\| \leq \mathfrak{F} \lambda_{pn}, \quad p \in \mathcal{S} \right\}. \quad (2.27)$$

Proof. To show the equivalence between (2.17) and (2.26) for the definition of \mathbf{W}_-^h , we write $\mathbf{v}^h \in \mathbf{W}_-^h$ as $\mathbf{v}^h = \sum_{p \in \mathcal{S}} (v_{pn} \mathbf{n}_p + \mathbf{v}_{p\tau}) \phi_p$, where ϕ_p are the scalar nodal basis functions of $\mathbf{V}^{s,h}$ restricted to Γ_c^s . Therefore, we can write the normal part as $v_n^h = \sum_{p \in \mathcal{S}} v_{pn} \mathbf{n}_p \phi_p$. Since $\phi_p \geq 0$, we get $v_n^h \leq 0$ if and only if $v_{pn} \leq 0$, $p \in \mathcal{S}$. Therefore, (2.17) and (2.26) lead to the same space \mathbf{W}^h .

To prove the equivalence between (2.18) and (2.27) for the definition of $\mathbf{M}^h(\boldsymbol{\lambda}^h)$, we write each function $\boldsymbol{\mu}^h \in \mathbf{M}^h$ in terms of the basis functions ψ_p as $\boldsymbol{\mu}^h = \sum_{p \in \mathcal{S}} (\mu_{pn} \mathbf{n}_p + \boldsymbol{\mu}_{p\tau}) \psi_p$. Due to the biorthogonality of the basis functions ϕ_p and ψ_p stated in (2.12) we have

$$\langle \phi_p, \psi_q \rangle = \delta_{pq} D_p, \quad D_p = \int_{\Gamma_c^s} \phi_p \, ds > 0.$$

Thus, we get

$$\langle \boldsymbol{\mu}^h, \mathbf{v}^h \rangle = \sum_{p \in \mathcal{S}} (\mu_{pn} v_{pn} + \boldsymbol{\mu}_{p\tau} \mathbf{v}_{p\tau}) D_p. \quad (2.28)$$

Since each function $\mathbf{v}^h \in \mathbf{W}_-^h$ can now be written as $\mathbf{v}^h = \sum_{p \in \mathcal{S}} (v_{pn} \mathbf{n}_p + \mathbf{v}_{p\tau}) \phi_p$ with $v_{pn} \leq 0$, we obtain with $\lambda_n^h = \sum_{p \in \mathcal{S}} \lambda_{pn} \psi_p$ the relation

$$\langle \mathfrak{F} \lambda_n^h, \|\mathbf{v}_\tau^h\|_h \rangle = \mathfrak{F} \sum_{p \in \mathcal{S}} \lambda_{pn} \|\mathbf{v}_{p\tau}\| D_p. \quad (2.29)$$

Combining (2.28) and (2.29) allows us to write the inequality

$$\langle \boldsymbol{\mu}^h, \mathbf{v}^h \rangle \leq \langle \mathfrak{F} \lambda_n^h, \|\mathbf{v}_\tau^h\|_h \rangle, \quad \mathbf{v}^h \in \mathbf{W}_-^h,$$

in (2.18) point-wise decoupled as

$$\mu_{pn} v_{pn} + \boldsymbol{\mu}_{p\tau} \mathbf{v}_{p\tau} \leq \mathfrak{F} \lambda_{pn} \|\mathbf{v}_{p\tau}\|, \quad v_{pn} \leq 0, \quad p \in \mathcal{S}, \quad (2.30)$$

due to the arbitrary choice of v_{pn} and $\mathbf{v}_{p\tau}$. Choosing $\mathbf{v}_{p\tau} = 0$ in (2.30) leads to the condition

$$\mu_{pn} v_{pn} \leq 0, \quad v_{pn} \leq 0, \quad p \in \mathcal{S},$$

and therefore $\mu_{pn} \geq 0$. The choice $v_{pn} = 0$ and $\mathbf{v}_{p\tau} = \boldsymbol{\mu}_{p\tau}$ leads to

$$\|\boldsymbol{\mu}_{p\tau}\| \leq \mathfrak{F} \lambda_{pn}, \quad p \in \mathcal{S}.$$

Therefore, the equivalence between the definition (2.18) and (2.27) of the space $\mathbf{M}^h(\boldsymbol{\lambda}^h)$ is shown. \square

Before we state the algebraic version of the discrete hybrid variational inequality, we give two remarks concerning the choice of the space $\mathbf{M}^h(\boldsymbol{\lambda}^h)$.

Remark 2.4. Using $\mathbf{M}^h(\boldsymbol{\lambda}^h)$ as discretization space for $\mathbf{M}(\boldsymbol{\lambda})$ is not a conforming approach for the Lagrange multiplier space, i.e., $\mathbf{M}^h(\boldsymbol{\lambda}^h) \not\subset \mathbf{M}(\boldsymbol{\lambda})$.

Remark 2.5. Using standard Lagrange multiplier spaces, the definitions (2.18) and (2.27) for the space $\mathbf{M}^h(\boldsymbol{\lambda}^h)$ do not give the same spaces. In that case, the set defined by (2.27) is a subset of the set defined in (2.18).

Defining the gap at the node $p \in \mathcal{S}$ by

$$g_p := \frac{1}{D_p} \int_{\Gamma_p^s} g \psi_p \, ds = \frac{1}{D_p} \langle g, \psi_p \rangle, \quad p \in \mathcal{S},$$

we arrive at the point-wise decoupled formulation of the weak contact constraints (2.19b) having the same structure as the continuous ones, see (2.1) and (2.2), but restricted to the coefficients of the displacement \mathbf{u}^h and the Lagrange multiplier $\boldsymbol{\lambda}^h$.

Lemma 2.6. *The weak formulation of the contact constraints (2.19b) is equivalent to the point-wise conditions*

$$\hat{u}_{pn} \leq g_p, \quad \lambda_{pn} \geq 0, \quad \lambda_{pn}(\hat{u}_{pn} - g_p) = 0, \quad p \in \mathcal{S}, \quad (2.31)$$

and

$$\begin{cases} \|\boldsymbol{\lambda}_{p\tau}\| \leq \mathfrak{F}|\lambda_{pn}|, \\ \|\boldsymbol{\lambda}_{p\tau}\| < \mathfrak{F}|\lambda_{pn}| \Rightarrow \hat{\mathbf{u}}_{p\tau} = \mathbf{0}, \\ \|\boldsymbol{\lambda}_{p\tau}\| = \mathfrak{F}|\lambda_{pn}| \Rightarrow \exists \alpha \in \mathbb{R} : \boldsymbol{\lambda}_{p\tau} = \alpha^2 \hat{\mathbf{u}}_{p\tau}, \end{cases} \quad p \in \mathcal{S}. \quad (2.32)$$

Proof. The proof is based on the biorthogonality of the basis functions (2.12) and the fact that the jump of the constrained basis functions associated with the nodes on the master side vanishes in a weak sense, see (2.23). We write the functions \mathbf{u}^h and $\dot{\mathbf{u}}^h$ in terms of the constrained basis functions as

$$\mathbf{u}^h = \sum_{p \in \mathcal{S}} \hat{\mathbf{u}}_p \hat{\phi}_p, \quad \dot{\mathbf{u}}^h = \sum_{p \in \mathcal{S}} \hat{\mathbf{u}}_p \hat{\phi}_p, \quad (2.33)$$

where the coefficients $\hat{\mathbf{u}}_p$ and $\hat{\mathbf{u}}_p$ are introduced in (2.24) and (2.25), and use for $\boldsymbol{\lambda}^h$ and $\boldsymbol{\mu}^h$ the representations

$$\boldsymbol{\lambda}^h = \sum_{p \in \mathcal{S}} \lambda_p \psi_p, \quad \boldsymbol{\mu}^h = \sum_{p \in \mathcal{S}} \mu_p \psi_p. \quad (2.34)$$

Due to (2.23) and the biorthogonality relation (2.12), we obtain by inserting (2.33) and (2.34) into the weak formulation of the contact constraints (2.19b), and by dividing by the factor D_p : find $\boldsymbol{\lambda}^h \in \mathbf{M}^h(\boldsymbol{\lambda}^h)$, such that

$$\hat{u}_{pn}(\mu_{pn} - \lambda_{pn}) + \hat{\mathbf{u}}_{p\tau}(\boldsymbol{\mu}_{p\tau} - \boldsymbol{\lambda}_{p\tau}) \leq g_p(\mu_{pn} - \lambda_{pn}), \quad \boldsymbol{\mu}^h \in \mathbf{M}^h(\boldsymbol{\lambda}^h), \quad p \in \mathcal{S}. \quad (2.35)$$

The algebraic restrictions on the coefficients of the function $\boldsymbol{\mu}^h \in \mathbf{M}^h(\boldsymbol{\lambda}^h)$ are stated in Lemma 2.3. Using this lemma we observe from $\boldsymbol{\lambda}^h \in \mathbf{M}^h(\boldsymbol{\lambda}^h)$

$$\lambda_{pn} \geq 0, \quad \|\boldsymbol{\lambda}_{p\tau}\| \leq \mathfrak{F}\lambda_{pn}, \quad p \in \mathcal{S}.$$

The choice $\mu_{pn} = \lambda_{pn} + \mu_{pn} \geq 0$, since $\mu_{pn} \geq 0$, and $\boldsymbol{\mu}_{p\tau} = \boldsymbol{\lambda}_{p\tau}$ in (2.35) leads to the condition $\hat{u}_{pn} \leq g_p$, whereas the choice $\mu_{pn} = 0$ and $\mu_{pn} = 2\lambda_{pn}$ with $\boldsymbol{\mu}_{p\tau} = \boldsymbol{\lambda}_{p\tau}$ leads to $\lambda_{pn}(\hat{u}_{pn} - g_p) = 0$. Thus, the contact conditions in normal direction stated in (2.31) are proven. To deduce the two missing frictional conditions in (2.32), we apply the same techniques as mentioned in Subsection 2.1.2. In particular we refer to Figure 2.1. The opposite direction can be shown by multiplying (2.31) and (2.32) with the corresponding basis functions, and then by building the sum over all nodes $p \in \mathcal{S}$. \square

At the end we give the algebraic formulation of the weak form of the field equation (2.19a). Therefore, we define for each node $p, q \in \mathcal{N} \cup \mathcal{M} \cup \mathcal{S}$ the entry of the mass matrix by

$$\mathbf{M}_{ik}[pq] := m(\phi_q \mathbf{e}_k, \phi_p \mathbf{e}_i), \quad 1 \leq i, k \leq d,$$

and the entry of the right hand side by

$$\mathbf{f}_i[p] := f(\phi_p \mathbf{e}_i), \quad 1 \leq i \leq d.$$

In the case of linearized elasticity, see (1.38), the form $a(\cdot, \cdot)$ is bilinear and the stiffness matrix can be introduced by

$$\mathbf{K}_{ik}[pq] := a(\phi_q \mathbf{e}_k, \phi_p \mathbf{e}_i), \quad 1 \leq i, k \leq d. \quad (2.36)$$

With the definitions of the coupling matrices \mathbf{D}_d and \mathbf{M}_d between the finite element basis functions ϕ_p and the basis functions ψ_p for the Lagrange multiplier, see (2.21), we write (2.19a) in the case of linearized elasticity as

$$\mathbf{M}\ddot{\mathbf{u}} + \mathbf{K}\mathbf{u} + \mathbf{C}\boldsymbol{\lambda} = \mathbf{f}, \quad \mathbf{C} := \begin{pmatrix} \mathbf{0} \\ \mathbf{B}_d \\ \mathbf{D}_d \end{pmatrix}. \quad (2.37)$$

We remark that the zero block in the coupling matrix \mathbf{C} refers to the lines associated with the nodes in the set \mathcal{N} . For a general nonlinear material law, the stiffness term $\mathbf{K}\mathbf{u}$ in (2.37) has to be replaced by the algebraic vector $\mathbf{K}(\mathbf{u})$ with the entries

$$\mathbf{K}(\mathbf{u})[p] := a(\mathbf{u}^h, \phi_p). \quad (2.38)$$

We obtain any matrix $\hat{\mathbf{A}}$ with respect to the constrained basis functions from the matrix \mathbf{A} with respect to the standard basis by the transformation $\hat{\mathbf{A}} = \mathbf{Q}_d \mathbf{A} \mathbf{Q}_d^\top$, i.e.,

$$\hat{\mathbf{A}} = \begin{pmatrix} \text{Id} & 0 & 0 \\ 0 & \text{Id} & \tilde{\mathbf{B}}_d^\top \\ 0 & 0 & \text{Id} \end{pmatrix} \begin{pmatrix} \mathbf{A}_{\mathcal{N}\mathcal{N}} & \mathbf{A}_{\mathcal{N}\mathcal{M}} & \mathbf{A}_{\mathcal{N}\mathcal{S}} \\ \mathbf{A}_{\mathcal{M}\mathcal{N}} & \mathbf{A}_{\mathcal{M}\mathcal{M}} & \mathbf{A}_{\mathcal{M}\mathcal{S}} \\ \mathbf{A}_{\mathcal{S}\mathcal{N}} & \mathbf{A}_{\mathcal{S}\mathcal{M}} & \mathbf{A}_{\mathcal{S}\mathcal{S}} \end{pmatrix} \begin{pmatrix} \text{Id} & 0 & 0 \\ 0 & \text{Id} & 0 \\ 0 & \tilde{\mathbf{B}}_d & \text{Id} \end{pmatrix}. \quad (2.39)$$

Here, the \mathbf{A}_{**} are the corresponding sub-matrices of \mathbf{A} belonging to the indicated set of nodes. A straightforward computation of $\hat{\mathbf{A}}$ yields

$$\hat{\mathbf{A}} = \begin{pmatrix} \mathbf{A}_{\mathcal{N}\mathcal{N}} & \mathbf{A}_{\mathcal{N}\mathcal{M}} + \mathbf{A}_{\mathcal{N}\mathcal{S}} \tilde{\mathbf{B}}_d & \mathbf{A}_{\mathcal{N}\mathcal{S}} \\ \mathbf{A}_{\mathcal{M}\mathcal{N}} + \tilde{\mathbf{B}}_d^\top \mathbf{A}_{\mathcal{S}\mathcal{N}} & \mathbf{A}_{\mathcal{M}\mathcal{M}} + \mathbf{A}_{\mathcal{M}\mathcal{S}} \tilde{\mathbf{B}}_d + \tilde{\mathbf{B}}_d^\top \mathbf{A}_{\mathcal{S}\mathcal{M}} + \tilde{\mathbf{B}}_d^\top \mathbf{A}_{\mathcal{S}\mathcal{S}} \tilde{\mathbf{B}}_d & \mathbf{A}_{\mathcal{M}\mathcal{S}} + \tilde{\mathbf{B}}_d^\top \mathbf{A}_{\mathcal{S}\mathcal{S}} \\ \mathbf{A}_{\mathcal{S}\mathcal{N}} & \mathbf{A}_{\mathcal{S}\mathcal{M}} + \mathbf{A}_{\mathcal{S}\mathcal{S}} \tilde{\mathbf{B}}_d & \mathbf{A}_{\mathcal{S}\mathcal{S}} \end{pmatrix}.$$

Furthermore, the vector \mathbf{f} of the right hand side transforms into the constrained basis by

$$\hat{\mathbf{f}} = \mathbf{Q}_d \mathbf{f} = \begin{pmatrix} \mathbf{f}_{\mathcal{N}} \\ \mathbf{f}_{\mathcal{M}} + \tilde{\mathbf{B}}_d^\top \mathbf{f}_{\mathcal{S}} \\ \mathbf{f}_{\mathcal{S}} \end{pmatrix}. \quad (2.40)$$

Due to (2.23) the matrix \mathbf{B}_d describing the coupling between the dual basis function for the Lagrange multiplier and the finite element basis functions on the master side in (2.21) vanishes in the constrained basis. Moreover, the matrix \mathbf{D}_d does not change, since the basis functions on the slave side are the same in the standard and the constrained basis, see, (2.22). Then, we can write (2.37) with respect to the constrained basis as

$$\hat{\mathbf{M}}\hat{\mathbf{u}} + \hat{\mathbf{K}}\hat{\mathbf{u}} + \hat{\mathbf{C}}\boldsymbol{\lambda} = \hat{\mathbf{f}}, \quad \hat{\mathbf{C}} := \begin{pmatrix} \mathbf{0} \\ \mathbf{D}_d \end{pmatrix}. \quad (2.41)$$

Now, the zero block in the definition of the coupling matrix with respect to the constrained basis $\hat{\mathbf{C}}$ refers to the nodes in the set $\mathcal{N} \cup \mathcal{M}$.

3. Optimal a priori error estimates

In this chapter, we provide an optimal a priori bound for the discretization error of the mortar method using dual shape functions for the Lagrange multiplier. The results have been published in [80, 81, 83]. We restrict ourselves to the detailed presentation for the case without friction and lowest order finite elements in the two-dimensional case, [83]. Furthermore, numerical examples are given to confirm the theoretical ones. The generalization to second order finite elements can be found in [79]. The frictional case was studied by means of a frictional antiplane model in [81]. Furthermore, the extension to piezo-electric materials can be found in [80].

The optimal a priori error estimates are given for the discretization error in the H^1 -norm for the displacement and in the $H^{-1/2}$ -norm for the Lagrange multiplier. The interest in contact problems and variational inequalities has led to an increased research activity in this field. Abstract error estimates for variational inequalities can be found, e.g., in [18, 47, 53] and a priori bounds for the discretization error of unilateral contact problems are given, e.g., in [61, 62]. Recently a lot of work has been done to analyze mortar formulations based on standard Lagrange multipliers. A priori error estimates for the displacements in the H^1 -norm and for the Lagrange multiplier in the $H^{-1/2}$ -norm of order $h^{3/4}$ have been established, see, e.g., [9, 10, 33, 111], under H^2 -regularity assumption. Using additional regularity assumptions on the Lagrange multiplier, order h has been shown, see, e.g., [33, 72]. Although the order h is optimal, the regularity assumptions are quite strong and restrictive. These first a priori results have been considerably improved during the last couple of years. In [8], order $h^{1/2+\nu}$, $0 < \nu < 1/2$, and order $h\sqrt{|\log h|}$ a priori results are given for the H^1 -norm if the solution is $H^{3/2+\nu}$ - and H^2 -regular, respectively. A new and stronger result is given in [10], where order $h\sqrt[4]{|\log h|}$ can be found. In [73], quadratic finite elements in combination with standard Lagrange multiplier spaces are discussed and a priori estimates for the discretization error are given. A priori error estimates for quadratic finite elements were also discussed in [7]. Very recently, a priori error estimates for a one-sided contact problem with Coulomb friction were achieved in [74].

Most of the theoretical results are obtained for standard Lagrange multiplier spaces and the two dimensional setting. Here, we achieve for the case of linear mortar finite elements based on dual basis functions, as introduced in Subsection 2.2.1, for the Lagrange multipliers optimal a priori error estimates of order $h^{1/2+\nu}$ for the displacements and the Lagrange multiplier if the solution is $H^{3/2+\nu}$ -regular for $0 < \nu \leq 1/2$. The techniques are based on introducing locally defined truncation operators measuring the non-conformity of the discretization and on Sobolev–Slobodeckij norms. A various number of numerical examples illustrating the performance of the approach and confirming the theoretical results are presented.

This chapter is organized as follows. We start with the presentation of the result for the discretization in case of lowest order finite elements without friction in Section 3.1. Section 3.2 contains various numerical examples confirming the theory. In Section 3.3, we deal with the question how to interpret the discontinuous discrete Lagrange multiplier as a continuous function. Section 3.4 shows the extension to the case of second order finite elements. The error estimate for a frictional antiplane problem is given in Section 3.5. Finally, we present in Section 3.6 a numerical example illustrating the numerically achieved error decay in the case of a contact problem with Coulomb's friction law.

3.1. Theoretical results

In this subsection, we observe the optimal a priori result for the discretization error of the hybrid formulation of the static version of the linearized contact problem introduced in Chapter 2 in combination with linearized elasticity (1.38) as material law. To be able to give a perspicuous presentation of the theory, we restrict ourselves to lowest order finite elements and to the case without friction for the two-dimensional case as published in [83]. We start with the presentation of the weak formulation and the statement of additional assumptions in Subsection 3.1.1. In Subsection 3.1.2, we then derive the optimal a priori error estimate for the discretization error.

3.1.1. Problem statement

To achieve optimal a priori error estimates, we assume that the two bodies Ω^s and Ω^m are in contact in their initial configuration. So far, their common boundary part in the reference setting is the possible contact boundary and we have the relation $\Gamma_c^s = \Gamma_c^m$ and for the gap function we have $g = 0$. In addition to this assumption, the normal vector \mathbf{n} is assumed to be constant over Γ_c^s . Furthermore, we assume $\mathbf{u}_D^i = \mathbf{0}$ for the given Dirichlet data such that there is no need to distinguish between the spaces \mathbf{V} and \mathbf{V}_0 and we write in the following always \mathbf{V} . Defining the bilinear form $b(\cdot, \cdot)$ on the product space $\mathbf{V} \times \mathbf{M}$ by

$$b(\mathbf{v}, \boldsymbol{\mu}) := \langle \boldsymbol{\mu}_n, [\mathbf{v}]_n \rangle, \quad \boldsymbol{\mu} \in \mathbf{M}, \quad \mathbf{v} \in \mathbf{V},$$

we get the hybrid formulation of the static contact problem without friction from (2.6) as: find $(\mathbf{u}, \boldsymbol{\lambda}) \in \mathbf{V} \times \mathbf{M}_+$ such that

$$a(\mathbf{u}, \mathbf{v}) + b(\mathbf{v}, \boldsymbol{\lambda}) = f(\mathbf{v}), \quad \mathbf{v} \in \mathbf{V}, \quad (3.1a)$$

$$b(\mathbf{u}, \boldsymbol{\mu} - \boldsymbol{\lambda}) \leq 0, \quad \boldsymbol{\mu} \in \mathbf{M}_+, \quad (3.1b)$$

where now the admissible subset $\mathbf{M}_+ \subset \mathbf{M}$ for the Lagrange multiplier is given by

$$\mathbf{M}_+ := \{ \boldsymbol{\mu} \in \mathbf{M} : \langle \boldsymbol{\mu}, \boldsymbol{\eta} \rangle \leq 0, \quad \boldsymbol{\eta} \in \mathbf{W} \text{ with } \eta_n \leq 0 \}. \quad (3.2)$$

We remark, that from this definition, we get directly $\boldsymbol{\lambda}_\tau = \mathbf{0}$ for the tangential part of the Lagrange multiplier and therefore the required condition to the contact stress for the case without friction.

Existence and uniqueness of a solution $(\mathbf{u}, \boldsymbol{\lambda}) \in \mathbf{V} \times \mathbf{M}_+$ of (3.1) has been stated, e.g., in [62]. For a more general overview concerning existence of a solution for contact problems we refer to [42]. The proof is based on the inf-sup property for the spaces \mathbf{V} and \mathbf{M} . This property states the existence of a constant $\gamma > 0$ such that

$$\inf_{\mathbf{0} \neq \boldsymbol{\mu} \in \mathbf{M}} \sup_{\mathbf{0} \neq \mathbf{v} \in \mathbf{V}} \frac{b(\mathbf{v}, \boldsymbol{\mu})}{\|\mathbf{v}\|_{1,\Omega} \|\boldsymbol{\mu}\|_{-\frac{1}{2}, \Gamma_c^s}} \geq \gamma. \quad (3.3)$$

Here, we denote by $\|\cdot\|_{1,\Omega}$ the broken H^1 -norm on the product space $H^1(\Omega^s) \times H^1(\Omega^m)$.

Following the proof of Lemma 2.3, we obtain the discretized version of the space \mathbf{M}_+ introduced in (3.2) as

$$\mathbf{M}_+^h := \left\{ \boldsymbol{\mu}^h = \sum_{p \in \mathcal{S}} \boldsymbol{\mu}_p \psi_p \in \mathbf{M}^h : \boldsymbol{\mu}_p = \mu_{pn} \mathbf{n}, \mu_{pn} \geq 0, p \in \mathcal{S} \right\}. \quad (3.4)$$

Now, the discretized version of (3.1) reads as: find $(\mathbf{u}^h, \boldsymbol{\lambda}^h) \in \mathbf{V}^h \times \mathbf{M}_+^h$ such that

$$a(\mathbf{u}^h, \mathbf{v}^h) + b(\mathbf{v}^h, \boldsymbol{\lambda}^h) = f(\mathbf{v}^h), \quad \mathbf{v}^h \in \mathbf{V}^h, \quad (3.5a)$$

$$b(\mathbf{u}^h, \boldsymbol{\mu}^h - \boldsymbol{\lambda}^h) \leq 0, \quad \boldsymbol{\mu}^h \in \mathbf{M}_+^h. \quad (3.5b)$$

Since for the spaces \mathbf{V}^h and \mathbf{M}_n^h with $\mathbf{M}_+^h \subset \mathbf{M}_n^h := \{\boldsymbol{\mu}^h \in \mathbf{M}^h : \boldsymbol{\mu}^h \times \mathbf{n} = 0\}$ the discrete version of the inf-sup condition (3.3) holds also in the case of dual basis functions for the Lagrange multiplier, [137], we have existence and uniqueness of the solution $(\mathbf{u}^h, \boldsymbol{\lambda}^h) \in \mathbf{V}^h \times \mathbf{M}_+^h$ of the discretized version (3.5).

In the following, we denote by $\gamma_a \subset \Gamma_c^s$ the actual contact set, i.e., $[\mathbf{u}]_n = 0$ on γ_a and $[\mathbf{u}]_n < 0$ on $\gamma_c := \Gamma_c^s \setminus \gamma_a$. If the displacement \mathbf{u} is a continuous function, then the actual contact zone γ_a is a well defined and closed subset of Γ_c^s .

3.1.2. Error estimates

The starting point to establish a priori error estimates for the discretization errors in the primal and dual variables is the following abstract lemma, see, e.g., [73].

Lemma 3.1. *Let $(\mathbf{u}, \boldsymbol{\lambda}) \in \mathbf{V} \times \mathbf{M}_+$ be the solution of (3.1) and let $(\mathbf{u}^h, \boldsymbol{\lambda}^h) \in \mathbf{V}^h \times \mathbf{M}_+^h$ be the solution of the discrete formulation (3.5). Then there exists a constant $0 < C < \infty$ independent of the meshsize h , such that*

$$\begin{aligned} \|\mathbf{u} - \mathbf{u}^h\|_{1,\Omega} + \|\boldsymbol{\lambda} - \boldsymbol{\lambda}^h\|_{-\frac{1}{2}, \Gamma_c^s} &\leq C \left\{ \inf_{\mathbf{v}^h \in \mathbf{V}^h} \|\mathbf{u} - \mathbf{v}^h\|_{1,\Omega} + \inf_{\boldsymbol{\mu}^h \in \mathbf{M}_n^h} \|\boldsymbol{\lambda} - \boldsymbol{\mu}^h\|_{-\frac{1}{2}, \Gamma_c^s} \right. \\ &\quad \left. + \max(b(\mathbf{u}, \boldsymbol{\lambda}^h), 0)^{\frac{1}{2}} + \max(b(\mathbf{u}^h, \boldsymbol{\lambda}), 0)^{\frac{1}{2}} \right\}. \end{aligned}$$

Proof. The proof can be found in [73] for scalar-valued standard Lagrange multipliers and quadratic finite elements. It applies also to our situation. For convenience of the

reader, we briefly recall the basic steps. Starting with $a(\mathbf{u} - \mathbf{u}^h, \mathbf{u} - \mathbf{u}^h)$, we find for $\mathbf{v}^h \in \mathbf{V}^h$ using (3.1) and (3.5)

$$\begin{aligned} a(\mathbf{u} - \mathbf{u}^h, \mathbf{u} - \mathbf{u}^h) &= a(\mathbf{u} - \mathbf{u}^h, \mathbf{u} - \mathbf{v}^h) + a(\mathbf{u} - \mathbf{u}^h, \mathbf{v}^h - \mathbf{u}^h) \\ &= a(\mathbf{u} - \mathbf{u}^h, \mathbf{u} - \mathbf{v}^h) - b(\mathbf{v}^h - \mathbf{u}^h, \boldsymbol{\lambda}) + b(\mathbf{v}^h - \mathbf{u}^h, \boldsymbol{\lambda}^h) \\ &= a(\mathbf{u} - \mathbf{u}^h, \mathbf{u} - \mathbf{v}^h) - b(\mathbf{v}^h - \mathbf{u}, \boldsymbol{\lambda} - \boldsymbol{\lambda}^h) - b(\mathbf{u} - \mathbf{u}^h, \boldsymbol{\lambda} - \boldsymbol{\lambda}^h). \end{aligned}$$

Using the continuity of the bilinear forms $a(\cdot, \cdot)$ and $b(\cdot, \cdot)$, the trace theorem and Korn's inequality, we obtain the upper bound

$$\|\mathbf{u} - \mathbf{u}^h\|_{1,\Omega}^2 \leq C \left(\|\mathbf{u} - \mathbf{u}^h\|_{1,\Omega} + \|\boldsymbol{\lambda} - \boldsymbol{\lambda}^h\|_{-\frac{1}{2},\Gamma_c^s} \right) \|\mathbf{u} - \mathbf{v}^h\|_{1,\Omega} - b(\mathbf{u} - \mathbf{u}^h, \boldsymbol{\lambda} - \boldsymbol{\lambda}^h). \quad (3.6)$$

In terms of the discrete inf-sup condition for the spaces \mathbf{V}^h and \mathbf{M}_n^h , [137], and observing that $\|\boldsymbol{\mu}^h\|_{-\frac{1}{2},\Gamma_c^s} = \|\boldsymbol{\mu}_n^h\|_{-\frac{1}{2},\Gamma_c^s}$, $\boldsymbol{\mu}^h \in \mathbf{M}_n^h$, we find the upper bound

$$\begin{aligned} \|\boldsymbol{\mu}^h - \boldsymbol{\lambda}^h\|_{-\frac{1}{2},\Gamma_c^s} &\leq C \sup_{\mathbf{w}^h \in \mathbf{V}^h} \frac{b(\mathbf{w}^h, \boldsymbol{\mu}^h - \boldsymbol{\lambda}^h)}{\|\mathbf{w}^h\|_{1,\Omega}} \\ &= C \sup_{\mathbf{w}^h \in \mathbf{V}^h} \frac{b(\mathbf{w}^h, \boldsymbol{\mu}^h - \boldsymbol{\lambda}) + a(\mathbf{u}^h - \mathbf{u}, \mathbf{w}^h)}{\|\mathbf{w}^h\|_{1,\Omega}} \\ &\leq C \left(\|\boldsymbol{\mu}^h - \boldsymbol{\lambda}\|_{-\frac{1}{2},\Gamma_c^s} + \|\mathbf{u}^h - \mathbf{u}\|_{1,\Omega} \right). \end{aligned}$$

Thus, we arrive due to the triangle inequality at the estimate

$$\|\boldsymbol{\lambda} - \boldsymbol{\lambda}^h\|_{-\frac{1}{2},\Gamma_c^s} \leq C \left(\|\boldsymbol{\mu}^h - \boldsymbol{\lambda}\|_{-\frac{1}{2},\Gamma_c^s} + \|\mathbf{u}^h - \mathbf{u}\|_{1,\Omega} \right).$$

Setting $\boldsymbol{\mu} = \mathbf{0}$ in (3.1) and $\boldsymbol{\mu}^h = \mathbf{0}$ in (3.5), we find $b(\mathbf{u}, \boldsymbol{\lambda}) \geq 0$ and $b(\mathbf{u}^h, \boldsymbol{\lambda}^h) \geq 0$. We note that \mathbf{M}_+ and \mathbf{M}_+^h are convex cones. Using $\boldsymbol{\mu} = 2\boldsymbol{\lambda}$ and $\boldsymbol{\mu}^h = 2\boldsymbol{\lambda}^h$, we get $b(\mathbf{u}, \boldsymbol{\lambda}) \leq 0$ and $b(\mathbf{u}^h, \boldsymbol{\lambda}^h) \leq 0$, respectively. In terms of $b(\mathbf{u}, \boldsymbol{\lambda}) = b(\mathbf{u}^h, \boldsymbol{\lambda}^h) = 0$, the third term on the right side of (3.6) can be written as

$$-b(\mathbf{u} - \mathbf{u}^h, \boldsymbol{\lambda} - \boldsymbol{\lambda}^h) = b(\mathbf{u}, \boldsymbol{\lambda}^h) + b(\mathbf{u}^h, \boldsymbol{\lambda}) \leq \max(b(\mathbf{u}, \boldsymbol{\lambda}^h), 0) + \max(b(\mathbf{u}^h, \boldsymbol{\lambda}), 0). \quad \square$$

Next we made same remarks concerning the last additional two terms on the right side of the estimate in Lemma 3.1 coming in due to the non-conformity of our approach.

Remark 3.2. The term $\max(b(\mathbf{u}^h, \boldsymbol{\lambda}), 0)$ takes into account the discrete penetration of the two bodies on the actual contact set γ_a . The term $\max(b(\mathbf{u}, \boldsymbol{\lambda}^h), 0)$ can be greater than zero if the normal component of the discrete Lagrange multiplier λ_n^h is negative on a part of γ_c . We recall that \mathbf{M}_+^h is not a subspace of \mathbf{M}_+ , and thus the normal component λ_n^h of $\boldsymbol{\lambda}^h \in \mathbf{M}_+^h$ can be smaller than zero. The first two terms in the upper bound of Lemma 3.1 are the best approximation errors. They reflect the quality of the approximation of the spaces \mathbf{V}^h and \mathbf{M}_n^h . The third and the fourth term measure the non-conformity of the approach.

To prove optimal a priori error estimates under the H^s -regularity assumption for the displacements \mathbf{u} with $3/2 < s \leq 2$, we have to consider the two last terms for the bilinear form $b(\cdot, \cdot)$ in the upper bound of Lemma 3.1. In a first step, we briefly recall the definitions of the mortar projection $\Pi^h : [L^2(\Gamma_c^s)]^d \rightarrow \mathbf{W}^h$ and its dual operator $\Pi_*^h : [L^2(\Gamma_c^s)]^d \rightarrow \mathbf{M}^h$

$$\begin{aligned} \int_{\Gamma_c^s} (\Pi^h \mathbf{w}) \boldsymbol{\mu}^h \, ds &:= \int_{\Gamma_c^s} \mathbf{w} \boldsymbol{\mu}^h \, ds, & \boldsymbol{\mu}^h \in \mathbf{M}^h, \\ \int_{\Gamma_c^s} \mathbf{v}^h (\Pi_*^h \boldsymbol{\mu}) \, ds &:= \int_{\Gamma_c^s} \mathbf{v}^h \boldsymbol{\mu} \, ds, & \mathbf{v}^h \in \mathbf{W}^h. \end{aligned}$$

In terms of the stability of Π^h and Π_*^h , which can be found for the general mortar setting with dual basis functions for the Lagrange multipliers in [137], both operators satisfy an approximation property

$$\|\mathbf{w} - \Pi^h \mathbf{w}\|_{0, \Gamma_c^s} \leq Ch^\tau |\mathbf{w}|_{\tau, \Gamma_c^s}, \quad \|\boldsymbol{\mu} - \Pi_*^h \boldsymbol{\mu}\|_{0, \Gamma_c^s} \leq Ch^\nu |\boldsymbol{\mu}|_{\nu, \Gamma_c^s}, \quad (3.7)$$

for $\mathbf{w} \in [H^\tau(\Gamma_c^s)]^2$, $0 \leq \tau \leq 2$, and $\boldsymbol{\mu} \in [H^\nu(\Gamma_c^s)]^2$, $0 \leq \nu \leq 1$.

The proof of the upper bound of $b(\mathbf{u}, \boldsymbol{\lambda}^h)$ is based on a regularity assumption on the actual contact zone.

Assumption 3.3. *Regularity assumption on γ_a . We assume that the number of points in $\overline{\gamma_a} \cap \overline{\gamma_c}$ is finite.*

We now give two lemmas providing upper bounds for the consistency errors.

Lemma 3.4. *Let $(\mathbf{u}, \boldsymbol{\lambda}) \in \mathbf{V} \times \mathbf{M}_+$ be the solution of (3.1) and let $(\mathbf{u}^h, \boldsymbol{\lambda}^h) \in \mathbf{V}^h \times \mathbf{M}_+^h$ be the solution of the discrete formulation (3.5). Under the regularity assumption $\mathbf{u} \in [H^{\frac{3}{2}+\nu}(\Omega)]^2$, $0 < \nu \leq \frac{1}{2}$, we have the a priori error estimate*

$$b(\mathbf{u}^h, \boldsymbol{\lambda}) \leq C \left(h^{1+2\nu} |\mathbf{u}|_{\frac{3}{2}+\nu, \Omega}^2 + h^{\frac{1}{2}+\nu} |\mathbf{u}|_{\frac{3}{2}+\nu, \Omega} \|\mathbf{u} - \mathbf{u}^h\|_{1, \Omega} \right).$$

for a positive constant $C < \infty$ independent of h .

Proof. For standard Lagrange multipliers, we refer to [73]. Although our dual basis functions of \mathbf{M}^h are not positive, we can apply the same techniques. Using the discrete saddle point formulation (3.5) and the definition of the mortar projection, we find

$$b(\mathbf{u}^h, \boldsymbol{\mu}^h - \boldsymbol{\lambda}^h) = \int_{\Gamma_c^s} (\boldsymbol{\mu}_n^h - \boldsymbol{\lambda}_n^h) ((\Pi^h[\mathbf{u}^h])\mathbf{n}) \, ds \leq 0, \quad \boldsymbol{\mu}^h \in \mathbf{M}_+^h.$$

The normal component of the mortar projection of $[\mathbf{u}^h]$ can be written as $(\Pi^h[\mathbf{u}^h])\mathbf{n} = \sum_{p \in \mathcal{S}} \alpha_{pn} \phi_p$. Writing the normal components of $\boldsymbol{\mu}^h, \boldsymbol{\lambda}^h \in \mathbf{M}_+^h$ as linear combination

3. Optimal a priori error estimates

of the dual basis functions yields $\mu_n^h = \sum_{p \in \mathcal{S}} \beta_{pn} \psi_p$ and $\lambda_n^h = \sum_{p \in \mathcal{S}} \gamma_{pn} \psi_p$, $\beta_{pn}, \gamma_{pn} \geq 0$. Setting $\beta_{pn} := \gamma_{pn} + \delta_{pq}$, we obtain by (2.12)

$$0 \geq b(\mathbf{u}^h, \boldsymbol{\mu}^h - \boldsymbol{\lambda}^h) = \int_{\Gamma_c^s} \psi_q ((\Pi^h[\mathbf{u}^h])\mathbf{n}) \, ds = \alpha_{qn} \int_{\Gamma_c^s} \phi_q \, ds.$$

We recall that $\phi_q \geq 0$ and thus $\alpha_{qn} \leq 0$, $q \in \mathcal{S}$. This results in combination with $\boldsymbol{\lambda} \in \mathbf{M}_+$ in the inequality

$$\int_{\Gamma_c^s} \lambda_n ((\Pi^h[\mathbf{u}^h])\mathbf{n}) \, ds \leq 0. \quad (3.8)$$

In contrast to the general mortar setting with crosspoints, Π^h restricted to the finite element trace space on the slave side is the identity. The approximation properties (3.7) yield due to (3.8) the upper bound

$$\begin{aligned} b(\mathbf{u}^h, \boldsymbol{\lambda}) &= \int_{\Gamma_c^s} \lambda_n ([\mathbf{u}^h]_n - (\Pi^h[\mathbf{u}^h])\mathbf{n} + (\Pi^h[\mathbf{u}^h])\mathbf{n}) \, ds \\ &\leq \int_{\Gamma_c^s} (\lambda_n - (\Pi_*^h \boldsymbol{\lambda})\mathbf{n}) ([\mathbf{u}^h]_n - (\Pi^h[\mathbf{u}^h])\mathbf{n}) \, ds \\ &= \int_{\Gamma_c^s} (\lambda_n - (\Pi_*^h \boldsymbol{\lambda})\mathbf{n}) ((\Pi^h \mathbf{u}^{h,m})\mathbf{n} - u_n^{h,m}) \, ds \\ &\leq \|\boldsymbol{\lambda} - \Pi_*^h \boldsymbol{\lambda}\|_{0, \Gamma_c^s} \left(\|(\mathbf{u}^m - \mathbf{u}^{h,m}) - \Pi^h(\mathbf{u}^m - \mathbf{u}^{h,m})\|_{0, \Gamma_c^s} + \|\mathbf{u}^m - \Pi^h \mathbf{u}^m\|_{0, \Gamma_c^s} \right) \\ &\leq h^\nu |\boldsymbol{\lambda}|_{\nu, \Gamma_c^s} \left(h^{\frac{1}{2}} |\mathbf{u}^m - \mathbf{u}^{h,m}|_{\frac{1}{2}, \Gamma_c^s} + h^{1+\nu} |\mathbf{u}^m|_{1+\nu, \Gamma_c^s} \right) \\ &\leq C \left(h^{\frac{1}{2}+\nu} |\mathbf{u}|_{\frac{3}{2}+\nu, \Omega} \|\mathbf{u} - \mathbf{u}^h\|_{1, \Omega} + h^{1+2\nu} |\mathbf{u}|_{\frac{3}{2}+\nu, \Omega}^2 \right). \end{aligned}$$

□

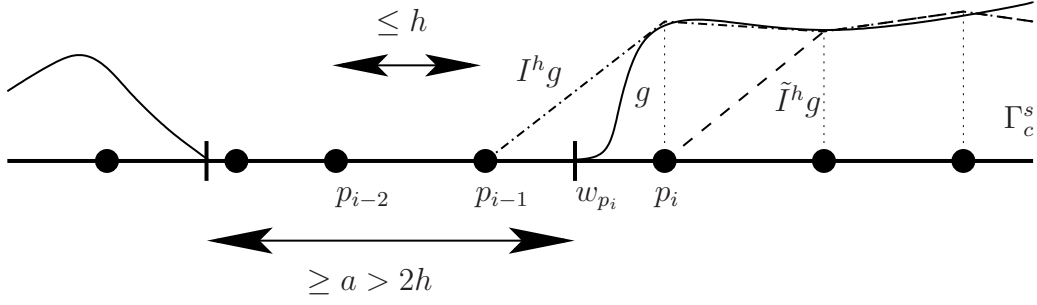
A similar bound for the term $b(\mathbf{u}, \boldsymbol{\lambda}^h)$ can be established.

Lemma 3.5. *Let $(\mathbf{u}, \boldsymbol{\lambda}) \in \mathbf{V} \times \mathbf{M}_+$ be the solution of (3.1) and let $(\mathbf{u}^h, \boldsymbol{\lambda}^h) \in \mathbf{V}^h \times \mathbf{M}_+^h$ be the solution of the discrete formulation (3.5). Under Assumption 3.3 and the regularity assumption $\mathbf{u} \in [H^{\frac{3}{2}+\nu}(\Omega)]^2$, $0 < \nu \leq \frac{1}{2}$, we have the a priori error estimate*

$$b(\mathbf{u}, \boldsymbol{\lambda}^h) \leq C h^{\frac{1}{2}+\nu} |\mathbf{u}|_{\frac{3}{2}+\nu, \Omega} \|\boldsymbol{\lambda} - \boldsymbol{\lambda}^h\|_{-\frac{1}{2}, \Gamma_c^s}$$

for a positive constant $C < \infty$ independent of $h < h_0$.

Proof. The regularity assumptions guarantee that $[\mathbf{u}]_n$ restricted to Γ_c^s is continuous. We denote by I^h the Lagrange interpolation operator with respect to the mesh on the slave side. Based on I^h , we consider a modified interpolation operator \tilde{I}^h . To simplify the notation we write the set of nodes on the slave side of $\tilde{\Gamma}_c^s$ introduced as \mathcal{S} now


 Figure 3.1.: Functions g , $I^h g$ and $\tilde{I}^h g$.

as $\mathcal{S} := \{p_i : 1 \leq i \leq |\mathcal{S}|\}$, where $|\mathcal{S}|$ denotes the total number of nodes in \mathcal{S} , and let $\mathcal{W}_c := \{w_j : 1 \leq j \leq N_w\}$ be the set of points in $\overline{\gamma}_a \cap \overline{\gamma}_c$. The minimum distance between the elements in \mathcal{W}_c is denoted by a , i.e.,

$$a := \inf \{ \|w_j - w_k\| : 1 \leq j \neq k \leq N_w \}.$$

By Assumption 3.3 we have $N_w < \infty$ and thus $a > 0$. For $h < \frac{a}{2} =: h_0$, we find between two neighbor points in \mathcal{W}_c at least two vertices in \mathcal{S} .

We now define the modified Lagrange interpolation operator \tilde{I}^h as

$$\left(\tilde{I}^h [\mathbf{u}]_n \right) (p_i) := \begin{cases} [\mathbf{u}]_n(p_i) & \text{if } \text{supp}(\phi_{p_i}) \subset \overline{\gamma}_c, \\ 0 & \text{otherwise,} \end{cases} \quad (3.9)$$

where ϕ_{p_i} is the standard nodal basis function associated with the node $p_i \in \mathcal{S}$, see Figure 3.1. Using $b(\mathbf{u}, \boldsymbol{\lambda}) = 0$, we find

$$b(\mathbf{u}, \boldsymbol{\lambda}^h) = \int_{\Gamma_c^s} \left([\mathbf{u}]_n - \tilde{I}^h [\mathbf{u}]_n \right) (\lambda_n^h - \lambda_n) \, ds + \int_{\Gamma_c^s} \tilde{I}^h [\mathbf{u}]_n (\lambda_n^h - \lambda_n) \, ds. \quad (3.10)$$

By construction we have $\tilde{I}^h [\mathbf{u}]_n \leq 0$ and $\text{supp}(\tilde{I}^h [\mathbf{u}]_n) \subset \text{supp}([\mathbf{u}]_n) = \overline{\gamma}_c$. Using the strong point-wise contact condition $[\mathbf{u}]_n \lambda_n = 0$ we find

$$\int_{\Gamma_c^s} \tilde{I}^h [\mathbf{u}]_n \lambda_n \, ds = 0. \quad (3.11)$$

Furthermore, we get in terms of (3.4) the relation

$$\int_{\Gamma_c^s} \tilde{I}^h [\mathbf{u}]_n \lambda_n^h \, ds \leq 0, \quad (3.12)$$

Due to (3.11) and (3.12) the second term on the right side of (3.10) vanishes and we get from (3.10) the estimate

$$b(\mathbf{u}, \boldsymbol{\lambda}^h) \leq \| [\mathbf{u}]_n - \tilde{I}^h [\mathbf{u}]_n \|_{\frac{1}{2}, \Gamma_c^s} \| \boldsymbol{\lambda}^h - \boldsymbol{\lambda} \|_{-\frac{1}{2}, \Gamma_c^s}. \quad (3.13)$$

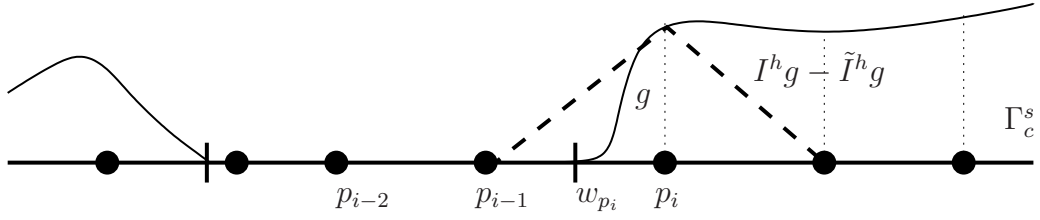


Figure 3.2.: Difference of the interpolated functions $I^h g - \tilde{I}^h g$.

To estimate the term $\|[\mathbf{u}]_n - \tilde{I}^h[\mathbf{u}]_n\|_{\frac{1}{2}, \Gamma_c^s}$, we define $g := -[\mathbf{u}]_n$ and consider the difference $I^h g - \tilde{I}^h g$ of the interpolated functions, see Figures 3.1 and 3.2.

In terms of the inverse inequality, see, e.g., [16], we get

$$\|I^h g - \tilde{I}^h g\|_{\frac{1}{2}, \Gamma_c^s}^2 \leq \frac{C}{h} \|I^h g - \tilde{I}^h g\|_{0, \Gamma_c^s}^2 \leq C \sum_{p_i \in \mathcal{M}_c} (g(p_i))^2, \quad (3.14)$$

where the set of points \mathcal{M}_c on the contact boundary Γ_c^s is defined by

$$\mathcal{M}_c := \{p_i \in \mathcal{S} : \tilde{I}^h g(p_i) \neq I^h g(p_i)\}.$$

Let $w_{p_i} \in \mathcal{W}_c$ be the unique closest point to $p_i \in \mathcal{M}_c$. Without loss of generality, we consider a lexicographically ordering of the indices and the case that $g = 0$ in the left neighborhood of w_{p_i} and $g > 0$ in the right neighborhood of w_{p_i} .

For $h < \frac{a}{2}$, we have $I^h g - \tilde{I}^h g = 0$ on $[p_{i-2}, p_{i-1}]$, see Figure 3.2. The regularity assumption on \mathbf{u} yields $g \in H^{1+\nu}(\Gamma_c^s)$ and moreover $g = 0$ on $[p_{i-2}, w_{p_i}]$. Now, the Cauchy–Schwarz inequality gives for each point $p_i \in \mathcal{M}_c$ the estimate

$$\begin{aligned} (g(p_i))^2 &= \left(\int_{w_{p_i}}^{p_i} g'(s) \, ds \right)^2 = \frac{1}{|w_{p_i} - p_{i-2}|^2} \left(\int_{w_{p_i}}^{p_i} \int_{p_{i-2}}^{w_{p_i}} \frac{g'(s) - g'(t)}{|s - t|^{\frac{1+2\nu}{2}}} |s - t|^{\frac{1+2\nu}{2}} \, dt \, ds \right)^2 \\ &\leq \frac{1}{|w_{p_i} - p_{i-2}|^2} \int_{p_{i-2}}^{p_i} \int_{p_{i-2}}^{p_i} \frac{(g'(s) - g'(t))^2}{|s - t|^{1+2\nu}} \, dt \, ds \int_{w_{p_i}}^{p_i} \int_{p_{i-2}}^{w_{p_i}} |s - t|^{1+2\nu} \, dt \, ds \\ &\leq C \frac{1}{|w_{p_i} - p_{i-2}|^2} |g'|_{\nu, [p_{i-2}, p_i]}^2 h^{1+2\nu} |p_i - w_{p_i}| |w_{p_i} - p_{i-2}| \\ &= C |g'|_{\nu, [p_{i-2}, p_i]}^2 h^{1+2\nu} \frac{|p_i - w_{p_i}|}{|w_{p_i} - p_{i-2}|} \leq C |g'|_{\nu, [p_{i-2}, p_i]}^2 h^{1+2\nu}, \end{aligned}$$

where we used the shape-regularity of the triangulation. To obtain an upper bound for $\|I^h g - \tilde{I}^h g\|_{\frac{1}{2}, \Gamma_c^s}$, we have to sum over all $p_i \in \mathcal{M}_c$. We observe that by Assumption 3.3, the number of elements in \mathcal{M}_c is finite. In terms of (3.13) and (3.14), we find now the

bound

$$\begin{aligned}
 b(\mathbf{u}, \boldsymbol{\lambda}^h) &\leq \|\boldsymbol{\lambda} - \boldsymbol{\lambda}^h\|_{-\frac{1}{2}, \Gamma_c^s} (\|g - I^h g\|_{\frac{1}{2}, \Gamma_c^s} + \|I^h g - \tilde{I}^h g\|_{\frac{1}{2}, \Gamma_c^s}) \\
 &\leq Ch^{\frac{1}{2}+\nu} |g|_{1+\nu, \Gamma_c^s} \|\boldsymbol{\lambda} - \boldsymbol{\lambda}^h\|_{-\frac{1}{2}, \Gamma_c^s} \\
 &\leq Ch^{\frac{1}{2}+\nu} |\mathbf{u}|_{\frac{3}{2}+\nu, \Omega} \|\boldsymbol{\lambda} - \boldsymbol{\lambda}^h\|_{-\frac{1}{2}, \Gamma_c^s}.
 \end{aligned}$$

□

Now, we combine the previous results and formulate the optimal a priori error estimates for two-body contact problems.

Theorem 3.6. *Let $(\mathbf{u}, \boldsymbol{\lambda}) \in \mathbf{V} \times \mathbf{M}_+$ be the solution of (3.1) and let $(\mathbf{u}^h, \boldsymbol{\lambda}^h) \in \mathbf{V}^h \times \mathbf{M}_+^h$ be the solution of the discrete formulation (3.5). Under Assumption 3.3 and the regularity assumption $\mathbf{u} \in [H^{\frac{3}{2}+\nu}(\Omega)]^2$, $0 < \nu \leq \frac{1}{2}$, we have the a priori error estimate*

$$\|\mathbf{u} - \mathbf{u}^h\|_{1, \Omega} + \|\boldsymbol{\lambda} - \boldsymbol{\lambda}^h\|_{-\frac{1}{2}, \Gamma_c^s} \leq Ch^{\frac{1}{2}+\nu} |\mathbf{u}|_{\frac{3}{2}+\nu, \Omega}$$

for a positive constant C .

Proof. Using the well known approximation property for the spaces \mathbf{V}^h and \mathbf{M}^h , the proof is a direct consequence of Lemmas 3.1-3.5 by applying Young's inequality. □

At the end of this subsection we give two remarks concerning a priori estimates for the Lagrange multiplier.

Remark 3.7. It is possible to establish an optimal a priori estimate for the Lagrange multiplier in the weighted $L^2(\Gamma_c^s)$ -norm $\|\boldsymbol{\lambda} - \boldsymbol{\lambda}^h\|_{-\frac{1}{2}, h, \Gamma_c^s}$ given by

$$\|\boldsymbol{\mu}\|_{-\frac{1}{2}, h, \Gamma_c^s}^2 := \sum_{e \in \mathcal{T}_{h, \Gamma_c^s}} h_e \|\boldsymbol{\mu}\|_{0, e}^2, \quad (3.15)$$

with $h_e := |e|$. The proof follows the same lines as for the $H^{-1/2}(\Gamma_c^s)$ -norm and uses an inverse estimate.

Remark 3.8. The same theoretical results can be obtained if a different dual Lagrange multiplier space is used, e.g., piecewise constant dual Lagrange multipliers or continuous piecewise cubic dual Lagrange multipliers as proposed in [138].

3.2. Numerical examples

In this section, we provide several numerical examples illustrating the performance of the approach and confirming the theoretical results obtained in the previous section. We consider different examples for two-body contact problems. We focus on the discretization errors of the displacement in the L^2 - and the H^1 -norm and of the Lagrange multiplier

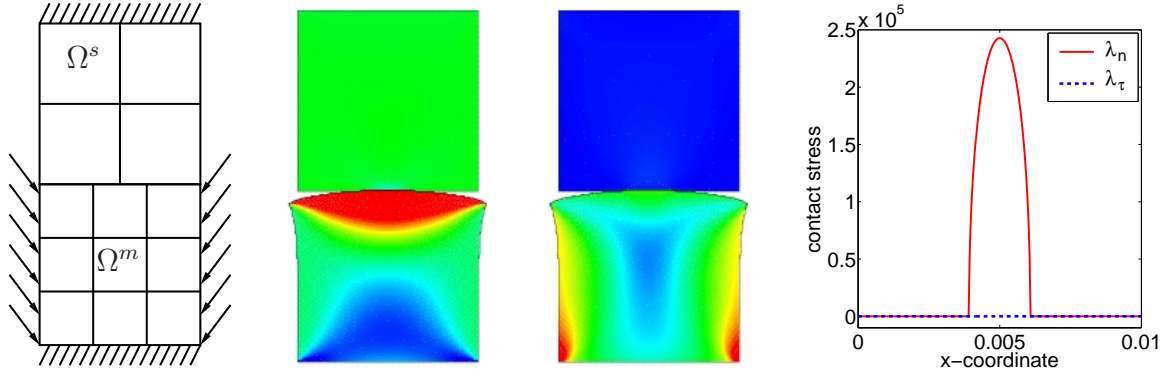


Figure 3.3.: Example 1: Problem definition and initial triangulation (left), stress components σ_{xx} and the effective von Mises stress σ_{eff} on distorted domains (distortion scaled by factor 1000) (middle), and contact stress in normal and tangential direction (right).

in the weighted L^2 -norm (3.15) on the contact boundary. In general, contact problems do not admit an analytical solution. To evaluate the discretization errors, we compute a reference solution denoted by \mathbf{u}_{ref} for the displacements and a reference solution $\boldsymbol{\lambda}_{\text{ref}}$ for the Lagrange multiplier corresponding to a finer mesh. We note that in all our examples, the meshsize h_{ref} for the reference solution satisfies $h_{\text{ref}} \leq 1/4 h$. A reference meshsize of $h_{\text{ref}} = 1/2 h$ does not guarantee reliable numbers for the discretization errors. For the iterative solution of the non-linear system, we use an inexact primal dual active set strategy, see Chapter 4. In each outer iteration step, we apply one linear multigrid cycle. We start with a coarse triangulation and use uniform refinement techniques. Each element is decomposed into four sub-elements within the next refinement step. In all examples we work with plane strain, see (1.33).

First example

In our first example, we consider the problem depicted in Figure 3.3. The two bodies in their reference configuration are scaled squares, $\Omega^m := (0, 0.01) \times (0, 0.01)$ and $\Omega^s := (0.0, 0.01) \times (0.01, 0.02)$. On Ω^m , we set $E^m = 15 \times 10^9$ and $\nu^m = 0.2$ and on Ω^s , we use a different material with $E^s = 20 \times 10^9$ and $\nu^s = 0.4$. The lower boundary of Ω^m is clamped. The applied load \mathbf{p}^m is given by $(10^5, -10^6)^\top$ on the left side and by $(-10^5, -10^6)^\top$ on the right side of Ω^m . Homogeneous Neumann boundary conditions are applied to both sides of Ω^s , and inhomogeneous Dirichlet data are given on the top of Ω^s . The displacements are set to be $\mathbf{u}_D^s = (0.0, -5 \times 10^{-7})^\top$.

The initial triangulation on level 0 is shown in the left picture in Figure 3.3. We recall that the normal component of the Lagrange multiplier $-\lambda_n^h$ of the mortar discretization approximates the contact pressure. In the right picture in Figure 3.3, we give the normal and tangential component of $\boldsymbol{\lambda}^h$ on level 6. The normal component is non-zero only in the part of Γ_c^s where the two bodies are actually in contact. As expected, the tangential

Table 3.1.: Example 1: Relative $L^2(\Omega)$ -, relative $H^1(\Omega)$ -error of \mathbf{u}^h with respect to \mathbf{u}_{ref} , weighted $L^2(\Gamma_c^s)$ -error of $\boldsymbol{\lambda}^h$ with respect to $\boldsymbol{\lambda}_{\text{ref}}$ and the numerical convergence orders.

level	$\ \mathbf{u}^h - \mathbf{u}_{\text{ref}}\ _{0,\Omega} / \ \mathbf{u}_{\text{ref}}\ _{0,\Omega}$		$ \mathbf{u}^h - \mathbf{u}_{\text{ref}} _{1,\Omega} / \mathbf{u}_{\text{ref}} _{1,\Omega}$		$\ \boldsymbol{\lambda}^h - \boldsymbol{\lambda}_{\text{ref}}\ _{-\frac{1}{2},h,\Gamma_c^s}$	
0	$6.447659e - 02$	—	$4.447386e - 01$	—	$9.507368e + 02$	—
1	$1.947047e - 02$	1.73	$2.422984e - 01$	0.87	$3.709632e + 02$	1.36
2	$5.719462e - 03$	1.77	$1.323250e - 01$	0.87	$1.937997e + 02$	0.94
3	$1.798368e - 03$	1.67	$7.137496e - 02$	0.89	$8.890783e + 01$	1.12
4	$5.181605e - 04$	1.80	$3.815553e - 02$	0.90	$3.743692e + 01$	1.25
5	$1.551852e - 04$	1.74	$2.012575e - 02$	0.92	$1.503053e + 01$	1.32
6	$4.544415e - 05$	1.77	$1.027931e - 02$	0.97	$5.607133e + 00$	1.42

component is equal to zero since we are in the setting without friction. The distorted domains with the stress component $\boldsymbol{\sigma}_{xx}$ and the effective von Mises stress σ_{eff} are shown in the middle in Figure 3.3. The effective von Mises stress is given in terms of the pressure p by the relation

$$\sigma_{\text{eff}}^2 := \sum_{i,j=1}^d |\boldsymbol{\sigma}_{ij} - \delta_{ij}p|^2, \quad p := \frac{1}{d} \text{tr}(\boldsymbol{\sigma}). \quad (3.16)$$

We use the finite element solution on level 8 as reference solution $(\mathbf{u}_{\text{ref}}, \boldsymbol{\lambda}_{\text{ref}})$. On level 8, we have 262.144 elements on Ω^s and 589.824 elements on Ω^m . In Table 3.1, we give the discretization errors of the displacements in the relative $L^2(\Omega)$ -norm and in the relative $H^1(\Omega)$ -norm. The error in the Lagrange multiplier is measured in a weighted $L^2(\Gamma_c^s)$ -norm introduced in Remark 3.7. The convergence rates in the $L^2(\Gamma_c^s)$ -norm for the displacements are approximately 1.8. Asymptotically, the convergence rates tend to one in the $H^1(\Omega)$ -norm. As in the linear case, we observe better convergence rates for the Lagrange multiplier. The best approximation error of the Lagrange multiplier in the weighted $L^2(\Gamma_c^s)$ -norm is of order $h^{3/2}$.

Second example

In our second example, [73], we use the same geometry and the same material parameters as in the first Example. The upper part of Ω^s and the lower part of Ω^m are clamped. Inhomogeneous Neumann data are applied to the left part of Ω^s and to the right part of Ω^m . The boundary forces are given by $\mathbf{p}^s = (10^5, -10^6)^\top$ and $\mathbf{p}^m = (-10^5, -10^6)^\top$, see Figure 3.4.

In the middle picture in Figure 3.4, the stress component $\boldsymbol{\sigma}_{xx}$ is shown on the distorted domains. The normal component of the Lagrange multiplier is given in the right picture. In contrast to Example 1, we observe a singularity at the left endpoint of the contact

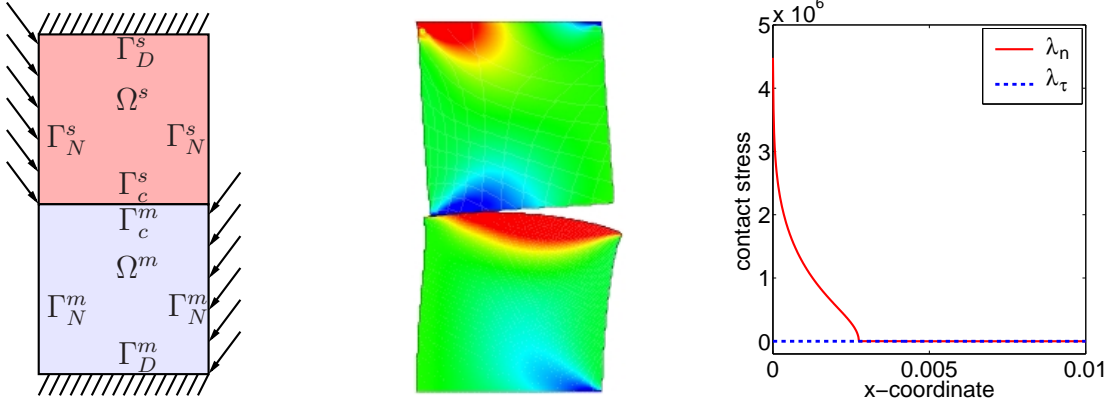


Figure 3.4.: Example 2: Problem definition (left), stress component σ_{xx} on distorted domains (distortion scaled by factor 1000) (middle), and contact stress in normal and tangential direction (right).

Table 3.2.: Example 2: Relative $L^2(\Omega)$ -, relative $H^1(\Omega)$ -error of \mathbf{u}^h with respect to \mathbf{u}_{ref} , weighted $L^2(\Gamma_c^s)$ -error of $\boldsymbol{\lambda}^h$ with respect to $\boldsymbol{\lambda}_{\text{ref}}$ and the numerical convergence orders.

level	$\ \mathbf{u}^h - \mathbf{u}_{\text{ref}}\ _{0,\Omega} / \ \mathbf{u}_{\text{ref}}\ _{0,\Omega}$		$ \mathbf{u}^h - \mathbf{u}_{\text{ref}} _{1,\Omega} / \mathbf{u}_{\text{ref}} _{1,\Omega}$		$\ \boldsymbol{\lambda}^h - \boldsymbol{\lambda}_{\text{ref}}\ _{-\frac{1}{2},h,\Gamma_c^s}$	
0	$6.314604e - 01$	—	$8.113448e - 01$	—	$4.648877e + 03$	—
1	$3.513681e - 01$	0.85	$5.138377e - 01$	0.66	$2.210844e + 03$	1.07
2	$1.414198e - 01$	1.31	$2.786256e - 01$	0.88	$1.668986e + 03$	0.41
3	$5.196291e - 02$	1.44	$1.502248e - 01$	0.89	$9.087467e + 02$	0.88
4	$1.885312e - 02$	1.46	$8.271511e - 02$	0.86	$4.278806e + 02$	1.09
5	$6.983378e - 03$	1.43	$4.614857e - 02$	0.84	$1.994283e + 02$	1.10
6	$2.611373e - 03$	1.42	$2.576322e - 02$	0.84	$9.358784e + 01$	1.09
7	$9.293584e - 04$	1.49	$1.399176e - 02$	0.88	$4.454642e + 01$	1.07

zone. Here, we use bilinear finite elements and a conforming triangulation on the possible contact boundary Γ_c^s . The finite element solution on level 8 is taken as reference solution. Due to the lower regularity of the solution, we cannot expect a convergence rate of order h . The discretization errors for the relative $L^2(\Omega)$ - and $H^1(\Omega)$ -norm of the displacement are given in column three and four of Table 3.2, respectively. The error of the Lagrange multiplier in the weighted $L^2(\Gamma_c^s)$ -norm can be found in the last column. Asymptotically, the convergence rates tend to 0.9 in the $H^1(\Omega)$ -norm. As in Example 1, we observe a higher convergence rate for the Lagrange multiplier. The convergence rate for the $L^2(\Gamma_c^s)$ -norm is approximately 1.5. The low regularity of the problem is reflected in smaller numerical convergence rates.

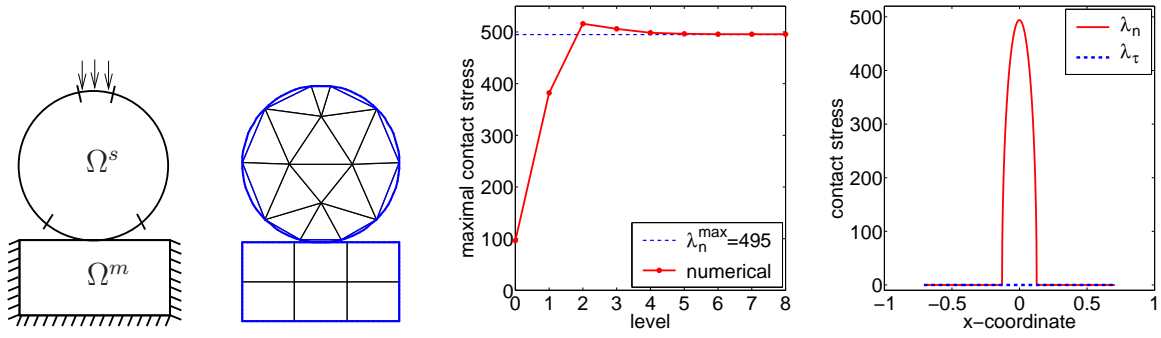


Figure 3.5.: Example 3: Problem definition and initial triangulation (left), maximal contact stress (middle) and contact stress (right).

Third example

Our third example is the Hertzian contact problem of a linear elastic circle with a plane. In this example, the contact stress can be computed analytically, see, e.g., [69, 88, 91]. So we are able to compare the numerically computed boundary stress to the analytical one. If an elastic circle with radius r and material parameters E^s and ν^s is pressed by a single point load $\mathbf{f}^s = (0, -f)^\top$ on the top to a rigid plane, the analytical contact pressure is given by

$$p_n(x) = \frac{2f}{\pi b^2} \sqrt{(b^2 - x^2)}, \quad x \leq b, \quad b := 2\sqrt{\frac{fr(1 - \nu^2)}{E\pi}}, \quad (3.17)$$

where b is the half-width of the contact surface and x is the distance to the center of the contact surface. In our setting, we replace the rigid plane by a linear elastic rectangle. Young's modulus of the rectangle is set to be larger than the one of the circle. We apply homogeneous Dirichlet boundary conditions at the bottom and at the two sides of the rectangle. On the circle with radius $r = 1$, we set the material parameters to be $E^s = 7000$ and $\nu^s = 0.3$. For the rectangle with height 1, we use $E^m = 10^6$ and $\nu^m = 0.45$. The circle, assumed to be the slave side, is pressed by a point load $\mathbf{f}^s = (0, -100)^\top$ at the top of the rectangle. The problem definition and the geometry are shown in Figure 3.5. As done in [21, 98], we replace the point load by a surface load to avoid a strong singularity on the upper part of the circle. In order to obtain a unique discrete solution, we eliminate the horizontal degrees of freedom of the two inner nodes on the vertical symmetry axis, see Figure 3.5.

Using (3.17), the maximal normal contact stress of the Hertzian contact problem is then given by $\lambda_n^{\max} = 494.8$, and for the half width of the contact zone we find $b = 0.129$. The pictures on the right in Figure 3.5 illustrates the numerical approximation of the contact stress. From level 4 on, the discrete maximal normal stress is a very good approximation of the analytical one. In the right picture, the normal and tangential contribution of the Lagrange multiplier are given.

To compute the discretization errors, we use the mortar finite element solution on level 8 as reference solution. The errors are given in Table 3.3. Asymptotically, we observe

3. Optimal a priori error estimates

Table 3.3.: Example 3: Relative $L^2(\Omega)$ -, relative $H^1(\Omega)$ -error of \mathbf{u}^h with respect to \mathbf{u}_{ref} , weighted $L^2(\Gamma_c^s)$ -error of $\boldsymbol{\lambda}^h$ with respect to $\boldsymbol{\lambda}_{\text{ref}}$ and the numerical convergence orders.

level	$\ \mathbf{u}^h - \mathbf{u}_{\text{ref}}\ _{0,\Omega}/\ \mathbf{u}_{\text{ref}}\ _{0,\Omega}$		$ \mathbf{u}^h - \mathbf{u}_{\text{ref}} _{1,\Omega}/ \mathbf{u}_{\text{ref}} _{1,\Omega}$		$\ \boldsymbol{\lambda}^h - \boldsymbol{\lambda}_{\text{ref}}\ _{-\frac{1}{2},h,\Gamma_c^s}$	
1	$5.227370e - 02$	—	$4.663629e - 01$	—	$5.845408 + 01$	—
2	$1.381026e - 02$	1.92	$3.214708e - 01$	0.54	$4.998951 + 01$	0.23
3	$4.844067e - 03$	1.51	$1.807113e - 01$	0.83	$2.120954 + 01$	1.24
4	$1.350194e - 03$	1.84	$9.735769e - 02$	0.89	$8.377665 + 00$	1.34
5	$4.175901e - 04$	1.69	$5.111927e - 02$	0.93	$3.269378 + 00$	1.36
6	$1.102450e - 04$	1.92	$2.584385e - 02$	0.98	$1.168388 + 00$	1.48

Table 3.4.: Example 3: Relative $H^1(\Omega)$ -error of \mathbf{u}^h with respect to \mathbf{u}_{ref} and the maximal contact stress $(\lambda_n^h)^{\max}$ for dual linear, dual constant and dual cubic Lagrange multipliers.

level	$ \mathbf{u}^h - \mathbf{u}_{\text{ref}} _{1,\Omega}/ \mathbf{u}_{\text{ref}} _{1,\Omega}$		$(\lambda_n^h)^{\max}$		
	constant	cubic	linear	constant	cubic
1	$4.663629e - 01$	$4.663629e - 01$	382.057	382.057	382.057
2	$3.214712e - 01$	$3.214712e - 01$	514.166	514.172	514.172
3	$1.807105e - 01$	$1.807104e - 01$	504.190	504.229	504.231
4	$9.735749e - 02$	$9.735742e - 02$	496.765	496.775	496.775
5	$5.111913e - 02$	$5.111915e - 02$	494.805	494.809	494.809
6	$2.584384e - 02$	$2.584384e - 02$	494.264	494.266	494.266
7			494.174	494.175	494.175
8			494.202	494.202	494.202

optimal convergence rates. In the $L^2(\Gamma_c^s)$ -norm, the convergence rate tends to two with increasing number of refinement steps, whereas the convergence rate in the $H^1(\Omega)$ -norm tends to 1.0. We observe asymptotically a convergence rate of 1.5 for the Lagrange multiplier in the weighted $L^2(\Gamma_c^s)$ -norm on the contact zone. This results from the fact that the error in the energy norm restricted to a band of width h can be bounded by $C\sqrt{h}\|\mathbf{u}\|_{1,\Omega}$.

In a last test, we consider the influence of the choice of the dual Lagrange multiplier on the displacement and the maximal contact stress. To do so, we compare three different dual Lagrange multipliers. In addition to the linear Lagrange multiplier, we use discontinuous piecewise constant and continuous piecewise cubic Lagrange multipliers, [138].

Table 3.4 shows in the first two columns the relative $H^1(\Omega)$ -error for the dual constant and the dual cubic Lagrange multipliers. If we compare the results of Table 3.4 with the one of Table 3.3, we find that all our three dual Lagrange multipliers yields almost the same results. The differences in the H^1 -norm of the error is negligible. This is also true for the maximal contact stress. The last three columns of Table 3.4 show $(\lambda_n^h)^{\max}$ for the three different discretization methods.

3.3. Visualization of discontinuous Lagrange multiplier

Due to the discontinuity of the dual basis functions ψ_p for the Lagrange multiplier the Lagrange multiplier λ^h is discontinuous itself. Therefore one has to take care how to visualize this discontinuous function. Instead of λ^h we plot in Figures 3.3, 3.4 and 3.5 and all over this thesis the linear continuous function $\tilde{\lambda}^h$ defined by

$$\tilde{\lambda}^h = \sum_{p \in \mathcal{S}} \tilde{\lambda}_p \phi_p \quad (3.18)$$

with the coefficients $\tilde{\lambda}_p$ given by

$$\tilde{\lambda}_p := \frac{\int_{\Gamma_c^s} \lambda^h \phi_p \, ds}{\int_{\Gamma_c^s} \phi_p \, ds}, \quad p \in \mathcal{S}. \quad (3.19)$$

We remark that from this definition directly follows after summation over all nodes $p \in \mathcal{S}$, that the lowest order momentum is the same for $\tilde{\lambda}^h$ as for λ^h , i.e.,

$$\int_{\Gamma_c^s} \tilde{\lambda}^h \, ds = \int_{\Gamma_c^s} \lambda^h \, ds.$$

Due to the biorthogonality relation (2.12), definition (3.19) leads to $\tilde{\lambda}_p = \lambda_p$, where λ_p are the coefficients of λ^h and therefore we get from (3.18)

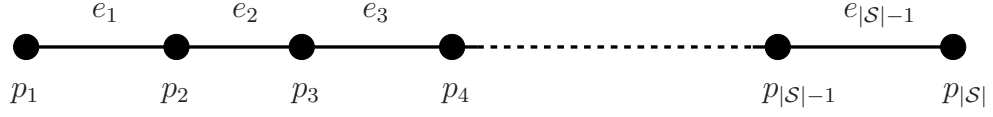
$$\tilde{\lambda}^h = \sum_{p \in \mathcal{S}} \lambda_p \phi_p. \quad (3.20)$$

Similar to the result of Theorem 3.6 and Remark 3.7 we can establish optimal a priori error estimates in the $H^{-\frac{1}{2}}(\Gamma_c^s)$ -norm and the weighted $L^2(\Gamma_c^s)$ -norm for the modified Lagrange multiplier $\tilde{\lambda}^h$.

Theorem 3.9. *Under the regularity assumptions of Theorem 3.6, the optimal a priori error estimates*

$$\|\lambda - \tilde{\lambda}^h\|_{-\frac{1}{2}, \Gamma_c^s} \leq Ch |\mathbf{u}|_{2, \Omega}, \quad \|\lambda - \tilde{\lambda}^h\|_{-\frac{1}{2}, h, \Gamma_c^s} \leq Ch |\mathbf{u}|_{2, \Omega}$$

hold for the modified Lagrange multiplier (3.18).


 Figure 3.6.: Ordering of nodes p_i and edges e_i of Γ_c^s .

Proof. In addition to the approximation property (3.7) in L^2 , the dual mortar projection satisfies the approximation property in $H^{-\frac{1}{2}}$ and the stability condition in $H^{\frac{1}{2}}$, [137]. So far we have for $\nu \in \{-\frac{1}{2}, 0\}$ with the trace theorem the estimates

$$\|\boldsymbol{\lambda} - \Pi_*^h \boldsymbol{\lambda}\|_{\nu, \Gamma_c^s} \leq Ch^{\frac{1}{2}-\nu} |u|_{2, \Omega}, \quad |\Pi_*^h \boldsymbol{\lambda}|_{\frac{1}{2}, \Gamma_c^s} \leq C |\boldsymbol{\lambda}|_{\frac{1}{2}, \Gamma_c^s}. \quad (3.21)$$

Due to the shape of the basis functions $\psi_p - \phi_p$ the mean value of $\boldsymbol{\lambda}^h - \tilde{\boldsymbol{\lambda}}^h$ vanishes, i.e.,

$$\int_{\Gamma_c^s} \boldsymbol{\lambda}^h - \tilde{\boldsymbol{\lambda}}^h \, ds = 0. \quad (3.22)$$

Introducing Π_0^h as the $L^2(\Gamma_c^s)$ -projection onto the piecewise constant functions on each edge $e \in \mathcal{T}_{h, \Gamma_c^s}$, we observe due to (3.22)

$$\begin{aligned} \|\boldsymbol{\lambda}^h - \tilde{\boldsymbol{\lambda}}^h\|_{-\frac{1}{2}, \Gamma_c^s} &= \sup_{\mathbf{0} \neq \mathbf{v} \in [H_{00}^{1/2}(\Gamma_c^s)]^2} \frac{\langle \boldsymbol{\lambda}^h - \tilde{\boldsymbol{\lambda}}^h, \mathbf{v} - \Pi_0^h \mathbf{v} \rangle}{\|\mathbf{v}\|_{\frac{1}{2}, \Gamma_c^s}} \\ &\leq \sup_{\mathbf{0} \neq \mathbf{v} \in [H_{00}^{1/2}(\Gamma_c^s)]^2} \frac{\|\boldsymbol{\lambda}^h - \tilde{\boldsymbol{\lambda}}^h\|_{0, \Gamma_c^s} \|\mathbf{v} - \Pi_0^h \mathbf{v}\|_{0, \Gamma_c^s}}{\|\mathbf{v}\|_{\frac{1}{2}, \Gamma_c^s}} \\ &\leq C\sqrt{h} \sup_{\mathbf{0} \neq \mathbf{v} \in [H_{00}^{1/2}(\Gamma_c^s)]^2} \frac{\|\boldsymbol{\lambda}^h - \tilde{\boldsymbol{\lambda}}^h\|_{0, \Gamma_c^s} \|\mathbf{v}\|_{\frac{1}{2}, \Gamma_c^s}}{\|\mathbf{v}\|_{\frac{1}{2}, \Gamma_c^s}} \\ &\leq C\sqrt{h} \|\boldsymbol{\lambda}^h - \tilde{\boldsymbol{\lambda}}^h\|_{0, \Gamma_c^s}. \end{aligned}$$

Due to the triangle inequality and Remark 3.7 we have

$$\|\boldsymbol{\lambda} - \tilde{\boldsymbol{\lambda}}^h\|_{0, \Gamma_c^s} \leq \|\boldsymbol{\lambda} - \boldsymbol{\lambda}^h\|_{0, \Gamma_c^s} + \|\boldsymbol{\lambda}^h - \tilde{\boldsymbol{\lambda}}^h\|_{0, \Gamma_c^s} \leq C\sqrt{h} |\mathbf{u}|_{2, \Omega} + \|\boldsymbol{\lambda}^h - \tilde{\boldsymbol{\lambda}}^h\|_{0, \Gamma_c^s}$$

and therefore, it remains to show that

$$\|\boldsymbol{\lambda}^h - \tilde{\boldsymbol{\lambda}}^h\|_{0, \Gamma_c^s} \leq C\sqrt{h} |\mathbf{u}|_{2, \Omega}. \quad (3.23)$$

In the following, we use for the boundary nodes p_i and the edges e_i of Γ_c^s , assumed to be a straight line, the lexicographical ordering as depicted in Figure 3.6. Taking into account the definition of the dual basis functions ψ_p in terms of the standard basis functions ϕ_p , see (2.13), we obtain with

$$\Delta \phi_{p_i} := \begin{cases} \phi_{p_i} - \phi_{p_{i+1}} & \text{on } e_i, \\ 0 & \text{otherwise,} \end{cases} \quad \Delta \boldsymbol{\lambda}_{p_i} := \boldsymbol{\lambda}_{p_i} - \boldsymbol{\lambda}_{p_{i+1}},$$

using (3.20) and the representation (2.13) for the dual basis functions the relation

$$\boldsymbol{\lambda}^h - \tilde{\boldsymbol{\lambda}}^h = \sum_{i=1}^{|\mathcal{S}|} \boldsymbol{\lambda}_{p_i} (\psi_{p_i} - \phi_{p_i}) = \sum_{i=1}^{|\mathcal{S}|-1} (\boldsymbol{\lambda}_{p_i} - \boldsymbol{\lambda}_{p_{i+1}}) \Delta \phi_{p_i} = \sum_{i=1}^{|\mathcal{S}|-1} \Delta \boldsymbol{\lambda}_{p_i} \Delta \phi_{p_i}.$$

To do so, we estimate

$$\|\boldsymbol{\lambda}^h - \tilde{\boldsymbol{\lambda}}^h\|_{0,\Gamma_c^s}^2 = \sum_{i=1}^{|\mathcal{S}|-1} (\Delta \boldsymbol{\lambda}_{p_i})^2 \|\Delta \phi_{p_i}\|_{0,e_i}^2 \leq Ch \sum_{i=1}^{|\mathcal{S}|-1} (\Delta \boldsymbol{\lambda}_{p_i})^2. \quad (3.24)$$

Writing $\Pi_*^h \boldsymbol{\lambda} = \sum_{i=1}^{|\mathcal{S}|} \boldsymbol{\alpha}_{p_i} \phi_{p_i}$, we observe after applying the triangle inequality due to (3.21) and Remark 3.7 the estimate

$$\begin{aligned} \left\| \sum_{i=1}^{|\mathcal{S}|} (\boldsymbol{\lambda}_{p_i} \psi_{p_i} - \boldsymbol{\alpha}_{p_i} \phi_{p_i}) \right\|_{0,\Gamma_c^s}^2 &= \|\boldsymbol{\lambda}^h - \Pi_*^h \boldsymbol{\lambda}\|_{0,\Gamma_c^s}^2 \\ &\leq \|\boldsymbol{\lambda}^h - \boldsymbol{\lambda}\|_{0,\Gamma_c^s}^2 + \|\boldsymbol{\lambda} - \Pi_*^h \boldsymbol{\lambda}\|_{0,\Gamma_c^s}^2 \\ &\leq Ch |\mathbf{u}|_{2,\Omega}^2. \end{aligned} \quad (3.25)$$

Taken into account the definition of the dual basis functions (2.13), we observe the proportionality relation

$$\left\| \sum_{i=1}^{|\mathcal{S}|} (\boldsymbol{\lambda}_{p_i} \psi_{p_i} - \boldsymbol{\alpha}_{p_i} \phi_{p_i}) \right\|_{0,\Gamma_c^s}^2 \sim h \sum_{i=1}^{|\mathcal{S}|-1} ((2\boldsymbol{\lambda}_{p_i} - \boldsymbol{\lambda}_{p_{i+1}} - \boldsymbol{\alpha}_{p_i})^2 + (2\boldsymbol{\lambda}_{p_{i+1}} - \boldsymbol{\lambda}_{p_i} - \boldsymbol{\alpha}_{p_{i+1}})^2).$$

A simple algebraic computation leads to the estimate

$$(\boldsymbol{\lambda}_{p_i} - \boldsymbol{\lambda}_{p_{i+1}})^2 \leq C((2\boldsymbol{\lambda}_{p_i} - \boldsymbol{\lambda}_{p_{i+1}} - \boldsymbol{\alpha}_{p_i})^2 + (2\boldsymbol{\lambda}_{p_{i+1}} - \boldsymbol{\lambda}_{p_i} - \boldsymbol{\alpha}_{p_{i+1}})^2 + (\boldsymbol{\alpha}_{p_i} - \boldsymbol{\alpha}_{p_{i+1}})^2)$$

and therefore we obtain from (3.24) by using (3.25) at the estimate

$$\begin{aligned} \|\boldsymbol{\lambda}^h - \tilde{\boldsymbol{\lambda}}^h\|_{0,\Gamma_c^s}^2 &\leq C \left(\|\boldsymbol{\lambda}^h - \Pi_*^h \boldsymbol{\lambda}\|_{0,\Gamma_c^s}^2 + h \sum_{i=1}^{|\mathcal{S}|-1} (\boldsymbol{\alpha}_{p_i} - \boldsymbol{\alpha}_{p_{i+1}})^2 \right) \\ &\leq Ch \left(|\mathbf{u}|_{2,\Omega}^2 + \sum_{i=1}^{|\mathcal{S}|-1} (\boldsymbol{\alpha}_{p_i} - \boldsymbol{\alpha}_{p_{i+1}})^2 \right). \end{aligned} \quad (3.26)$$

From the definition of the $H^{\frac{1}{2}}(\Gamma_c^s)$ -seminorm restricted to the edge e

$$|v|_{\frac{1}{2},e}^2 := \int_e \int_e \frac{(v(s) - v(t))^2}{(s-t)^2} ds dt, \quad (3.27)$$

we observe for a linear function v on the edge e_i

$$|v|_{\frac{1}{2},e_i}^2 = (v(p_i) - v(p_{i+1}))^2.$$

Moreover, we can deduce from the definition (3.27)

$$\sum_{i=1}^{|\mathcal{S}|-1} |\Pi_*^h \boldsymbol{\lambda}|_{\frac{1}{2}, e_i}^2 \leq |\Pi_*^h \boldsymbol{\lambda}|_{\frac{1}{2}, \Gamma_c^s}^2.$$

Now, we can estimate the second term on the right side in (3.26)

$$\sum_{i=1}^{|\mathcal{S}|-1} (\boldsymbol{\alpha}_{p_i} - \boldsymbol{\alpha}_{p_{i+1}})^2 = \sum_{i=1}^{|\mathcal{S}|-1} |\Pi_*^h \boldsymbol{\lambda}|_{\frac{1}{2}, e_i}^2 \leq |\Pi_*^h \boldsymbol{\lambda}|_{\frac{1}{2}, \Gamma_c^s}^2 \leq C |\boldsymbol{\lambda}|_{\frac{1}{2}, \Gamma_c^s}^2 \leq C |\mathbf{u}|_{2, \Gamma_c^s}^2,$$

where we used the stability of Π_*^h , see (3.21). Inserting this estimate into (3.26), we observe the desired relation (3.23). \square

3.4. Extension to quadratic finite elements

In this subsection, we shortly present the theoretical results and numerical examples for the extension of the optimal a priori error estimate stated in Section 3.1-3.2 to the situation of quadratic finite elements. Subsection 3.4.1 contains the obtained theoretical result, whereas in Subsection 3.4.2 two numerical examples confirming the theoretical result are given. The results have been published in [79], where the details can be found.

3.4.1. Theoretical results

In this section, we denote by $\mathbf{V}^{h,i}$ the finite element space of order $i = 1, 2$. We remark that in all other sections we neglect the index i , since always the case $i = 1$ was considered. In the same way we introduce the space $\mathbf{M}^{h,j}$, $j = 1, 2$, as the higher order space for the discrete Lagrange multiplier. For the definition of the dual basis functions for the quadratic case, i.e., $j = 2$, we refer to [105, 136]. The admissible space $\mathbf{M}_+^{h,j} \subset \mathbf{M}^{h,j}$ for the case $j = 2$ is defined according to the definition for the case $j = 1$, see (3.4), i.e., each coefficient of the normal part of the corresponding function $\boldsymbol{\lambda}^{h,j} \in \mathbf{M}_+^{h,j}$ is enforced to be positive. For the three different pairings $\mathbf{V}^{h,1} \times \mathbf{M}_+^{h,1}$, $\mathbf{V}^{h,2} \times \mathbf{M}_+^{h,1}$ and $\mathbf{V}^{h,2} \times \mathbf{M}_+^{h,2}$, we denote the finite element solutions by $(\mathbf{u}^{h,1}, \boldsymbol{\lambda}^{h,1})$, $(\mathbf{u}^{h,2}, \boldsymbol{\lambda}^{h,1})$ and $(\mathbf{u}^{h,2}, \boldsymbol{\lambda}^{h,2})$, respectively. We note that although using the same notation, the first solution component of $(\mathbf{u}^{h,2}, \boldsymbol{\lambda}^{h,1})$ and $(\mathbf{u}^{h,2}, \boldsymbol{\lambda}^{h,1})$ is different. In addition to the result in Section 3.1 for $(\mathbf{u}^{h,i}, \boldsymbol{\lambda}^{h,j}) \in \mathbf{V}^{h,i} \times \mathbf{M}_+^{h,j}$ with $(i, j) = (1, 1)$, we observe the following a priori error estimate.

Theorem 3.10. *Let $(u, \lambda) \in \mathbf{V} \times \mathbf{M}_+$ be the solution of (3.1) and let $(u^{h,i}, \lambda^{h,j}) \in \mathbf{V}^{h,i} \times \mathbf{M}_+^{h,j}$ be the solution of the discrete problem (3.5) with the spaces $\mathbf{V}^{h,i}$ and $\mathbf{M}^{h,j}$ instead of $\mathbf{V}^{h,i}$ and $\mathbf{M}^{h,j}$, respectively. Under Assumption 3.3 and the regularity assumption*

Table 3.5.: Example 1: Relative $H^1(\Omega)$ -error with respect to $\mathbf{u}_{\text{ref}}^i$ and numerical convergence orders.

level	$ \mathbf{u}^{h,i} - \mathbf{u}_{\text{ref}}^i _{1,\Omega} / \mathbf{u}_{\text{ref}}^i _{1,\Omega}$					
	$(i, j) = (1, 1)$		$(i, j) = (2, 1)$		$(i, j) = (2, 2)$	
0	$4.447386e - 01$	—	$1.765461e - 01$	—	$1.374306e - 01$	—
1	$2.422984e - 01$	0.87	$7.444445e - 02$	1.25	$7.274920e - 02$	0.92
2	$1.323250e - 01$	0.87	$3.841333e - 02$	0.95	$3.757366e - 02$	0.95
3	$7.137496e - 02$	0.89	$2.010207e - 02$	0.93	$1.959540e - 02$	0.94
4	$3.815553e - 02$	0.90	$1.070640e - 02$	0.91	$9.984628e - 03$	0.97
5	$2.012575e - 02$	0.92	$5.505093e - 03$	0.96	$4.633481e - 03$	1.11
6	$1.027931e - 02$	0.97	—	—	—	—

$\mathbf{u} \in [H^{\frac{3}{2}+\nu}(\Omega)]^2$, $0 < \nu \leq \frac{1}{2}$ for $i = 1$, and $0 < \nu < 1$ for $i = 2$, we have for the two-dimensional case the a priori error estimate

$$\|\mathbf{u} - \mathbf{u}^{h,i}\|_{1,\Omega} + \|\boldsymbol{\lambda} - \boldsymbol{\lambda}^{h,j}\|_{-\frac{1}{2},\Gamma_c^s} \leq Ch^{\frac{1}{2}+\nu} |\mathbf{u}|_{\frac{3}{2}+\nu,\Omega}$$

for a positive constant C .

Proof. The proof can be found in [79]. It follows the same lines as the proof of Theorem 3.6 for the lowest order case. The estimates observed in the Lemmas 3.1 and 3.5 can be proven by the same techniques, whereas in the proof of Lemma 3.4 the inequality (3.8) does not hold for the quadratic case. Thus, we have to work additionally with the L^2 -projection onto the space of piecewise constant functions with respect to the mesh $\mathcal{T}_{h,\Gamma_c^s}$ of Γ_c^s to get the estimate in Lemma 3.4 for the quadratic case. \square

3.4.2. Numerical examples

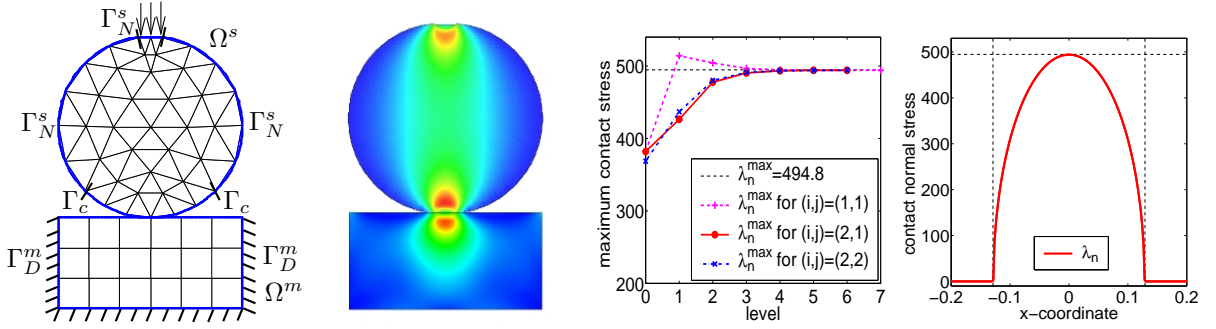
We now present as in Section 3.2 the numerically observed relative errors and convergence orders for the pairings $(i, j) \in \{(1, 1), (2, 1), (2, 2)\}$.

First example

Considering the same example as the first Example in Section 3.2, see Figure 3.3, we observe the results presented in Table 3.5 for the displacement and in Table 3.6 for the Lagrange multiplier. We use again the finite element solution on level 8 as our reference solution $(\mathbf{u}_{\text{ref}}^1, \boldsymbol{\lambda}_{\text{ref}}^1)$ for the lowest order case. For the other cases, we use the solutions on level 7 as $(\mathbf{u}_{\text{ref}}^2, \boldsymbol{\lambda}_{\text{ref}}^1)$ and $(\mathbf{u}_{\text{ref}}^2, \boldsymbol{\lambda}_{\text{ref}}^2)$. Table 3.5 shows the relative errors in the $H^1(\Omega)$ -seminorm. The absolute discretization error for the Lagrange multiplier is measured in a weighted $L^2(\Gamma_c^s)$ -norm, see Remark (3.7), and can be seen in Table 3.6. The values for the pairing $(i, j) = (1, 1)$ are the same as in Table 3.1. To make the comparison with the other

Table 3.6.: Example 1: Weighted $L^2(\Gamma_c^s)$ -error of $\lambda^{h,j}$ with respect to λ_{ref}^j and numerical convergence orders.

level	$\ \lambda^{h,j} - \lambda_{\text{ref}}^j\ _{-\frac{1}{2},h,\Gamma_c^s}$					
	$(i,j) = (1,1)$		$(i,j) = (2,1)$		$(i,j) = (2,2)$	
0	$9.507368e + 02$	—	$1.058862e + 03$	—	$2.896468e + 02$	—
1	$3.709632e + 02$	1.36	$2.976714e + 02$	1.83	$2.084812e + 02$	0.47
2	$1.937997e + 02$	0.94	$1.639180e + 02$	0.86	$3.263949e + 01$	2.67
3	$8.890783e + 01$	1.12	$7.607820e + 01$	1.11	$1.786991e + 01$	0.87
4	$3.743692e + 01$	1.25	$3.725874e + 01$	1.03	$9.317617e + 00$	0.94
5	$1.503053e + 01$	1.32	$1.427542e + 01$	1.38	$1.973473e + 00$	2.24
6	$5.607133e + 00$	1.42	—	—	—	—


 Figure 3.7.: Example 2: Problem definition and initial triangulation, effective von Mises stress σ_{eff} in (3.16) on the distorted domains, maximum contact stress on the levels for the three different discretization methods and normal contact stress.

pairings easier, we present these values again. Comparing the discretization errors in the $H^1(\Omega)$ -seminorm, we observe almost the same qualitative results for all three settings. The convergence orders tend asymptotically to one. However, there are some quantitative differences. Comparing the results of $(i,j) = (1,1)$ on level l with the ones of $(i,j) = (2,1)$ or $(i,j) = (2,2)$ on level $l - 1$, we find a factor of improvement of approximately two. The difference in the accuracy for the $H^1(\Omega)$ -seminorm between $(i,j) = (2,1)$ and $(i,j) = (2,2)$ are negligible. This is not the case for the discretization error in the weighted $L^2(\Gamma_c^s)$ -norm for the Lagrange multiplier. For the Lagrange multiplier, we can compare the cases $(i,j) = (1,1)$ and $(i,j) = (2,1)$ on level l with $(i,j) = (2,2)$ on level $l - 1$. The full quadratic approach yields better results.

Table 3.7.: Example 2: Relative $H^1(\Omega)$ -error with respect to $\mathbf{u}_{\text{ref}}^i$ and numerical convergence orders.

level	$ \mathbf{u}^{h,i} - \mathbf{u}_{\text{ref}}^i _{1,\Omega} / \mathbf{u}_{\text{ref}}^i _{1,\Omega}$					
	$(i, j) = (1, 1)$		$(i, j) = (2, 1)$		$(i, j) = (2, 2)$	
0	$4.663632e - 01$	—	$3.159307e - 01$	—	$3.903263e - 01$	—
1	$3.214737e - 01$	0.54	$1.592747e - 01$	0.99	$1.376072e - 01$	1.50
2	$1.807130e - 01$	0.83	$6.777325e - 02$	1.23	$5.656398e - 02$	1.28
3	$9.735853e - 02$	0.89	$2.992646e - 02$	1.18	$2.422295e - 02$	1.22
4	$5.111965e - 02$	0.93	$1.340727e - 02$	1.16	$1.028243e - 02$	1.23
5	$2.584391e - 02$	0.98	—	—	—	—

 Table 3.8.: Example 2: Weighted $L^2(\Gamma_c^s)$ -error of $\lambda^{h,j}$ with respect to λ_{ref}^j and numerical convergence orders.

level	$\ \lambda^{h,j} - \lambda_{\text{ref}}^j\ _{-\frac{1}{2},h,\Gamma_c^s}$					
	$(i, j) = (1, 1)$		$(i, j) = (2, 1)$		$(i, j) = (2, 2)$	
0	$5.845412e + 01$	—	$5.849757e + 01$	—	$1.323412e + 02$	—
1	$4.999477e + 01$	0.23	$4.129640e + 01$	0.50	$3.621992e + 01$	1.87
2	$2.121223e + 01$	1.24	$1.814467e + 01$	1.19	$1.389391e + 01$	1.38
3	$8.378905e + 00$	1.34	$7.316218e + 00$	1.31	$5.230080e + 00$	1.41
4	$3.269796e + 00$	1.36	$2.813967e + 00$	1.38	$2.015976e + 00$	1.38
5	$1.168347e + 00$	1.48	—	—	—	—

Second example

Our second example is the Hertzian contact problem of a linear elastic circular disc on a plane as considered in Section 3.2. However, we use a slightly modified mesh as initial triangulation, see Figure 3.7. Using (3.17), the maximum contact stress in normal direction of the Hertzian contact problem is then given by $\lambda_n^{\max} = 494.8$, and for the half width of the contact zone, we find $b = 0.129$. The third picture in Figure 3.7 illustrates the numerical approximation of the maximum value of the normal contact stress for all three discretization methods on the different levels. From level 3 on, the discrete maximum normal stress is a very good approximation of the analytical one for all three discretization methods. In the right picture, the normal contribution of the Lagrange multiplier $\lambda_n^{h,1}$ on level 7 is given. The dashed black lines mark the analytical values of the half width b of the contact zone and the maximum pressure λ_n^{\max} .

For the computation of the discretization errors, we use for the lowest order case the finite element solution on level 7 as reference solution $(\mathbf{u}_{\text{ref}}^1, \lambda_{\text{ref}}^1)$. For the cases $(i, j) = (2, 1)$ and $(i, j) = (2, 2)$, we use the finite element solutions on level 6. The errors

in the $H^1(\Omega)$ -seminorm for the displacements are given in Table 3.7 and the errors for the Lagrange multipliers in the weighted $L^2(\Gamma_c^s)$ -norm are presented in Table 3.8. Asymptotically, we observe optimal convergence rates. In the $H^1(\Omega)$ -seminorm, the convergence rate for the case $(i, j) = (1, 1)$ tends to one with increasing number of refinement steps. For the cases $(i, j) = (2, 1)$ and $(i, j) = (2, 2)$, we even observe convergence rates of about 1.2. Asymptotically a convergence rate of 1.5 for the Lagrange multiplier in the weighted $L^2(\Gamma_c^s)$ -norm is achieved. We mention that for the cases $(i, j) = (2, 1)$ and $(i, j) = (2, 2)$ we only observe a convergence order of 1.4.

3.5. Extension to simplified frictional problem

The case with friction was studied for a frictional antiplane problem with a constant friction bound. Here, only the frictional tangential constraints are important and therefore one has not to take care on the normal constraints in the presentation. The estimates of these constraints were already considered in Section 3.1. Thus the presentation can be done in more clearer way resulting in an improvement of the readability. In Subsection 3.5.1 we shortly present the problem formulation and the achieved theoretical results. Some numerical examples are given in Subsection 3.5.2. The results have been published in [81].

3.5.1. Frictional antiplane problem and theoretical results

We consider the antiplane shear deformation of two three-dimensional elastic bodies in frictional contact on their common boundary $\Gamma_c^s = \Gamma_c^m$. The antiplane shear (or longitudinal shear, generalized shear) may be viewed as complementary to plane strain deformation and represents the Mode III fracture mode for crack problems. This model was considered by many authors, see for instance [15, 78, 112]. The bodies are assumed to be in contact during the whole deformation process. To model the friction, we use Tresca's law and denote the a priori given constant friction bound by g_f . For cylindrical bodies subject to antiplane shear, we assume that the external forces \mathbf{f}^i and \mathbf{p}^i are only acting in axial direction of Ω^i . Thus, the displacement is parallel to the axial direction of the cylindrical bodies and independent of the radial direction. Therefore the displacement of the origin three-dimensional setting can be described by a scalar function on the two-dimensional radial cross section Ω^s and Ω^m of the two bodies and both the governing equations and the frictional boundary conditions are quite simple. The Lamé-operator (1.38) results in the Laplace-operator acting on the one-dimensional displacement field u modeling the displacement in axial direction. On the common contact interface Γ_c^s , we assume Tresca's friction law for the scalar-valued Lagrange multiplier λ playing the role of the conormal derivative.

To give the weak formulation we denote in the rest of this section the scalar valued spaces by V , W , M and V^h , W^h , M^h defined according to the vector values spaces \mathbf{V} , \mathbf{W} , \mathbf{M} and \mathbf{V}^h , \mathbf{W}^h , \mathbf{M}^h . The bilinear form $b(\cdot, \cdot)$ on the product space is now defined by $V \times M$ by $b(v, \mu) := \langle \mu, [v] \rangle$, $\mu \in M$, $v \in V$. Now, we get the hybrid formulation of

the frictional antiplane problem from (2.6) as: find $(u, \lambda) \in V \times M_\tau$ such that

$$a(u, v) + b(v, \lambda) = f(v), \quad v \in V, \quad (3.28a)$$

$$b(u, \mu - \lambda) \leq 0, \quad \mu \in M_\tau, \quad (3.28b)$$

where now the admissible set M_τ for the Lagrange multiplier is given by

$$M_\tau := \{\mu \in : \langle \mu, \eta \rangle \leq \langle g_f, |\eta| \rangle, \eta \in W\}. \quad (3.29)$$

We remark that in this section the bilinear form $a(\cdot, \cdot)$ is defined in terms of the Laplace-operator. Following the proof of Lemma 2.3, we obtain the discretized version of the space M_τ introduced in (3.29) as

$$M_\tau^h := \left\{ \mu^h = \sum_{p \in \mathcal{S}} \mu_p \psi_p \in M^h : |\mu_p| \leq g_f, p \in \mathcal{S} \right\}.$$

For the considered frictional problem we observe a similar result as in Lemma 3.1.

Lemma 3.11. *Let $(u, \lambda) \in V \times M_\tau$ be the solution of (3.28) and let $(u^h, \lambda^h) \in V^h \times M_\tau^h$ be the solution of the corresponding discretized version. Then there exists a positive constant C independent of the meshsize h , such that*

$$\|u - u^h\|_{1,\Omega} + \|\lambda - \lambda^h\|_{-\frac{1}{2},\Gamma_c^s} \leq C \left\{ \inf_{v^h \in V^h} \|u - v^h\|_{1,\Omega} + \inf_{\mu^h \in M_\tau^h} \|\lambda - \mu^h\|_{-\frac{1}{2},\Gamma_c^s} + b(u, \lambda^h - \lambda)^{\frac{1}{2}} \right\}.$$

The proof is based on the same techniques as used in the proof of Lemma 3.1. The last term on the right side can be estimated under a similar assumption as made in Assumption 3.3 by using the same techniques as in the proof of Lemma 3.5. Then, we arrive at the following optimal a priori error estimate.

Theorem 3.12. *Let $(u, \lambda) \in V \times M_\tau$ be the solution of (3.28) and let $(u^h, \lambda^h) \in V^h \times M_\tau^h$ be the solution of the corresponding discretized version. Under a suitable assumption similar to Assumption 3.3 and the regularity assumption $u \in H^{\frac{3}{2}+\nu}(\Omega)$, $0 < \nu \leq \frac{1}{2}$, we have the a priori error estimate*

$$\|u - u^h\|_{1,\Omega} + \|\lambda - \lambda^h\|_{-\frac{1}{2},\Gamma_c^s} \leq Ch^{\frac{1}{2}+\nu} |u|_{\frac{3}{2}+\nu,\Omega}$$

for a positive constant C independent of the meshsize $h < h_0$.

3.5.2. Numerical examples

In this last subsection, we confirm our theoretical results for the discretization error. We use the material constants for granite, so that Young's modulus $E = 106$ and Poisson's ratio $\nu = 0.25$. These are related to the Lamé parameters λ and μ by (1.33), since in all examples we work with plane strain. We focus on the discretization errors of the solution u in the $L^2(\Omega)$ - and the $H^1(\Omega)$ -norm. The error of the Lagrange multiplier is considered in a weighted $L^2(\Gamma_c^s)$ -norm, see Remark 3.7. Since there is in general no analytical solution available, we use for computing the discretization errors a reference solution u_{ref} and λ_{ref} on a fine mesh satisfying $h_{\text{ref}} \leq 1/4 h$. The use of $h_{\text{ref}} = 1/2 h$ as reference meshsize does not yield reliable values for the discretization errors.

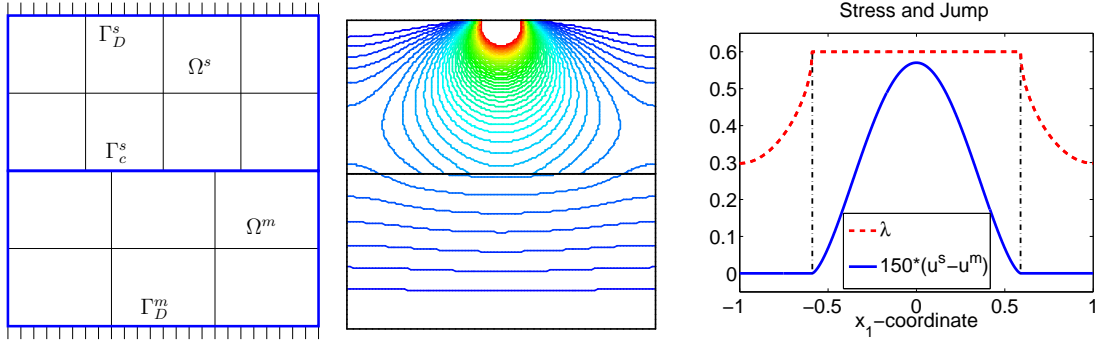


Figure 3.8.: Example 1: Problem definition and grid on level 0 (left), contour lines of the solution (middle), Lagrange multiplier λ^h and amplified jump $[u^h]$ on Γ_c^s (right).

Table 3.9.: Example 1: Relative $L^2(\Omega)$ -error and relative $H^1(\Omega)$ -error of u^h with respect to u_{ref} , weighted $L^2(\Gamma_c^s)$ -error of λ^h with respect to λ_{ref} and the numerical convergence rates.

level	$\ u^h - u_{\text{ref}}\ _{0,\Omega} / \ u_{\text{ref}}\ _{0,\Omega}$		$ u^h - u_{\text{ref}} _{1,\Omega} / u_{\text{ref}} _{1,\Omega}$		$\ \lambda^h - \lambda_{\text{ref}}\ _{-\frac{1}{2},h,\Gamma_c^s}$	
0	1.210198e + 00	—	8.679373e - 01	—	1.525284e - 01	—
1	1.762545e - 01	2.78	5.503170e - 01	0.66	6.264323e - 02	1.28
2	4.855714e - 02	1.86	3.744576e - 01	0.56	7.003110e - 03	3.16
3	1.342324e - 02	1.85	1.969682e - 01	0.93	1.907398e - 03	1.88
4	3.395710e - 03	1.98	9.866146e - 02	1.00	7.817159e - 04	1.29
5	8.468612e - 04	2.00	4.907663e - 02	1.01	2.646597e - 04	1.56
6	2.062731e - 04	2.04	2.395136e - 02	1.03	8.864475e - 05	1.58

First example

In this section, we consider the example shown in the left picture in Figure 3.8. We set the lower rectangle $\Omega^m = [-1, 1] \times [0, 1]$ and the upper as $\Omega^s = [-1, 1] \times [1, 2]$. On Γ_D^m , being the bottom of the lower rectangle Ω^m , we set the Dirichlet values equal to $u_D^m = 0$. We assign at the top boundary of the upper body Ω^s given Dirichlet values $u_D^s = 0.22 \exp(-60x_1^2)$. On all the remaining boundary segments, we set homogeneous Neumann boundary conditions. For the friction bound we use $g_f = 0.6$. The contour lines of the numerical solution u^h are presented in the middle picture in Figure 3.8, while the right picture in Figure 3.8 shows the Lagrange multiplier λ^h and the jump $[u^h]$ amplified with the factor 150 at the interface Γ_c^s . The discretization errors and the convergence rates are presented in Table 3.9. Here, we use the finite element solution on Level 8 as reference solution u_{ref} . The grid on Level 0 is shown in the left picture in Figure 3.8. On Level 8, we have 525 825 nodes on Ω^s and 394.497 on Ω^m . The convergence rates in the

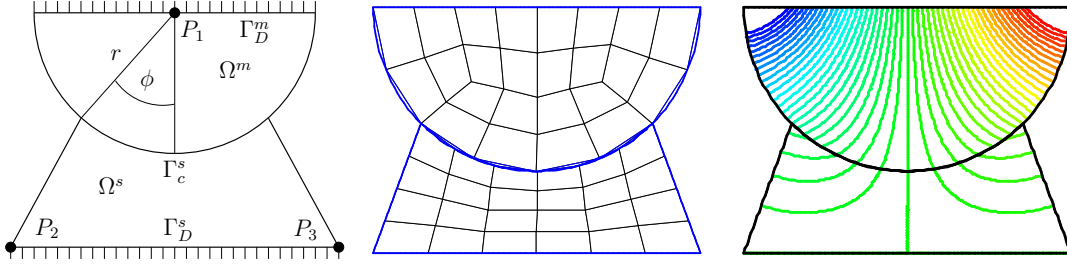


Figure 3.9.: Example 2: Problem definition (left), grid on level 1 (middle) and contour lines of the solution (right).

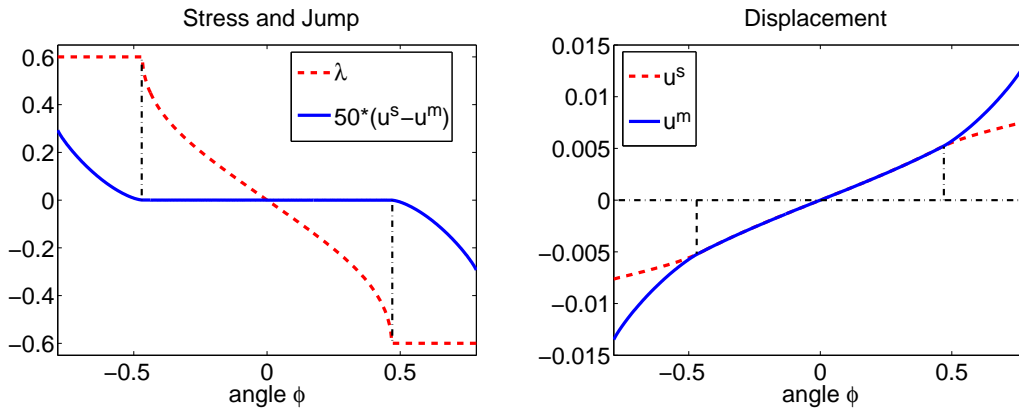


Figure 3.10.: Example 2: Lagrange multiplier λ^h and amplified jump $[u^h]$ (left) and displacement $u^{s,h}$ on slave side and $u^{m,h}$ on master side for $g_f = 0.6$.

L^2 -norm are asymptotically 2.0 and in the $H^1(\Omega)$ -norm, we get 1.0. As also observed in the linear case, we get better convergence rates for the Lagrange multiplier. The best approximation error in the weighted $L^2(\Gamma_c^s)$ -norm is of order $h^{1.5}$.

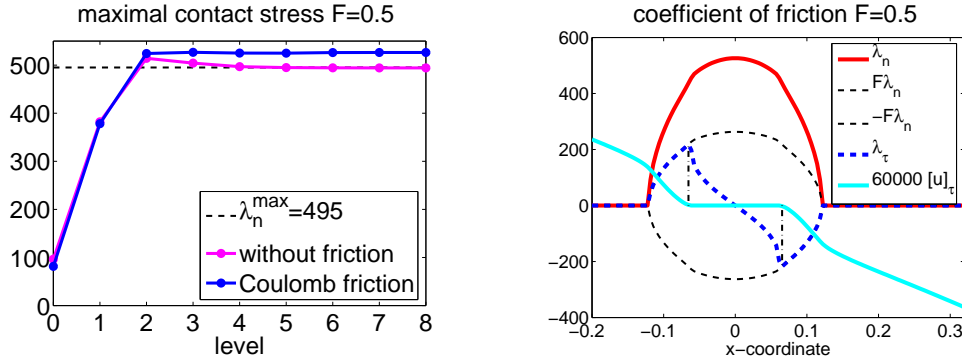
Second example

Now, we consider the problem depicted in the left picture in Figure 3.9. Here, the interface Γ_c^s is a curved one. To fix the geometry, we set the three points P_1 , P_2 and P_3 equal to $P_1 = (0, 1.5)$, $P_2 = (-1, 0)$ and $P_3 = (1, 0)$. The radius r of the upper half disc is set to be $r = 1$ and for the angle ϕ we choose $\phi = \pi/4$. The lower body plays the role of the slave side Ω^s and the upper one the role of the master side Ω^m . We fix the domain at the bottom of the master side Ω^m . At the top boundary of the upper body Ω^s , we set the Dirichlet value to $u_D^s = 0.055x_1$. As in the first example, we set the friction bound equal to $g_f = 0.6$.

The right picture in Figure 3.9 shows the contour lines of the solution. Figure 3.10 shows the Lagrange multiplier λ^h , the jump $[u^h]$ amplified to the factor 50 and the solution of the master and slave side $u^{h,m}$, $u^{h,s}$ on the interface Γ_c^s . The discretization

Table 3.10.: Example 2: Relative $L^2(\Omega)$ -error and relative $H^1(\Omega)$ -error of u^h with respect to u_{ref} , weighted $L^2(\Gamma_c^s)$ -error of λ^h with respect to λ_{ref} and the numerical convergence orders.

level	$\ u^h - u_{\text{ref}}\ _{0,\Omega} / \ u_{\text{ref}}\ _{0,\Omega}$		$ u^h - u_{\text{ref}} _{1,\Omega} / u_{\text{ref}} _{1,\Omega}$		$\ \lambda^h - \lambda_{\text{ref}}\ _{-\frac{1}{2},h,\Gamma_c^s}$	
0	$8.934322e - 02$	—	$3.231679e - 01$	—	$7.718450e - 02$	—
1	$3.096022e - 02$	1.53	$1.893279e - 01$	0.77	$2.216194e - 02$	1.80
2	$8.651862e - 03$	1.84	$1.034272e - 01$	0.87	$8.133636e - 03$	1.45
3	$2.427230e - 03$	1.83	$5.643122e - 02$	0.87	$3.781621e - 03$	1.10
4	$6.665729e - 04$	1.86	$3.041368e - 02$	0.89	$1.303146e - 03$	1.54
5	$1.791767e - 04$	1.90	$1.613158e - 02$	0.91	$3.521447e - 04$	1.89
6	$4.652240e - 05$	1.95	$8.311285e - 03$	0.96	$1.671239e - 04$	1.08


 Figure 3.11.: Visualization of maximal contact stress λ_n^{\max} for the cases without friction and with Coulomb's friction law (left) for the coefficients of friction $\mathfrak{F} = 0.5$ and of the contact constraints (right) for the Hertzian contact problem.

errors and the corresponding convergence rates are listed in Table 3.10. Again we use as reference solution the solution on Level 8. The grid on Level 1 is presented in the middle in Figure 3.9.

3.6. Numerical convergence studies for a frictional contact problem

In this last section we investigate numerically the discretization errors and the convergence orders for the Hertzian contact problem in combination with Coulomb's friction law, see (1.27). We use exactly the same setting and the same parameters as in the third example presented in Figure 3.5 in Section 3.2 for the case without friction. The tangential condition $\lambda_{p\tau} = \mathbf{0}$ for the Lagrange multiplier is now replaced by the weak

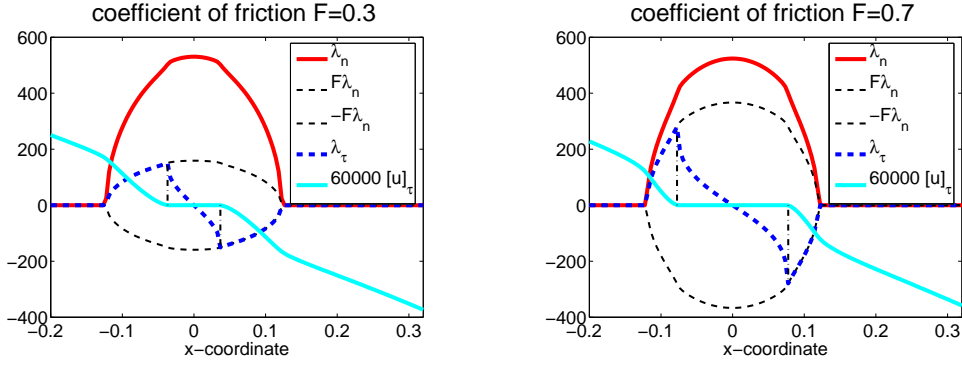


Figure 3.12.: Visualization of contact constraints for the Hertzian contact problem with Coulomb's friction model for the coefficients of friction $\mathfrak{F} = 0.3$ and $\mathfrak{F} = 0.7$.

Table 3.11.: Coulomb friction: Relative $H^1(\Omega)$ -error of \mathbf{u}^h with respect to \mathbf{u}_{ref} , weighted $L^2(\Gamma_c^s)$ -error of $\boldsymbol{\lambda}^h$ with respect to $\boldsymbol{\lambda}_{\text{ref}}$ and the numerical convergence orders for the Hertzian contact problem with $\mathfrak{F} = 0.5$.

level	$ \mathbf{u}^h - \mathbf{u}_{\text{ref}} _{1,\Omega} / \mathbf{u}_{\text{ref}} _{1,\Omega}$		$\ \boldsymbol{\lambda}^h - \boldsymbol{\lambda}_{\text{ref}}\ _{-\frac{1}{2},h,\Gamma_c^s}$	
1	$4.465867e - 01$	—	$5.065628 + 01$	—
2	$3.056095e - 01$	0.55	$2.381819 + 01$	1.09
3	$1.693210e - 01$	0.85	$1.037995 + 01$	1.20
4	$9.155008e - 02$	0.89	$3.909448 + 00$	1.41
5	$4.857727e - 02$	0.91	$1.493191 + 00$	1.39
6	$2.450933e - 02$	0.99	$0.523946 + 00$	1.51

point-wise decoupled constraints (2.32).

For the choices $\mathfrak{F} = 0.5$ the contact stress in normal and tangential direction are presented in the right picture in Figure 3.11, whereas the left picture in this Figure shows the maximal contact stress λ_n^{max} in comparison to the case without friction. The maximal contact stress is larger for the case with friction compared to the case without friction. Figure 3.12 shows the contact stress for the values $\mathfrak{F} = 0.3$ and $\mathfrak{F} = 0.7$ for the coefficient of friction. Comparing these pictures, we observe that the zone, where the nodes are sticky in tangential direction, i.e., $[\mathbf{u}]_\tau = \mathbf{0}$, increases with the coefficient of friction. In the rest of the actual contact zone we have $\|\boldsymbol{\lambda}_\tau\| = \mathfrak{F}\lambda_n$ and thus the results perfectly perform Coulomb's friction law.

The numerically obtained discretization errors and convergence rates are shown in Table 3.11. As for Table 3.3 we use as reference solutions the solution on level 8. Comparing Table 3.11 with the results for the case without friction, see Table 3.3, we observe quantitatively and qualitatively the same behavior for the $H^1(\Omega)$ -error of the displacement and the weighted $L^2(\Gamma_c^s)$ -error of the Lagrange multiplier.

Part III.
Numerical algorithms

4. Semi-smooth Newton method for normal constraints

The numerical simulation of nonlinear multibody contact problems for linear elasticity plays an important role in many applications in mechanics. The interest in such type of problems led to many research activities in the recent years both from the numerical and the theoretical point of view. The main problem for the corresponding numerical algorithms is to deal with the nonlinearity of such problems, arising from the non-penetration condition for the involved bodies. Here, we provide a semi-smooth Newton algorithm, which equivalently can be interpreted as a primal-dual active set approach. For primal-dual active set strategies we also refer to, e.g., [75, 76, 86] in the framework of abstract variational inequalities and to, e.g., [104, 129, 130] in the framework of contact problems. By applying the primal-dual active set strategy, we get a series of linear problems, which can be solved iteratively by an optimal multigrid method. Using only one multigrid step in each active set step, we obtain an inexact strategy resulting in an efficient and powerful algorithm. Alternative approaches for such type of problems are FETI-methods, see, e.g., [36, 37, 38], monotone multigrid techniques, see, e.g., [93, 94, 96] and Dirichlet–Neumann algorithms, [6, 43, 98].

In this chapter, we formulate the semi-smooth Newton method for the contact problem without friction as considered in Subsection 3.1.1. The results have been published in [79, 84]. Newton-type methods for contact problems with friction have already been used in, [2, 3]. Similar methods are also studied in the more recent contributions [27], where the performance of generalized Newton-type methods for frictional contact problems is shown to be superior to interior point methods. The methods presented in [3, 27, 28] rely on the reformulation of the contact and friction conditions using nonsmooth equations and on generalized differentiability concepts. Here, we apply similar strategies but use a different complementarity function. Additionally, we study and exploit the structures arising in Newton-type steps and relate them to primal-dual active set strategies. We also apply our algorithm to two-body contact problems which are discretized in terms of mortar techniques. While the algorithm can be interpreted as a semi-smooth Newton method, the extension to more general nonlinear material laws is quite natural, since the additional nonlinearity can be treated within the same iterative loop. This approach will be investigated in Chapter 6. Furthermore, such type of algorithms for contact problems can easily be used in combination with elasto-plastic materials as done in [26, 29].

Computing generalized derivatives of nonsmooth functionals is a delicate issue. While in [3] mainly intuitive arguments are used, the papers [27, 28] use the concept of Bouligand-differentiability. This concept allows the use of globalization (e.g., linesearch) strategies, but calculating the search direction requires the solution of a nonlinear system in each

Newton step. Although, we won't consider globalization techniques in this thesis, due to excellent numerical experiences. The concept of semi-smoothness [75, 121, 122] as used in this thesis has the advantage that the search direction can be found by solving a linear system.

We start in Section 4.1 with a short introduction to semi-smooth Newton methods. In Section 4.2, we present the applied nonlinear complementarity function. The degrees of freedom of the arising linear system are reduced in Section 4.3 such that only a system with respect to the primal variable has to be solved. The resulting algorithm is stated in Section 4.4. Finally, Section 4.5 contains various numerical examples demonstrating the performance of the given algorithm.

4.1. Semi-smooth Newton methods

Following [32], we start with a short overview about the concept of generalized Jacobians and the semi-smooth Newton method. Let $\mathbf{F} : \mathbb{R}^n \rightarrow \mathbb{R}^n$ be a locally Lipschitz function, then \mathbf{F} is almost everywhere differentiable. Defining by X_F the set of points where \mathbf{F} is differentiable, the set of generalized Jacobians of \mathbf{F} at the point \mathbf{x} is given by

$$\partial\mathbf{F}(\mathbf{x}) := \text{conv} \left\{ \lim_{\substack{\mathbf{x}_i \rightarrow \mathbf{x}, \\ \mathbf{x}_i \in X_F}} D_F(\mathbf{x}_i) \right\},$$

where $D_F(\mathbf{x}) \in \mathbb{R}^{n \times n}$ denotes the standard Jacobian of \mathbf{F} at the point \mathbf{x} and by "conv" we indicate the convex hull. The corresponding generalized or semi-smooth Newton method for the equation $\mathbf{F}(\mathbf{x}) = \mathbf{0}$ reads as follows: starting with some $\mathbf{x}^0 \in \mathbb{R}^n$, the next iterate $\mathbf{x}^k = \mathbf{x}^{k-1} + \Delta\mathbf{x}^k$, $k = 1, 2, 3, \dots$, is obtained such that the increment $\Delta\mathbf{x}^k \in \mathbb{R}^n$ satisfies the relation

$$\mathbf{0} \in \mathbf{F}(\mathbf{x}^{k-1}) + \partial\mathbf{F}(\mathbf{x}^{k-1})\Delta\mathbf{x}^k.$$

For the numerical realization of this method one has to choose any $\mathbf{V}^k \in \partial\mathbf{F}(\mathbf{x}^{k-1})$ and solve the equation

$$\mathbf{0} = \mathbf{F}(\mathbf{x}^{k-1}) + \mathbf{V}^k \Delta\mathbf{x}^k \quad (4.1)$$

to obtain the increment $\Delta\mathbf{x}^k$. This method has been considered, e.g., in [122], for the case that the function \mathbf{F} is semi-smooth. In this article, the semi-smoothness of the function $\mathbf{F} : U \rightarrow \mathbb{R}^n$ on the open subset $U \subset \mathbb{R}^n$ implies that

$$\lim_{\mathbf{h} \rightarrow \mathbf{0}} \frac{1}{\|\mathbf{h}\|} \|\mathbf{F}(\mathbf{x} + \mathbf{h}) - \mathbf{F}(\mathbf{x}) - \mathbf{V}\mathbf{h}\| = \mathbf{0}, \quad \mathbf{x} \in U,$$

holds, where \mathbf{V} is an arbitrary element of the generalized Jacobian $\partial\mathbf{F}(\mathbf{x} + \mathbf{h})$. A more general concept of generalized derivatives can be found in [24, 75]. Here, semi-smooth Newton methods are regarded for slantly differentiable functions. The function $\mathbf{F} : U \rightarrow \mathbb{R}^n$ is called slantly differentiable in the open subset U if there exists a family of mappings $\mathbf{G} : U \rightarrow \mathcal{L}(\mathbb{R}^n, \mathbb{R}^n)$ such that

$$\lim_{\mathbf{h} \rightarrow \mathbf{0}} \frac{1}{\|\mathbf{h}\|} \|\mathbf{F}(\mathbf{x} + \mathbf{h}) - \mathbf{F}(\mathbf{x}) - \mathbf{G}(\mathbf{x} + \mathbf{h})\mathbf{h}\| = \mathbf{0}, \quad \mathbf{x} \in U.$$

It can easily be seen that a semi-smooth function is slantly differentiable, whereas for a slantly differentiable function the slanting functions $\mathbf{G}(\mathbf{x} + \mathbf{h})$ are not required to be elements of $\partial\mathbf{F}(\mathbf{x} + \mathbf{h})$. In [86, 104] a slantly differentiable function is also referred to as a Newton differentiable function.

In the following sections, we have to work with nonsmooth functions of the type

$$\mathbf{F}(\mathbf{x}) := \max\{\mathbf{a}, \mathbf{x}\}, \quad (4.2)$$

where the max-operator has to be interpreted componentwise. The generalized derivative \mathbf{V}^k in the semi-smooth Newton method (4.1) is chosen as the matrix $D_F(\mathbf{x})$ with the diagonal elements

$$(D_F(\mathbf{x}))_{ii} := \begin{cases} 0 & \text{if } a_i \geq x_i, \\ 1 & \text{if } a_i < x_i, \end{cases} \quad (4.3)$$

for $i = 1, \dots, n$. Following [75], we observe that this choice is also a slanting function of (4.2). We remark that the arbitrary choice for the case $a_i = x_i$ does not influence the convergence rate of the proposed algorithms.

4.2. Nonlinear complementarity function

The algebraic version of the point-wise decoupled constraints for the case without friction can be obtained from Lemma 2.6. For the coefficients $\hat{\mathbf{u}}_p$ of the displacement vector \mathbf{u} with respect to the constrained basis $\hat{\boldsymbol{\phi}}$ and the coefficients $\boldsymbol{\lambda}_p$ for the Lagrange multiplier, the constraints read

$$\hat{u}_{pn} \leq g_p, \quad \lambda_{pns} \geq 0, \quad \lambda_{pns}(\hat{u}_{pn} - g_p) = 0, \quad \boldsymbol{\lambda}_{p\tau s} = \mathbf{0}, \quad p \in \mathcal{S}. \quad (4.4)$$

The frictional constraints (2.32) in Lemma 2.6 are now replaced by the condition $\boldsymbol{\lambda}_{p\tau s} = \mathbf{0}$. Here, we use the scaled values $\lambda_{pns} := D_p \lambda_{pn}$ and $\boldsymbol{\lambda}_{p\tau s} := D_p \boldsymbol{\lambda}_{p\tau}$ instead of λ_{pn} and $\boldsymbol{\lambda}_{p\tau}$, respectively. The use of the scaling factor $D_p > 0$ which is proportional to the local meshsize is motivated by the fact that the $H^{-1/2}(\Gamma_c^s)$ -norm for the Lagrange multiplier and the $H^{1/2}(\Gamma_c^s)$ -norm for the displacement now have the same error reduction. We remark that the proposed scaling factors yield better numerical convergence rates for the inexact version of the algorithm. From (4.4) we observe that for each node $p \in \mathcal{S}$, we have for the pair $(\hat{u}_{pn}, \lambda_{pns})$ either $\hat{u}_{pn} = g_p$ and $\lambda_{pns} \geq 0$ or $\hat{u}_{pn} < g_p$ and $\lambda_{pns} = 0$. In the first case the node p is in contact, whereas in the second situation, the node p is free. We have to construct an iterative algorithm which finally determines for each node $p \in \mathcal{S}$ its correct state. To do so, we recall, that the algebraic version of equation (2.10) for the projection operator restricted to each node $p \in \mathcal{S}$ reads as

$$\lambda_{pns} = \max\{0, \lambda_{pns} + c(\hat{u}_{pn} - g_p)\},$$

where we used again the scaled values λ_{pns} instead of λ_{pn} . This motivates the definition of the nonlinear complementarity function, see also [3, 75],

$$C_n(\hat{u}_{pn}, \lambda_{pns}) := \lambda_{pns} - \max\{0, \lambda_{pns} + c(\hat{u}_{pn} - g_p)\}, \quad (4.5)$$

for some constant $c > 0$. The semi-smooth Newton method, which results in a primal-dual active set strategy, is based on the following theorem.

Theorem 4.1. *The pair $(\hat{\mathbf{u}}_p, \boldsymbol{\lambda}_p)$ satisfies the contact constraints (4.4) if and only if it satisfies the condition*

$$C_n(\hat{u}_{pn}, \lambda_{pns}) = 0, \quad \boldsymbol{\lambda}_{p\tau s} = \mathbf{0}, \quad p \in \mathcal{S}. \quad (4.6)$$

Proof. The equivalence for the tangential constraint $\boldsymbol{\lambda}_{p\tau s}$ is obvious. We first show that (4.4) implies (4.6). From (4.4) we deduce either $\hat{u}_{pn} = g_p$ and $\lambda_{pns} \geq 0$ or $\hat{u}_{pn} < g_p$ and $\lambda_{pns} = 0$. In the first case, we compute

$$C_n(\hat{u}_{pn}, \lambda_{pns}) = \lambda_{pns} - \max\{0, \lambda_{pns}\} = \lambda_{pns} - \lambda_{pns} = 0.$$

In the second one, we get

$$C_n(\hat{u}_{pn}, \lambda_{pns}) = -\max\{0, c(\hat{u}_{pn} - g_p)\} = 0.$$

Thus, we arrive at the desired relation $C_n(\hat{u}_{pn}, \lambda_{pns}) = 0$ for both situations.

Assuming (4.6), we have to distinguish between the two cases $\lambda_{pns} + c(\hat{u}_{pn} - g_p) > 0$ and $\lambda_{pns} + c(\hat{u}_{pn} - g_p) \leq 0$. For the former case, we derive from the condition $C_n(\hat{u}_{pn}, \lambda_{pns}) = 0$

$$0 = C_n(\hat{u}_{pn}, \lambda_{pns}) = -c(\hat{u}_{pn} - g_p),$$

and thus we have $u_{pn} = g_p$. This leads directly to $\lambda_{pns} > 0$ and (4.4) holds. For the case $\lambda_{pns} + c(\hat{u}_{pn} - g_p) \leq 0$, condition $C_n(\hat{u}_{pn}, \lambda_{pns}) = 0$ yields

$$0 = C_n(\hat{u}_{pn}, \lambda_{pns}) = \lambda_{pns}$$

and therefore we get from $c(\hat{u}_{pn} - g_p) \leq 0$ the constraint $\hat{u}_{pn} \leq g_p$ and arrive again at (4.4). \square

To derive the semi-smooth Newton method for the equation (4.4), we compute for each node $p \in \mathcal{S}$ the generalized derivative D_{C_n} of $C_n(\cdot, \cdot)$. We obtain for the variation $(\delta\hat{u}_{pn}, \delta\lambda_{pns}) \in \mathbb{R} \times \mathbb{R}$

$$D_{C_n}(\hat{u}_{pn}, \lambda_{pns})(\delta\hat{u}_{pn}, \delta\lambda_{pns}) = \delta\lambda_{pns} - \chi_{\mathcal{A}}(\lambda_{pns} + c(\hat{u}_{pn} - g_p))(\delta\lambda_{pns} + c\delta\hat{u}_{pn}), \quad (4.7)$$

where we used the generalized Jacobian (4.3). Here, $\chi_{\mathcal{A}}$ denotes the characteristic function of the set $\mathcal{A}_n := \{p \in \mathcal{S} : \lambda_{pns} + c(\hat{u}_{pn} - g_p) > 0\}$, i.e.,

$$\chi_{\mathcal{A}} := \begin{cases} 1 & \text{if } \lambda_{pns} + c(\hat{u}_{pn} - g_p) > 0, \\ 0 & \text{if } \lambda_{pns} + c(\hat{u}_{pn} - g_p) \leq 0. \end{cases}$$

Let $(\hat{u}_{pn}^{k-1}, \lambda_{pns}^{k-1})$ be the previous iterate; we obtain the new iterate

$$(\hat{u}_{pn}^k, \lambda_{pns}^k) = (\hat{u}_{pn}^{k-1}, \lambda_{pns}^{k-1}) + (\delta\hat{u}_{pn}^{k-1}, \delta\lambda_{pns}^{k-1})$$

of the semi-smooth step by solving the equation

$$D_{C_n}(\hat{u}_{pn}^{k-1}, \lambda_{pns}^{k-1})(\delta \hat{u}_{pn}^{k-1}, \delta \lambda_{pns}^{k-1}) = -C_n(\hat{u}_{pn}^k, \lambda_{pns}^k). \quad (4.8)$$

Separating the nodes $p \in \mathcal{S}$ into the active set \mathcal{A}_n^k and the inactive set \mathcal{I}_n^k according to

$$\mathcal{A}_n^k := \{p \in \mathcal{S} : \lambda_{pns}^{k-1} + c(\hat{u}_{pn}^{k-1} - g_p) > 0\}, \quad (4.9a)$$

$$\mathcal{I}_n^k := \{p \in \mathcal{S} : \lambda_{pns}^{k-1} + c(\hat{u}_{pn}^{k-1} - g_p) \leq 0\}, \quad (4.9b)$$

a straightforward computation of (4.8) shows that the new iterate $(\hat{u}_{pn}^k, \lambda_{pns}^k)$ satisfies

$$\hat{u}_{pn}^k = g_p, \quad p \in \mathcal{A}_n^k, \quad (4.10a)$$

$$\lambda_{pns}^k = 0, \quad p \in \mathcal{I}_n^k. \quad (4.10b)$$

Thus, we obtain a Dirichlet boundary condition for the new displacement in normal direction if the node p is active, i.e., $p \in \mathcal{A}_n^k$. For an inactive node $p \in \mathcal{I}_n^k$, (4.10b) corresponds to a Neumann boundary condition for the normal component of the Lagrange multiplier. Thus, for the normal contact constraints the semi-smooth Newton method leads to a primal-dual active set strategy. Combining the conditions (4.10) with the algebraic version of the field equation (2.41) and the tangential condition $\boldsymbol{\lambda}_{p\tau s} = \mathbf{0}$, we have to solve in each Newton step the linear equation system

$$\hat{\mathbf{K}}\hat{\mathbf{u}}^k + \hat{\mathbf{C}}\boldsymbol{\lambda}^k = \hat{\mathbf{f}}, \quad (4.11a)$$

$$\hat{u}_{pn}^k = g_p, \quad p \in \mathcal{A}_n^k, \quad (4.11b)$$

$$\lambda_{pns}^k = 0, \quad p \in \mathcal{I}_n^k, \quad (4.11c)$$

$$\boldsymbol{\lambda}_{p\tau s}^k = \mathbf{0}, \quad p \in \mathcal{S} \quad (4.11d)$$

for the new iterates $(\hat{\mathbf{u}}^k, \boldsymbol{\lambda}^k)$.

4.3. Elimination of the Lagrange multiplier

Next, we give the complete algebraic representation of the linear system (4.11) and eliminate the degrees of freedom of the Lagrange multiplier such that only a linear system with respect to the primal variable has to be solved. To do so, we decompose the diagonal coupling matrix \mathbf{D}_d between the Lagrange multiplier basis functions and the finite element basis functions on the slave side Γ_c^s introduced in (2.21) into

$$\mathbf{D}_d = \begin{pmatrix} \mathbf{D}_{\mathcal{I}_n^k} & \mathbf{0} \\ \mathbf{0} & \mathbf{D}_{\mathcal{A}_n^k} \end{pmatrix},$$

where the two blocks are associated with the nodes in the corresponding subsets as indicated by the subscript. Furthermore, we define the matrix $\mathbf{N}_{\mathcal{A}_n^k} \in \mathbb{R}^{|\mathcal{A}_n^k| \times d|\mathcal{A}_n^k|}$, where $|\mathcal{A}_n^k|$ denotes the number of nodes in \mathcal{A}_n^k , by

$$\mathbf{N}_{\mathcal{A}_n^k} := \begin{pmatrix} \ddots & \ddots & 0 & \dots & 0 & 0 & 0 \\ 0 & 0 & \mathbf{n}_p^\top & 0 & 0 & 0 & 0 \\ 0 & 0 & 0 & \dots & 0 & \ddots & \ddots \end{pmatrix}, \quad p \in \mathcal{A}_n^k.$$

In addition to the vector \mathbf{n}_p , we define the vectors $\boldsymbol{\tau}_{p_i}$, $1 \leq i \leq (d-1)$, spanning the tangent plane at the node p such that $\{\mathbf{n}_p, \boldsymbol{\tau}_{p_1}\}$ in the two-dimensional case or $\{\mathbf{n}_p, \boldsymbol{\tau}_{p_1}, \boldsymbol{\tau}_{p_2}\}$ in the three-dimensional case, respectively, is an orthonormal basis in \mathbb{R}^d . We define the scaled tangential matrix $\mathbf{T}_{\mathcal{A}_n^k} \in \mathbb{R}^{(d-1)|\mathcal{A}_n^k| \times d|\mathcal{A}_n^k|}$ for $d = 3$ by

$$\mathbf{T}_{\mathcal{A}_n^k} := \begin{pmatrix} \ddots & \ddots & 0 & \cdots & 0 & 0 & 0 \\ 0 & 0 & \boldsymbol{\tau}_{p_1}^\top & & 0 & 0 \\ 0 & 0 & \boldsymbol{\tau}_{p_2}^\top & & 0 & 0 \\ 0 & 0 & 0 & \cdots & 0 & \ddots & \ddots \end{pmatrix}, \quad p \in \mathcal{A}_n^k.$$

Since in the two-dimensional case, we have only one tangent vector, the definition of the matrix $\mathbf{T}_{\mathcal{A}_n^k}$ contains only one line for each node $p \in \mathcal{A}_n^k$. Now, the algebraic representation of (4.11) is given by

$$\begin{pmatrix} \hat{\mathbf{K}}_{\mathcal{N}\mathcal{N}} & \hat{\mathbf{K}}_{\mathcal{N}\mathcal{M}} & \hat{\mathbf{K}}_{\mathcal{N}\mathcal{I}_n^k} & \hat{\mathbf{K}}_{\mathcal{N}\mathcal{A}_n^k} & \mathbf{0} & \mathbf{0} \\ \hat{\mathbf{K}}_{\mathcal{M}\mathcal{N}} & \hat{\mathbf{K}}_{\mathcal{M}\mathcal{M}} & \hat{\mathbf{K}}_{\mathcal{M}\mathcal{I}_n^k} & \hat{\mathbf{K}}_{\mathcal{M}\mathcal{A}_n^k} & \mathbf{0} & \mathbf{0} \\ \hat{\mathbf{K}}_{\mathcal{I}_n^k\mathcal{N}} & \hat{\mathbf{K}}_{\mathcal{I}_n^k\mathcal{M}} & \hat{\mathbf{K}}_{\mathcal{I}_n^k\mathcal{I}_n^k} & \hat{\mathbf{K}}_{\mathcal{I}_n^k\mathcal{A}_n^k} & \mathbf{D}_{\mathcal{I}_n^k} & \mathbf{0} \\ \hat{\mathbf{K}}_{\mathcal{A}_n^k\mathcal{N}} & \hat{\mathbf{K}}_{\mathcal{A}_n^k\mathcal{M}} & \hat{\mathbf{K}}_{\mathcal{A}_n^k\mathcal{I}_n^k} & \hat{\mathbf{K}}_{\mathcal{A}_n^k\mathcal{A}_n^k} & \mathbf{0} & \mathbf{D}_{\mathcal{A}_n^k} \\ \mathbf{0} & \mathbf{0} & \mathbf{0} & \mathbf{0} & \mathbf{Id}_{\mathcal{I}_n^k} & \mathbf{0} \\ \mathbf{0} & \mathbf{0} & \mathbf{0} & \mathbf{N}_{\mathcal{A}_n^k} & \mathbf{0} & \mathbf{0} \\ \mathbf{0} & \mathbf{0} & \mathbf{0} & \mathbf{0} & \mathbf{0} & \mathbf{T}_{\mathcal{A}_n^k} \end{pmatrix} \begin{pmatrix} \hat{\mathbf{u}}_{\mathcal{N}}^k \\ \hat{\mathbf{u}}_{\mathcal{M}}^k \\ \hat{\mathbf{u}}_{\mathcal{I}_n^k}^k \\ \hat{\mathbf{u}}_{\mathcal{A}_n^k}^k \\ \boldsymbol{\lambda}_{\mathcal{I}_n^k}^k \\ \boldsymbol{\lambda}_{\mathcal{A}_n^k}^k \end{pmatrix} = \begin{pmatrix} \hat{\mathbf{f}}_{\mathcal{N}} \\ \hat{\mathbf{f}}_{\mathcal{M}} \\ \hat{\mathbf{f}}_{\mathcal{I}_n^k} \\ \hat{\mathbf{f}}_{\mathcal{A}_n^k} \\ \mathbf{0} \\ \mathbf{g}_{\mathcal{A}_n^k} \end{pmatrix}. \quad (4.12)$$

Here, $\mathbf{g}_{\mathcal{A}_n^k}$ denotes the vector containing the entries g_p associated with the active nodes $p \in \mathcal{A}_n^k$. We remark that although the system (4.12) seems to have more lines than unknowns, it is a regular one. The total number of lines is exactly the number of unknowns. Formally, the two last lines are one line and belong all nodes in the subset \mathcal{A}_n^k . The second to last line contains only one component of each unknown and the last line the remaining ones, i.e. one component in the two-dimensional case and two components in the three-dimensional case. Due to the dual basis functions for the Lagrange multiplier space, the degrees of freedom for the Lagrange multiplier $\boldsymbol{\lambda}^k$ can be locally eliminated in the linear system (4.12). Static condensation yields

$$\boldsymbol{\lambda}^k = \mathbf{D}_d^{-1} \left(\hat{\mathbf{f}}_S - \hat{\mathbf{K}}_{S\mathcal{N}} \hat{\mathbf{u}}_{\mathcal{N}}^k - \hat{\mathbf{K}}_{S\mathcal{M}} \hat{\mathbf{u}}_{\mathcal{M}}^k - \hat{\mathbf{K}}_{SS} \hat{\mathbf{u}}_S^k \right). \quad (4.13)$$

To get the reduced system for the displacements $\hat{\mathbf{u}}^k$, we can easily eliminate the fifth row and the fifth column of (4.12), since $\boldsymbol{\lambda}_{\mathcal{I}_n^k}^k = \mathbf{0}$. To do so, we apply the matrix $\mathbf{T}_{\mathcal{A}_n^k}$ to the fourth row and write the result into its second (and third) component. We note that $\mathbf{T}_{\mathcal{A}_n^k} \mathbf{D}_{\mathcal{A}_n^k} \boldsymbol{\lambda}_{\mathcal{A}_n^k}^k = \mathbf{0}$, since $\mathbf{T}_{\mathcal{A}_n^k} \boldsymbol{\lambda}_{\mathcal{A}_n^k}^k = \mathbf{0}$ and $\mathbf{D}_{\mathcal{A}_n^k}$ is a diagonal matrix containing the same entries for each node $p \in \mathcal{A}_n^k$. Now, we move the sixth row into the first component of

the fourth row. The resulting system to solve is then given by

$$\begin{pmatrix} \hat{\mathbf{K}}_{\mathcal{N}\mathcal{N}} & \hat{\mathbf{K}}_{\mathcal{N}\mathcal{M}} & \hat{\mathbf{K}}_{\mathcal{N}\mathcal{I}_n^k} & \hat{\mathbf{K}}_{\mathcal{N}\mathcal{A}_n^k} \\ \hat{\mathbf{K}}_{\mathcal{M}\mathcal{N}} & \hat{\mathbf{K}}_{\mathcal{M}\mathcal{M}} & \hat{\mathbf{K}}_{\mathcal{M}\mathcal{I}_n^k} & \hat{\mathbf{K}}_{\mathcal{M}\mathcal{A}_n^k} \\ \hat{\mathbf{K}}_{\mathcal{I}_n^k\mathcal{N}} & \hat{\mathbf{K}}_{\mathcal{I}_n^k\mathcal{M}} & \hat{\mathbf{K}}_{\mathcal{I}_n^k\mathcal{I}_n^k} & \hat{\mathbf{K}}_{\mathcal{I}_n^k\mathcal{A}_n^k} \\ \mathbf{0} & \mathbf{0} & \mathbf{0} & \mathbf{N}_{\mathcal{A}_n^k} \\ \mathbf{T}_{\mathcal{A}_n^k} \hat{\mathbf{K}}_{\mathcal{A}_n^k\mathcal{N}} & \mathbf{T}_{\mathcal{A}_n^k} \hat{\mathbf{K}}_{\mathcal{A}_n^k\mathcal{M}} & \mathbf{T}_{\mathcal{A}_n^k} \hat{\mathbf{K}}_{\mathcal{A}_n^k\mathcal{I}_n^k} & \mathbf{T}_{\mathcal{A}_n^k} \hat{\mathbf{K}}_{\mathcal{A}_n^k\mathcal{A}_n^k} \end{pmatrix} \begin{pmatrix} \hat{\mathbf{u}}_{\mathcal{N}}^k \\ \hat{\mathbf{u}}_{\mathcal{M}}^k \\ \hat{\mathbf{u}}_{\mathcal{I}_n^k}^k \\ \hat{\mathbf{u}}_{\mathcal{A}_n^k}^k \end{pmatrix} = \begin{pmatrix} \hat{\mathbf{f}}_{\mathcal{N}} \\ \hat{\mathbf{f}}_{\mathcal{M}} \\ \hat{\mathbf{f}}_{\mathcal{I}_n^k} \\ \mathbf{g}_{\mathcal{A}_n^k} \\ \mathbf{T}_{\mathcal{A}_n^k} \hat{\mathbf{f}}_{\mathcal{A}_n^k} \end{pmatrix}. \quad (4.14)$$

Although it seems that this linear system has more lines than unknowns, this is not correct. Formally, the two last lines are one line and belong to all nodes in \mathcal{A}_n^k . These two lines arise from a splitting of the fourth line of the system (4.12) into its normal and tangential components. Thus, the linear system (4.14) is regular.

4.4. Inexact semi-smooth Newton method

In this section, we formulate an efficient inexact version of the primal-dual active set strategy derived in Section 4.2. The system (4.14) is linear and the conditions resulting for the contact constraints (4.11b) and (4.11c) are boundary conditions which can easily be included in existing finite element codes. Hence, the proposed iterative algorithm is extremely flexible. To construct efficient iterative solvers, we solve the linear system (4.14) not exactly but just apply m multigrid steps of an efficient multigrid method. Thus, the new iterate is only an approximation which is used to proceed the iteration. The combination of primal-dual active set strategies and multigrid methods has also been considered in [97].

Denoting by

$$\hat{\mathbf{u}}^{k,i} = \text{MG}(\hat{\mathbf{u}}^{k,i-1}, \mathcal{A}_n^k, \mathcal{I}_n^k) \quad (4.15)$$

one iteration step of a linear multigrid solver for the linear system (4.14), we can formulate our inexact primal-dual active set strategy, as stated in Algorithm 1. As one iteration step of the linear multigrid method we denote anywhere in this thesis a recursive call to three pre-smoothing steps on the linear system, one coarsening step, one \mathcal{W} -multigrid cycle, one coarse to fine prolongation and three post-smoothing steps on the linear system. For the smoother we use a symmetric Gauß-Seidel iteration. We remark that the levels of the grids are not changed within the k -loop in Algorithm 1. They are only changed in step 6 within the iteration step of the linear multigrid.

Furthermore, we mention that the actual set of active nodes \mathcal{A}_n^k , indicating Dirichlet data, is not necessarily resolved on the coarser grids. Thus, we have to modify the standard transfer operators. There are different options; one is to use a non-conforming approach, see [134]. Furthermore, the transfer operators have to be adapted to the fact, that the linear system (4.14) is formulated with respect to the new constrained finite element basis. The essential idea is to correct the coarse grid spaces and use a natural embedding, see [139, 140, 141].

Solving the linear system (4.14) in step 5-7 exactly, we get the exact version of Algorithm 1. We refer to this case in the following by the choice $m = \infty$. In the exact case,

Algorithm 1 (Inexact) primal-dual active set strategy

- 1: set $k = 1$
- 2: initialize \mathcal{A}_N^1 and \mathcal{I}_n^1 , such that $\mathcal{S} = \mathcal{A}_n^1 \cup \mathcal{I}_n^1$ and $\mathcal{A}_n^1 \cap \mathcal{I}_n^1 = \emptyset$
- 3: initialize $\hat{\mathbf{u}}^{1,0}$ as an initial solution for the multigrid
- 4: set $c > 0$ and $m \in \mathbb{N}$ and the tolerance ε_u
- 5: **for** $i = 1, \dots, m$ **do**
- 6:

$$\hat{\mathbf{u}}^{k,i} = \text{MG}(\hat{\mathbf{u}}^{k,i-1}, \mathcal{A}_n^k, \mathcal{I}_n^k)$$

- 7: **end for**
- 8: **if** $\|\hat{\mathbf{u}}^{k,0} - \hat{\mathbf{u}}^{k,m}\| / \|\hat{\mathbf{u}}^{k,0}\| < \varepsilon_u$ **then**
- 9: stop
- 10: **end if**
- 11: compute the Lagrange multiplier

$$\boldsymbol{\lambda}^k = \mathbf{D}_d^{-1} \left(\hat{\mathbf{f}}_S - \hat{\mathbf{K}}_{SN} \hat{\mathbf{u}}_N^{k,m} - \hat{\mathbf{K}}_{SM} \hat{\mathbf{u}}_M^{k,m} - \hat{\mathbf{K}}_{SS} \hat{\mathbf{u}}_S^{k,m} \right)$$

- 12: update the active set \mathcal{A}_n^{k+1} and the inactive set \mathcal{I}_n^{k+1} by

$$\begin{aligned} \mathcal{A}_n^{k+1} &:= \{p \in \mathcal{S} : \lambda_{pns}^k + c(\hat{u}_{pn}^{k,m} - g_p) > 0\} \\ \mathcal{I}_n^{k+1} &:= \{p \in \mathcal{S} : \lambda_{pns}^k + c(\hat{u}_{pn}^{k,m} - g_p) \leq 0\} \end{aligned}$$

- 13: set $\hat{\mathbf{u}}^{k+1,0} = \hat{\mathbf{u}}^{k,m}$
 - 14: set $k = k + 1$
 - 15: go to step 5
-

we can also terminate the algorithm when the active and inactive sets \mathcal{A}_n^{k+1} and \mathcal{I}_n^{k+1} in step 12 are the same as in the previous step, without checking the stopping criterion in step 8 based on the relative error. Furthermore, we mention that in each Newton, step we only have to change the lines of the original stiffness matrix belonging to the contact nodes as described in (4.14). Therefore, there is no need to reassemble the whole stiffness matrix in each iteration step if we store the original part $\hat{\mathbf{K}}_{S^*}$. We conclude with some remarks concerning the influence of the parameter c and the momentum of lowest order for the Lagrange multiplier.

Remark 4.2. In the exact version of Algorithm 1 the positive parameter c has no influence on the sequence \mathcal{A}_n^k and \mathcal{I}_n^k . However, the parameter c plays an important role for the inexact strategy. Here, we observe numerically convergence for $c \geq c_0$, where $0 < c_0 < \infty$ depends on the material parameter E and ν , [84].

Remark 4.3. For a pure Neumann problem in all steps, both for the exact and the inexact strategy, the momentum of lowest order is the same, i.e., $\int_{\Gamma_s} \boldsymbol{\lambda}^{h,k} ds$ is constant for all steps. This holds even for the inexact case, since we compute $\boldsymbol{\lambda}^{h,k}$ by (4.13).

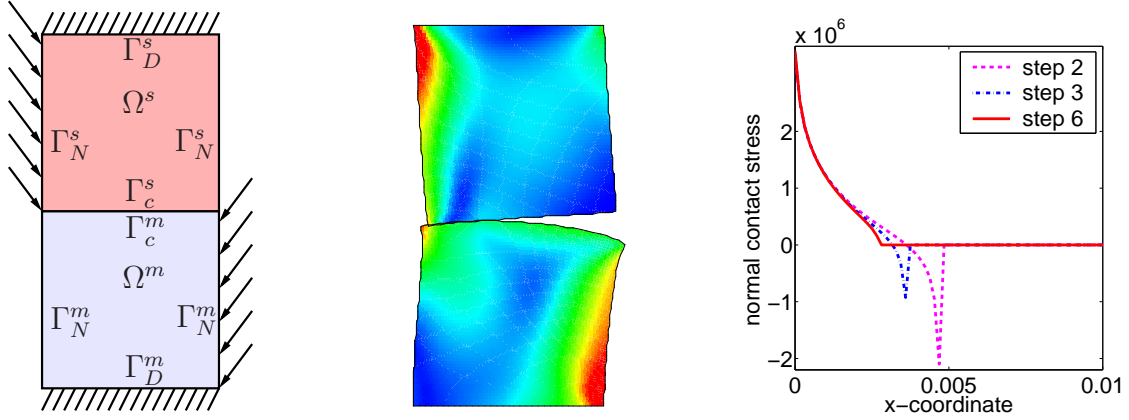


Figure 4.1.: Example 1: Problem definition (left), distorted body with the effective von Mises stress σ_{eff} (middle) (distortion amplified by factor 1000) and normal contact stress for different steps of the active set strategy on level 6 for the case $\mathcal{A}_n^1 = \emptyset$ (right).

4.5. Numerical studies

Now, we investigate the numerical behavior of the inexact primal-dual active set strategy formulated in Algorithm 1. These results have been published in [84] for the lowest order finite elements and in [79] for the higher order cases introduced in Section 3.4.

4.5.1. First example

We consider the second example in Section 3.2. For convenience of the reader, we show the problem definition in the left picture in Figure 4.1 once more. For the geometric and the material data as well as for the applied boundary conditions, we refer to Section 3.2. In this example, the contact stress is non-symmetric on the possible contact boundary Γ_c^s and has a singularity. The triangulation on level 0 consists of one quadrilateral per body, such that the possible contact part Γ_c^s of Ω^s consists of two nodes. The middle picture in Figure 4.1 shows the distorted body with the effective von Mises stress σ_{eff} .

First we concentrate on the exact approach, i.e., $m = \infty$ in Algorithm 1. For the first step of our active set strategy, we choose $\mathcal{A}_n^1 = \emptyset$ and thus $\mathcal{I}_n^1 = \mathcal{S}$. To find the correct active set on the higher levels, we consider three different strategies. One possibility is that level $l + 1$ inherits the active set from level l , called the nested case. Alternatively, we set on each level either all nodes of \mathcal{S} inactive, i.e., $\mathcal{A}_n^1 = \emptyset$, or all nodes active, i.e., $\mathcal{A}_n^1 = \mathcal{S}$. We mention that there are many other ways to initialize \mathcal{A}_n^1 on each level. For all three strategies considered here, the resulting number of steps K_l of the primal-dual active set strategy is shown in Table 4.1. The second column contains the number of nodes p on Γ_c^s . Column three of Table 4.1 contains the number of steps K_l for each level for the nested case. In the fourth column, the number of active nodes in each step are given. In column five and six, the same is done for the case starting with $\mathcal{A}_n^1 = \emptyset$ on each

Table 4.1.: Example 1: Exact primal-dual active set strategy.

l	$ \mathcal{S} $	nested case			$\mathcal{A}_n^1 = \emptyset$						$\mathcal{A}_n^1 = \mathcal{S}$		
		K_l	$ \mathcal{A}_n^k $		K_l						K_l		
0	2	2	0	1	2	0	1					2	
1	3	1	1		2	0	1					2	
2	5	2	1	2	2	0	2					2	
3	9	1	3		3	0	4	3				3	
4	17	1	5		4	0	8	6	5			4	
5	33	2	9	10	4	0	16	12	10			4	
6	65	2	19	18	6	0	31	24	21	19	18	6	
7	129	2	35	36	7	0	61	47	42	38	37	36	
8	257	1	71		8	0	122	93	81	76	73	72	71

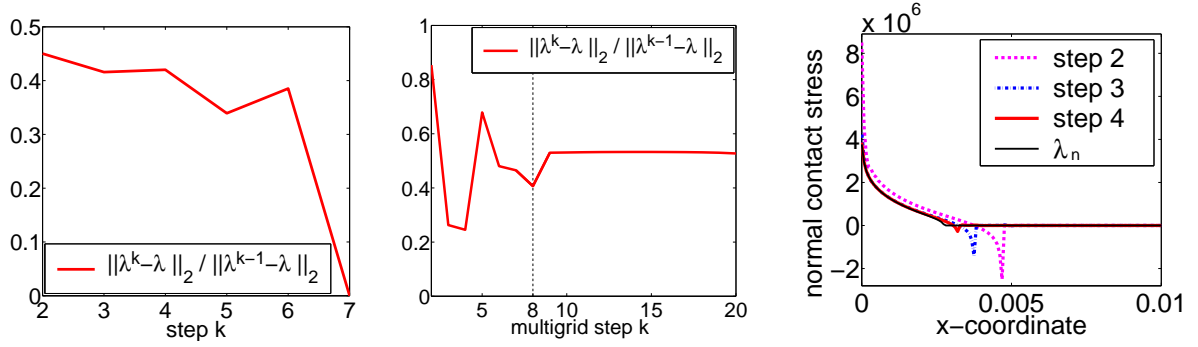


Figure 4.2.: Example 1: Relative error of the Lagrange multiplier for the exact active set strategy on level 6 (left) and the inexact strategy (middle) for the choice $\mathcal{A}_n^1 = \emptyset$, normal contact stress after different multigrid steps for the inexact strategy (right).

level. In the last column, the number of steps K_l for the active set strategy is shown if we start on each level l with $\mathcal{A}_n^1 = \mathcal{S}$. We observe that the number of the active set steps K_l is independent of the refinement level if we use the active set on the previous level as start set \mathcal{A}_n^1 , whereas in the cases $\mathcal{A}_n^1 = \emptyset$ and $\mathcal{A}_n^1 = \mathcal{S}$, the number of steps K_l depends linearly on the level l . In the right picture of Figure 4.1, the normal component λ_n of the Lagrange multiplier at different active set steps on level 6 is presented for the case $\mathcal{A}_n^1 = \emptyset$.

Next, we consider the inexact strategy for this example by setting $c = 10^{13}$ and $m = 1$ in Algorithm 1. To analyze the convergence, we consider the relative error for the Lagrange multiplier in each step given by $\|\lambda^k - \lambda\|_2 / \|\lambda^{k-1} - \lambda\|_2$. The behavior of the convergence is shown in Figure 4.2. In the left picture, the convergence of the Lagrange multiplier for the exact strategy on level 6 for the case $\mathcal{A}_n^1 = \emptyset$ is presented. Here, we observe

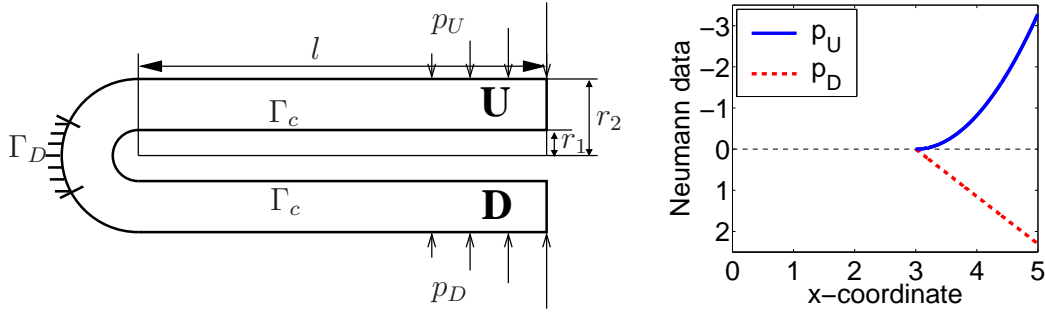


Figure 4.3.: Example 2: Problem definition (left), and applied Neumann data p_U and p_D (right).

superlinear convergence rates. For the number of active set steps, we refer to Table 4.1. The picture in the middle of Figure 4.2 contains the convergence of the Lagrange multiplier for the inexact strategy. Here, we consider level 6 and the case $\mathcal{A}_n^1 = \emptyset$ as done for the exact strategy. The correct active set is found for the first time in the eighth step. In the following, we denote the multigrid step on level l , in which the correct active set is found for the first time, by M_l . After that, the active set does not change any more, and we observe constant convergence rates for the multigrid iteration. Until step 8, the nonlinear influence of finding the correct active set yields oscillating convergence rates. The right picture in Figure 4.2 shows the normal part of the Lagrange multiplier for different steps of the inexact strategy.

4.5.2. Second example

Next, we consider an artificial self-contact problem and compare the nested case with a non-nested one for the exact strategy. The body Ω is shown in Figure 4.3. We set the length l of the two arms equal to $l = 5.0$, the inner radius r_1 of the connecting arc equal to $r_1 = 0.2$ and the outer radius r_2 equal to $r_2 = 0.5$. The possible contact boundary Γ_c on the upper arm **U** is assumed to play the role of the slave side and Γ_c of the lower arm **D** the role of the master side. For the material parameters, we set $E = 1000$ and $\nu = 0.3$, so the initial gap is given by $g = 0.4$. As shown in the left picture in Figure 4.3, we fix the body at the outer part of the connecting arc on the left side. On the remaining boundary parts, we assume homogenous Neumann boundary conditions except at the top and the bottom part. Here, we apply the surface loads presented in the right picture in Figure 4.3 pressing the two arms together. Of course, this problem is not a physically sensible one but only a mathematical test example for our method.

For our computations, we use an automatically generated finite element mesh consisting of 52 triangles on level 0. The possible boundary region Γ_c of the slave side contains 10 nodes, whereas on the master side we have 9 nodes. Hence, the meshes are non-conforming at the contact zones. The deformed body and the resulting contact stress are presented in Figure 4.4. For initializing the active set \mathcal{A}_n^1 , we either follow the nested approach, choose $\mathcal{A}_n^1 = \{p = (p_x, p_y)^\top \in \mathcal{S} : p_x \geq 3.9\}$ or start with $\mathcal{A}_n^1 = \emptyset$. The

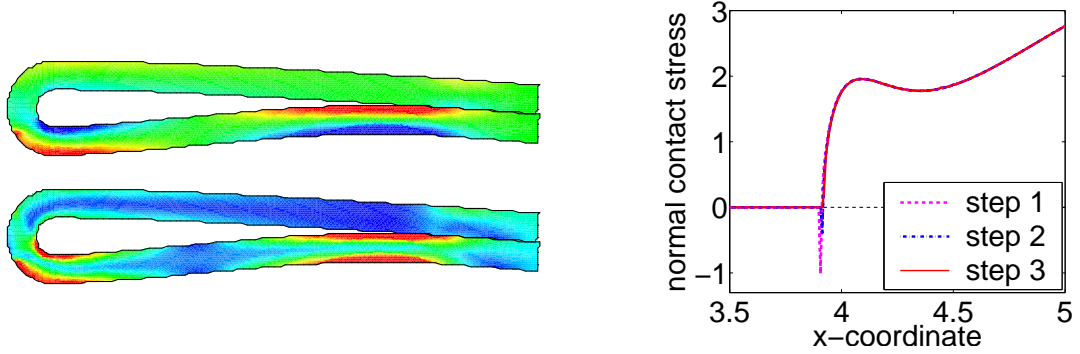


Figure 4.4.: Example 2: Distorted body with σ_{xx} (left upper), the effective von Mises stress σ_{eff} (left lower) and the normal contact of the contact stress λ_n for the steps of the active set strategy on level 6 for the case $\mathcal{A}_n^1 = \{p \in \mathcal{S} : p_x \geq 3.9\}$.

Table 4.2.: Example 2: Exact primal-dual active set strategy.

l	$ \mathcal{S} $	nested case				$\mathcal{A}_n^1 = \{p \in \mathcal{S} : p_x \geq 3.9\}$				
		K_l	$ \mathcal{A}_n^k $			K_l	$ \mathcal{A}_n^k $			
0	9	10	0	10	...	2	2	3	2	
1	17	4	3	7	6	5	1	5		
2	33	1	9				1	9		
3	65	2	17	18			1	18		
4	129	1	35				2	36	35	
5	257	2	69	70			2	71	70	
6	513	1	139				3	141	140	139

number of active set steps K_l for these three cases are summarized in Table 4.2. For the nested case, we need a large number of steps on the lowest levels. After level 2, the number of steps K_l decreases rapidly. In the second case, the initial set \mathcal{A}_n^1 is very close to the correct contact zone, but the number of steps K_l still depends asymptotically linearly on the level. We mention that for this example, the nodes will be released very slowly, such that we need a large number of steps K_l if we choose $\mathcal{A}_n^1 = \emptyset$. \mathcal{A}_n^1 being smaller than the correct contact zone, in the second step \mathcal{A}_n^2 becomes too large and the additional active nodes will be released very slowly. The right picture in Figure 4.4 shows the normal part λ_n of the Lagrange multiplier for the three steps for the second case on level 6.

4.5.3. Third example

We compare the exact and the inexact approach for the three different discretizations introduced in Section 3.4 for the Hertzian contact problem. Although considered already

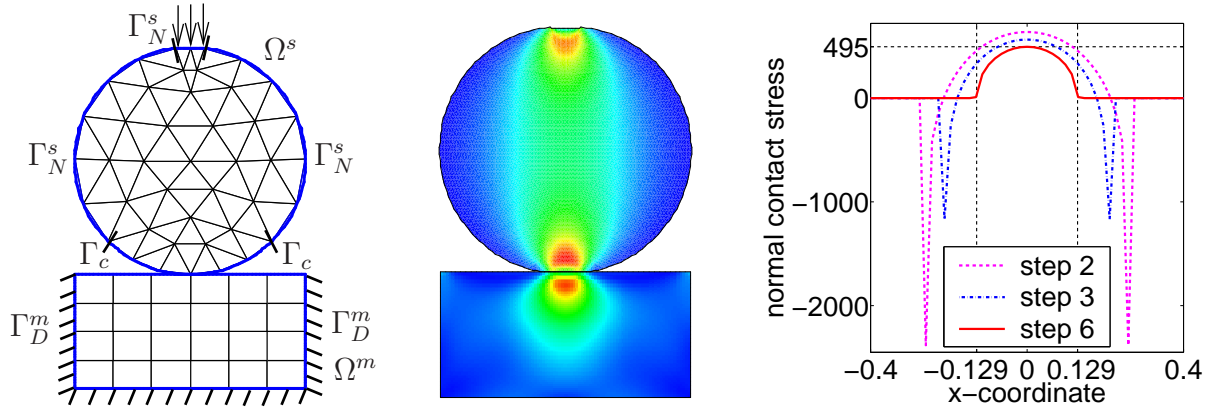


Figure 4.5.: Example 3: Problem definition (left), distorted body with effective von Mises stress σ_{eff} (middle) and normal contact stress for different steps of the active set strategy on level 4 (right).

Table 4.3.: Example 3: Step M_l , in which the correct active set is found for the first time for the inexact primal-dual active set strategy Algorithm 1 for all three discretizations and different choices of \mathcal{A}_n^1 .

l	$(i, j) = (1, 1)$				$(i, j) = (2, 1)$				$(i, j) = (2, 2)$			
	N_s^1	N_a	nest.	\mathcal{S}	N_s^1	N_a	nest.	\mathcal{S}	N_s^2	N_a	nest.	\mathcal{S}
0	7	1	4	4	7	1	4	4	13	3	4	4
1	13	3	2	5	13	3	2	5	25	5	1	6
2	25	5	1	7	25	5	1	6	49	9	1	8
3	49	9	1	8	49	9	1	8	97	17	1	9
4	97	17	1	10	97	17	1	9	193	31	2	11
5	193	31	2	11	193	33	1	9	385	63	3	12
6	385	63	3	11	—	—	—	—	—	—	—	—

in Section 3.2 for the lowest order case and in Section 3.4 for the higher order case, the problem definition and the initial triangulation on level 0 are shown in the left picture in Figure 4.5 for convenience. In our algorithm, we set $c = 10^4$ and $m = 1$, i.e., we update the active set after each multigrid step. For the initial choice of the active set, we consider two strategies. First we consider the nested case. To show that our method is robust, we set in a second test $\mathcal{A}_n^1 = \mathcal{S}$, which is considerably larger than the correct contact zone. Let M_l be the minimal step k in Algorithm 1 on level l , in which the correct active set \mathcal{A}_n is found for the first time and does not change anymore.

In Table 4.3, we show the number of multigrid iterations M_l to detect the correct active set on level l for different choices of (i, j) . In the first column of each discretization (i, j) , the number of contact points is given. We remark that for $(i, j) = (2, 2)$ we have also degrees of freedoms on the edges $e \in \mathcal{T}_{h, \Gamma_c^s}$ and thus $N_s^2 = 2N_s^1 - 1$. For the case

Table 4.4.: Example 3: Step K_l , in which the correct active set is found for the first time for the exact primal-dual active set strategy Algorithm 1 for all three discretizations and different choices of \mathcal{A}_n^1 .

l	$(i, j) = (1, 1)$				$(i, j) = (2, 1)$				$(i, j) = (2, 2)$			
	N_s^1	N_a	nest.	\mathcal{S}	N_s^1	N_a	nest.	\mathcal{S}	N_s^2	N_a	nest.	\mathcal{S}
0	7	1	4	4	7	1	4	4	13	3	4	4
1	13	3	2	5	13	3	2	4	25	5	1	6
2	25	5	1	7	25	5	1	5	49	9	1	8
3	49	9	1	7	49	9	1	7	97	17	1	8
4	97	17	1	8	97	17	1	8	193	31	2	10
5	193	31	2	10	193	33	1	9	385	63	3	10
6	385	63	2	11	—	—	—	—	—	—	—	—

Table 4.5.: Example 3: Total multigrid steps for the nonlinear problem for the nested approach and the linear elasticity problem without contact for $(i, j) = (1, 1)$.

level l	0	1	2	3	4	5	6
nonlinear contact problem	4	22	19	16	15	16	15
linear elasticity problem	1	23	19	17	16	16	15

$(i, j) = (1, 1)$ and $(i, j) = (2, 1)$, the contact constraints are checked only at the nodes $p \in \mathcal{S}$ and thus we have $N_s^1 = |\mathcal{S}|$. For $(i, j) = (2, 1)$, we have to modify the decomposition of the total degrees of freedom $\mathcal{N} \cup \mathcal{M} \cup \mathcal{S}$. Here, the degrees of freedom associated with an edge $e \in \mathcal{T}_{h, \Gamma_c}$ are formally related to the subset \mathcal{M} . For details we refer to [79]. The second column contains the final number of contact nodes of the correct active set \mathcal{A}_n . In the next two columns, the steps M_l for the two different choices for \mathcal{A}_n^1 are presented. For the lowest order case, we have computed solutions up to level 6, whereas for the other two cases this is done only up to level 5 since then the number of unknowns for the displacements are equal. In Table 4.4, we present the number of steps K_l to find the correct active set for the exact algorithm.

For the nested case, the number M_l or K_l is independent on the level l for both algorithms. For the case $\mathcal{A}_n^1 = \mathcal{S}$, the number M_l or K_l depends linearly on l . To compare the inexact algorithm with the exact approach, we observe that the number of steps for all discretizations (i, j) and all initial choices for \mathcal{A}_n^1 are almost equal. Table 4.5 shows the total number of multigrid steps necessary to solve the contact problem with the nested approach for each refinement level l . In comparison to that, the second line displays the total multigrid steps needed to solve the corresponding linear elasticity problem neglecting the contact constraints. We observe for both problems almost the same iteration numbers. Thus, there is no reason to solve the algebraic system exactly.

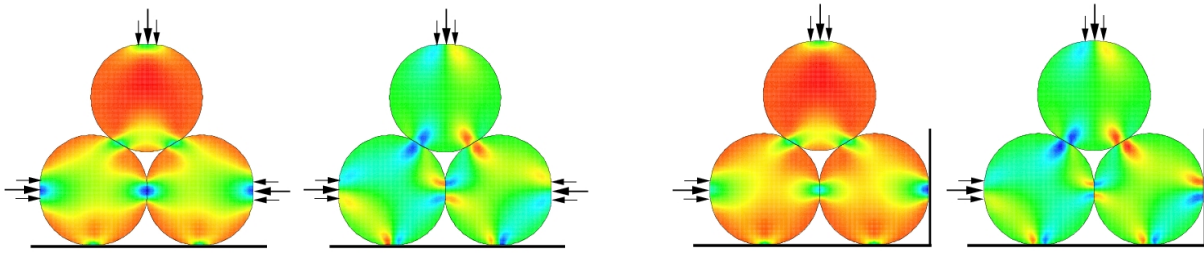


Figure 4.6.: Example 4: Stress components σ_{xx} and σ_{xy} for a symmetric (left) and non-symmetric (right) setting.

We summarize the results in the following remark.

Remark 4.4. If we use the nested update for the inexact strategy, the correct active set is found in the first few steps of the multigrid method. Combined with the optimal multigrid method and the dual Lagrange multiplier, which allows the local basis transformation and the local static condensation, this approach yields a powerful and efficient iterative algorithm.

4.5.4. Fourth example

Finally, we consider an example with more than two subdomains. We use three circles and a rigid obstacle, see Figure 4.6, and two different sets of boundary data. The possible contact zone can be decomposed into two different types: the contact between two elastic circles and the contact between one elastic circle and the rigid obstacle. For this example, one circle has to have a master as well as a slave interface. The contact between the rigid obstacle and the elastic body is also discretized in terms of dual Lagrange multipliers defined on the elastic body which is the slave side. The two pictures in the left of Figure 4.6 show the stress components σ_{xx} and σ_{xy} of a symmetric boundary data. In the two pictures on the right, the rigid obstacle forms a L-shape, and the solution is non-symmetric.

5. Semi-smooth Newton method for frictional constraints

Solving contact problems with friction in the three-dimensional case is a challenging task in mechanics and of crucial importance in various applications. The main difficulty lies in the conditions for contact and friction, which are inherently nonlinear and complicate the theoretical analysis as well as the design of efficient numerical algorithms.

In this chapter, we introduce our algorithm for contact problems with friction. We extend the methods presented in Chapter 4 for the treatment of the non-penetration condition to the case of friction. Now, we have to solve a linear problem with boundary conditions of Dirichlet, Neumann or Robin type on the contact zone Γ_c^s in each iteration step. We remark that for the non-penetration only boundary conditions of Dirichlet- and Neumann-type occur, see (4.11). As in the previous chapter, a local elimination of the degrees of freedom associated with the Lagrange multiplier can be applied, such that the resulting system only has to be solved for the primal variable. This algorithm perfectly fits into the abstract framework used in Chapter 4 and inherits the advantages mentioned there, i.e., the simple implementation and the numerical efficiency. As has been published in [82], this approach can be regarded as a semi-smooth Newton method guaranteeing fast local convergence. Furthermore, semi-smooth Newton methods for frictional contact problems are investigated in [3] within the framework of a modified augmented Lagrangian approach and in [27, 28] where a different nonlinear complementarity function is used.

Contributions to theoretical and numerical results for contact problems with friction in the three-dimensional case are quite rare. We refer to the recent papers [39, 64], where FETI domain decomposition techniques are combined with quadratic programming methods. The quadratic constraints are approximated by the intersection of rotated squares in order to make the application of optimization algorithms possible. Improvements are proposed in [99, 100]. A different idea is followed in [46, 93], where monotone multigrid methods are used to construct a globally convergent solver. The implementation of these methods relies on a multilevel hierarchy of spaces and requires the use of modified coarse grid basis functions and suitable coarse grid constraints.

The structure of this chapter is similar to Chapter 4. First of all, we deal with Tresca's friction law in Section 5.1-5.4. We start with the introduction of the nonlinear complementarity function and the presentation of some suitable modifications for the resulting Robin-type condition for the sliding nodes in Section 5.1. The modifications cause a stabilization of the numerical algorithm. Section 5.2 contains the algebraic version and the elimination of the degrees of freedom associated with the Lagrange multiplier. The inexact semi-smooth Newton method is formulated in Section 5.3. The following Section 5.4

illustrates its numerical performance and flexibility. Finally, we extend the considered methods to the case of Coulomb's friction law. In Section 5.5 we present a widely used fixed point based approach, whereas Section 5.6 contains a new full Newton method.

5.1. Nonlinear complementarity function

Due to Lemma 2.6, we can write the algebraic version of the point-wise decoupled static frictional constraints (1.30) in the case of a given friction bound $g_f(\cdot) : \Gamma_c^s \rightarrow \mathbb{R}$, also referred to as Tresca's friction law, in terms of the coefficients $\hat{\mathbf{u}}_p$ of the displacement vector \mathbf{u} with respect to the constrained basis $\hat{\phi}$ and the coefficients $\boldsymbol{\lambda}_p$ for the Lagrange multiplier as

$$\begin{cases} \|\boldsymbol{\lambda}_{p\tau s}\| \leq b_p, \\ \|\boldsymbol{\lambda}_{p\tau s}\| < b_p \Rightarrow \hat{\mathbf{u}}_{p\tau} = \mathbf{0}, \\ \|\boldsymbol{\lambda}_{p\tau s}\| = b_p \Rightarrow \exists \alpha \in \mathbb{R} : \boldsymbol{\lambda}_{p\tau s} = \alpha^2 \hat{\mathbf{u}}_{p\tau}, \end{cases} \quad p \in \mathcal{S}, \quad (5.1)$$

where the friction bound b_p associated with the node $p \in \mathcal{S}$ is defined by

$$b_p := \int_{\Gamma_c^s} g_f \phi_p \, d\mathbf{s}.$$

We remark, that we have $b_p = g_f D_p$ if the friction bound g_f is a constant function. As done in Section 4.2, we again use the scaled values for the coefficients of the Lagrange multiplier. From this condition, we observe that for each node $p \in \mathcal{S}$, we have for the pair $(\boldsymbol{\lambda}_{p\tau s}, \hat{\mathbf{u}}_{p\tau})$ either $\|\boldsymbol{\lambda}_{p\tau s}\| < b_p$ and $\hat{\mathbf{u}}_{p\tau} = \mathbf{0}$ or $\|\boldsymbol{\lambda}_{p\tau s}\| = b_p$ and $\boldsymbol{\lambda}_{p\tau s} = \alpha^2 \hat{\mathbf{u}}_{p\tau}$. In the first situation the node p is a sticky node, whereas in the second case p is a slip node. Motivated by the fact that we can write the algebraic version of equation (2.11) for the projection operator restricted to each node $p \in \mathcal{S}$ as

$$\boldsymbol{\lambda}_{p\tau s} = b_p \frac{\boldsymbol{\lambda}_{p\tau s} + c \hat{\mathbf{u}}_{p\tau}}{\max\{b_p, \|\boldsymbol{\lambda}_{p\tau s} + c \hat{\mathbf{u}}_{p\tau}\|\}},$$

our semi-smooth Newton algorithm is based on the nonlinear complementarity function

$$C_\tau(\hat{\mathbf{u}}_{p\tau}, \boldsymbol{\lambda}_{p\tau s}) := \max\{b_p, \|\boldsymbol{\lambda}_{p\tau s} + c \hat{\mathbf{u}}_{p\tau}\|\} \boldsymbol{\lambda}_{p\tau s} - b_p (\boldsymbol{\lambda}_{p\tau s} + c \hat{\mathbf{u}}_{p\tau}). \quad (5.2)$$

for any positive parameter $c > 0$. Similar to Theorem 4.1, we get the following equivalence.

Theorem 5.1. *The pair $(\boldsymbol{\lambda}_{p\tau s}, \hat{\mathbf{u}}_{p\tau})$ satisfies the frictional contact constraints (5.1) if and only if it satisfies the condition*

$$C_\tau(\hat{\mathbf{u}}_{p\tau}, \boldsymbol{\lambda}_{p\tau s}) = \mathbf{0}, \quad p \in \mathcal{S}. \quad (5.3)$$

Proof. We first show that the conditions (5.1) lead to (5.3). For the pair $(\boldsymbol{\lambda}_{p\tau s}, \hat{\mathbf{u}}_{p\tau})$ satisfying (5.1) we have either $\|\boldsymbol{\lambda}_{p\tau s}\| < b_p$ and $\hat{\mathbf{u}}_{p\tau} = \mathbf{0}$ or $\|\boldsymbol{\lambda}_{p\tau s}\| = b_p$ and $\boldsymbol{\lambda}_{p\tau s} = \alpha^2 \hat{\mathbf{u}}_{p\tau}$. In the first situation we deduce

$$C_\tau(\hat{\mathbf{u}}_{p\tau}, \boldsymbol{\lambda}_{p\tau s}) = \max\{b_p, \|\boldsymbol{\lambda}_{p\tau s}\|\} \boldsymbol{\lambda}_{p\tau s} - b_p \boldsymbol{\lambda}_{p\tau s} = \mathbf{0},$$

whereas in the second case, we get

$$C_\tau(\hat{\mathbf{u}}_{p\tau}, \boldsymbol{\lambda}_{p\tau s}) = \max\left\{b_p, \left(1 + \frac{c}{\alpha^2}\right)b_p\right\} \boldsymbol{\lambda}_{p\tau s} - b_p \left(1 + \frac{c}{\alpha^2}\right) \boldsymbol{\lambda}_{p\tau s} = \mathbf{0}.$$

Thus, we have the relation $C_\tau(\hat{\mathbf{u}}_{p\tau}, \boldsymbol{\lambda}_{p\tau s}) = \mathbf{0}$ for both cases.

If for the pair $(\hat{\mathbf{u}}_{p\tau}, \boldsymbol{\lambda}_{p\tau s})$ the relations $C_\tau(\hat{\mathbf{u}}_{p\tau}, \boldsymbol{\lambda}_{p\tau s}) = \mathbf{0}$ holds, we observe for the case $\|\boldsymbol{\lambda}_{p\tau s} + c\hat{\mathbf{u}}_{p\tau}\| < b_p$

$$\mathbf{0} = C_\tau(\hat{\mathbf{u}}_{p\tau}, \boldsymbol{\lambda}_{p\tau s}) = b_p \boldsymbol{\lambda}_{p\tau s} - b_p (\boldsymbol{\lambda}_{p\tau s} + c\hat{\mathbf{u}}_{p\tau}) = -cb_p \hat{\mathbf{u}}_{p\tau}.$$

Thus, we get due to $c > 0$ and $b_p > 0$ the relation $\hat{\mathbf{u}}_{p\tau} = \mathbf{0}$. This leads directly to $\|\boldsymbol{\lambda}_{p\tau s}\| < b_p$ and the conditions (5.1) are satisfied. If $\|\boldsymbol{\lambda}_{p\tau s} + c\hat{\mathbf{u}}_{p\tau}\| \geq b_p$ holds, we deduce from

$$\mathbf{0} = C_\tau(\hat{\mathbf{u}}_{p\tau}, \boldsymbol{\lambda}_{p\tau s}) = \|\boldsymbol{\lambda}_{p\tau s} + c\hat{\mathbf{u}}_{p\tau}\| \boldsymbol{\lambda}_{p\tau s} - b_p (\boldsymbol{\lambda}_{p\tau s} + c\hat{\mathbf{u}}_{p\tau})$$

the relations $\|\boldsymbol{\lambda}_{p\tau s}\| = b_p$ and

$$\boldsymbol{\lambda}_{p\tau s} = \gamma \hat{\mathbf{u}}_{p\tau}, \quad \gamma := \frac{cb_p}{\|\boldsymbol{\lambda}_{p\tau s} + c\hat{\mathbf{u}}_{p\tau}\| - b_p}.$$

Since $\|\boldsymbol{\lambda}_{p\tau s} + c\hat{\mathbf{u}}_{p\tau}\| \geq b_p$ and $c > 0$ we have $\gamma > 0$ and thus conditions (5.1) are again satisfied. \square

In the following, we derive for equation (5.3) the semi-smooth Newton method. Unfortunately, both the Euclidean norm and the max-function are not smooth and not differentiable in the classical sense. However, they are semi-smooth and slantly differentiable in the sense of [75, 122], see also Section 4.1, which justifies the application of a semi-smooth Newton method. We note that in the first term of (5.2), the Euclidean norm appears for non-zero arguments only. This is due to the fact that if $\|\boldsymbol{\lambda}_{p\tau s} + c\hat{\mathbf{u}}_{p\tau}\| = 0$, we obtain $\max(b_p, \|\boldsymbol{\lambda}_{p\tau s} + c\hat{\mathbf{u}}_{p\tau}\|) = b_p$ and the Euclidean norm vanishes. Therefore, the only non-differentiability that matters in (5.2) is the $\max\{\cdot, \cdot\}$ -function. In each semi-smooth Newton step, the derivative of the Euclidean norm only occurs for points that are differentiable in the classical sense.

We now use the generalized Jacobian (4.3) for $p \in \mathcal{S}$ to compute the generalized derivative D_{C_τ} of $C_\tau(\cdot, \cdot)$. For the variation $(\delta \hat{\mathbf{u}}_{p\tau}, \delta \boldsymbol{\lambda}_{p\tau s}) \in \mathbb{R}^{(d-1)} \times \mathbb{R}^{(d-1)}$, we obtain

$$\begin{aligned} D_{C_\tau}(\hat{\mathbf{u}}_{p\tau}, \boldsymbol{\lambda}_{p\tau s})(\delta \hat{\mathbf{u}}_{p\tau}, \delta \boldsymbol{\lambda}_{p\tau s}) &= \max\{b_p, \|\boldsymbol{\lambda}_{p\tau s} + c\hat{\mathbf{u}}_{p\tau}\|\} \delta \boldsymbol{\lambda}_{p\tau s} \\ &+ \chi_{\mathcal{A}} \frac{\boldsymbol{\lambda}_{p\tau s} (\boldsymbol{\lambda}_{p\tau s} + c\hat{\mathbf{u}}_{p\tau})^\top}{\|\boldsymbol{\lambda}_{p\tau s} + c\hat{\mathbf{u}}_{p\tau}\|} (\delta \boldsymbol{\lambda}_{p\tau s} + c \delta \hat{\mathbf{u}}_{p\tau}) - b_p (\delta \boldsymbol{\lambda}_{p\tau s} + c \delta \hat{\mathbf{u}}_{p\tau}). \end{aligned} \quad (5.4)$$

Here, $\chi_{\mathcal{A}}$ denotes the characteristic function of the set $\mathcal{A}_\tau := \{p \in \mathcal{S} : \|\boldsymbol{\lambda}_{p\tau s} + c\hat{\mathbf{u}}_{p\tau}\| > b_p\}$, i.e.,

$$\chi_{\mathcal{A}} := \begin{cases} 1 & \text{if } \|\boldsymbol{\lambda}_{p\tau s} + c\hat{\mathbf{u}}_{p\tau}\| > b_p, \\ 0 & \text{if } \|\boldsymbol{\lambda}_{p\tau s} + c\hat{\mathbf{u}}_{p\tau}\| \leq b_p. \end{cases}$$

We note that $\boldsymbol{\lambda}_{p\tau s} (\boldsymbol{\lambda}_{p\tau s} + c\hat{\mathbf{u}}_{p\tau})^\top$ is a $(d-1) \times (d-1)$ -matrix, either zero or of rank one. For a current iterate $(\hat{\mathbf{u}}_{p\tau}^{k-1}, \boldsymbol{\lambda}_{p\tau s}^{k-1})$, one derives the new iterate

$$(\hat{\mathbf{u}}_{p\tau}^k, \boldsymbol{\lambda}_{p\tau s}^k) = (\hat{\mathbf{u}}_{p\tau}^{k-1}, \boldsymbol{\lambda}_{p\tau s}^{k-1}) + (\delta\hat{\mathbf{u}}_{p\tau}^k, \delta\boldsymbol{\lambda}_{p\tau s}^k)$$

of the semi-smooth Newton step by solving the equation

$$D_{C_\tau}(\hat{\mathbf{u}}_{p\tau}^{k-1}, \boldsymbol{\lambda}_{p\tau s}^{k-1})(\delta\hat{\mathbf{u}}_{p\tau}^k, \delta\boldsymbol{\lambda}_{p\tau s}^k) = -C_\tau(\hat{\mathbf{u}}_{p\tau}^{k-1}, \boldsymbol{\lambda}_{p\tau s}^{k-1}). \quad (5.5)$$

The characteristic function $\chi_{\mathcal{A}}$ in (5.4) separates the nodes $p \in \mathcal{S}$ into the inactive set \mathcal{I}_τ^k and the active set \mathcal{A}_τ^k according to

$$\mathcal{I}_\tau^k := \{p \in \mathcal{S} : \|\boldsymbol{\lambda}_{p\tau s}^{k-1} + c\hat{\mathbf{u}}_{p\tau}^{k-1}\| - b_p \leq 0\}, \quad (5.6a)$$

$$\mathcal{A}_\tau^k := \{p \in \mathcal{S} : \|\boldsymbol{\lambda}_{p\tau s}^{k-1} + c\hat{\mathbf{u}}_{p\tau}^{k-1}\| - b_p > 0\}, \quad (5.6b)$$

Using this notation and substituting (5.4) in (5.5) gives after a straightforward computation that the new iterate $(\hat{\mathbf{u}}_{p\tau}^k, \boldsymbol{\lambda}_{p\tau s}^k)$ satisfies

$$\hat{\mathbf{u}}_{p\tau}^k = \mathbf{0}, \quad p \in \mathcal{I}_\tau^k, \quad (5.7a)$$

$$(\text{Id}_{d-1} - M_p^{k-1}) \boldsymbol{\lambda}_{p\tau s}^k - cM_p^{k-1} \hat{\mathbf{u}}_{p\tau}^k = \mathbf{h}_p^{k-1}, \quad p \in \mathcal{A}_\tau^k, \quad (5.7b)$$

with $M_p^{k-1} := e_p^{k-1}(\text{Id}_{d-1} - F_p^{k-1})$, the scalar value e_p^{k-1} and the $(d-1) \times (d-1)$ -matrix F_p^{k-1} given by

$$e_p^{k-1} := \frac{b_p}{\|\boldsymbol{\lambda}_{p\tau s}^{k-1} + c\hat{\mathbf{u}}_{p\tau}^{k-1}\|}, \quad F_p^{k-1} := \frac{\boldsymbol{\lambda}_{p\tau s}^{k-1} (\boldsymbol{\lambda}_{p\tau s}^{k-1} + c\hat{\mathbf{u}}_{p\tau}^{k-1})^\top}{b_p \|\boldsymbol{\lambda}_{p\tau s}^{k-1} + c\hat{\mathbf{u}}_{p\tau}^{k-1}\|}, \quad (5.8)$$

and the vector $\mathbf{h}_p^{k-1} \in \mathbb{R}^{d-1}$

$$\mathbf{h}_p^{k-1} := e_p^{k-1} F_p^{k-1} (\boldsymbol{\lambda}_{p\tau s}^{k-1} + c\hat{\mathbf{u}}_{p\tau}^{k-1}). \quad (5.9)$$

While on the inactive set \mathcal{I}_τ^k Dirichlet conditions are imposed due to (5.7a), the condition on the active set \mathcal{A}_τ^k stated in (5.7b) is of Robin type since it involves both the displacement $\hat{\mathbf{u}}_{p\tau}^k$ and the Lagrange multiplier $\boldsymbol{\lambda}_{p\tau s}^k$. The sets \mathcal{A}_τ^k and \mathcal{I}_τ^k approximate the sets of slip and sticky nodes, respectively. The Robin condition can easily be handled if we rewrite (5.7b) as

$$-\boldsymbol{\lambda}_{p\tau s}^k + L_p^{k-1} \hat{\mathbf{u}}_{p\tau}^k = \mathbf{r}_p^{k-1}. \quad (5.10)$$

We note that \mathbf{r}_p^{k-1} enters in the right hand side and the matrix L_p^{k-1} gives a contribution to the matrix of the system. Comparing (5.10) with (5.7b) and (5.9), and assuming that $\text{Id}_{d-1} - M_p^{k-1}$ is regular, and we obtain the relations

$$L_p^{k-1} := c(\text{Id}_{d-1} - M_p^{k-1})^{-1} M_p^{k-1} = c((\text{Id}_{d-1} - M_p^{k-1})^{-1} - \text{Id}_{d-1}), \quad (5.11a)$$

$$\mathbf{r}_p^{k-1} := -(\text{Id}_{d-1} - M_p^{k-1})^{-1} \mathbf{h}_p^{k-1}. \quad (5.11b)$$

This Robin condition only guarantees positive definiteness of the system matrix if L_p^{k-1} is positive definite. Note that for $L_p^{k-1} = 0$, we find a pure Neumann condition. The degeneration of Robin to Dirichlet boundary conditions is not included in the form (5.11), but this is not required in our situation, since nodes p with a Dirichlet condition belong to the set \mathcal{I}_τ^k and therefore are not handled by (5.10). One can easily see that during the iteration process the matrix $\text{Id}_{d-1} - M_p^{k-1}$ is not necessary regular and therefore not invertible. However, in the case of convergence, $\text{Id}_{d-1} - M_p^{k-1}$ tends to a positive definite and symmetric matrix. This observation motivates the introduction of three possible modifications of the Robin system (5.7b) such that a regular matrix $\text{Id}_{d-1} - M_p^{k-1}$ is obtained. Two of these modifications give a positive definite and symmetric matrix L_p^{k-1} . We remark that all modifications converge in the limit case to the original system (5.7b) and thus preserve the local convergence properties of the algorithm.

Remark 5.2. From (5.9), we observe the relation $\mathbf{h}_p^{k-1} = \boldsymbol{\lambda}_p^{k-1}$. Inserting this result into (5.11b) one ends up with

$$\mathbf{r}_p^{k-1} = \frac{-\|\boldsymbol{\lambda}_{p\tau s}^{k-1} + c_\tau \hat{\mathbf{u}}_{p\tau}^{k-1}\|^2}{\|\boldsymbol{\lambda}_{p\tau s}^{k-1} + c_\tau \hat{\mathbf{u}}_{p\tau}^{k-1}\|^2 - g\|\boldsymbol{\lambda}_{p\tau s}^{k-1} + c_\tau \hat{\mathbf{u}}_{p\tau}^{k-1}\| + (\boldsymbol{\lambda}_{p\tau s}^{k-1} + c_\tau \hat{\mathbf{u}}_{p\tau}^{k-1})^\top \boldsymbol{\lambda}_p^{k-1}} \boldsymbol{\lambda}_p^{k-1}$$

and therefore the vector \mathbf{r}_p^{k-1} is linearly dependent to $\boldsymbol{\lambda}_p^{k-1}$.

5.1.1. Modification of the Robin system

To obtain a robust and convergent scheme, we replace the matrix F_p^{k-1} by a scaled matrix $\tilde{F}_{p,l}^{k-1}$, $l = 1, 2, 3$. The index l stands for one of the three possibilities considered in this work. Our numerical results show that the scaling is essential for the robustness of the iteration scheme. According to the definition of M_p^{k-1} and (5.9), we replace in (5.7b) M_p^{k-1} by $\tilde{M}_{p,l}^{k-1}$ and \mathbf{h}_p^{k-1} by $\tilde{\mathbf{h}}_{p,l}^{k-1}$ given by

$$\tilde{M}_{p,l}^{k-1} := e_p^{k-1}(\text{Id}_2 - \tilde{F}_{p,l}^{k-1}), \quad \tilde{\mathbf{h}}_{p,l}^{k-1} := e_p^{k-1} \tilde{F}_{p,l}^{k-1} (\boldsymbol{\lambda}_{\tau,p,s}^{k-1} + c_\tau \hat{\mathbf{u}}_{\tau,p}^{k-1}), \quad l = 1, 2, 3.$$

In a second step, we replace the matrix $\text{Id}_{d-1} - M_p^{k-1}$ by $\text{Id}_{d-1} - \beta_{p,l}^{k-1} \tilde{M}_{p,l}^{k-1}$ with a scaling factor $\beta_{p,l}^{k-1} > 0$, such that the resulting matrix is regular. Then, the form (5.10) of the Robin boundary conditions reads as $-\boldsymbol{\lambda}_{\tau,p,s}^k + \tilde{L}_{p,l}^{k-1} \hat{\mathbf{u}}_{\tau,p}^k = \tilde{\mathbf{r}}_{p,l}^{k-1}$ with

$$\tilde{L}_{p,l}^{k-1} := c((\text{Id}_{d-1} - \beta_{p,l}^{k-1} \tilde{M}_{p,l}^{k-1})^{-1} - \text{Id}_{d-1}), \quad (5.12a)$$

$$\tilde{\mathbf{r}}_{p,l}^{k-1} := -(\text{Id}_{d-1} - \beta_{p,l}^{k-1} \tilde{M}_{p,l}^{k-1})^{-1} \tilde{\mathbf{h}}_{p,l}^{k-1}, \quad (5.12b)$$

for $l = 1, 2, 3$. We mention that similar modifications as done for the matrix F_p^{k-1} are used in primal-dual algorithms for the minimization of functionals involving Euclidean norms, see, e.g., [4, 22, 77].

Since for all modifications $\tilde{F}_{p,l}^{k-1} \rightarrow F_p^{k-1}$ and $\beta_{p,l}^{k-1} \rightarrow 1$ as $(\hat{\mathbf{u}}_{p\tau}^k, \boldsymbol{\lambda}_{p\tau s}^k)$ converges to the solution, the modifications do not degrade the local superlinear convergence.

Next, we present the three possible modifications used in this thesis.

First modification

We use a parameter $\beta_{p,1}^{k-1} \neq 1$ in $\text{Id}_{d-1} - \beta_{p,1}^{k-1} M_p$ in (5.12) only if $(\boldsymbol{\lambda}_{p\tau s}^{k-1})^\top (\boldsymbol{\lambda}_{p\tau s}^{k-1} + c\hat{\mathbf{u}}_{p\tau}^{k-1}) < 0$. This condition is equivalent to the fact that the angle between the two vectors is greater than 90 degree. Since in the limit case both vectors are parallel, the modification only applies when the iterates are far away from the solution. We define the scaled matrix

$$\tilde{F}_{p,1}^{k-1} := \frac{\boldsymbol{\lambda}_{p\tau s}^{k-1} (\boldsymbol{\lambda}_{p\tau s}^{k-1} + c\hat{\mathbf{u}}_{p\tau}^{k-1})^\top}{\max(b_p, \|\boldsymbol{\lambda}_{p\tau s}^{k-1}\|) \|\boldsymbol{\lambda}_{p\tau s}^{k-1} + c\hat{\mathbf{u}}_{p\tau}^{k-1}\|}. \quad (5.13)$$

Note that $\tilde{F}_{p,1}^{k-1}$ only differs from F_p^{k-1} if $\|\boldsymbol{\lambda}_{p\tau s}^{k-1}\| > b_p$, i.e., if the Lagrange multiplier is not in the feasible set given in (5.1). Defining

$$\alpha_p^{k-1} := \frac{(\boldsymbol{\lambda}_{p\tau s}^{k-1})^\top (\boldsymbol{\lambda}_{p\tau s}^{k-1} + c\hat{\mathbf{u}}_{p\tau}^{k-1})}{\|\boldsymbol{\lambda}_{p\tau s}^{k-1}\| \|\boldsymbol{\lambda}_{p\tau s}^{k-1} + c\hat{\mathbf{u}}_{p\tau}^{k-1}\|}, \quad \delta_p^{k-1} := \min \left\{ \frac{\|\boldsymbol{\lambda}_{p\tau s}^{k-1}\|}{b_p}, 1 \right\},$$

it is easy to see that $\gamma_{\tilde{F}_{p,1}}^1 = \alpha_p^{k-1} \delta_p^{k-1}$ is an eigenvalue of $\tilde{F}_{p,1}^{k-1}$ with $\boldsymbol{\lambda}_{p\tau s}^{k-1}$ as eigenvector. The second eigenvalue $\gamma_{\tilde{F}_{p,1}}^2 = 0$ belongs to an eigenvector which is orthogonal to $\boldsymbol{\lambda}_{p\tau s}^{k-1} + c\hat{\mathbf{u}}_{p\tau}^{k-1}$. Therefore, the eigenvalues of $\tilde{M}_{p,1}^{k-1}$ are $\gamma_{\tilde{M}_{p,1}}^1 = e_p^{k-1} (1 - \alpha_p^{k-1} \delta_p^{k-1})$ and $\gamma_{\tilde{M}_{p,1}}^2 = e_p^{k-1}$. Since $-1 \leq \alpha_p^{k-1} \leq 1$ and $0 \leq \delta_p^{k-1} \leq 1$, we get due to $0 < e_p^{k-1} < 1$ the relation $0 \leq \gamma_{\tilde{M}_{p,1}}^1 < 2$ and $0 < \gamma_{\tilde{M}_{p,1}}^2 < 1$. Using (5.12) with

$$\beta_{p,1}^{k-1} := \begin{cases} \frac{1}{1 - \alpha_p^{k-1} \delta_p^{k-1}} & \text{if } \alpha_p^{k-1} < 0, \\ 1 & \text{otherwise.} \end{cases}$$

yields a unsymmetric matrix $\tilde{L}_{p,1}^{k-1}$ with positive eigenvalues.

Second modification

In contrast to the first modification, we want to obtain a symmetric matrix $\tilde{F}_{p,2}^{k-1}$. Here, we need a parameter $\beta_{p,2}^{k-1} \neq 1$ in (5.12) for all cases with $\alpha_p^{k-1} \neq 1$. We replace F_p^{k-1} by the symmetrization of (5.13), namely

$$\tilde{F}_{p,2}^{k-1} := \frac{\boldsymbol{\lambda}_{p\tau s}^{k-1} (\boldsymbol{\lambda}_{p\tau s}^{k-1} + c\hat{\mathbf{u}}_{p\tau}^{k-1})^\top + (\boldsymbol{\lambda}_{p\tau s}^{k-1} + c\hat{\mathbf{u}}_{p\tau}^{k-1}) (\boldsymbol{\lambda}_{p\tau s}^{k-1})^\top}{2 \max(b_p, \|\boldsymbol{\lambda}_{p\tau s}^{k-1}\|) \|\boldsymbol{\lambda}_{p\tau s}^{k-1} + c\hat{\mathbf{u}}_{p\tau}^{k-1}\|}. \quad (5.14)$$

One can prove that the eigenvalues of $\tilde{F}_{p,2}^{k-1}$ are $\gamma_{\tilde{F}_{p,2}}^{1,2} = \frac{1}{2}(\alpha_p^{k-1} \pm 1)\delta_p^{k-1} \in [-1, 1]$, and therefore the eigenvalues of the matrix $\tilde{M}_{p,2}^{k-1}$ are $\gamma_{\tilde{M}_{p,2}}^{1,2} = \frac{1}{2}e_p^{k-1}(2 - (\alpha_p^{k-1} \pm 1)\delta_p^{k-1})$. Using the same arguments as before, we get $0 \leq \gamma_{\tilde{M}_{p,2}}^{1,2} < 2$. Setting

$$\beta_{p,2}^{k-1} := \frac{2}{2 - (\alpha_p^{k-1} - 1)\delta_p^{k-1}}$$

results in a symmetric and positive definite matrix $\tilde{L}_{p,2}^{k-1}$.

Third modification

In the third modification, we use the matrix

$$\tilde{F}_{p,3}^{k-1} := \frac{\boldsymbol{\lambda}_{p\tau s}^{k-1} (\boldsymbol{\lambda}_{p\tau s}^{k-1})^\top}{\max(b_p, \|\boldsymbol{\lambda}_{p\tau s}^{k-1}\|)^2} \quad (5.15)$$

instead of F_p^{k-1} . Obviously, this matrix is symmetric and positive semidefinite with the eigenvalues $\gamma_{\tilde{F}_{p,3}}^1 = 0$ and $\gamma_{\tilde{F}_{p,3}}^2 = (\delta_p^{k-1})^2$. Therefore, we get for the eigenvalues of the matrix $\tilde{M}_{p,3}^{k-1}$ due to $0 < e_p^{k-1} < 1$ the relation $0 \leq \gamma_{\tilde{M}_{p,3}} < 1$, and the matrix $\tilde{L}_{p,3}^{k-1}$ defined by (5.12) with $\beta_{p,3}^{k-1} = 1$ is symmetric and positive definite. We remark that the matrix $\tilde{F}_{p,3}^{k-1}$ converges in the limit case to the matrix F_p^{k-1} since the solution for a node $p \in \mathcal{A}_\tau$ satisfies

$$\frac{\boldsymbol{\lambda}_{p\tau s} + c\hat{\mathbf{u}}_{p\tau}}{\|\boldsymbol{\lambda}_{p\tau s} + c\hat{\mathbf{u}}_{p\tau}\|} = \frac{\boldsymbol{\lambda}_{p\tau s}}{b_p}.$$

Remark 5.3. Similar to Remark 5.2, we observe that $\tilde{\mathbf{h}}_{p,l}^{k-1}$ and $\tilde{\mathbf{r}}_{p,l}^{k-1}$ are linearly dependent to $\boldsymbol{\lambda}_p^{k-1}$ for the first and the third modification as for the unmodified case (5.9) and (5.11b).

Remark 5.4. There is some freedom in choosing the nonlinear complementarity function to express the complementarity conditions for the Tresca friction law. For $b_p > 0$, we can also work with

$$\bar{C}_\tau(\hat{\mathbf{u}}_{p\tau}, \boldsymbol{\lambda}_{p\tau s}) := \boldsymbol{\lambda}_{p\tau s} - b_p \frac{(\boldsymbol{\lambda}_{p\tau s} + c\hat{\mathbf{u}}_{p\tau})}{\max\{b_p, \|\boldsymbol{\lambda}_{p\tau s} + c\hat{\mathbf{u}}_{p\tau}\|\}} \quad (5.16)$$

instead of (5.2). Complementarity functions closely related to (5.16) for dealing with friction conditions have been used in [3] obtained from a modified augmented Lagrangian approach and in [27, 28] where the nonlinear complementarity function is expressed in terms of the min-function instead of the max-function. A semi-smooth Newton iteration for the solution of $\bar{C}_\tau(\hat{\mathbf{u}}_{p\tau}, \boldsymbol{\lambda}_{p\tau s}) = \mathbf{0}$ leads to an iteration rule that also employs the active and inactive sets defined in (5.6), but results in a modified iteration step on the active set \mathcal{A}_τ^k . Our numerical experience yields that algorithms based on (5.2) perform more robust compared to those based on (5.16).

5.1.2. Extension to the case $b_p = 0$

Up to now, we have assumed $b_p > 0$ for all $p \in \mathcal{S}$. The reason for this assumption is that for $b_p = 0$ one cannot deduce $\boldsymbol{\lambda}_{p\tau s} = \mathbf{0}$ from the condition $C_\tau(\hat{\mathbf{u}}_{p\tau}, \boldsymbol{\lambda}_{p\tau s}) = \mathbf{0}$. However, if Tresca's friction law is combined with fixed point ideas in order to model contact problems with Coulomb's friction law, we have to set $b_p = \mathfrak{F}\lambda_{pns}$ and thus $b_p = 0$ naturally occurs for all points which are not in contact. This fact makes the case $b_p = 0$ rather important. Fortunately, nodes p with $b_p = 0$ can also be handled using (5.7) within the setting (5.13)-(5.15).

In the following, we consider $p \in \mathcal{S}$ with $b_p = 0$. If $\|\boldsymbol{\lambda}_{p\tau s}^{k-1} + c\hat{\mathbf{u}}_{p\tau}^{k-1}\| > 0$ holds, then $p \in \mathcal{A}_\tau^k$ since $b_p = 0$. In the case $\|\boldsymbol{\lambda}_{p\tau s}^{k-1} + c\hat{\mathbf{u}}_{p\tau}^{k-1}\| = 0$, we have to set $p \in \mathcal{A}_\tau^k$. In both cases, we set $\tilde{M}_{p,l}^{k-1} = 0$ and (5.7b) leads to the desired homogeneous Neumann condition $\boldsymbol{\lambda}_{p\tau s}^k = \mathbf{0}$. We mention that for $\|\boldsymbol{\lambda}_{p\tau s}^{k-1} + c\hat{\mathbf{u}}_{p\tau}^{k-1}\| > 0$ and $\|\boldsymbol{\lambda}_{p\tau s}^{k-1}\| > 0$, we automatically get $p \in \mathcal{A}_\tau^k$ and $e_p^{k-1} = 0$ due to (5.6b) and (5.8) and therefore $\tilde{M}_{p,l}^{k-1} = 0$. In particular, these matrices are well defined for this case. So only for the cases $\|\boldsymbol{\lambda}_{p\tau s}^{k-1} + c\hat{\mathbf{u}}_{p\tau}^{k-1}\| = 0$ or $\|\boldsymbol{\lambda}_{p\tau s}^{k-1}\| = 0$, we have to enforce the node p to be in \mathcal{A}_τ^k .

5.2. Elimination of the Lagrange multiplier

As in Section 4.3, we give the algebraic representation of the linear system which has to be solved in each semi-smooth Newton step in the case of a frictional contact problem. Combining this approach for the frictional constraints in tangential direction with the method for the contact constraints in normal direction presented in Chapter 4, the linear system stated in (4.11) has now to be replaced by

$$\hat{\mathbf{K}}\hat{\mathbf{u}}^k + \hat{\mathbf{C}}\boldsymbol{\lambda}^k = \hat{\mathbf{f}}, \quad (5.17a)$$

$$\hat{u}_{pn}^k = g_p, \quad p \in \mathcal{A}_n^k, \quad (5.17b)$$

$$\lambda_{pns}^k = 0, \quad p \in \mathcal{I}_n^k, \quad (5.17c)$$

$$\hat{\mathbf{u}}_{p\tau}^k = \mathbf{0}, \quad p \in \mathcal{I}_\tau^k, \quad (5.17d)$$

$$-\boldsymbol{\lambda}_{p\tau s}^k + \tilde{L}_p^{k-1}\hat{\mathbf{u}}_{p\tau}^k = \tilde{\mathbf{r}}_p^{k-1}, \quad p \in \mathcal{A}_\tau^k. \quad (5.17e)$$

Equations (5.17) can be interpreted as a semi-smooth Newton method for the nonlinear complementarity function $C(\cdot, \cdot)$ defined by the combination of the complementarity functions $C_n(\cdot, \cdot)$, see (4.5), and $C_\tau(\cdot, \cdot)$, see (5.2), as

$$C(\hat{\mathbf{u}}_p, \boldsymbol{\lambda}_p) := \begin{pmatrix} C_n(\hat{u}_{pn}, \lambda_{pns}) \\ C_\tau(\hat{\mathbf{u}}_{p\tau}, \boldsymbol{\lambda}_{p\tau s}) \end{pmatrix}. \quad (5.18)$$

Summarizing Theorems 4.1 and 5.1, we observe that then the contact constraints are equivalent to the condition $C(\hat{\mathbf{u}}_p, \boldsymbol{\lambda}_p) = \mathbf{0}$. Each possible contact node $p \in \mathcal{S}$ belongs in each iteration step to one of the four subsets $\mathcal{S}_i^k \subset \mathcal{S}$, $1 \leq i \leq 4$, with $\mathcal{S} = \bigcup_{1 \leq i \leq 4} \mathcal{S}_i^k$, where the disjoint subsets \mathcal{S}_i^k are given by

Table 5.1.: Boundary conditions for the contact nodes $p \in \mathcal{S}$.

old iterate	\mathcal{S}_1^k	\mathcal{S}_2^k	\mathcal{S}_3^k	\mathcal{S}_4^k	new iterate
$\lambda_{pns}^{k-1} + c(\hat{u}_{pn}^{k-1} - g_p) \leq 0$	•	•			$\lambda_{pns}^k = 0$
$\lambda_{pns}^{k-1} + c(\hat{u}_{pn}^{k-1} - g_p) > 0$			•	•	$\hat{u}_{pn}^k = g_p$
$\ \boldsymbol{\lambda}_{p\tau s}^{k-1} + c\hat{\mathbf{u}}_{p\tau}^{k-1}\ - b_p \leq 0$	•		•		$\hat{\mathbf{u}}_{p\tau}^k = \mathbf{0}$
$\ \boldsymbol{\lambda}_{p\tau s}^{k-1} + c\hat{\mathbf{u}}_{p\tau}^{k-1}\ - b_p > 0$		•		•	$-\boldsymbol{\lambda}_{p\tau s}^k + \tilde{L}_{p,l}^{k-1}\hat{\mathbf{u}}_{p\tau}^k = \tilde{\mathbf{r}}_{p,l}^{k-1}$

- $\mathcal{S}_1^k := \mathcal{I}_n^k \cap \mathcal{I}_\tau^k$: sticky node not in contact,
- $\mathcal{S}_2^k := \mathcal{I}_n^k \cap \mathcal{A}_\tau^k$: slip node not in contact,
- $\mathcal{S}_3^k := \mathcal{A}_n^k \cap \mathcal{I}_\tau^k$: sticky node in contact,
- $\mathcal{S}_4^k := \mathcal{A}_n^k \cap \mathcal{A}_\tau^k$: slip node in contact.

The criteria for the old iterate $(\hat{\mathbf{u}}_p^{k-1}, \boldsymbol{\lambda}_p^{k-1})$ which assigns the node $p \in \mathcal{S}$ to the correct subset and the boundary condition for the new iterate $(\hat{\mathbf{u}}_p^k, \boldsymbol{\lambda}_p^k)$ are illustrated in Table 5.1. Using Tresca's friction law, nodes can stick in tangential direction without being in contact with the obstacle. These nodes belong to the set \mathcal{S}_1^k .

To formulate the reduced linear system, we summarize the nodes in the sets \mathcal{N} and \mathcal{M} in the set $\tilde{\mathcal{N}} := \mathcal{N} \cup \mathcal{M}$ and define the matrix $\mathbf{L}_{\mathcal{S}_i^k}$ and the vector $\mathbf{r}_{\mathcal{S}_i^k}$ via

$$\mathbf{L}_{\mathcal{S}_i^k} := \text{diag}\{\tilde{L}_{p,l}^{k-1}\}_{p \in \mathcal{S}_i^k} \in \mathbb{R}^{(d-1)|\mathcal{S}_i^k| \times (d-1)|\mathcal{S}_i^k|},$$

$$\mathbf{r}_{\mathcal{S}_i^k} := \{\tilde{\mathbf{r}}_{p,l}^{k-1}\}_{p \in \mathcal{S}_i^k} \in \mathbb{R}^{(d-1)|\mathcal{S}_i^k|}.$$

After eliminating the Lagrange multiplier $\boldsymbol{\lambda}^k$, the system (5.17) can be written as

$$\mathbf{A}_{SSN}^k \hat{\mathbf{u}}^k = \mathbf{f}_{SSN}^k. \quad (5.19)$$

To give the definition of the matrix \mathbf{A}_{SSN}^k and the right hand side \mathbf{f}_{SSN}^k , we use the decomposition of the coefficient vector for the displacement $\hat{\mathbf{u}}^k$ according to the subsets of \mathcal{S} and obtain

$$\hat{\mathbf{u}}^k = \begin{pmatrix} \hat{\mathbf{u}}_{\tilde{\mathcal{N}}}^k \\ \hat{\mathbf{u}}_{\mathcal{S}_1^k}^k \\ \hat{\mathbf{u}}_{\mathcal{S}_2^k}^k \\ \hat{\mathbf{u}}_{\mathcal{S}_3^k}^k \\ \hat{\mathbf{u}}_{\mathcal{S}_4^k}^k \end{pmatrix}, \quad \mathbf{f}_{SSN}^k := \begin{pmatrix} \hat{\mathbf{f}}_{\tilde{\mathcal{N}}} \\ \mathbf{N}_{\mathcal{S}_1^k} \hat{\mathbf{f}}_{\mathcal{S}_1^k}^k \\ \mathbf{N}_{\mathcal{S}_2^k} \hat{\mathbf{f}}_{\mathcal{S}_2^k}^k \\ \mathbf{g}_{\mathcal{S}_3^k} \\ \mathbf{g}_{\mathcal{S}_4^k} \\ \mathbf{0} \\ \mathbf{T}_{\mathcal{S}_2^k} \hat{\mathbf{f}}_{\mathcal{S}_2^k}^k + \mathbf{r}_{\mathcal{S}_2^k}^k \\ \mathbf{0} \\ \mathbf{T}_{\mathcal{S}_4^k} \hat{\mathbf{f}}_{\mathcal{S}_4^k}^k + \mathbf{r}_{\mathcal{S}_4^k}^k \end{pmatrix}.$$

The system matrix \mathbf{A}_{SSN}^k is given by $\mathbf{A}_{SSN}^k :=$

$$\begin{pmatrix} \hat{\mathbf{K}}_{\tilde{\mathcal{N}}\tilde{\mathcal{N}}} & \hat{\mathbf{K}}_{\tilde{\mathcal{N}}\mathcal{S}_1^k} & \hat{\mathbf{K}}_{\tilde{\mathcal{N}}\mathcal{S}_2^k} & \hat{\mathbf{K}}_{\tilde{\mathcal{N}}\mathcal{S}_3^k} & \hat{\mathbf{K}}_{\tilde{\mathcal{N}}\mathcal{S}_4^k} \\ \mathbf{N}_{\mathcal{S}_1^k} \hat{\mathbf{K}}_{\mathcal{S}_1^k \tilde{\mathcal{N}}} & \mathbf{N}_{\mathcal{S}_1^k} \hat{\mathbf{K}}_{\mathcal{S}_1^k \mathcal{S}_1^k} & \mathbf{N}_{\mathcal{S}_1^k} \hat{\mathbf{K}}_{\mathcal{S}_1^k \mathcal{S}_2^k} & \mathbf{N}_{\mathcal{S}_1^k} \hat{\mathbf{K}}_{\mathcal{S}_1^k \mathcal{S}_3^k} & \mathbf{N}_{\mathcal{S}_1^k} \hat{\mathbf{K}}_{\mathcal{S}_1^k \mathcal{S}_4^k} \\ \mathbf{N}_{\mathcal{S}_2^k} \hat{\mathbf{K}}_{\mathcal{S}_2^k \tilde{\mathcal{N}}} & \mathbf{N}_{\mathcal{S}_2^k} \hat{\mathbf{K}}_{\mathcal{S}_2^k \mathcal{S}_1^k} & \mathbf{N}_{\mathcal{S}_2^k} \hat{\mathbf{K}}_{\mathcal{S}_2^k \mathcal{S}_2^k} & \mathbf{N}_{\mathcal{S}_2^k} \hat{\mathbf{K}}_{\mathcal{S}_2^k \mathcal{S}_3^k} & \mathbf{N}_{\mathcal{S}_2^k} \hat{\mathbf{K}}_{\mathcal{S}_2^k \mathcal{S}_4^k} \\ \mathbf{0} & \mathbf{0} & \mathbf{0} & \mathbf{N}_{\mathcal{S}_3^k} & \mathbf{0} \\ \mathbf{0} & \mathbf{0} & \mathbf{0} & \mathbf{0} & \mathbf{N}_{\mathcal{S}_4^k} \\ \mathbf{0} & \mathbf{T}_{\mathcal{S}_1^k} & \mathbf{0} & \mathbf{0} & \mathbf{0} \\ \mathbf{T}_{\mathcal{S}_2^k} \hat{\mathbf{K}}_{\mathcal{S}_2^k \tilde{\mathcal{N}}} & \mathbf{T}_{\mathcal{S}_2^k} \hat{\mathbf{K}}_{\mathcal{S}_2^k \mathcal{S}_1^k} & \mathbf{T}_{\mathcal{S}_2^k} \hat{\mathbf{K}}_{\mathcal{S}_2^k \mathcal{S}_2^k} + \mathbf{L}_{\mathcal{S}_2^k} \mathbf{T}_{\mathcal{S}_2^k} & \mathbf{T}_{\mathcal{S}_2^k} \hat{\mathbf{K}}_{\mathcal{S}_2^k \mathcal{S}_3^k} & \mathbf{T}_{\mathcal{S}_2^k} \hat{\mathbf{K}}_{\mathcal{S}_2^k \mathcal{S}_4^k} \\ \mathbf{0} & \mathbf{0} & \mathbf{0} & \mathbf{T}_{\mathcal{S}_3^k} & \mathbf{0} \\ \mathbf{T}_{\mathcal{S}_4^k} \hat{\mathbf{K}}_{\mathcal{S}_4^k \tilde{\mathcal{N}}} & \mathbf{T}_{\mathcal{S}_4^k} \hat{\mathbf{K}}_{\mathcal{S}_4^k \mathcal{S}_1^k} & \mathbf{T}_{\mathcal{S}_4^k} \hat{\mathbf{K}}_{\mathcal{S}_4^k \mathcal{S}_2^k} & \mathbf{T}_{\mathcal{S}_4^k} \hat{\mathbf{K}}_{\mathcal{S}_4^k \mathcal{S}_3^k} & \mathbf{T}_{\mathcal{S}_4^k} \hat{\mathbf{K}}_{\mathcal{S}_4^k \mathcal{S}_4^k} + \mathbf{L}_{\mathcal{S}_4^k} \mathbf{T}_{\mathcal{S}_4^k} \end{pmatrix},$$

where the matrices \mathbf{N}_* and \mathbf{T}_* are the same as introduced in Section 4.3 with respect to the nodes in the subset of \mathcal{S} indicated by the subscript. This linear system is a regular one although the number of lines seems to be larger than the number of unknowns. Formally, lines 2 and 6 are one line belonging to the nodes in \mathcal{S}_1^k , lines 3 and 7 are one line belonging to all nodes in \mathcal{S}_2^k , lines 4 and 8 are one line belonging to all nodes in \mathcal{S}_3^k and lines 5 and 9 are one line belonging to all nodes in \mathcal{S}_4^k . The second and the third line in (5.19) contain the normal part for all nodes $p \in \mathcal{S}_1^k$ and $p \in \mathcal{S}_2^k$, respectively, not being in contact. The stick condition $\hat{\mathbf{u}}_{p\tau}^k$ for the nodes $p \in \mathcal{S}_1^k$, i.e. nodes not in contact, is enforced by the sixth line and for the nodes $p \in \mathcal{S}_3^k$, i.e. nodes in contact, by the eighth line. Lines 4 and 5 contain the non-penetration condition $\hat{u}_{pn}^k = g_p$ for the sticky nodes $p \in \mathcal{S}_3^k$ and for the slip nodes $p \in \mathcal{S}_4^k$, respectively. The Robin type boundary condition for the nodes $p \in \mathcal{S}_2^k$, being active in tangential direction and not in contact is formulated in line 7 and for the nodes $p \in \mathcal{S}_4^k$ being active in tangential direction and in contact in the last line.

Due to the use of dual shape functions for the Lagrange multiplier, the elimination of the Lagrange multiplier $\boldsymbol{\lambda}^k$ from (5.17) is possible without solving a linear system. The linear system (5.19) can efficiently be obtained by a local modification of the original stiffness matrix $\hat{\mathbf{K}}$. The eliminated Lagrange multiplier $\boldsymbol{\lambda}^k$ can then be calculated using (4.13).

5.3. Inexact semi-smooth Newton method

Similar to the linear system (4.14), the conditions for the new iterate stated in (5.17) are again boundary conditions which can be easily inserted into existing finite element codes. Again, we solve the linear system (5.19) not exactly, but apply only m multigrid steps of an efficient multigrid method. Like in (4.15), we denote by

$$\hat{\mathbf{u}}^{k,i} = \text{MG}(\hat{\mathbf{u}}^{k,i-1}, \mathcal{A}_n^k, \mathcal{I}_n^k, \mathcal{A}_\tau^k, \mathcal{I}_\tau^k, \boldsymbol{\lambda}^{k-1})$$

one iteration step of the linear multigrid solver for the linear system (5.19). Then, we can formulate our inexact semi-smooth Newton method, see Algorithm 2.

Algorithm 2 (Inexact) semi-smooth Newton method

- 1: set $k = 1$
- 2: initialize $\hat{\mathbf{u}}^{0,0}$ and $\boldsymbol{\lambda}^0$ as an initial solution
- 3: set $c > 0$, $m \in \mathbb{N}$ and the tolerance ε_u
- 4: define the active and the inactive sets

$$\begin{aligned} \mathcal{A}_n^k &:= \{p \in \mathcal{S} : \lambda_{pns}^{k-1} + c(\hat{u}_{pn}^{k-1,m} - g_p) > 0\} \\ \mathcal{I}_n^k &:= \{p \in \mathcal{S} : \lambda_{pns}^{k-1} + c(\hat{u}_{pn}^{k-1,m} - g_p) \leq 0\} \\ \mathcal{A}_\tau^k &:= \{p \in \mathcal{S} : \|\lambda_{p\tau s}^{k-1} + c\hat{\mathbf{u}}_{p\tau}^{k-1,m}\| - b_p > 0\} \\ \mathcal{I}_\tau^k &:= \{p \in \mathcal{S} : \|\lambda_{p\tau s}^{k-1} + c\hat{\mathbf{u}}_{p\tau}^{k-1,m}\| - b_p \leq 0\} \end{aligned}$$

- 5: **for** $i = 1, \dots, m$ **do**

- 6:

$$\hat{\mathbf{u}}^{k,i} = \text{MG}(\hat{\mathbf{u}}^{k,i-1}, \mathcal{A}_n^k, \mathcal{I}_n^k, \mathcal{A}_\tau^k, \mathcal{I}_\tau^k, \boldsymbol{\lambda}^{k-1})$$

- 7: **end for**

- 8: **if** $\|\hat{\mathbf{u}}^{k,m} - \hat{\mathbf{u}}^{k,0}\| / \|\hat{\mathbf{u}}^{k,m}\| < \varepsilon_u$ **then**

- 9: stop

- 10: **end if**

- 11: compute the Lagrange multiplier

$$\boldsymbol{\lambda}^k = \mathbf{D}_d^{-1} \left(\hat{\mathbf{f}}_S - \hat{\mathbf{K}}_{SN} \hat{\mathbf{u}}_N^{k,m} - \hat{\mathbf{K}}_{SM} \hat{\mathbf{u}}_M^{k,m} - \hat{\mathbf{K}}_{SS} \hat{\mathbf{u}}_S^{k,m} \right)$$

- 12: set $\hat{\mathbf{u}}^{k+1,0} = \hat{\mathbf{u}}^{k,m}$

- 13: set $k = k + 1$

- 14: go to step 4

As for Algorithm 1, we get the exact version of Algorithm 2 if we solve the linear system (5.19) in step 6-8 exactly, which is referred to by $m = \infty$ in the following. In contrast to Remark 4.2, the parameter c influences the choice of the inactive and active sets \mathcal{I}_τ^k and \mathcal{A}_τ^k in tangential direction not only in the inexact version but also in the exact version. Finally, we mention that in each Newton step, we only have to modify the lines of the original stiffness matrix belonging to the contact nodes as described in (5.19), and thus there is no need to reassemble the whole stiffness matrix $\hat{\mathbf{K}}$ in each iteration step if the part $\hat{\mathbf{K}}_{S^*}$ is stored.

5.4. Numerical studies for Tresca friction

As a first example for a three-dimensional contact problem with Tresca friction, we consider a one-body contact problem. The main purpose is to study the convergence and the performance of Algorithm 2. We consider a linearly elastic cube $\Omega = [0, 1]^3$ with material parameters $E = 200$ and $\nu = 0.3$ and take the x_1x_2 -plane as the rigid

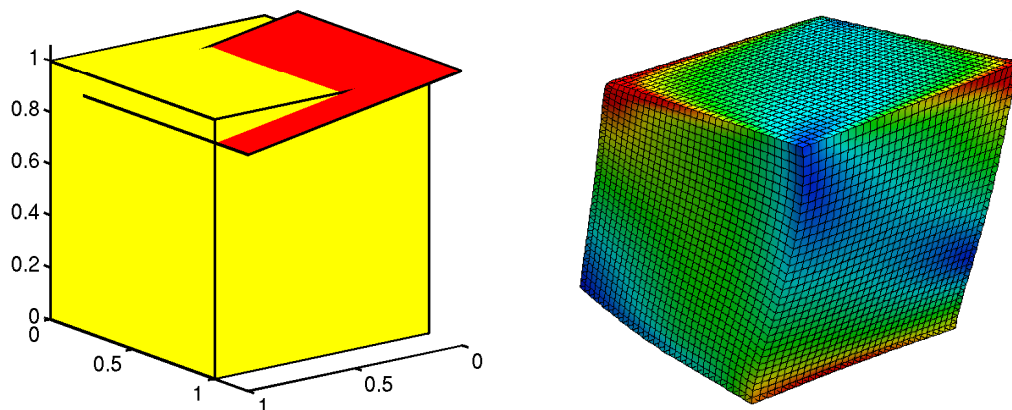


Figure 5.1.: Problem definition with prescribed Dirichlet boundary condition (left) and distorted body with effective von Mises stress σ_{eff} . The lower surface in the plot is subject to contact with Tresca's friction law.

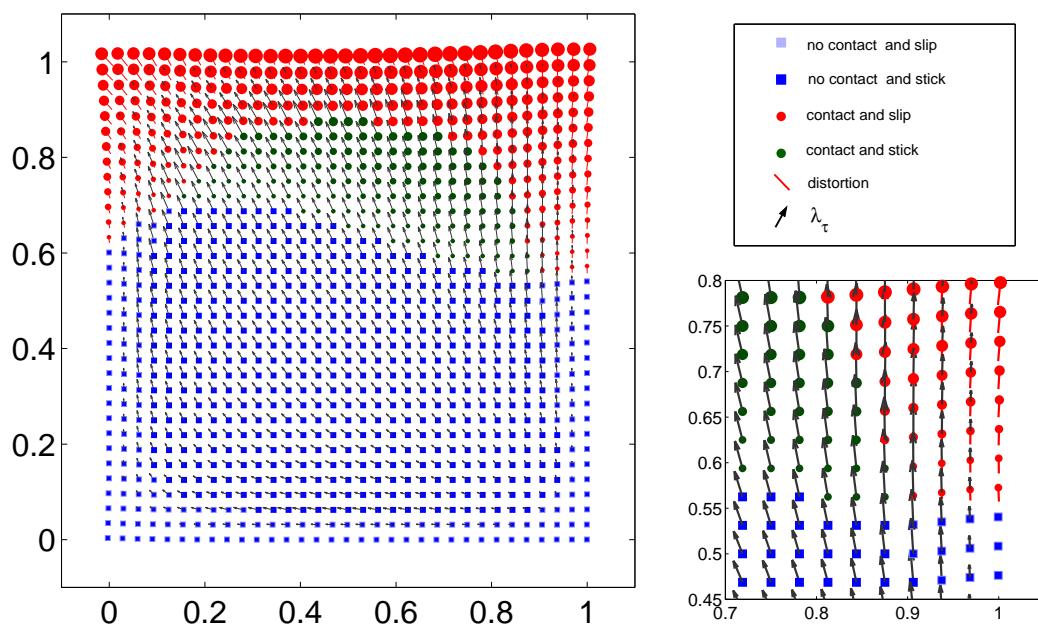


Figure 5.2.: Visualization of the solution at the nodes $p \in \mathcal{S}$ for Tresca's friction law on Level 5 (left), legend (upper right) and cutout (lower right).

obstacle which implies that the initial gap is $g = 0$. The cube is subject to the Dirichlet distortion $\mathbf{u}_D = (0, 0.2, 0.06 - 0.15x_1)^\top$ on its upper surface $[0, 1]^2 \times \{1\}$ as indicated in the left picture in Figure 5.1. For Tresca's friction law, we choose for the friction bound the function $g_f = 800x_1x_2(1 - x_1)(1 - x_2)$. The right picture in Figure 5.1 shows the distorted body with the effective von Mises stress σ_{eff} . To get a better understanding of the different types of nodes that occur for contact problems with Tresca friction, we show

Table 5.2.: Performance of Algorithm 2 for the exact approach ($m = \infty$) for $\mathbf{u}^{0,0} = \mathbf{0}$, $\boldsymbol{\lambda}^0 = \mathbf{0}$ for all levels and $\varepsilon_u = 10^{-9}$ with the modification (5.13).

l	$ \mathcal{A}_n^k / \mathcal{A}_\tau^k $ for $k = 2, 3, 4, 5, 6, 7, 8, 9$							
0	2/0	2/0						
1	6/4	5/8	5/8	5/8	5/8	5/8		
2	15/16	12/16	12/16	12/16	12/16			
3	49/32	38/37	33/39	33/39	33/39	33/39		
4	171/66	132/102	116/118	112/122	112/123	112/123	112/123	
5	651/252	506/357	443/411	412/435	406/444	406/446	406/446	406/446

in Figure 5.2 the nodes of the contact surface on Level 5. Different types of nodes are marked differently, according to the legend in Figure 5.2. We note that for each node the displacement is parallel to the Lagrange multiplier $\boldsymbol{\lambda}_{p\tau}$ as required. To investigate the performance of Algorithm 2, we first concentrate on the exact approach. In each step, our algorithm updates the set of nodes being in contact and being not in contact given by \mathcal{A}_n^k and \mathcal{I}_n^k , respectively, as well as the slip and stick sets \mathcal{A}_τ^k and \mathcal{I}_τ^k and at the same time performs a Newton step to adopt the direction of the distortion $\mathbf{u}_{p\tau}$ to the direction of $\boldsymbol{\lambda}_{p\tau}$ for the slipping nodes. For our tests, we initialize the algorithm on each level with $\mathbf{u}_h^{0,0} = \mathbf{0}$ and $\boldsymbol{\lambda}_h^0 = \mathbf{0}$, leading to $\mathcal{A}_n^1 = \mathcal{A}_\tau^1 = \emptyset$. We terminate the iteration process if the relative change in the solution is less than $\varepsilon_u = 10^{-9}$. In the complementarity function, we use $c = 100$. Algorithm 2 yields a fast and stable convergence on all levels. Table 5.2 shows the number of iterations needed on different refinement levels, and the number of nodes belonging to the active sets \mathcal{A}_n^k and \mathcal{A}_τ^k for the first modification (5.13). We remark that for the second (5.14) and the third modification (5.15) only minor differences occur. Note that in each iteration step one linear system has to be solved. The number of iterations increases only weakly on finer levels. It seems to depend linearly on the level. Usually, after the exact active sets for both friction and contact condition are found, the method requires about 3–4 additional iterations to converge. In these steps, the algorithm adjusts, for $p \in \mathcal{S}$, the direction of the tangential traction $\boldsymbol{\lambda}_{p\tau}$ to the tangential displacement $\hat{\mathbf{u}}_{p\tau}$.

Next, we compare the convergence and the behavior of the factors α_p^{k-1} and $\beta_{p,l}^{k-1}$ for the three modifications (5.13)–(5.15). The left picture in Figure 5.3 shows the errors $\|\boldsymbol{\lambda}_h^k - \boldsymbol{\lambda}_h^*\|_2$ on Level 5 in a logarithmic plot for the initialization $\mathbf{u}^{0,0} = (1, 1, 0)^\top$ and $\boldsymbol{\lambda}^0 = (-1, -1, 0)^\top$. Here, $\boldsymbol{\lambda}_h^*$ denotes the Lagrange multiplier of the solution. Due to the different initialization and the smaller tolerance $\varepsilon_u = 10^{-14}$, additional iteration steps are needed compared to Table 5.2. In the middle picture of Figure 5.3, we present the cosine α_p^{k-1} of the angle between the vectors $\boldsymbol{\lambda}_{p\tau s}^{k-1}$ and $\boldsymbol{\lambda}_{p\tau s}^{k-1} + c\mathbf{u}_{p\tau}^{k-1}$, and in the right picture the behavior of the scaling factor $\beta_{p,l}^{k-1}$, $l = 1, 2$, for the node $p = (0.0625, 1, 0)^\top \in \mathcal{A}_\tau^k$ for all k . We observe a superlinear convergence for all modifications. Comparing the

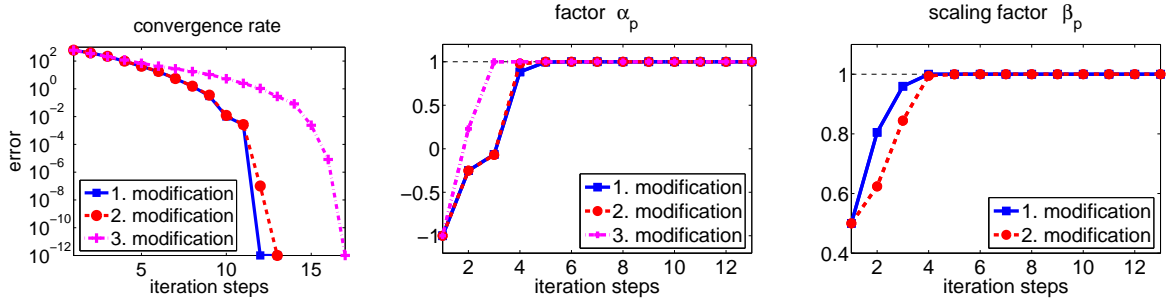


Figure 5.3.: Convergence of $\boldsymbol{\lambda}^k$ on Level 5, $c = 100$ and $\varepsilon_u = 10^{-14}$ (left), behavior of $\alpha_{p,l}^{k-1}$ (middle) and β_p^{k-1} (right) at the node $(0.0625, 1, 0)^\top \in \mathcal{S}$ for $\mathbf{u}^{0,0} = (1, 1, 0)^\top$ and $\boldsymbol{\lambda}^0 = (-1, -1, 0)^\top$.

Table 5.3.: Comparison between the exact ($m = \infty$) and the inexact ($m = 1$) strategy with $c = 100$ using (5.13) and $\varepsilon_u = 10^{-10}$.

strategy		exact		inexact		nested	
level l	DOF	K_l	MG-steps	M_l	MG-steps	M_l	MG-steps
1	27	3	41	3	11	2	10
2	125	3	44	3	13	2	12
3	729	4	59	4	14	5	13
4	4913	6	65	6	14	7	12
5	35937	7	85	8	17	7	14

behavior of the factor $\alpha_{p,l}^{k-1}$, the first and the second modification show almost the same behavior. Although the factor $\alpha_{p,l}^{k-1}$ tends faster towards 1 for the third modification, we observe a slower convergence. For the factor β_p^{k-1} we obtain a better behavior for the first modification than for the second one. From now on, we use modification one for all computations.

Next, we compare the exact version of Algorithm 2, i.e., $m = \infty$, with the inexact version obtained by using $m = 1$, i.e., we update the active and inactive sets after each multigrid step. We denote by K_l the iteration step in which the correct active and inactive sets are found for the first time and kept afterwards. For the inexact approach, we denote this step by M_l . Table 5.3 shows the numbers K_l and M_l on each level and the necessary numbers of multigrid iterations to solve the full nonlinear problem on level l . We observe that the numbers K_l and M_l are almost the same and seem to depend linearly on the level l . Therefore, there is no need to solve the linear system exactly. Furthermore, we compare the inexact approach, where we start with $\mathbf{u}^{0,0} = \mathbf{0}$ and $\boldsymbol{\lambda}^0 = \mathbf{0}$ on each level, with the nested approach in which we inherit $\mathbf{u}^{0,0}$ and $\boldsymbol{\lambda}_h^0$ on level $l+1$ from level l . The values M_l and the numbers of multigrid iteration steps are shown in the last column of Table 5.3. We note that the inexact semi-smooth Newton method can be interpreted as a nonlinear multigrid method.

The numerical studies for this problem are closed with a Remark.

Remark 5.5. We recall that the parameter c can be seen as a weight for the tangential distortion $\hat{\mathbf{u}}_{p\tau}$ in the sum with the tangential component $\lambda_{p\tau s}$ of the Lagrange multiplier. Thus, it plays a similar role for the tangential component as for the normal component. As observed in Remark 4.2, we get for the inexact approach $m = 1$ a quite stable behavior of Algorithm 2 independent of the parameter c if this parameter is large enough, see [82].

5.5. Fixed point based algorithm for Coulomb friction

In this subsection, we extend Algorithm 2 to contact problems with Coulomb's friction law based on fixed point ideas. This approach is widely used in the literature. We refer to, e.g., [2, 92], or the basic textbooks [91, 106, 143].

5.5.1. Algorithm

For Coulomb's friction law, the friction bound $b_p = \mathfrak{F}|\lambda_{pns}|$ needs to be iteratively adjusted using the normal component of the Lagrange multiplier. Therefore, we get an additional outer loop for the update of the friction bound, see Algorithm 3. For points $p \in \mathcal{S}$ on the contact boundary which are not in contact, we directly get zero contact stress, i.e., $\lambda_p = \mathbf{0}$, and thus we are in the case of $b_p = 0$ as considered in Subsection 5.1.2.

We denote by mod_{**} the modulo-operator. Comparing this algorithm with Algorithm 2 for Tresca friction, we update the friction bound only after k_f steps of the (inexact) semi-smooth Newton method. Since we do not solve the resulting linear problems exactly, it is not guaranteed that $\lambda_{pns}^k \geq 0$ for all $p \in \mathcal{S}$. Therefore, we set $b_p^k = \mathfrak{F} \max\{0, \lambda_{pns}^k\}$. For the choice $m = k_f = 1$, the friction bound and the active and inactive sets are updated after each multigrid step. As stopping criterion, we use the relative error between the actual solution $\hat{\mathbf{u}}^{k,m}$ and the solution for the last friction bound $\hat{\mathbf{u}}^{k_c,m}$. For the choice $m = k_f = \infty$, we get the exact version of the algorithm. In this case, we solve the resulting Tresca friction problem exactly for each friction bound. Obviously, this approach is rather costly. However, for a small coefficient of friction \mathfrak{F} it can be shown that this discrete fixed point mapping is a contraction and thus converges, see [115].

5.5.2. Numerical examples for fixed point based Coulomb friction

In this subsection, we study the performance of Algorithm 3 for Coulomb friction. This friction model is physically more realistic than the Tresca model, since friction can only occur at nodes that are in contact with the obstacle.

5.5.2.1. First example

We consider the same geometry and data as for the example of Section 5.4 and choose the coefficient of friction $\mathfrak{F} = 1$. The distorted cube is depicted in the left picture in Figure 5.4. Note that its distortion is significantly different from the one obtained

Algorithm 3 Fixed point based algorithm for Coulomb friction

- 1: set $k = 1$
- 2: initialize $\hat{\mathbf{u}}^{0,0}$ and $\boldsymbol{\lambda}^0$ as an initial solution
- 3: set $c > 0$, $m \in \mathbb{N}$, $k_f \in \mathbb{N}$ and the tolerance ε_u
- 4: if $\text{mod}_{k_f}(k-1) = 0$, set $k_c = k-1$ and update the friction bound

$$b_p^{k_c} := \mathfrak{F} \max\{0, \lambda_{pns}^{k_c}\}$$

- 5: define the active and the inactive sets

$$\begin{aligned} \mathcal{A}_n^k &:= \{p \in \mathcal{S} : \lambda_{pns}^{k-1} + c(\hat{u}_{pn}^{k-1,m} - g_p) > 0\} \\ \mathcal{I}_n^k &:= \{p \in \mathcal{S} : \lambda_{pns}^{k-1} + c(\hat{u}_{pn}^{k-1,m} - g_p) \leq 0\} \\ \mathcal{A}_\tau^k &:= \{p \in \mathcal{S} : \|\lambda_{p\tau s}^{k-1} + c\hat{\mathbf{u}}_{p\tau}^{k-1,m}\| - b_p^{k_c} > 0\} \\ \mathcal{I}_\tau^k &:= \{p \in \mathcal{S} : \|\lambda_{p\tau s}^{k-1} + c\hat{\mathbf{u}}_{p\tau}^{k-1,m}\| - b_p^{k_c} \leq 0\} \end{aligned}$$

- 6: **for** $i = 1, \dots, m$ **do**

7:

$$\hat{\mathbf{u}}^{k,i} = \text{MG}(\hat{\mathbf{u}}^{k,i-1}, \mathcal{A}_n^k, \mathcal{I}_n^k, \mathcal{A}_\tau^k, \mathcal{I}_\tau^k, \hat{\mathbf{u}}^{k-1,m}, \boldsymbol{\lambda}^{k-1})$$

8: **end for**

- 9: **if** $k > k_f$ and $\|\hat{\mathbf{u}}^{k,m} - \hat{\mathbf{u}}^{k_c,m}\| / \|\hat{\mathbf{u}}^{k,m}\| < \varepsilon_u$ **then**

10: stop

11: **end if**

12: compute the Lagrange multiplier

$$\boldsymbol{\lambda}^k = \mathbf{D}_d^{-1} \left(\hat{\mathbf{f}}_S - \hat{\mathbf{K}}_{SN} \hat{\mathbf{u}}_N^{k,m} - \hat{\mathbf{K}}_{SM} \hat{\mathbf{u}}_M^{k,m} - \hat{\mathbf{K}}_{SS} \hat{\mathbf{u}}_S^{k,m} \right)$$

13: set $\hat{\mathbf{u}}^{k+1,0} = \hat{\mathbf{u}}^{k,m}$

14: set $k = k + 1$

15: go to step 4

with Tresca's friction law, see Figure 5.1. The right picture in Figure 5.4 shows the visualization of the constraint $\|\boldsymbol{\lambda}_{p\tau s}\| \leq \mathfrak{F}|\lambda_{pns}|$ that holds for all $p \in \mathcal{S}$. The few nodes where this inequality holds in a strict sense are the sticky nodes, i.e., $\mathbf{u}_{p\tau} = \mathbf{0}$, which are in contact with the obstacle, i.e., $u_{pn} = g_p = 0$. We remark that the solution has a singularity at the node $(1, 1, 0)^\top$.

As done for Tresca's friction law in Figure 5.2, we also visualize the different types of contact nodes for Coulomb's law. In contrast to Tresca's model, Coulomb's law only allows three kinds of nodes, since nodes that are not in contact with the obstacle are not subjected to any frictional constraints. The size of the bullets in Figure 5.5 is proportional to the normal contact force $|\lambda_{pns}|$.

We apply the inexact version of Algorithm 3 with $m = k_f = 1$ to solve the contact problem with Coulomb's friction law. We use $c = 100$, $\varepsilon_u = 10^{-10}$ and initialize the

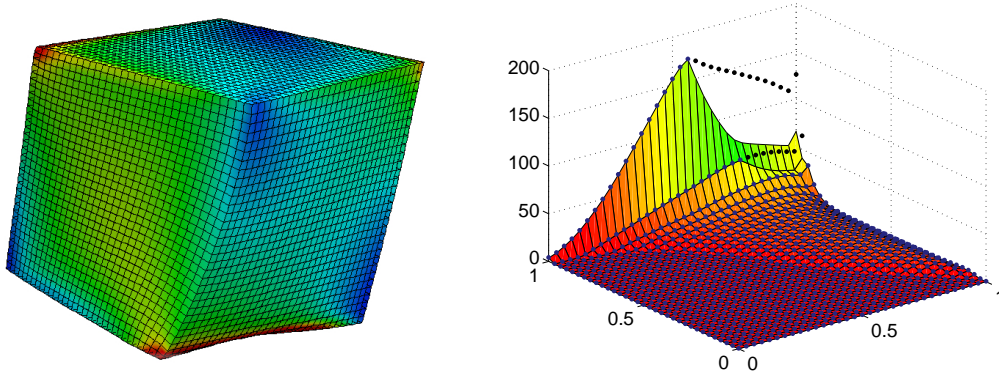


Figure 5.4.: Distorted body with effective von Mises stress σ_{eff} (left). The lower surface in the plot is subject to contact and Coulomb friction. Visualization of the friction bound $\mathfrak{F}|\lambda_{pn}|$ (small balls) and of $\|\lambda_{p\tau}\|$ (right).

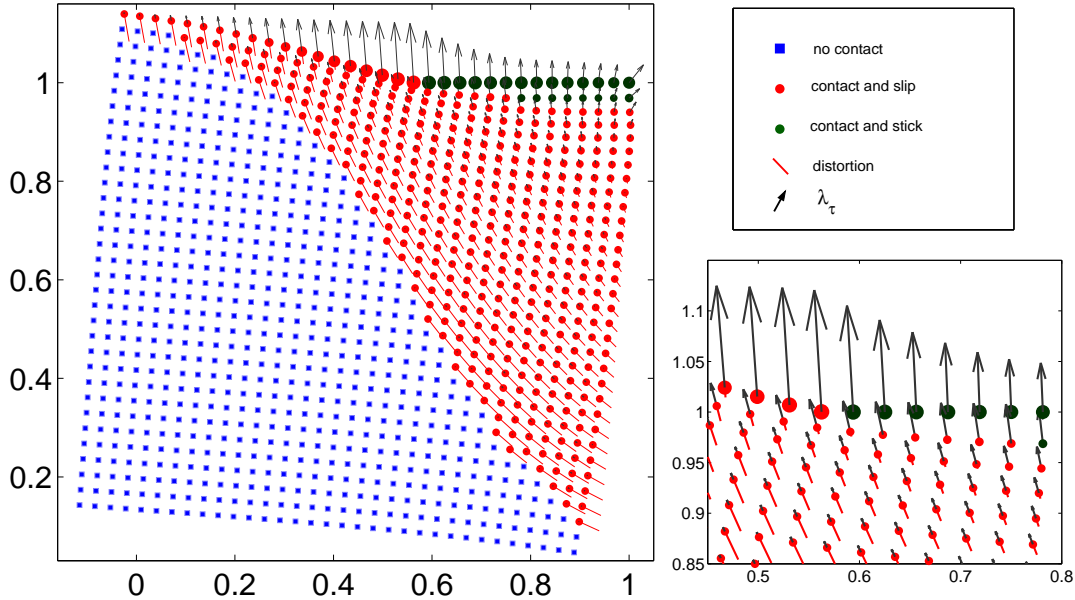


Figure 5.5.: Visualization of the solution at the nodes $p \in \mathcal{S}$ for Coulomb friction on level 5 (left), legend (upper right) and cutout (lower right).

iteration with $\mathbf{u}^{0,0} = \mathbf{0}$ and $\boldsymbol{\lambda}_h^0 = \mathbf{0}$ on each level. Figure 5.6 shows the behavior of our algorithm on various levels. The number of nodes contained in the active sets are plotted over the iteration steps k . We denote by k_{max} the number of iteration steps necessary to meet the given tolerance and by K_l the iteration step in which the correct active sets are found for the first time and do not change afterwards. The number K_l is marked by a dashed vertical line in Figure 5.6. We observe that both k_{max} and K_l appear to be almost independent of the level l . Looking at Figure 5.6 more closely, we note that on each level, there are only minor changes of the active nodes after $k = 10$. Table 5.4 shows

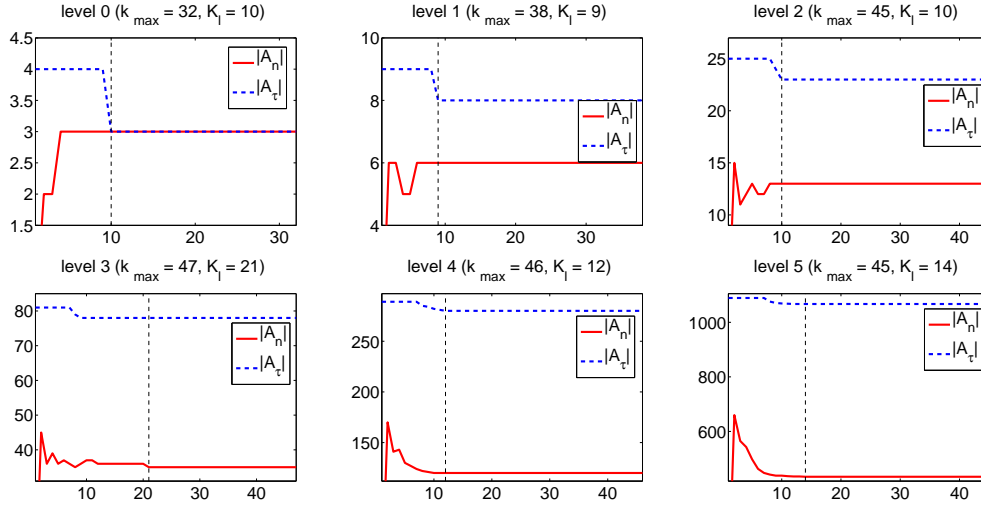


Figure 5.6.: Behavior of Algorithm 3: Numbers $|\mathcal{A}_n^k|$ and $|\mathcal{A}_\tau^k|$ of active nodes in each iteration step k on each level l . We used the parameters $c = 100$, $m = k_f = 1$ and $\varepsilon_u = 10^{-10}$. Initialization: $\mathbf{u}^{0,0} = \mathbf{0}$ and $\boldsymbol{\lambda}^0 = \mathbf{0}$.

Table 5.4.: Behavior of Algorithm 3: K_l and k_{\max} on each level l for $c = 100$, $m = k_f = 1$ and $\varepsilon_u = 10^{-10}$.

level l	DOF	$\mathbf{u}^{0,0} = \mathbf{0}, \boldsymbol{\lambda}^0 = \mathbf{0}$		nested approach	
		K_l	k_{\max}	K_l	k_{\max}
0	8	10	32	10	32
1	27	9	38	3	34
2	125	10	45	5	32
3	729	21	47	3	37
4	4913	12	46	4	38
5	35937	14	45	5	36

a comparison between the initialization $\mathbf{u}^{0,0} = \mathbf{0}$ and $\boldsymbol{\lambda}^0 = \mathbf{0}$ on each level and the nested approach. As expected, the correct active sets are found earlier and fewer iterations are required for the nested approach.

5.5.2.2. Second example

Now, we consider a curved contact interface subject to Coulomb's friction law. A two-dimensional cross section of our geometry is shown in Figure 5.7. The lower domain Ω^m , assumed to be the master side, models a spherical shell that is fixed at the outer boundary. The body modeled by the domain Ω^s which is assumed to be the slave side is pressed against this shell. At the top surface of Ω^s , we apply the Dirichlet data $\mathbf{u}_D^s = (0, 0, -0.2)^\top$. The geometry is given by $r_i = 0.7$, $r_a = 1.0$, $r = 0.6$, $h = 0.5$ and

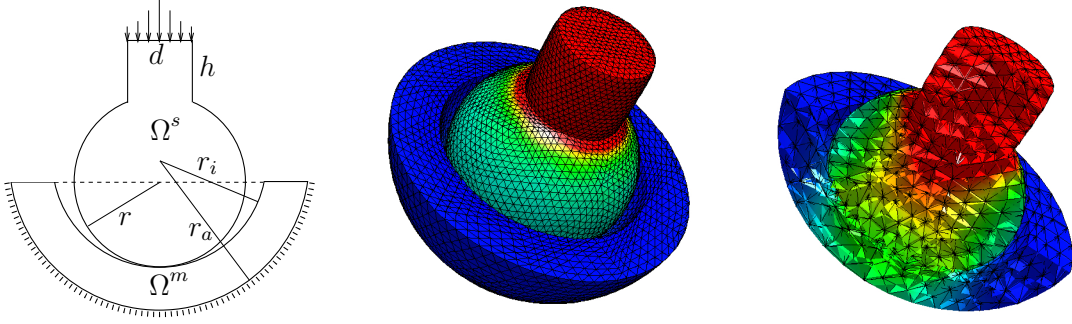


Figure 5.7.: Problem definition (left), deformed mesh with effective von Mises stress σ_{eff} on Level 3 (middle), two-dimensional cross section of the deformed mesh on Level 2 (right) for $\mathfrak{z} = 0.5$.

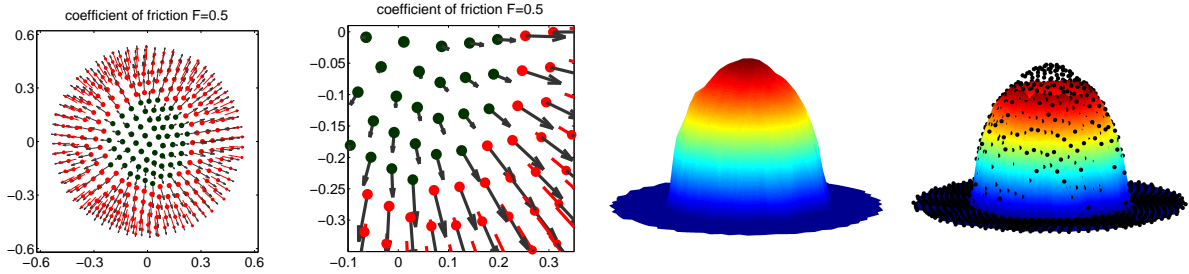


Figure 5.8.: Visualization of the nodes being in contact together with the deformation and the stress vectors on Level 3 for $\mathfrak{z} = 0.5$ (first), and a cutout (second) – for the legend we refer to Figure 5.5 – and visualization of λ_n (third) and $\|\lambda_\tau\|$ (fourth) with the friction bound $0.5|\lambda_n|$ (dotted).

$d = 0.3$. In Ω^s , we use a Young modulus $E^s = 300$ and a Poisson ratio $\nu^s = 0.3$, while in Ω^m we have $E^m = 400$ and $\nu^m = 0.3$.

The results for the coefficient of friction $\mathfrak{z} = 0.5$ are shown in Figures 5.7-5.8. Figure 5.7 shows the deformed bodies with the effective von Mises stress σ_{eff} on Level 3 and a two-dimensional cross section on Level 2. In Figure 5.8, we show the nodes being in contact, their relative tangential slip $\hat{\mathbf{u}}_{p\tau}$ (lines) and the tangential contact pressure $\lambda_{p\tau}$ (arrows). We remark that in the second picture, the nodes with only an arrow are the sticky nodes, the others are slip ones. In the two pictures on the right, the normal and the tangential part of the Lagrange multiplier together with the friction bound is plotted. The comparison of the result for various coefficients of friction \mathfrak{z} is shown in Figures 5.9-5.10. In the first one, the visualization of the contact nodes together with the relative tangential slip and the tangential contact pressure is displayed. Figure 5.10 shows a two-dimensional plot of the normal and tangential part of the Lagrange multiplier and the friction bound for all nodes $p \in \mathcal{S}$ over their distance to the midpoint of the contact zone on the surface of Ω^s . The small oscillations in the plot occur due to the fact that all nodes $p \in \mathcal{S}$ in the whole contact zone are projected onto a straight radial line and

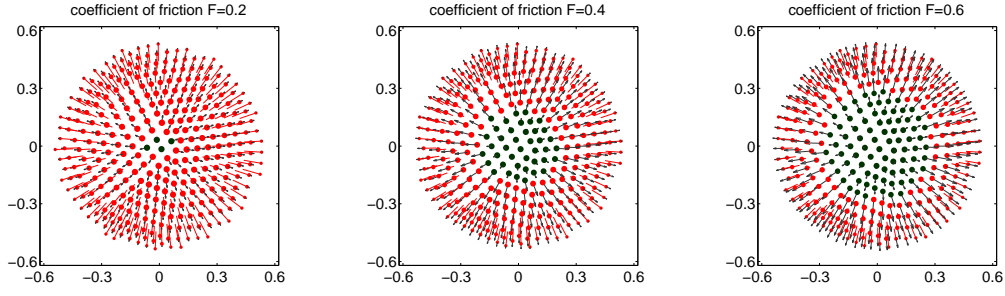


Figure 5.9.: Visualization of the nodes being in contact together with the deformation and stress vector on Level 3 for $\mathfrak{F} = 0.2, 0.4, 0.6$ – for the legend we refer to Figure 5.5.

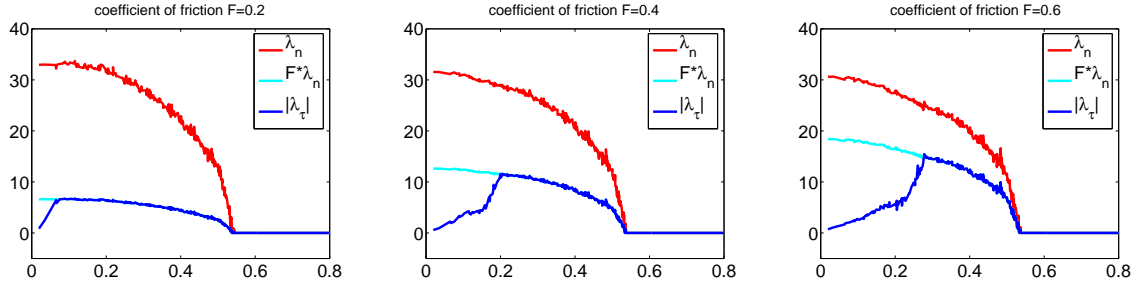


Figure 5.10.: Two-dimensional visualization of Lagrange multipliers for $\mathfrak{F} = 0.2, 0.4, 0.6$.

that we work with an unstructured mesh. We observe that the number of sticky nodes decreases for smaller \mathfrak{F} .

Next, we consider the performance of Algorithm 3 for the coefficient of friction $\mathfrak{F} = 0.5$. For the initialization, we set $\hat{\mathbf{u}}_p^{0,0} = 0.1\mathbf{n}_p$ for $p \in \mathcal{S}$, $\hat{\mathbf{u}}_p^{0,0} = \mathbf{0}$ for $p \notin \mathcal{S}$ and $\boldsymbol{\lambda}_p^0 = 0.0001\mathbf{n}_p$ on each level. Using the parameters $c = 100$, $m = k_f = 1$ and $\varepsilon_u = 10^{-9}$, we get the performance of Algorithm 3 shown in Figure 5.11. Here, the number of nodes in $|\mathcal{A}_n^k|$ and $|\mathcal{A}_\tau^k|$ are shown for Level 1-3. Again, the dashed vertical line marks the step K_l in which the correct active sets are found for the first time and remain unchanged afterwards. A comparison between this approach and the nested approach for various coefficients of friction is shown in Table 5.5. Although for $\mathfrak{F} = 0.2$ the convergence rates of the multigrid method for Level 1 and 2 are worse, the obtained results show qualitatively the same behavior as for the cube in the first example.

For the next setting, we use the same data and geometry as above, see Figure 5.7, but enforce a non-symmetric boundary traction at the top of Ω^s instead of the Dirichlet data, namely, we apply the surface traction $\mathbf{p}^s = (15, 0, -150 \exp(-100r^2))^\top$, where r denotes the distance to the midpoint of the top surface of Ω^s . The results for $\mathfrak{F} = 0.7$ are presented in Figure 5.12.

Finally, we remark that the behavior of Algorithm 1 for this example in the case without friction is investigated in [85].

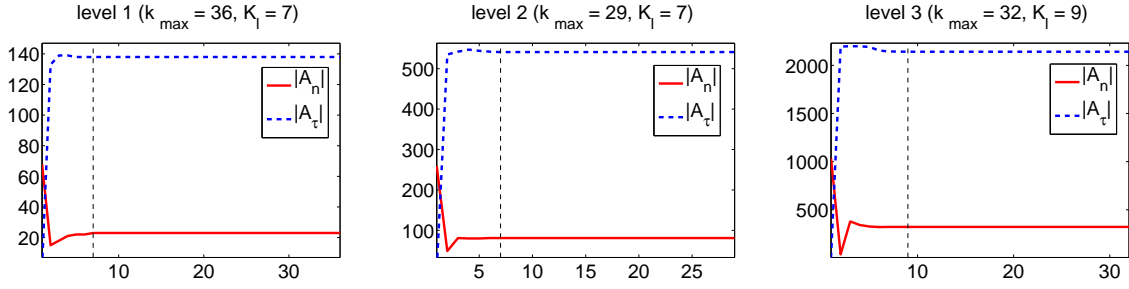


Figure 5.11.: Behavior of Algorithm 3: Numbers $|\mathcal{A}_n^k|$ and $|\mathcal{A}_\tau^k|$ in each iteration step k on Levels 1, 2, 3 for $\mathfrak{z} = 0.5$. We use the parameters $c = 100$, $m = k_f = 1$ and $\varepsilon_u = 10^{-9}$.

Table 5.5.: Behavior of Algorithm 3: Necessary numbers k_{\max} and K_l on each level for $c = 100$, $m = k_f = 1$, $\varepsilon_u = 10^{-9}$ and $\mathfrak{z} = 0.2, 0.4, 0.6$.

level	DOF	$\hat{\mathbf{u}}_p^{0,0} = 0.1 \mathbf{n}_p, \boldsymbol{\lambda}_p^0 = 0.0001 \mathbf{n}_p$						nested approach					
		K_l			k_{\max}			K_l			k_{\max}		
		0.2	0.4	0.6	0.2	0.4	0.6	0.2	0.4	0.6	0.2	0.4	0.6
0	104	4	4	4	12	16	21	4	4	4	12	16	21
1	541	10	5	5	111	20	33	1	3	2	91	20	25
2	3384	5	7	6	67	27	26	2	3	2	62	21	22
3	23694	9	11	9	33	32	32	3	3	2	29	21	21

5.5.2.3. Axially symmetric example

Finally, we consider two rotationally symmetric examples in the three-dimensional case, see also [85]. The geometry of the first example is shown in the first picture in Figure 5.13. Due to the rotational symmetry this example can be reduced to a two-dimensional setting. The resulting geometry is sketched in the second picture in Figure 5.13. For the geometry, we choose $L = 5$, $H = 15$, $r_i = 27$, $r_a = 30$, $M = (34.5, 7.0)^\top$ and $\phi = 13$. The softer inner body Ω^s , playing the role of the slave side, is modeled using the material data $\lambda^s = 57.6923$ and $\mu^s = 38.4615$. For the outer body Ω^m , playing the role of the master side, we set $\lambda^m = 576.923$ and $\mu^m = 384.615$. At the top of the inner cylinder, we apply Neumann data $p^s = (17.0, 0)^\top$. Due to the rotational symmetry, we have homogeneous Dirichlet data in the radial direction on the left side of Ω^s where $r = 0$ holds. We fix Ω^m at the three segments Γ_D^m , as shown in the second picture in Figure 5.13. For the coefficient of friction we choose $\mathfrak{z} = 0.7$. We remark that the two bodies penetrate in their reference configuration.

The Lamé operator in cylindrical coordinates can be found in [89]. We denote by u_r the displacement in the radial direction, by u_z the displacement in the axial direction and by u_θ the displacement in circumferential direction. The rotational symmetry conditions

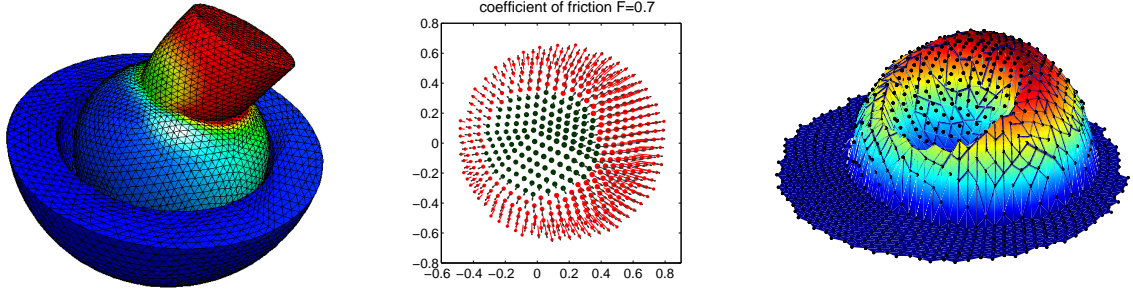


Figure 5.12.: Non-symmetric boundary data: Deformed mesh with effective von Mises stress σ_{eff} on Level 3 (left), visualization of the nodes being in contact together with the deformation and the stress vectors (middle) and of $\|\boldsymbol{\lambda}_\tau\|$ (right) with the friction bound $0.7|\lambda_n|$ (dotted).

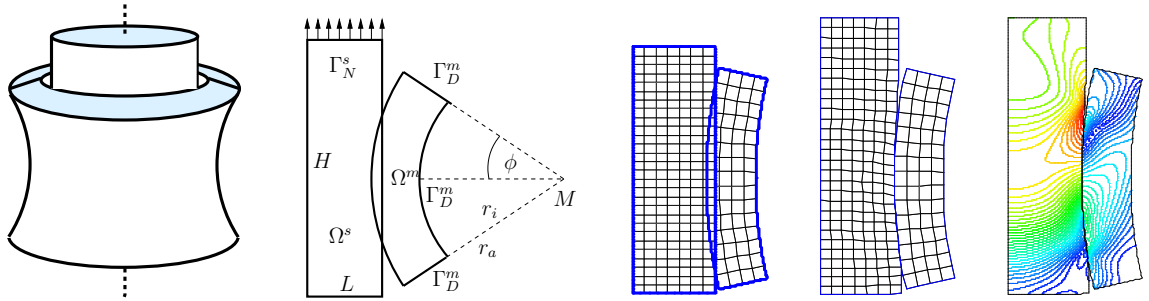


Figure 5.13.: Problem definition for $d = 3$, problem definition for $d = 2$, initial grid on level 0, distorted grid on level 0 and effective von Mises stress on level 2.

imply $u_\theta = 0$ and therefore we get the relations $\boldsymbol{\varepsilon}_{r\theta} = \boldsymbol{\varepsilon}_{\theta r} = \boldsymbol{\varepsilon}_{z\theta} = \boldsymbol{\varepsilon}_{\theta z} = 0$. For the other entries of the strain tensor $\boldsymbol{\varepsilon}$, we get

$$\boldsymbol{\varepsilon}_{rr} = \frac{\partial u_r}{\partial r}, \quad \boldsymbol{\varepsilon}_{zz} = \frac{\partial u_z}{\partial z}, \quad \boldsymbol{\varepsilon}_{\theta\theta} = \frac{1}{r} \left(\frac{\partial u_\theta}{\partial \theta} + u_r \right), \quad \boldsymbol{\varepsilon}_{rz} = \boldsymbol{\varepsilon}_{zr} = \frac{1}{2} \left(\frac{\partial u_r}{\partial z} + \frac{\partial u_z}{\partial r} \right).$$

The stress-strain relations now read as

$$\begin{pmatrix} \boldsymbol{\sigma}_{rr} \\ \boldsymbol{\sigma}_{zz} \\ \boldsymbol{\sigma}_{\theta\theta} \\ \boldsymbol{\sigma}_{rz} \end{pmatrix} = \begin{pmatrix} \lambda + 2\mu & \lambda & \lambda & 0 \\ \lambda & \lambda + 2\mu & \lambda & 0 \\ \lambda & \lambda & \lambda + 2\mu & 0 \\ 0 & 0 & 0 & \mu \end{pmatrix} \begin{pmatrix} \boldsymbol{\varepsilon}_{rr} \\ \boldsymbol{\varepsilon}_{zz} \\ \boldsymbol{\varepsilon}_{\theta\theta} \\ 2\boldsymbol{\varepsilon}_{rz} \end{pmatrix}.$$

To construct dual Lagrange multipliers for this case, we consider an arbitrary edge of the triangulation of Ω^s on Γ_c^s . We assume $s \in [0, 1]$ to be the local coordinate of the parameterization of the edge. For $s = 0$, we get the first point $p_a = (r_a, z_a)^\top \in \mathcal{S}$ in the rz -plane, and for $s = 1$, we have the second point $p_e = (r_e, z_e)^\top \in \mathcal{S}$. Due to the use of cylindrical coordinates, we have to work with weighted integrals, and the dual Lagrange

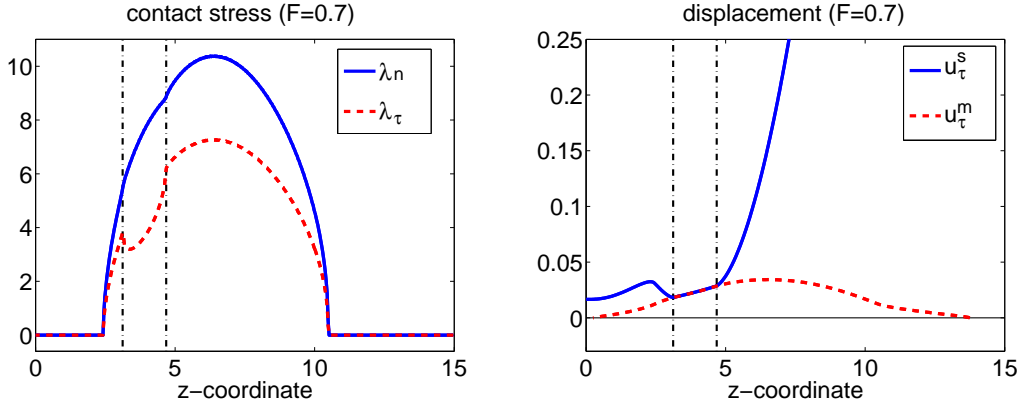


Figure 5.14.: Normal part λ_n^h and tangential part λ_τ of the Lagrange multiplier λ , tangential part u_τ^s of the displacement on the slave side and tangential part u_τ^m of the displacement on the master side.

multiplier is defined by

$$\int_0^1 \psi_p(s)\phi_q(s)r(s) ds = \delta_{pq} \int_0^1 \phi_p(s)r(s) ds, \quad p, q \in \mathcal{S}, \quad (5.20)$$

where $r(s) = r_a + s(r_e - r_a)$. If we use linear elements $\psi_{p_a} = \alpha_a + \beta_a s$ and $\psi_{p_e} = \alpha_e + \beta_e s$, the coefficients α_a , β_a , α_e and β_e can easily be computed. The weighted biorthogonality (5.20) yields

$$\begin{aligned} \alpha_a &= \frac{(r_e + 2r_a)(3r_e + r_a)}{r_e^2 + 4r_e r_a + r_a^2}, & \beta_a &= -\frac{2(2r_a^2 + 2r_e^2 + 5r_e r_a)}{r_e^2 + 4r_e r_a + r_a^2}, \\ \alpha_e &= -\frac{(2r_e + r_a)(r_e + r_a)}{r_e^2 + 4r_e r_a + r_a^2}, & \beta_e &= \frac{2(2r_a^2 + 2r_e^2 + 5r_e r_a)}{r_e^2 + 4r_e r_a + r_a^2}. \end{aligned}$$

Figure 5.14 shows the normal and the tangential parts of the discrete Lagrange multiplier on the contact interface. We remark that the two bodies are in contact for all nodes with $\lambda_n \neq 0$. In the tangential direction, we get two active zones where we have $|\lambda_\tau| = \mathfrak{F}|\lambda_n|$. Between these two sets, the two bodies are glued together in the tangential direction, i.e., $[\mathbf{u}]_\tau = \hat{\mathbf{u}}_\tau = 0$. The tangential part of the displacements on the slave and the master side is shown in the second picture in Figure 5.14.

Our second example will be the rotationally symmetric example from Subsection 5.5.2.2 restricted to the two-dimensional case. We consider Coulomb's friction law for the coefficient of friction $\mathfrak{F} = 0.45$ and the material parameters $\lambda^s = 173.077$, $\mu^s = 115.385$, $\lambda^m = 230.769$ and $\mu^m = 153.846$. At the top, we apply Dirichlet data given by $\mathbf{u}_D^s = (0.0, -0.2)^\top$. The grid on level 0, the distorted grid with the effective von Mises stress, the normal and tangential component of the Lagrange multiplier and the tangential component of the jump $[\mathbf{u}]_\tau$ are presented in Figure 5.15.

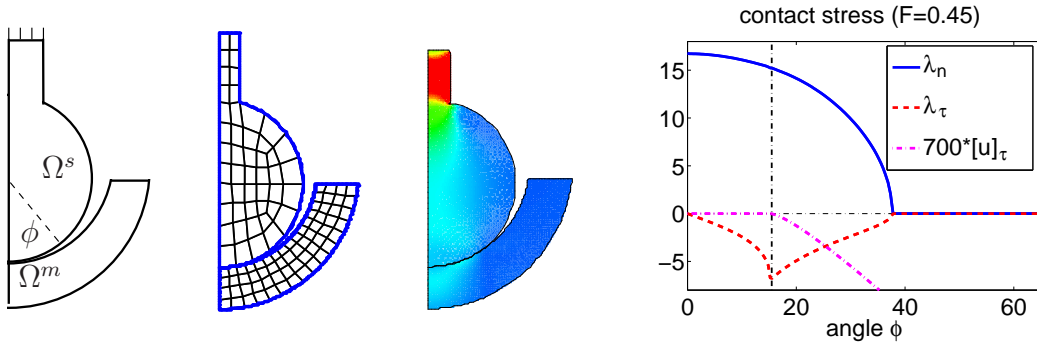


Figure 5.15.: Problem setting and grid on level 0 (left), distorted grid with effective von Mises stress (middle), normal and tangential component of the Lagrange multiplier and the amplified tangential component of the jump $[u]_\tau$ (right).

5.6. Full semi-smooth Newton approach for Coulomb friction

While Algorithm 3 for the solution of the contact problem with Coulomb's friction law is based on fixed point ideas, we now present a full Newton approach. The main advantage of this approach is its fast convergence which is due to the fact that the friction bound is updated in the Newton iteration and not via a fixed point loop. Our new method deals with the three physically feasible subsets (no contact, contact and slip, contact and stick) of the contact nodes, whereas the proposed full Newton approach for Coulomb's friction law in [28] works with three different sets for the normal direction and six sets in tangential direction.

5.6.1. Algorithm

In this section, we apply a fast direct solver [123, 124] to solve the linear system in each Newton step. To derive the full Newton iteration, b_p in (5.2) is replaced by $b_p(\hat{u}_{pn}, \lambda_{pns}) := \mathfrak{F} \max\{0, \lambda_{pns} + c(\hat{u}_{pn} - g_p)\}$ before deriving the Newton iteration step. In the two papers [27, 28] mentioned in the introduction, the authors have used $b_p(\lambda_{pns}) := \mathfrak{F} \max\{0, \lambda_{pns}\}$. The equivalence of these two choices follows from (4.5). In what follows, we use the latter replacement since then the Newton-type iteration automatically takes the form of an active set method that estimates the three relevant sets for Coulomb friction node not in contact, node in contact and stick or node in contact and slip in each iteration step. The resulting nonlinear complementarity function is

$$D_\tau(\hat{\mathbf{u}}_p, \boldsymbol{\lambda}_p) := \max\{\mathfrak{F}(\lambda_{pns} + c(\hat{u}_{pn} - g_p)), \|\boldsymbol{\lambda}_{p\tau s} + c\hat{\mathbf{u}}_{p\tau}\|\} \boldsymbol{\lambda}_{p\tau s} - \mathfrak{F} \max\{0, \lambda_{pns} + c(\hat{u}_{pn} - g_p)\} (\boldsymbol{\lambda}_{p\tau s} + c\hat{\mathbf{u}}_{p\tau}). \quad (5.21)$$

We mention that in contrast to $C_\tau(\cdot, \cdot)$, the function $D_\tau(\cdot, \cdot)$ depends on the normal parts of the displacement and the Lagrange multiplier. Similarly as in Section 5.1, we derive

a semi-smooth Newton step for the solution of $D_\tau(\hat{\mathbf{u}}_p, \boldsymbol{\lambda}_p) = \mathbf{0}$ and (4.5). Using the notation $b_p := \mathfrak{F}(\lambda_{pns} + c(\hat{u}_{pn} - g_p))$, we obtain as in (5.4) the generalized derivative D_{D_τ} of $D_\tau(\cdot, \cdot)$ by

$$\begin{aligned} D_{C_\tau}(\hat{\mathbf{u}}_p, \boldsymbol{\lambda}_{ps})(\delta\hat{\mathbf{u}}_p, \delta\boldsymbol{\lambda}_{ps}) &= \max\{b_p, \|\boldsymbol{\lambda}_{p\tau s} + c\hat{\mathbf{u}}_{p\tau}\|\}\delta\boldsymbol{\lambda}_{p\tau s} \\ &+ \chi_{\mathcal{I}_n \cup \mathcal{A}_m} \frac{\boldsymbol{\lambda}_{p\tau s} (\boldsymbol{\lambda}_{p\tau s} + c\hat{\mathbf{u}}_{p\tau})^\top}{\|\boldsymbol{\lambda}_{p\tau s} + c\hat{\mathbf{u}}_{p\tau}\|} (\delta\boldsymbol{\lambda}_{p\tau s} + c\delta\hat{\mathbf{u}}_{p\tau}) - \chi_{\mathcal{I}_\tau \cup \mathcal{A}_m} b_p (\delta\boldsymbol{\lambda}_{p\tau s} + c\delta\hat{\mathbf{u}}_{p\tau}) \quad (5.22) \\ &+ \chi_{\mathcal{I}_\tau} \mathfrak{F}(\delta\lambda_{pns} + c\delta\hat{u}_{pn}) \boldsymbol{\lambda}_{p\tau s} - \chi_{\mathcal{I}_\tau \cup \mathcal{A}_m} \mathfrak{F}(\delta\lambda_{pns} + c\delta\hat{u}_{pn}) (\boldsymbol{\lambda}_{p\tau s} + c\hat{\mathbf{u}}_{p\tau}), \end{aligned}$$

where the characteristic functions for the three disjoint sets

$$\begin{aligned} \mathcal{I}_n &:= \{p \in \mathcal{S} : b_p \leq 0\}, \\ \mathcal{I}_\tau &:= \{p \in \mathcal{S} : \|\boldsymbol{\lambda}_{p\tau s} + c\hat{\mathbf{u}}_{p\tau}\| - b_p < 0\}, \\ \mathcal{A}_m &:= \{p \in \mathcal{S} : \|\boldsymbol{\lambda}_{p\tau s} + c\hat{\mathbf{u}}_{p\tau}\| \geq b_p > 0\} \end{aligned} \quad (5.23)$$

are given by

$$\chi_\star := \begin{cases} 1 & \text{if } p \in \star, \\ 0 & \text{if } p \notin \star. \end{cases}$$

Defining according to (5.23) the disjoint sets in terms (5.22) of the old iterates

$$\begin{aligned} \mathcal{I}_n^k &:= \{p \in \mathcal{S} : b_p^{k-1} \leq 0\}, \\ \mathcal{I}_\tau^k &:= \{p \in \mathcal{S} : \|\boldsymbol{\lambda}_{p\tau s}^{k-1} + c\hat{\mathbf{u}}_{p\tau}^{k-1}\| - b_p^{k-1} < 0\}, \\ \mathcal{A}_m^k &:= \{p \in \mathcal{S} : \|\boldsymbol{\lambda}_{p\tau s}^{k-1} + c\hat{\mathbf{u}}_{p\tau}^{k-1}\| \geq b_p^{k-1} > 0\}, \end{aligned}$$

the new iterates for the semi-smooth Newton method applied to (5.21) or rather (5.10) in combination with the normal constraints (4.5) introduced in Section 4.2 satisfy similar to (5.7) and (4.10) for the normal constraints with $b_p^{k-1} := \mathfrak{F}(\lambda_{pns}^{k-1} + c(\hat{u}_{pn}^{k-1} - g_p))$ in terms of (5.22) the following conditions:

- For the nodes $p \in \mathcal{I}_n^k$, i.e., the node not in contact, we get

$$\lambda_{pns}^k = 0 \quad \text{and} \quad \boldsymbol{\lambda}_{p\tau s}^k = \mathbf{0}. \quad (5.24)$$

We note that $\mathcal{I}_n^k \subset \mathcal{A}_\tau^k$, where $\mathcal{A}_\tau^k := \{p \in \mathcal{S} : \|\boldsymbol{\lambda}_{p\tau s}^{k-1} + c\hat{\mathbf{u}}_{p\tau}^{k-1}\| - b_p^{k-1} \geq 0\}$. Furthermore, the choice for $\boldsymbol{\lambda}_{p\tau s}^k$ is not the strict consequence of the Newton iteration. It is derived directly from (5.21), namely from $\|\boldsymbol{\lambda}_{p\tau s} + c\hat{\mathbf{u}}_{p\tau}\| \boldsymbol{\lambda}_{p\tau s} = \mathbf{0}$, and thus also the limit case for the strict Newton iteration. Since the friction bound is zero for a free node, there is no need to adjust the direction between $\boldsymbol{\lambda}_{p\tau s}$ and $\hat{\mathbf{u}}_{p\tau}$ and thus the choice $\boldsymbol{\lambda}_{p\tau s}^k = \mathbf{0}$ is a consistent choice in the iteration process.

- For the nodes $p \in \mathcal{I}_\tau^k$, i.e., the sticky nodes in contact, we get

$$\hat{u}_{pn}^k = g_p \quad \text{and} \quad \hat{\mathbf{u}}_{p\tau}^k + (\mathfrak{F}\hat{\mathbf{u}}_{p\tau}^{k-1}/b_p^{k-1}) \lambda_{pns}^k = \hat{\mathbf{u}}_{p\tau}^{k-1}. \quad (5.25)$$

We note that $\mathcal{I}_\tau^k \subset \mathcal{A}_n^k$, where $\mathcal{A}_n^k := \{p \in \mathcal{S} : b_p^{k-1} > 0\}$. Furthermore, the constraint $\hat{u}_{pn}^k = g_p$ in normal direction was already used to derive the constraint $\hat{\mathbf{u}}_{p\tau}^k + (\mathfrak{F}\hat{\mathbf{u}}_{p\tau}^{k-1}/b_p^{k-1}) \lambda_{pns}^k = \hat{\mathbf{u}}_{p\tau}^{k-1}$.

- For the nodes $p \in \mathcal{A}_m^k$, i.e., the slip nodes in contact, we get

$$\begin{aligned} \hat{u}_{pn}^k &= g_p \quad \text{and} \\ -\boldsymbol{\lambda}_{p\tau s}^k + L_p^{k-1} \hat{\mathbf{u}}_{p\tau}^k + \mathfrak{F} \mathbf{v}_p^{k-1} \lambda_{pns}^k &= \mathbf{r}_p^{k-1} + b_p^{k-1} \mathbf{v}_p^{k-1}, \end{aligned} \quad (5.26)$$

where

$$\mathbf{v}_p^{k-1} := (\text{Id}_{d-1} - M_p^{k-1})^{-1} \frac{\boldsymbol{\lambda}_{p\tau s}^{k-1} + c \hat{\mathbf{u}}_{p\tau}^{k-1}}{\|\boldsymbol{\lambda}_{p\tau s}^{k-1} + c \hat{\mathbf{u}}_{p\tau}^{k-1}\|} \in \mathbb{R}^{d-1}$$

and b_p^{k-1} is used for the friction bound b_p in the matrices M_p^{k-1} and L_p^{k-1} . We remark, that $\mathcal{A}_m^k = \mathcal{A}_\tau^k \cap \mathcal{A}_n^k$ holds.

We mention that \mathcal{I}_n^k , \mathcal{I}_τ^k , and \mathcal{A}_m^k represent a disjoint decomposition of \mathcal{S} . Comparing (5.25) and (5.26) with (5.7a) and (5.7b), respectively, we observe that the main difference is the term involving λ_{pns}^k on the left hand side of (5.25) and (5.26).

Again, we apply the modifications stated in Subsection 5.1.1 and replace the matrices M_p^{k-1} and L_p^{k-1} and the vector \mathbf{r}_p^{k-1} by $\tilde{M}_{p,l}^{k-1}$, $\tilde{L}_{p,l}^{k-1}$ and $\tilde{\mathbf{r}}_{p,l}^{k-1}$, respectively. Therefore, we use the vector

$$\tilde{\mathbf{v}}_{p,l}^{k-1} := (\text{Id}_{d-1} - \beta_{p,l}^{k-1} \tilde{M}_{p,l}^{k-1})^{-1} \frac{(\boldsymbol{\lambda}_{p\tau s}^{k-1} + c \hat{\mathbf{u}}_{p\tau}^{k-1})}{\|\boldsymbol{\lambda}_{p\tau s}^{k-1} + c \hat{\mathbf{u}}_{p\tau}^{k-1}\|}$$

instead of \mathbf{v}_p^{k-1} . In (5.27) below, we briefly state the algebraic representation of the above system, where we use in addition to the notation introduced in Section 5.2

$$\mathbf{G} := \text{diag} \{ b_p^{k-1} \text{Id}_{d-1} \}_{p \in \mathcal{S}}$$

and

$$\mathbf{U} := \text{diag} \{ \hat{\mathbf{u}}_{p\tau}^{k-1} \}_{p \in \mathcal{S}}, \quad \mathbf{V} := \text{diag} \{ \tilde{\mathbf{v}}_{p,l}^{k-1} \}_{p \in \mathcal{S}}.$$

As in the previous sections, we use a sub-block notation for the matrices, e.g., $G_{\mathcal{I}_\tau^k}$. Defining now $\tilde{\mathcal{N}} := \mathcal{N} \cup \mathcal{M} \cup \mathcal{I}_n^k$, we obtain after eliminating the Lagrange multiplier the following linear system to be solved in each full Newton step for the contact problem with Coulomb's friction law:

$$\begin{pmatrix} \hat{\mathbf{K}}_{\tilde{\mathcal{N}}\tilde{\mathcal{N}}} & \hat{\mathbf{K}}_{\tilde{\mathcal{N}}\mathcal{I}_\tau^k} & \hat{\mathbf{K}}_{\tilde{\mathcal{N}}\mathcal{A}_m^k} \\ \mathbf{0} & \mathbf{N}_{\mathcal{I}_\tau^k} & \mathbf{0} \\ \mathbf{0} & \mathbf{0} & \mathbf{N}_{\mathcal{A}_m^k} \\ \mathbf{R}_{\mathcal{I}_\tau^k} \hat{\mathbf{K}}_{\mathcal{I}_\tau^k \tilde{\mathcal{N}}} & \mathbf{R}_{\mathcal{I}_\tau^k} \hat{\mathbf{K}}_{\mathcal{I}_\tau^k \mathcal{I}_\tau^k} - \mathbf{G}_{\mathcal{I}_\tau^k} \mathbf{T}_{\mathcal{I}_\tau^k} & \mathbf{R}_{\mathcal{I}_\tau^k} \hat{\mathbf{K}}_{\mathcal{I}_\tau^k \mathcal{A}_m^k} \\ \mathbf{T}'_{\mathcal{A}_m^k} \hat{\mathbf{K}}_{\mathcal{A}_m^k \tilde{\mathcal{N}}} & \mathbf{T}'_{\mathcal{A}_m^k} \hat{\mathbf{K}}_{\mathcal{A}_m^k \mathcal{I}_\tau^k} & \mathbf{T}'_{\mathcal{A}_m^k} \hat{\mathbf{K}}_{\mathcal{A}_m^k \mathcal{A}_m^k} + \mathbf{L}_{\mathcal{A}_m^k} \mathbf{T}_{\mathcal{A}_m^k} \end{pmatrix} \begin{pmatrix} \hat{\mathbf{u}}_{\tilde{\mathcal{N}}}^k \\ \hat{\mathbf{u}}_{\mathcal{I}_\tau^k}^k \\ \hat{\mathbf{u}}_{\mathcal{A}_m^k}^k \end{pmatrix} = \begin{pmatrix} \hat{\mathbf{f}}_{\tilde{\mathcal{N}}} \\ \mathbf{g}_{\mathcal{I}_\tau^k} \\ \mathbf{g}_{\mathcal{A}_m^k} \\ \mathbf{R}_{\mathcal{I}_\tau^k} \hat{\mathbf{f}}_{\mathcal{I}_\tau^k} - \mathbf{j}_{\mathcal{I}_\tau^k} \\ \mathbf{T}'_{\mathcal{A}_m^k} \hat{\mathbf{f}}_{\mathcal{A}_m^k} + \mathbf{r}'_{\mathcal{A}_m^k} \end{pmatrix} \quad (5.27)$$

with the notation

$$\mathbf{T}'_{\mathcal{A}_m^k} := \mathbf{T}_{\mathcal{A}_m^k} - \mathfrak{F} \mathbf{V}_{\mathcal{A}_m^k} \mathbf{N}_{\mathcal{A}_m^k}, \quad \mathbf{R}_{\mathcal{I}_\tau^k} := \mathfrak{F} \mathbf{U}_{\mathcal{I}_\tau^k} \mathbf{N}_{\mathcal{I}_\tau^k}$$

and

$$\mathbf{r}'_{\mathcal{A}_m^k} := \mathbf{r}_{\mathcal{A}_m^k} + \mathbf{G}_{\mathcal{A}_m^k} \mathbf{V}_{\mathcal{A}_m^k}, \quad \mathbf{j}_{\mathcal{I}_\tau^k} := \mathbf{G}_{\mathcal{I}_\tau^k} \mathbf{U}_{\mathcal{I}_\tau^k}.$$

Algorithm 4 Full semi-smooth Newton method for Coulomb's friction law

- 1: set $k = 1$
- 2: initialize $\hat{\mathbf{u}}^0$ and $\boldsymbol{\lambda}^0$ as an initial solution
- 3: set $c > 0$ and the tolerance ε_u
- 4: define for $b_p^{k-1} := \mathfrak{F}(\lambda_{pns}^{k-1} + c(\hat{u}_{pn}^{k-1} - g_p))$ the active and the inactive sets

$$\begin{aligned} \mathcal{I}_n^k &:= \{p \in \mathcal{S} : b_p^{k-1} \leq 0\} \\ \mathcal{I}_\tau^k &:= \{p \in \mathcal{S} : \|\boldsymbol{\lambda}_{p\tau s}^{k-1} + c\hat{\mathbf{u}}_{p\tau}^{k-1}\| - b_p^{k-1} < 0\} \\ \mathcal{A}_m^k &:= \{p \in \mathcal{S} : \|\boldsymbol{\lambda}_{p\tau s}^{k-1} + c\hat{\mathbf{u}}_{p\tau}^{k-1}\| \geq b_p^{k-1} > 0\} \end{aligned}$$

- 5: solve the linear system (5.27) to obtain the new iterate $\hat{\mathbf{u}}^k$ for the displacement
- 6: **if** $\|\hat{\mathbf{u}}^k - \hat{\mathbf{u}}^{k-1}\|/\|\hat{\mathbf{u}}^k\| < \varepsilon_u$ **then**
- 7: stop
- 8: **end if**
- 9: compute the Lagrange multiplier

$$\boldsymbol{\lambda}^k = \mathbf{D}_d^{-1} \left(\hat{\mathbf{f}}_s - \hat{\mathbf{K}}_{sN} \hat{\mathbf{u}}_N^k - \hat{\mathbf{K}}_{sM} \hat{\mathbf{u}}_M^k - \hat{\mathbf{K}}_{sS} \hat{\mathbf{u}}_S^k \right)$$

- 10: set $k = k + 1$
 - 11: go to step 4
-

We mention that as the linear systems (4.14) and (5.19) this system is a regular one although the number of lines seems to be different from the number of unknowns. This is due to the fact that formally lines 2 and 4 are one line belonging to the nodes $p \in \mathcal{I}_\tau^k$ and lines 3 and 5 are one line belonging to the nodes $p \in \mathcal{A}_m^k$. For the nodes $p \in \mathcal{I}_n^k$ no modification of the system is necessary. Thus, these nodes are formally assigned to the set $\tilde{\mathcal{N}} = \mathcal{N} \cup \mathcal{M} \cup \mathcal{I}_n^k$. Comparing the linear system (5.27) with (5.19), we observe that here, the normal and tangential components are point-wise coupled by the lines four and five. In Algorithm 4, the full semi-smooth Newton method for Coulomb's friction law is formulated.

5.6.2. Numerical examples for full Newton approach

As a numerical example, we consider the situation presented in the left picture in Figure 5.16, where a two-dimensional cross section of the problem definition is shown. The ring is fixed on its upper outer edge and the tool on its bottom. Note that the bodies penetrate in their reference configuration. We use Young modulus $E^m = 8.13 \times 10^8$ and a Poisson ratio $\nu^m = 0.3$ for the inner tool modeled by Ω^m , and $E^s = 9 \times 10^7$, $\nu^s = 0.3$ for the outer ring being the slave domain Ω^s . The coefficient of friction is $\mathfrak{F} = 0.7$. The deformed mesh with effective von Mises stress σ_{eff} is shown in the middle and the right of Figure 5.16. The pictures in Figure 5.17 depict the possible contact nodes on the ring being the slave side. The nodes without a line are nodes being not in contact with the

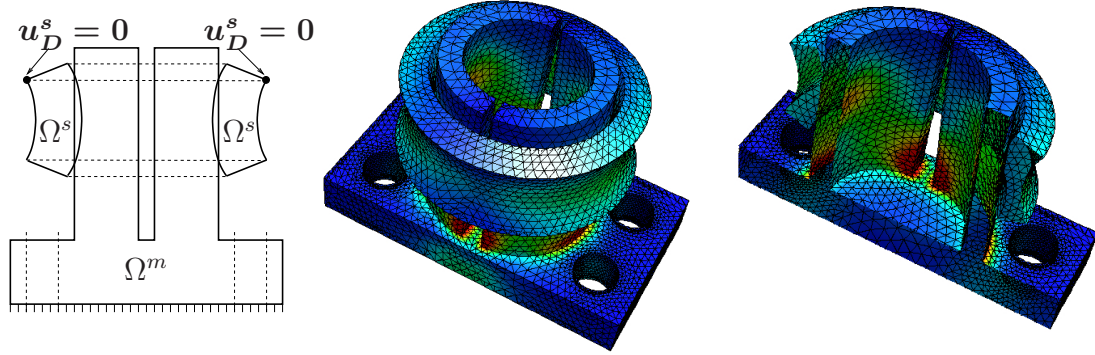


Figure 5.16.: Problem definition (left), deformed mesh with effective von Mises stress σ_{eff} (middle) and cross section of the deformed mesh (right) for $\mathfrak{z} = 0.7$.

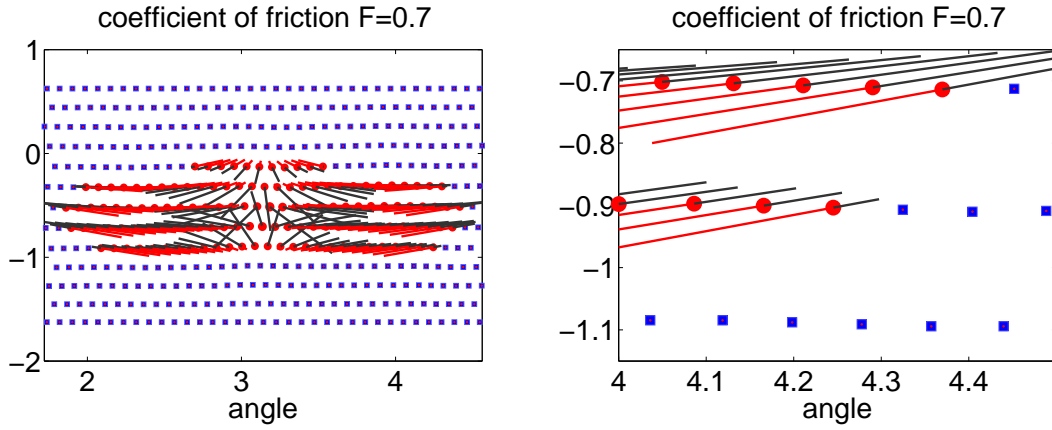


Figure 5.17.: Visualization of the nodes being in contact, together with the deformation and stress vectors for $\mathfrak{z} = 0.7$ (left), and a cutout (middle) – for the legend we refer to Figure 5.5.

inner tool.

To show the behavior of the full semi-smooth Newton approach formulated in Algorithm 4 in comparison to the fixed point based Algorithm 3, we compare the convergence rates of the Lagrange multiplier with those obtained from the fixed point based approach with $m = \infty$ and $k_f = 1$. Our algorithms are initialized with $\mathbf{u}^0 = \mathbf{u}^{0,0} = \mathbf{0}$ and $\boldsymbol{\lambda}^0 = \mathbf{0}$, and the parameter $c = 10^8$ and the tolerance $\varepsilon_u = 10^{-9}$ are used. The finite element mesh consists of 66.600 degrees of freedom. Figure 5.19 shows the relative error $\|\boldsymbol{\lambda}^k - \boldsymbol{\lambda}\|_2 / \|\boldsymbol{\lambda}\|_2$ for the fixed point based and the full Newton approach in a logarithmic scale for the examples presented in the Figures 5.16 and 5.7. We observe superlinear convergence of the full Newton approach, and only half of the iteration steps compared with the fixed point approach are required. For the fixed point approach the convergence rate $\|\boldsymbol{\lambda}^{k+1} - \boldsymbol{\lambda}\|_2 / \|\boldsymbol{\lambda}^k - \boldsymbol{\lambda}\|_2$ tends to approximately 0.3. In a last test, we investigate the influence of the coefficients of friction on the full Newton approach. The convergence rates

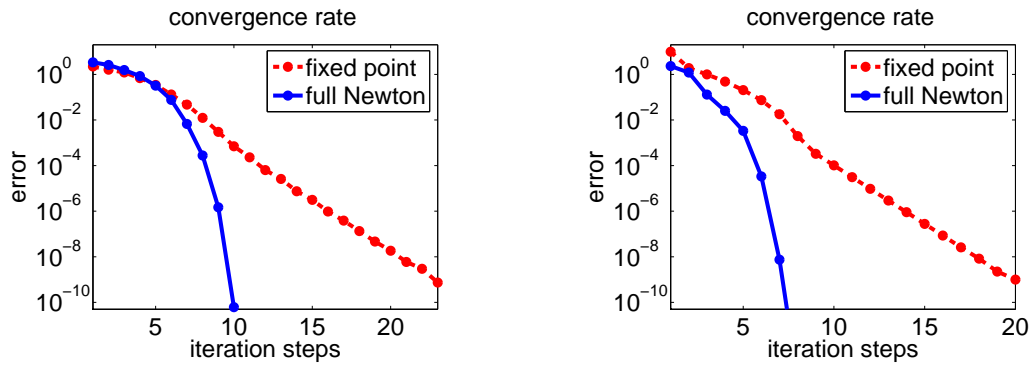


Figure 5.18.: Convergence rates for the examples of Figure 5.16 (left) and Figure 5.7 (right) for the fixed point based and the full Newton approach for $\mathfrak{F} = 0.7$.

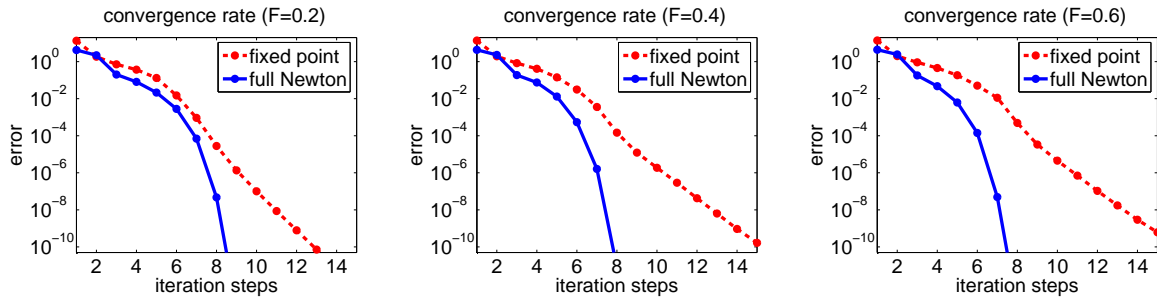


Figure 5.19.: Convergence rates for the example of Figure 5.7 for the fixed point based and the full Newton approach for $\mathfrak{F} = 0.2, 0.4, 0.6$.

for the example presented in Figure 5.7 for the coefficients of friction $\mathfrak{F} = 0.2, 0.4, 0.6$ are shown in Figure 5.19. We use the same initial values as in Figure 5.9. Again, we observe a similar behavior as before for all coefficients of friction. Therefore, the behavior of the full Newton method is independent of the size of the coefficient of friction.

Part IV.

More general applications

6. Large deformations

In this chapter, we extend the algorithms considered in the former sections to contact dynamics in combination with nonlinear material laws as introduced in Subsection 1.3. Since the contact constraints are treated by a semi-smooth Newton method, see Chapter 4 and 5, it is quite natural to handle both nonlinearities, the contact and the material ones, in one iteration loop. Furthermore, this approach even states a Newton method for the whole system. We show, that for the formulation of the Newton system with respect to the new constrained basis, the same modifications as in the linear case have to be applied to the original system with respect to the standard basis. Thus again, existing finite element codes can be easily generalized to our algorithms. We shortly comment on the algorithmic aspects in Section 6.1 and give some numerical examples illustrating the performance of the approach in Section 6.2. Finally, we mention that we will not consider damping strategies and globalization techniques in this Chapter as all over in this thesis. For an overview about damping strategies we refer the interested reader to the textbook [34]. A line search technique has been applied to the the semi-smooth methods introduced in this thesis within the framework of pseudo-rigid bodies in [95].

In the second part of this chapter we focus on energy-conserving time-discretization algorithms for dynamic contact problems. The simulation of dynamic contact problems using finite element techniques can already be found in [132]. The Hilber-Hughes-Taylor-scheme [71] and the generalized α -method introduced in [30] are numerically dissipative schemes. As an example for an algorithmic energy-conserving scheme we mention the energy-momentum method [127] and the method by Gonzales introduced in [55]. The second one is used within this work. These two methods conserves not only the energy but also the linear and the angular momentum. Based on [71] in [67] the authors introduced a controllable energy dissipation while conserving momenta in conservative strategies like [55]. A numerical approach which enforces the conservation of the total energy by an additional constraint can be found in [102]. Furthermore, in [101, 103] the generalized energy-momentum method was introduced. This approach combines the energy-momentum method with the generalized α -method. This approaches were applied to dynamic contact problems in combination with the algorithm introduced in Chapter 4 in [59]. A stabilized discontinuous mortar formulation in the framework of elastodynamics was introduced in [65, 66]. Based on the Hamilton theory [13, 70] presents an energy-conserving scheme for dynamic contact problems by using a discrete gradient of the Hamilton functional. For a detailed literature overview how to treat numerically the contact part to get an energy-conserving approach, we refer to the introduction of Section 6.3.

We start in Section 6.1 with the extension of our algorithm to the case of nonlinear material laws. Numerical examples illustrating its performance are given in Section 6.2.

Section 6.3 introduces the formulation and the numerical treatment for contact dynamics followed by a various set of numerical examples in Section 6.3.1.

6.1. Algorithmic aspects for nonlinear materials

By using a nonlinear stress-strain relation, the material part in the weak formulation (2.19) represented by $a(\cdot, \cdot)$, is no longer bilinear. It is just linear with respect to the second argument, i.e., the test function. Thus, neglecting the mass term, the algebraic version (2.37) reads

$$\mathbf{K}(\mathbf{u}) + \mathbf{C}\boldsymbol{\lambda} = \mathbf{f}, \quad (6.1)$$

where we replaced the original linear stiffness part $\mathbf{K}\mathbf{u}$ by the nonlinear functional $\mathbf{K}(\cdot) : \mathbb{R}^{dN_V} \rightarrow \mathbb{R}^{dN_V}$. Here, N_V denotes the total number of nodes of the finite element space \mathbf{V}^h . Reminding that the coefficient vector \mathbf{u} is the vector corresponding to the discrete function \mathbf{u}^h and using the same notation as in (2.36), the entries of this functional are given by

$$(\mathbf{K}(\mathbf{u}))_i[p] := \sum_{i=s,m} \int_{\Omega^i} \mathbf{P}^i(\mathbf{u}^{h,i}) : \nabla(\phi_p \mathbf{e}_i) \, d\mathbf{x}, \quad 1 \leq i \leq d, \quad 1 \leq p \leq N_V. \quad (6.2)$$

For possible nonlinear stress-strain relations $\mathbf{P}(\mathbf{u}^h)$, we refer to Subsection 1.3.

To apply Newton's method, we consider (2.37) with respect to the new constrained basis introduced in Section 2.3. To do so, we write the functional $\mathbf{K}(\mathbf{u})$ with respect to the constrained basis. The entries of this new functional $\hat{\mathbf{K}}(\hat{\mathbf{u}}) : \mathbb{R}^{dN_V} \rightarrow \mathbb{R}^{dN_V}$ are now given by replacing the test function ϕ_p in (6.2) by the constrained test function $\hat{\phi}_p$. Due to the linear behavior of the transformation (2.22) for the basis functions and the transformation formula (2.24) for the coefficient vector we directly get the relation

$$\hat{\mathbf{K}}(\hat{\mathbf{u}}) = \mathbf{Q}_d \mathbf{K}(\mathbf{Q}_d^\top \hat{\mathbf{u}}). \quad (6.3)$$

Denoting by $\partial\mathbf{K}(\mathbf{u})$ the Jacobian of $\mathbf{K}(\mathbf{u})$ with respect to the standard nodal basis and by $\partial\hat{\mathbf{K}}(\hat{\mathbf{u}})$ the Jacobian of $\hat{\mathbf{K}}(\hat{\mathbf{u}})$ with respect to the constrained basis, we obtain due to (6.3) by applying the chain rule the relation

$$\partial\hat{\mathbf{K}}(\hat{\mathbf{u}}) = \mathbf{Q}_d \partial\mathbf{K}(\mathbf{u}) \mathbf{Q}_d^\top. \quad (6.4)$$

This equation states, that the Jacobian of the stiffness term with respect to the new constrained basis can be obtained by the same transformation from the Jacobian with respect to the standard basis functions as the linear stiffness matrix with respect to the constrained basis is obtained by the original one as stated in (2.39). Thus, one can easily extend existing finite element codes with existing assembling routines for the Jacobian $\partial\mathbf{K}(\mathbf{u})$ to our semi-smooth Newton approach. Furthermore, we remark that the transformation (6.4) can be carried out locally in an efficient way.

To formulate Newton's method, we consider the algebraic form of (6.1) with respect to the constrained basis as stated in (2.41) and define the function

$$\mathbf{F}(\cdot, \cdot) : \mathbb{R}^{dN_V} \times \mathbb{R}^{dN_M} \rightarrow \mathbb{R}^{dN_V}$$

by

$$\mathbf{F}(\hat{\mathbf{u}}, \boldsymbol{\lambda}) := \hat{\mathbf{K}}(\hat{\mathbf{u}}) + \hat{\mathbf{C}}\boldsymbol{\lambda} - \hat{\mathbf{f}}. \quad (6.5)$$

Here, N_M denotes the number of nodes on the contact interface Γ_c^s , i.e. $N_M = |\mathcal{S}|$. For the definition of the transformed variables $\hat{\mathbf{C}}$ and $\hat{\mathbf{f}}$, we refer to (2.41) and (2.40), respectively. Together with the nonlinear contact conditions expressed by the semi-smooth function $C(\hat{\mathbf{u}}_p, \boldsymbol{\lambda}_p)$ in (5.18), we obtain our solution by solving the nonlinear system

$$\begin{pmatrix} \mathbf{F}(\hat{\mathbf{u}}, \boldsymbol{\lambda}) \\ \mathbf{C}(\hat{\mathbf{u}}, \boldsymbol{\lambda}) \end{pmatrix} = \mathbf{0}, \quad (6.6)$$

where for $p \in \mathcal{S}$ the entries $C(\hat{\mathbf{u}}_p, \boldsymbol{\lambda}_p)$ of the function

$$\mathbf{C}(\cdot, \cdot) : \mathbb{R}^{dN_V} \times \mathbb{R}^{dN_M} \rightarrow \mathbb{R}^{dN_M}$$

are given in (5.18). In the case of the full Coulomb approach introduced in Section 5.6, we have to replace the nonlinear complementarity function $C_\tau(\cdot, \cdot)$ in the frictional constraints (5.18) by the nonlinear complementarity function $D_\tau(\cdot, \cdot)$ introduced in (5.21).

In the following, we shortly present the semi-smooth Newton method for equation (6.6) for the case of the full Newton approach for Coulomb's friction law given by Algorithm 4. We mention that also Algorithms 1-3 can be extended in the same way to nonlinear material laws. The extension of the Algorithms 1, 2 and 4 gives rise to a semi-smooth Newton approach, while the extension of the fixed point based approach for Coulomb's friction law presented in Algorithm 3 does not lead to a Newton approach, since due to the fixed point based update of the friction bound this algorithm itself is not a full Newton method.

For the derivative of the function (6.5) in the direction $(\delta\hat{\mathbf{u}}, \delta\boldsymbol{\lambda})$ we compute

$$D\mathbf{F}(\hat{\mathbf{u}}, \boldsymbol{\lambda})(\delta\hat{\mathbf{u}}, \delta\boldsymbol{\lambda}) = \partial\hat{\mathbf{K}}(\hat{\mathbf{u}}) \delta\hat{\mathbf{u}} + \hat{\mathbf{C}} \delta\boldsymbol{\lambda} \quad (6.7)$$

Let $(\mathbf{u}^{k-1}, \boldsymbol{\lambda}^{k-1})$ be the previous iterate, we write the new iterate as

$$(\mathbf{u}^k, \boldsymbol{\lambda}^k) = (\mathbf{u}^{k-1}, \boldsymbol{\lambda}^{k-1}) + (\delta\mathbf{u}^k, \delta\boldsymbol{\lambda}^k),$$

we obtain the Newton increment for the first line of the Newton system applied to (6.6) by solving the linear equation system

$$D\mathbf{F}(\hat{\mathbf{u}}^k, \boldsymbol{\lambda}^k)(\delta\hat{\mathbf{u}}^k, \delta\boldsymbol{\lambda}^k) = -\mathbf{F}(\hat{\mathbf{u}}^k, \boldsymbol{\lambda}^k).$$

Using (6.5) and (6.7) this system reads

$$\partial\hat{\mathbf{K}}(\hat{\mathbf{u}}^{k-1}) \delta\hat{\mathbf{u}}^k + \hat{\mathbf{C}}\boldsymbol{\lambda}^k = \hat{\mathbf{f}} - \hat{\mathbf{K}}(\hat{\mathbf{u}}^{k-1}). \quad (6.8)$$

The semi-smooth Newton method applied to the second line in (6.6) is given in Subsection 5.6.1. After determining the three disjoint subsets \mathcal{I}_n^k , \mathcal{I}_τ^k and $\mathcal{A}_{\tau n}^k$ from the old iterate $(\hat{\mathbf{u}}^{k-1}, \boldsymbol{\lambda}^{k-1})$, the conditions for the nodes are given in (5.24) -(5.26). These conditions are formulated with respect to the entries $\hat{\mathbf{u}}_p^k$ of $\hat{\mathbf{u}}^k$. Thus, for the entries $\delta\hat{\mathbf{u}}_p^k$ of the increment $\delta\hat{\mathbf{u}}^k$ we have to work with

$$\delta\hat{u}_{pn}^k = g_p - \hat{u}_{pn}^{k-1} \quad \text{and} \quad \delta\hat{u}_{p\tau}^k + (\tilde{\nu}\hat{u}_{p\tau}^{k-1}/b_p^{k-1}) \lambda_{pns}^k = \mathbf{0} \quad (6.9)$$

instead of (5.25) for all sticky nodes $p \in \mathcal{I}_\tau^k$ and with

$$\begin{aligned} \delta \hat{u}_{pn}^k &= g_p - \hat{u}_{pn}^{k-1} \quad \text{and} \\ -\boldsymbol{\lambda}_{p\tau s}^k + L_{p,l}^{k-1} \delta \hat{\mathbf{u}}_{p\tau}^k + \mathfrak{F} \mathbf{v}_{p,l}^{k-1} \lambda_{pns}^k &= \mathbf{r}_{p,l}^{k-1} + b_p^{k-1} \mathbf{v}_{p,l}^{k-1} - L_{p,l}^{k-1} \hat{\mathbf{u}}_{p\tau}^{k-1} \end{aligned} \quad (6.10)$$

instead of (5.26) for all slip nodes $p \in \mathcal{A}_{\tau n}^k$. Since the Neumann boundary condition for the nodes not in contact is only expressed in the Lagrange multiplier we can directly use (5.24) for the nodes containing to the set \mathcal{I}_n^k . Comparing (6.8), (6.9) and (6.10) with the formulation achieved for the linear material law in Subsection 5.6.1, we obtain that only the right hand sides have to be adjusted and the stiffness matrix $\hat{\mathbf{K}}$ has to be replaced by the Jacobian $\partial \hat{\mathbf{K}}$. Using the same modifications given in Subsection 5.1.1 and the notations introduced in Subsection 5.6.1, we obtain similar to (5.27) after eliminating the Lagrange multiplier the linear system

$$\begin{pmatrix} \partial \hat{\mathbf{K}}_{\tilde{\mathcal{N}}\tilde{\mathcal{N}}} & \partial \hat{\mathbf{K}}_{\tilde{\mathcal{N}}\mathcal{I}_\tau^k} & \partial \hat{\mathbf{K}}_{\tilde{\mathcal{N}}\mathcal{A}_m^k} \\ \mathbf{0} & \mathbf{N}_{\mathcal{I}_\tau^k} & \mathbf{0} \\ \mathbf{0} & \mathbf{0} & \mathbf{N}_{\mathcal{A}_m^k} \\ \mathbf{R}_{\mathcal{I}_\tau^k} \partial \hat{\mathbf{K}}_{\mathcal{I}_\tau^k \tilde{\mathcal{N}}} & \mathbf{R}_{\mathcal{I}_\tau^k} \partial \hat{\mathbf{K}}_{\mathcal{I}_\tau^k \mathcal{I}_\tau^k} - \mathbf{G}_{\mathcal{I}_\tau^k} \mathbf{T}_{\mathcal{I}_\tau^k} & \mathbf{R}_{\mathcal{I}_\tau^k} \partial \hat{\mathbf{K}}_{\mathcal{I}_\tau^k \mathcal{A}_m^k} \\ \mathbf{T}'_{\mathcal{A}_m^k} \partial \hat{\mathbf{K}}_{\mathcal{A}_m^k \tilde{\mathcal{N}}} & \mathbf{T}'_{\mathcal{A}_m^k} \partial \hat{\mathbf{K}}_{\mathcal{A}_m^k \mathcal{I}_\tau^k} & \mathbf{T}'_{\mathcal{A}_m^k} \partial \hat{\mathbf{K}}_{\mathcal{A}_m^k \mathcal{A}_m^k} + \mathbf{L}_{\mathcal{A}_m^k} \mathbf{T}_{\mathcal{A}_m^k} \end{pmatrix} \begin{pmatrix} \delta \hat{\mathbf{u}}_{\tilde{\mathcal{N}}}^k \\ \delta \hat{\mathbf{u}}_{\mathcal{I}_\tau^k}^k \\ \delta \hat{\mathbf{u}}_{\mathcal{A}_m^k}^k \end{pmatrix} = \begin{pmatrix} \hat{\mathbf{f}}_{\tilde{\mathcal{N}}}^{NL} \\ \mathbf{g}_{\mathcal{I}_\tau^k}^{NL} \\ \mathbf{g}_{\mathcal{A}_m^k}^{NL} \\ \mathbf{R}_{\mathcal{I}_\tau^k} \hat{\mathbf{f}}_{\mathcal{I}_\tau^k}^{NL} \\ \mathbf{T}'_{\mathcal{A}_m^k} \hat{\mathbf{f}}_{\mathcal{A}_m^k}^{NL} + \mathbf{r}'_{\mathcal{A}_m^k}^{NL} \end{pmatrix} \quad (6.11)$$

for the increment $\delta \hat{\mathbf{u}}^k$, where the adjusted right hand sides are given by

$$\begin{aligned} \hat{\mathbf{f}}^{NL} &:= \hat{\mathbf{f}} - \hat{\mathbf{K}}(\hat{\mathbf{u}}^{k-1}), \\ \mathbf{g}^{NL} &:= \mathbf{g} - (\hat{u}_{pn}^{k-1})_{p \in S}, \\ \mathbf{r}'^{NL} &:= \mathbf{r}' - \mathbf{L}\mathbf{U}. \end{aligned}$$

We remark that due to the zero right hand side of the second equation in (6.9), the vector $\mathbf{j}_{\mathcal{I}_\tau^k}$ in (5.27) vanishes in (6.11). Although the number of the lines and the number of unknowns seems not to be same, they do so. This is due to the same reason mentioned after the linear system (5.27). Formally, lines 2 and 4 are one line belonging to the nodes $p \in \mathcal{I}_\tau^k$ and lines 3 and 5 are one line belonging to the nodes $p \in \mathcal{A}_m^k$. Since the linear system (6.11) is formulated for the increment $\delta \hat{\mathbf{u}}^k$, the Lagrange multiplier $\boldsymbol{\lambda}^k$ is obtained by the local post-process

$$\boldsymbol{\lambda}^k = \mathbf{D}_d^{-1} \left(\hat{\mathbf{f}}_S^{NL} - \partial \hat{\mathbf{K}}_{S\mathcal{N}} \delta \hat{\mathbf{u}}_{\mathcal{N}}^k - \partial \hat{\mathbf{K}}_{S\mathcal{M}} \delta \hat{\mathbf{u}}_{\mathcal{M}}^k - \partial \hat{\mathbf{K}}_{SS} \delta \hat{\mathbf{u}}_S^k \right).$$

Now, we summarize our explanations in Algorithm 5. This algorithm is a direct consequence of Algorithm 4. In contrast to that algorithm, the system matrix and the right hand side for the stiffness part have to be assembled in each iteration step, see step 5.

6.2. Numerical examples for nonlinear materials

In this section, we present two numerical examples with Coulomb's friction law to show the performance of Algorithm 5. The first example is in the two-dimensional setting,

Algorithm 5 Semi-smooth Newton method for nonlinear material with Coulomb friction

- 1: set $k = 1$
- 2: initialize $\hat{\mathbf{u}}^0$ and $\boldsymbol{\lambda}^0$ as an initial solution
- 3: set $c > 0$ and the tolerance ε_u
- 4: define for $b_p^{k-1} := \mathfrak{F}(\lambda_{pns}^{k-1} + c(\hat{u}_{pn}^{k-1} - g_p))$ the active and the inactive sets

$$\begin{aligned} \mathcal{I}_n^k &:= \{p \in \mathcal{S} : b_p^{k-1} \leq 0\} \\ \mathcal{I}_\tau^k &:= \{p \in \mathcal{S} : \|\boldsymbol{\lambda}_{p\tau s}^{k-1} + c\hat{\mathbf{u}}_{p\tau}^{k-1}\| - b_p^{k-1} < 0\} \\ \mathcal{A}_m^k &:= \{p \in \mathcal{S} : \|\boldsymbol{\lambda}_{p\tau s}^{k-1} + c\hat{\mathbf{u}}_{p\tau}^{k-1}\| \geq b_p^{k-1} > 0\} \end{aligned}$$

- 5: assemble the Jacobian $\partial\hat{\mathbf{K}}(\hat{\mathbf{u}}^{k-1})$ and the functional $\hat{\mathbf{K}}(\hat{\mathbf{u}}^{k-1})$
- 6: solve the linear system (6.11) to obtain the increment $\delta\hat{\mathbf{u}}^k$ and compute the new iterate $\hat{\mathbf{u}}^k = \hat{\mathbf{u}}^{k-1} + \delta\hat{\mathbf{u}}^k$ for the displacement
- 7: **if** $\|\hat{\mathbf{u}}^k - \hat{\mathbf{u}}^{k-1}\|/\|\hat{\mathbf{u}}^k\| < \varepsilon_u$ **then**
- 8: stop
- 9: **end if**
- 10: compute the Lagrange multiplier

$$\boldsymbol{\lambda}^k = \mathbf{D}_d^{-1} \left(\hat{\mathbf{f}}_S^{NL} - \partial\hat{\mathbf{K}}_{SN}\delta\hat{\mathbf{u}}_N^k - \partial\hat{\mathbf{K}}_{SM}\delta\hat{\mathbf{u}}_M^k - \partial\hat{\mathbf{K}}_{SS}\delta\hat{\mathbf{u}}_S^k \right)$$

- 11: set $k = k + 1$
 - 12: go to step 4
-

whereas the second one is in the three-dimensional case. We test different material nonlinearities for both examples.

Two-dimensional example

We consider the situation depicted in Figure 6.1. A half of an annulus modeled by the domain $\Omega^s := \{\mathbf{x} = (x_1, x_2)^\top \in \mathbb{R}^2 : 60 \leq \|\mathbf{x}\| \leq 100 \wedge x_2 \leq 0\}$, which is assumed to be the slave side, is pressed against the rectangle $\Omega^m := [-140, 140] \times [-225, -100]$, which is assumed to be the master side. We fix the rectangle at its lower side and apply the following unsymmetric Dirichlet boundary condition at the top boundary of the upper body:

$$\mathbf{u}_{D,l}^s = \begin{pmatrix} 0 \\ -8 \end{pmatrix}, \quad \mathbf{u}_{D,r}^s = \begin{pmatrix} 0 \\ -5 \end{pmatrix},$$

see also the left picture in Figure 6.1. All other boundary segments are subjected to homogeneous Neumann data. Furthermore, the left picture in Figure 6.1 shows the deformed initial mesh; all computations presented below are done on a fine mesh obtained after three uniform refinement steps. Thus, the domain Ω^s is discretized by 5313 nodes and domain Ω^m by 8385 nodes. As material parameters, we use Young moduli $E^s = 2100$, $E^m = 2986$ and Poisson ratio $\nu = 0.3$ for both bodies. Algorithm 5 is initialized

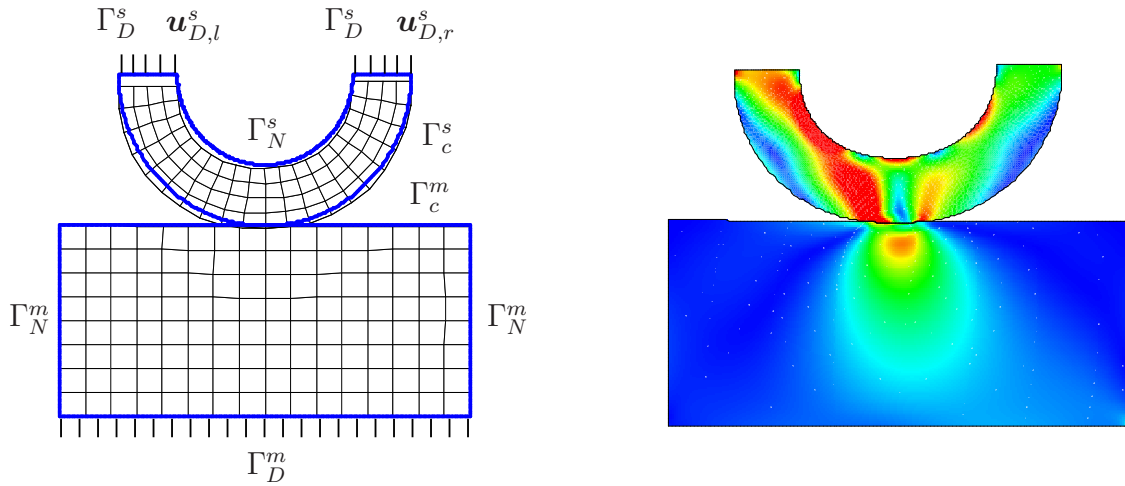


Figure 6.1.: Problem definition, initial configuration and deformed mesh on a coarse level (left) and effective stress on the deformed mesh on a fine level for the coefficient of friction $\mathfrak{F} = 0.6$ (right).

with $\hat{\mathbf{u}}^0 = \mathbf{0}$ and $\boldsymbol{\lambda}^0 = \mathbf{0}$. Furthermore, we set $c = 10^5$ and $\varepsilon_u = 10^{-10}$.

In the right picture in Figure 6.1, the effective von Mises stress on the distorted domains is shown for the coefficient of friction $\mathfrak{F} = 0.6$ and the neo-Hookean material law, see (1.43). Figure 6.2 shows the normal and the tangential part of the Lagrange multiplier as well as the friction bound $\pm\mathfrak{F}\lambda_n$ and the amplified tangential displacement for various values of the coefficient of friction \mathfrak{F} in combination with the neo-Hookean material law. One observes, that the contact constraints for Coulomb's friction model are verified and the region of sticky nodes (between the two vertical dashed lines) increases with the coefficient of friction \mathfrak{F} . Figure 6.3 shows the relative errors $\|\hat{\mathbf{u}}^k - \hat{\mathbf{u}}^{k-1}\|_2 / \|\hat{\mathbf{u}}^k\|_2$ in a logarithmic scale for various values for \mathfrak{F} for the neo-Hookean material law (left picture) and for the Saint Venant–Kirchhoff material, see (1.34), (right picture). As expected, we obtain asymptotically a superlinear convergence behavior of Algorithm 5.

Three-dimensional example

As an example in the three-dimensional case, we consider the situation illustrated in Figure 6.4. Two half-cylinders are pressed against each other. The upper half-cylinder Ω^s is only fixed at its right upper surface and pressed by the constant surface load

$$\mathbf{p}_N^s = \begin{pmatrix} 0 \\ 0 \\ -500 \end{pmatrix}$$

applied on its left upper surface against the lower half-cylinder. In a first setting (as indicated in the left picture in Figure 6.4) the lower half-cylinder, assumed to be the master body Ω^m , is fixed at its two lower surfaces. In a second setting we only fix the

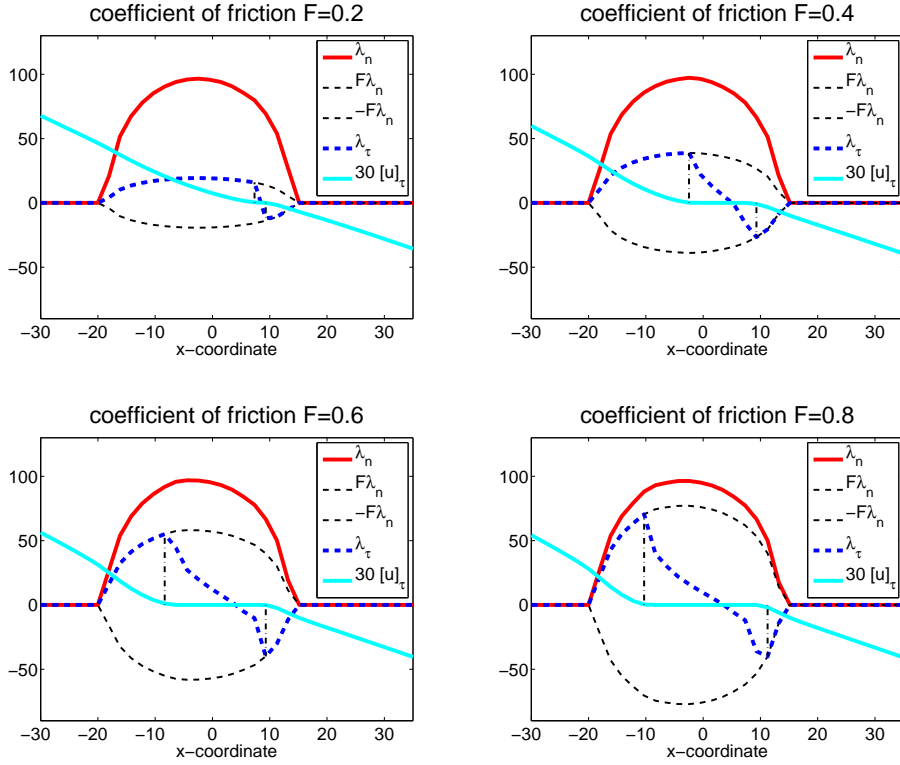


Figure 6.2.: Visualization of contact constraints for Coulomb's friction model for the coefficients of friction $\mathfrak{F} = 0.2, 0.4, 0.6, 0.8$.

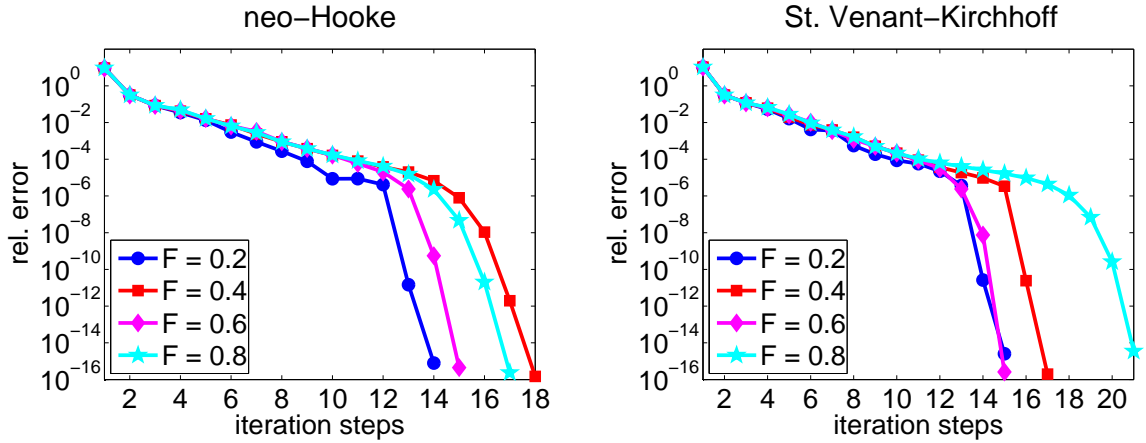


Figure 6.3.: Convergence behavior for $\mathfrak{F} = 0.2, 0.4, 0.6, 0.8$.

left lower surface of Ω^m and apply homogeneous Neumann boundary conditions, i.e., $\mathbf{p}_N^s = \mathbf{0}$, on the right lower surface. As the top view (right picture in Figure 6.4) shows, the situation is not symmetric with respect to the x_2 -axis. The axis of the two half-cylinders are orthogonal to the x_1x_3 -plane with midpoints $a_m = (0.15, -0.185)^\top$ and $a_s = (0.25, 0.175)^\top$. For the inner and outer radii of the cylinders we set $r_i^m = r_i^s = 0.115$

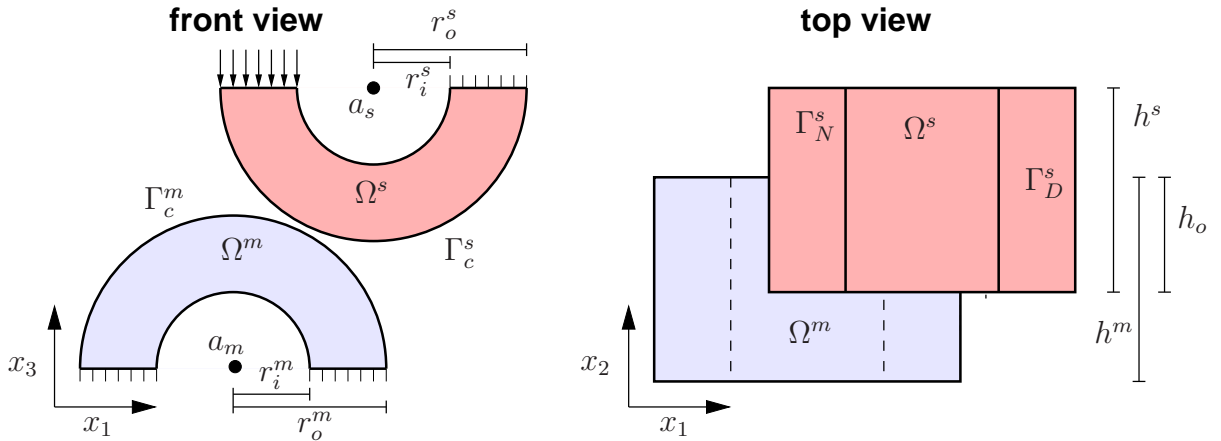


Figure 6.4.: Problem definition (first setting).

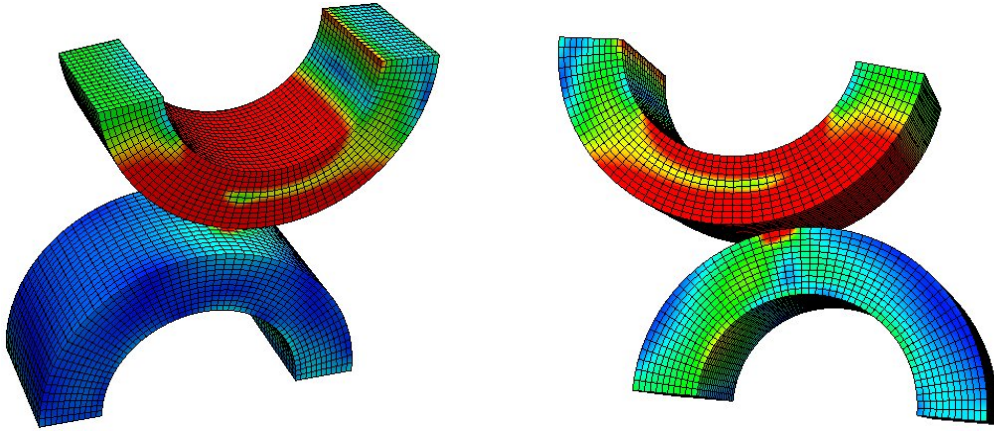


Figure 6.5.: Effective von Mises stress for the first setting.

and $r_o^m = r_o^s = 0.185$. For the length we set $h^m = h^s = 0.16$ and for the overlap we choose $h_o = 0.1$. We set the Young moduli equal to $E^m = 2.1 \times 10^5$ and $E^s = 1.8 \times 10^5$. For the Poisson ratios we choose $\nu^m = 0.3$ and $\nu^s = 0.25$. For the coefficient of friction, we set $\mathfrak{f} = 0.5$. We discretize the bodies with hexahedral finite elements; each body consists of 12 084 nodes. The deformed meshes with the finite element mesh and the effective von Mises stress for the neo-Hookean material are shown in Figure 6.5 for the first setting and in Figure 6.6 for the second setting. The left pictures in these figures show the view from the front, whereas the right pictures show the view from the back. Comparing these two figures, we observe a different effective stress for the second setting than for the first one. The major difference occurs in the lower half-cylinder.

In our algorithm, we choose the parameters $c = 10^6$, $\varepsilon_u = 10^{-10}$ and start the iteration process with $\hat{\mathbf{u}}^0 = \mathbf{0}$ and $\boldsymbol{\lambda}^0 = \mathbf{0}$. The convergence behavior of the two settings both for the neo-Hookean material law and the Saint Venant–Kirchhoff material law are presented in Figure 6.7. Again, we observe asymptotically a superlinear convergence behavior of Algorithm 5, whereas for the second setting in combination with the Saint Venant–

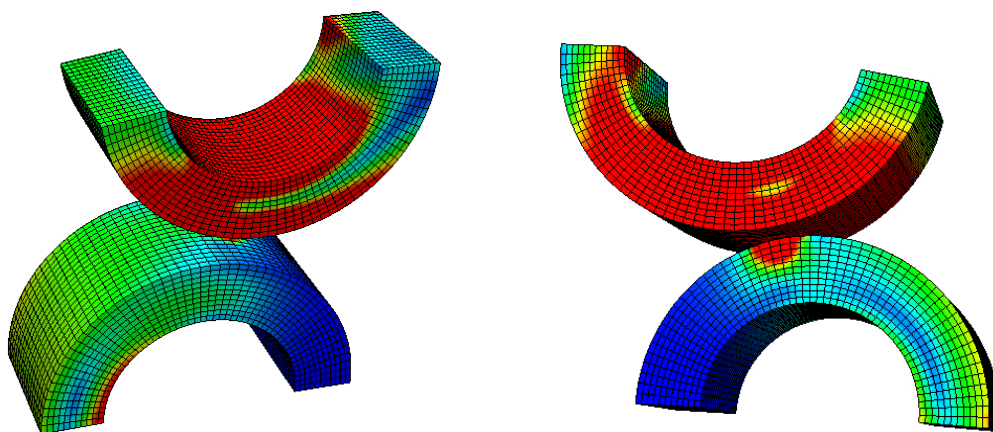


Figure 6.6.: Effective von Mises stress for the second setting.

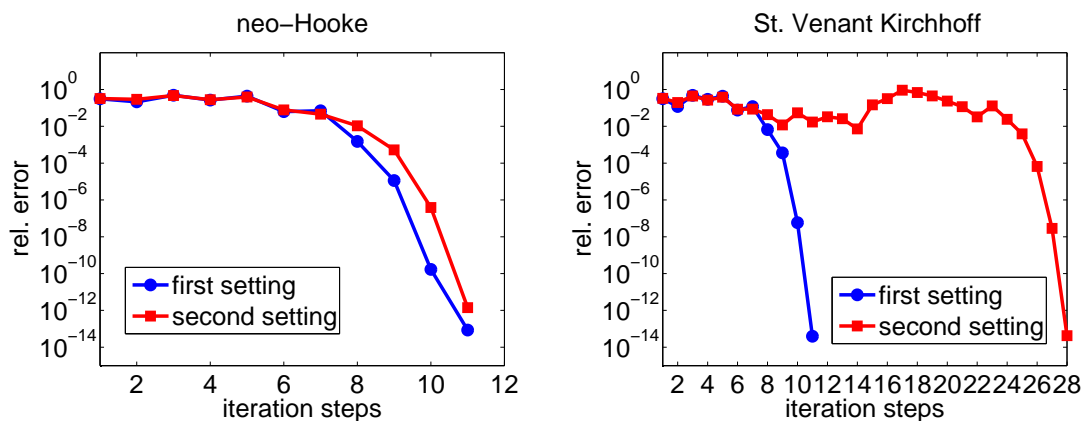


Figure 6.7.: Convergence behavior for neo-Hookean and Saint Venant–Kirchhoff material.

Kirchhoff material the superlinear behavior appears very late.

6.3. Contact dynamics with large deformations

In this section we extend the algorithm for nonlinear material laws introduced in the previous section to the case of dynamical contact problems. Some of the presented results have been published in [19, 41, 56]. In particular we focus on energy conserving time integration schemes based on the midpoint rule, which is a special case of the generalized α method, see [30]. The key to get an energy-conserving algorithm for the structural part is the treatment of the stress update in the time-stepping procedure. Here, we apply the method introduced in [55] for general nonlinear material laws, where the use of a discrete derivative to define the required algorithmic update of the second Piola–Kirchhoff stress tensor is proposed. This approach was extended in [67] to provide an energy-controlling time integration scheme for contact problems without friction enforcing the standard Karush-Kuhn-Tucker conditions at time discretization points. Furthermore,

in [127], the authors proposed an algorithmic update of the stress tensor based on the mean value theorem. However, this requires the solution of a nonlinear equation at each quadrature point to find this solution. For the Saint Venant–Kirchhoff material this equation degenerates to an equation with an explicit root. Recently, in [109] the method introduced in [127] was extended in a manner, such that the arising nonlinear algorithmic equations can be solved by the quadratically convergent Newton-Raphson method. To get energy-conserving time integration schemes for the contact part, we follow the approaches introduced in [107] for the frictionless contact problem and in [23] for the frictional case. For the energy-conserving scheme in case of frictionless case, [107] allows a small penetration of the bodies in order to fulfill the so called persistency condition in a discrete sense. This penetration tends towards zero if the time step size tends towards zero. To overcome this, [108] suggests an velocity update approach, where the additional non-physical algorithmic contact work is transferred to the kinetic part and the non-penetration condition is fulfilled. However, the discrete version of the persistency condition is no longer satisfied.

6.3.1. Energy conserving time integration

As already mentioned in the introduction, the time discretization of the weak form (2.6) is based on the midpoint rule. We define $t^k := k \Delta t$, $k = 0, \dots, N_T$, where the time step size is given by $\Delta t := T/N_T$. Furthermore, we denote by $\mathbf{u}^k(\mathbf{x}) \approx \mathbf{u}(\mathbf{x}, t^k)$ the approximation of the displacement field at time t^k . Defining

$$\Delta \mathbf{u}^k := \mathbf{u}^{k+1} - \mathbf{u}^k, \quad \Delta \dot{\mathbf{u}}^k := \dot{\mathbf{u}}^{k+1} - \dot{\mathbf{u}}^k$$

the relations based on the midpoint rule are given by

$$\mathbf{u}^{k+1/2} := \frac{1}{2}(\mathbf{u}^{k+1} + \mathbf{u}^k) = \mathbf{u}^k + \frac{\Delta \mathbf{u}^k}{2}, \quad (6.12a)$$

$$\dot{\mathbf{u}}^{k+1/2} := \frac{1}{2}(\dot{\mathbf{u}}^{k+1} + \dot{\mathbf{u}}^k) = \frac{\Delta \mathbf{u}^k}{\Delta t} = \frac{2}{\Delta t}(\mathbf{u}^{k+1/2} - \mathbf{u}^k), \quad (6.12b)$$

$$\ddot{\mathbf{u}}^{k+1/2} := \frac{\dot{\mathbf{u}}^{k+1} - \dot{\mathbf{u}}^k}{\Delta t} = \frac{2}{\Delta t^2} \Delta \mathbf{u}^k - \frac{2}{\Delta t} \dot{\mathbf{u}}^k. \quad (6.12c)$$

The evaluation of the first equation of the variational formulation (2.6) at time $t^{k+1/2}$ leads for all $\mathbf{v} \in \mathbf{V}_0$ to

$$\frac{2}{\Delta t^2} m(\Delta \mathbf{u}^k, \mathbf{v}) + a_{\text{algo}}\left((\mathbf{u}^k, \mathbf{u}^{k+1}), \mathbf{v}\right) + \langle [\mathbf{v}], \boldsymbol{\lambda}^{k+1/2} \rangle = f^{k+1/2}(\mathbf{v}) \quad (6.13)$$

with the right hand side

$$f^{k+1/2}(\mathbf{v}) := f_{k+1/2}(\mathbf{v}) + \frac{2}{\Delta t} m(\dot{\mathbf{u}}^k, \mathbf{v}), \quad (6.14)$$

where $f_{k+1/2}(\mathbf{v})$ is $f(\mathbf{v})$ evaluated at time $t^{k+1/2} := (k + 1/2)\Delta t$. Following [55], The algorithmic form $a_{\text{algo}}(\cdot, \cdot)$ in (6.13) is given by

$$a_{\text{algo}}\left((\mathbf{u}^k, \mathbf{u}^{k+1}), \mathbf{v}\right) := \sum_{i=s,m} \int_{\Omega^i} \mathbf{F}^i(\mathbf{u}^{k+1/2}) \mathbf{S}_{\text{algo}}^i(\mathbf{u}^k, \mathbf{u}^{k+1}) : \nabla \mathbf{v}^i \, d\mathbf{x} \quad (6.15)$$

with the algorithmic second Piola–Kirchhoff stress tensor

$$\mathbf{S}_{\text{algo}}(\mathbf{u}^k, \mathbf{u}^{k+1}) := 2 dW(\mathbf{C}^k, \mathbf{C}^{k+1})$$

and $dW(\mathbf{C}^k, \mathbf{C}^{k+1})$ is a discrete derivative of the energy functional defined by

$$dW(\mathbf{C}^k, \mathbf{C}^{k+1}) := \frac{\partial W}{\partial \mathbf{C}}(\mathbf{C}^{k+1/2}) + \left(\frac{W(\mathbf{C}^{k+1}) - W(\mathbf{C}^k) - \frac{\partial W}{\partial \mathbf{C}}(\mathbf{C}^{k+1/2}) : \mathbf{M}}{\|\mathbf{M}\|^2} \right) \mathbf{M}$$

with

$$\mathbf{M} := \mathbf{C}^{k+1} - \mathbf{C}^k, \quad \|\mathbf{M}\|^2 := \mathbf{M} : \mathbf{M}.$$

The discrete right Cauchy strain tensors are given by

$$\mathbf{C}^k = (\mathbf{F}(\mathbf{u}^k))^\top \mathbf{F}(\mathbf{u}^k), \quad \mathbf{C}^{k+1} = (\mathbf{F}(\mathbf{u}^{k+1}))^\top \mathbf{F}(\mathbf{u}^{k+1}), \quad \mathbf{C}^{k+1/2} = \frac{1}{2}(\mathbf{C}^k + \mathbf{C}^{k+1}).$$

We remark, that the form $a_{\text{algo}}(\cdot, \cdot)$ is no longer bilinear. It is only linear with respect to the second argument representing the test function.

For each time interval $[t^k, t^{k+1}]$, we linearize the non-penetration condition (1.17) in normal direction and end up with

$$[\Delta u]_n^k - g^k \leq 0, \quad \lambda_n^{k+1/2} \geq 0, \quad \lambda_n^{k+1/2}([\Delta u]_n^k - g^k) = 0, \quad (6.16)$$

where the gap g^k at time t^k is defined by

$$g^k(\mathbf{x}) := -(\varphi^{s,k}(\mathbf{x}) - \varphi^{m,k}(R_{t^k}(\mathbf{x}))) \mathbf{n}^k(\mathbf{x}).$$

Here, we denote by $\varphi^{s,k}(\mathbf{x}) := \mathbf{x} + \mathbf{u}^{s,k}(\mathbf{x}) \approx \mathbf{x} + \mathbf{u}^*(\mathbf{x}, t^k)$ the approximation of the deformation φ^* at time t^k , and $\mathbf{n}^k(\mathbf{x}) \approx \mathbf{n}(\mathbf{x}, t^k)$ is the outward unit normal vector to the approximated actual configuration at time t^k . The jump $[\Delta \mathbf{u}]^k$ is given by

$$[\Delta \mathbf{u}]^k := \Delta \mathbf{u}^{s,k}(\mathbf{x}) - \Delta \mathbf{u}^{m,k}(R_{t^k}(\mathbf{x})).$$

Furthermore we set $\lambda_n^{k+1/2} := \boldsymbol{\lambda}^{k+1/2} \mathbf{n}^k$ and $[\Delta u]_n^k := [\Delta \mathbf{u}]^k \mathbf{n}^k$. The corresponding tangential parts are given by $\boldsymbol{\lambda}_\tau^{k+1/2} := \boldsymbol{\lambda}^{k+1/2} - \lambda_n^{k+1/2} \mathbf{n}^k$ and $[\Delta \mathbf{u}]_\tau^k := [\Delta \mathbf{u}]^k - [\Delta u]_n^k \mathbf{n}^k$. As we assume the deformation over each time step (t^k, t^{k+1}) to be small, the conditions (6.16) give a suitable discretization of the continuous condition (1.17). Contact formulations by using the original version (1.17) of the non-penetration condition on combination with mortar methods can be found, e.g., in [145]. Similar to the variational version (2.6) we arrive for each time step $t^{k+1/2}$ at the time discretized variational formulation: find $(\Delta \mathbf{u}^k, \boldsymbol{\lambda}^{k+1/2}) \in \mathbf{V} \times \mathbf{M}(\boldsymbol{\lambda}^{k+1/2})$

$$\frac{2}{\Delta t^2} m(\Delta \mathbf{u}^k, \mathbf{v}) + a_{\text{algo}}((\mathbf{u}^k, \mathbf{u}^{k+1}), \mathbf{v}) + \langle [\mathbf{v}], \boldsymbol{\lambda}^{k+1/2} \rangle = f^{k+1/2}(\mathbf{v}), \quad (6.17a)$$

$$\langle [\Delta u]_n^k, \mu_n - \lambda_n^{k+1/2} \rangle + \langle [\Delta \mathbf{u}]_\tau^k, \boldsymbol{\mu}_\tau - \boldsymbol{\lambda}_\tau^{k+1/2} \rangle \leq \langle g^k, \mu_n - \lambda_n^{k+1/2} \rangle, \quad (6.17b)$$

for all $(\mathbf{v}, \boldsymbol{\mu}) \in \mathbf{V}_0 \times \mathbf{M}(\boldsymbol{\lambda}^{k+1/2})$. We remark, that we replaced in the friction law the term $[\dot{\mathbf{u}}_\tau]^{k+1/2}$ by its discrete version $[\Delta \mathbf{u}]_\tau^k / \Delta t$, where the factor $1/\Delta t$ does not have any influence on the variational inequality (6.17b).

After applying the space discretization, we observe as in Section 2.3 that the variational inequality (6.17b) is equivalent to the point-wise contact constraints

$$\Delta \hat{u}_{pn}^k \leq g_p^k, \quad \lambda_{pns}^{k+1/2} \geq 0, \quad \lambda_{pns}^{k+1/2} (\Delta \hat{u}_{pn}^k - g_p^k) = 0 \quad (6.18)$$

and

$$\begin{cases} \|\boldsymbol{\lambda}_{p\tau s}^{k+1/2}\| \leq \mathfrak{F} |\lambda_{pns}^{k+1/2}|, \\ \|\boldsymbol{\lambda}_{p\tau s}^{k+1/2}\| < \mathfrak{F} |\lambda_{pns}^{k+1/2}| \Rightarrow \Delta \hat{\mathbf{u}}_{p\tau}^k = \mathbf{0}, \\ \|\boldsymbol{\lambda}_{p\tau s}^{k+1/2}\| = \mathfrak{F} |\lambda_{pns}^{k+1/2}| \Rightarrow \exists \alpha \in \mathbb{R} : \boldsymbol{\lambda}_{p\tau s}^{k+1/2} = \alpha^2 \Delta \hat{\mathbf{u}}_{p\tau}^k, \end{cases} \quad (6.19)$$

for all possible contact nodes $p \in \mathcal{S}$. Analog to Section 2.3, the discrete gap is given by $g_p^k := D_p^{-1} \int_{\varphi^{s,k}(\Gamma_c^s)} g^k \psi_p \, ds$ and the scaled values by $\lambda_{pns}^{k+1/2} := D_p \lambda_{pn}^{k+1/2}$ and $\boldsymbol{\lambda}_{p\tau s}^{k+1/2} := D_p \boldsymbol{\lambda}_{p\tau}^{k+1/2} - \lambda_{pns}^{k+1/2} \mathbf{n}_p^k$. We follow with two remarks.

Remark 6.1. To fulfill the contact conditions correctly, we evaluate the contact integrals represented by the duality product $\langle \cdot, \cdot \rangle$ and the discrete gap g_p^k on the actual configuration $\varphi^{s,k}(\Gamma_c^s)$ at time t^k . Therefore the matrices \mathbf{D} and \mathbf{B} introduced in (2.21) and also the basis transformation (2.22) depend on t^k and the values for the Lagrange multiplier are defined on the actual configuration. For ease of notation, we neglected all the time indices in these quantities before.

Remark 6.2. It is well-known that due to the use of the midpoint scheme, spurious oscillations in the Lagrange multiplier occur. To avoid these oscillations, we remove the mass from the nodes in \mathcal{S} , see [56]. The idea of massless contact nodes has first been described in [90], where the modified mass matrix has to be obtained from the solution of a global minimization problem. Here, we use a simple under-integration scheme in the local neighborhood of the contact boundary. This approach is extremely cheap to realize and still provides an optimal discretization, see [57]. A further approach based on the Newmark scheme to overcome these oscillations can be found in [35].

To get an energy conserving discrete formulation of the contact, we use the approaches given in [23, 107]. Following [107], we modify the contact constraints in normal direction and replace (6.18) by the constraints

$$\begin{aligned} g_p^k > 0 &\Rightarrow \lambda_{pns}^{k+1/2} = 0, \\ g_p^k \leq 0 &\Rightarrow \lambda_{pns}^{k+1/2} \geq 0, \quad \Delta \hat{u}_{pn}^k \leq 0, \quad \lambda_{pns}^{k+1/2} \Delta \hat{u}_{pn}^k = 0. \end{aligned} \quad (6.20)$$

We remark that this algorithmic approach fulfills the so called persistency condition $\lambda_n(\mathbf{x}, t) \dot{g}(\mathbf{x}, t) = 0$, see [106], in a discrete sense. However, the geometrical non-penetration is violated and allows a small penetration when the two bodies come into contact. Fortunately, this violation tends towards zero if the time step size tends towards zero.

Defining the kinetic energy and the internal stress energy at time t^k by

$$\mathcal{K}_k := \frac{1}{2} \sum_{i=s,m} \int_{\Omega^i} \varrho^i \|\dot{\mathbf{u}}^{h,i,k}\|^2 \, d\mathbf{x}, \quad \mathcal{E}_k := \frac{1}{2} \sum_{i=s,m} \int_{\Omega^i} \mathbf{P}^{h,i,k} : \nabla \mathbf{u}^{h,i,k} \, d\mathbf{x},$$

the total energy $\mathcal{K}_k + \mathcal{E}_k + \mathcal{E}_k^c$ is constant in time, where the contact work \mathcal{E}_k^c performed up to time t^k is given by

$$\mathcal{E}_k^c := \sum_{j=0}^{k-1} \int_{\varphi^{h,s,j}(\Gamma_c^s)} \boldsymbol{\lambda}^{h,j+1/2} [\Delta \mathbf{u}^h]^j \, d\mathbf{s} = \sum_{j=0}^{k-1} \sum_{p \in \mathcal{S}} \boldsymbol{\lambda}_{p\tau s}^{j+1/2} \Delta \hat{\mathbf{u}}_{p\tau}^j.$$

6.3.2. Remarks on the algorithm

In each time step we apply Algorithm 5 to find the pair $(\Delta \hat{\mathbf{u}}^k, \boldsymbol{\lambda}^{k+1/2})$. Next, we comment on the Newton method for the structural part and present a small modification in the normal part $C_n(\cdot, \cdot)$ of the nonlinear complementarity function $C(\cdot, \cdot)$. This modification is necessary since we use the modified non-penetration constraint (6.20) but does not influence the structure and performance of our semi-smooth Newton approach.

Similar to (6.5) we define for each time step for the given previous displacement vector \mathbf{u}^k and the velocity vector $\dot{\mathbf{u}}^k$ the function

$$\mathbf{F}^k(\Delta \hat{\mathbf{u}}^k, \boldsymbol{\lambda}^{k+1/2}) := \frac{2}{\Delta t^2} \hat{\mathbf{M}} \Delta \hat{\mathbf{u}}^k + \hat{\mathbf{K}}_{\text{algo}}(\mathbf{u}^k, \mathbf{u}^{k+1}(\Delta \hat{\mathbf{u}}^k)) + \hat{\mathbf{C}}^k \boldsymbol{\lambda}^{k+1/2} - \hat{\mathbf{f}}^{k+1/2}, \quad (6.21)$$

where the nonlinear part $\hat{\mathbf{K}}_{\text{algo}}(\mathbf{u}^k, \mathbf{u}^{k+1})$ represents the algebraic representation of the form $a_{\text{algo}}(\cdot, \cdot)$ introduced in (6.15) with respect to the new constrained basis. We remark, that the displacement vector \mathbf{u}^{k+1} results from the time increment $\Delta \hat{\mathbf{u}}^k$ due to the transformation formula (2.24) for the coefficient vector via the formula

$$\mathbf{u}^{k+1} = \mathbf{u}^k + (\mathbf{Q}_d^k)^\top \Delta \hat{\mathbf{u}}^k.$$

The time index k in the definition of the matrix $\hat{\mathbf{C}}^k$ and in the transformation matrix \mathbf{Q}_d^k is a consequence of Remark 6.1. Furthermore, $\hat{\mathbf{f}}^{k+1/2}$ denotes the corresponding algebraic representation of the right hand side $f^{k+1/2}(\mathbf{v})$ introduced in (6.14) with respect to the constrained basis. To apply Newton's method to the function (6.21), we have to compute its Jacobian with respect to $\Delta \hat{\mathbf{u}}^k$ similar to formula (6.4) in terms of $\mathbf{K}_{\text{algo}}(\mathbf{u}^k, \mathbf{u}^{k+1})$ which denotes the algebraic representation of $a_{\text{algo}}(\cdot, \cdot)$ introduced in (6.15) with respect to the standard finite element basis. Thus, it is enough to compute the Jacobian of $\mathbf{K}_{\text{algo}}(\mathbf{u}^k, \mathbf{u}^{k+1})$ with respect to the standard nodal finite element basis. The Jacobian and also the corresponding function entering into the right hand side can be obtained locally by a linear transformation. Furthermore, we remark that the Jacobian of $\mathbf{K}_{\text{algo}}(\mathbf{u}^k, \mathbf{u}^{k+1})$ with respect to $\Delta \hat{\mathbf{u}}^k$ is the same as its Jacobian with respect to $\hat{\mathbf{u}}^{k+1}$.

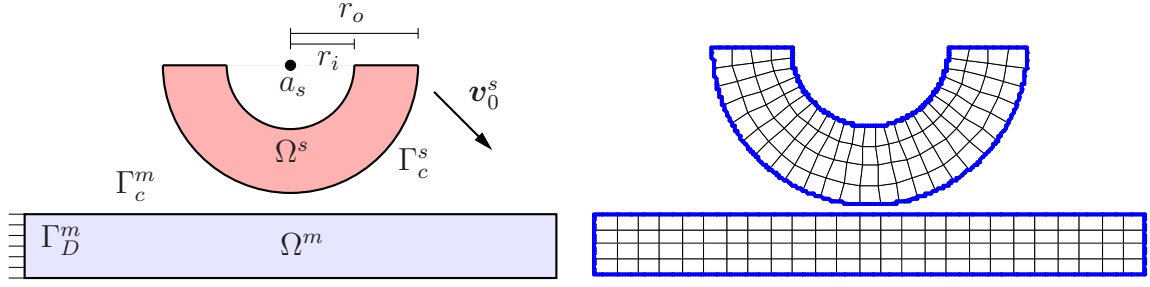


Figure 6.8.: Problem definition and initial coarse grid.

For the contact part, the components $C(\cdot, \cdot)$ of the nonlinear complementarity function $\mathbf{C}(\cdot, \cdot)$ in the nonlinear equation system (6.6) have to be replaced by

$$C(\boldsymbol{\lambda}_p^{k+1/2}, \Delta \hat{\mathbf{u}}_p^k) := \begin{pmatrix} \lambda_{pns}^{k+1/2} - \max\{0, \lambda_{pns}^{k+1/2} + c \tilde{g}_p^k\} \\ \max\{\mathfrak{F}(\lambda_{pns}^{k+1/2} + c \tilde{g}_p^k), \|\boldsymbol{\lambda}_{p\tau s}^{k+1/2} + c \Delta \hat{\mathbf{u}}_{p\tau}^k\|\} \lambda_{p\tau s}^{k+1/2} \\ - \max\{0, \mathfrak{F}(\lambda_{pns}^{k+1/2} + c \tilde{g}_p^k)\} (\boldsymbol{\lambda}_{p\tau s}^{k+1/2} + c \Delta \hat{\mathbf{u}}_{p\tau}^k) \end{pmatrix}, \quad (6.22)$$

for $p \in \mathcal{S}$, where we used the notation

$$\tilde{g}_p^k := \begin{cases} -\frac{\lambda_{pns}^{k+1/2}}{c} - g_p^k & \text{if } g_p^k > 0, \\ \Delta \hat{u}_{pn}^k & \text{if } g_p^k \leq 0. \end{cases}$$

One can easily show that the contact conditions (6.19) and (6.20) are equivalent to the condition $C(\boldsymbol{\lambda}_p^{k+1/2}, \Delta \hat{\mathbf{u}}_p^k) = \mathbf{0}$ for all $p \in \mathcal{S}$. The proof for the equivalence between the modified non-penetration condition (6.20) and the first line in (6.22) is similar to the proof of Theorem 4.1, whereas the equivalence between the frictional constraints (6.19) and the second line in (6.22) is stated in Theorem 5.1.

6.4. Numerical examples

In this section, we present three numerical examples for contact dynamics with large deformations illustrating the performance of the numerical approach presented in the previous section. For all three examples we compare Coulomb's friction law with the frictionless case. The first two examples are in the two-dimensional case, whereas the third one is a three-dimensional setting. For all three examples we use the neo-Hookean material law given in Subsection 1.3.3.

First example

The setting of our first example is illustrated in the left picture in Figure 6.8. A half-ring with initial velocity $\mathbf{v}_0^s = (10, -10)^\top$ hits upon a bar. The bar rests in its initial

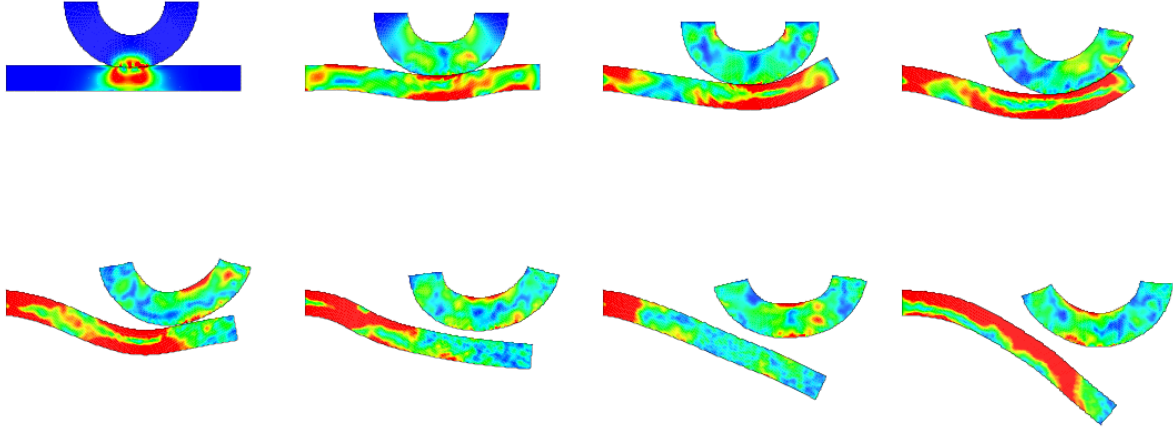


Figure 6.9.: Situation with effective von Mises stress without friction for $t^k = k\Delta t$ with $k = 9, 22, 35, 48, 61, 74, 87, 100$.

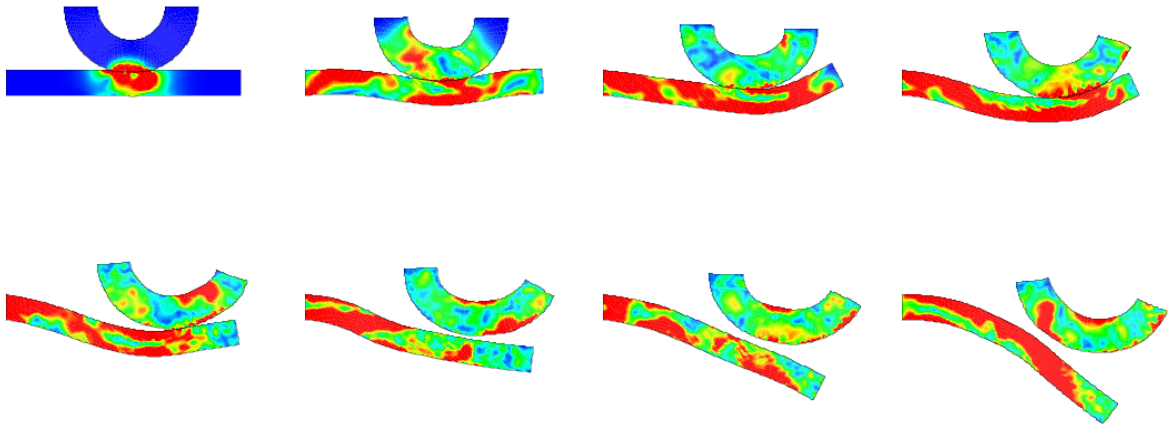


Figure 6.10.: Situation with effective von Mises stress with friction for $t^k = k\Delta t$ with $k = 9, 22, 35, 48, 61, 74, 87, 100$.

configuration and is fixed at its left side during the whole process. It is assumed to be the master side given by $\Omega^m = [-140, 140] \times [-115, -85]$. The half-ring plays the role of the slave body Ω^s . Its midpoint is given by $a_s = (0, 0)^\top$ and its inner and outer radii are given by $r_i = 40$ and $r_o = 80$, respectively. We use the neo-Hookean material law (1.43) with the material parameters $E^s = 2100$, $\nu^s = 0.3$ and $\varrho^s = 1.0$ for the half-ring and $E^m = 6986$, $\nu^m = 0.3$ and $\varrho^m = 0.3$ for the bar.

We consider the time interval $(0, 10)$ with the time step size $\Delta t = 0.1$. Our computations are made on a quadrilateral mesh obtained after two uniform refinement steps of the coarse mesh shown in the right picture in Figure 6.8. Each body is discretized by 1717 nodes. In our numerical algorithm we set the parameters in the nonlinear complementarity function to $c = 2000$. Figure 6.9 shows the distorted bodies with the effective

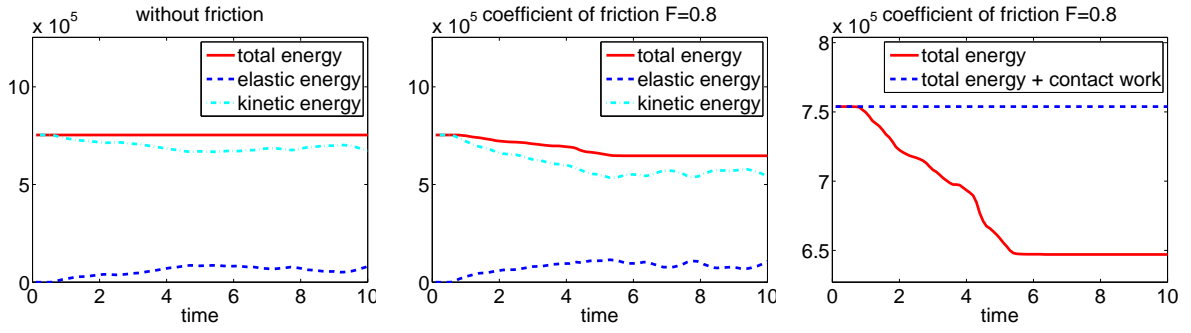


Figure 6.11.: Energy and contact work without (left) and with (middle and right) friction.

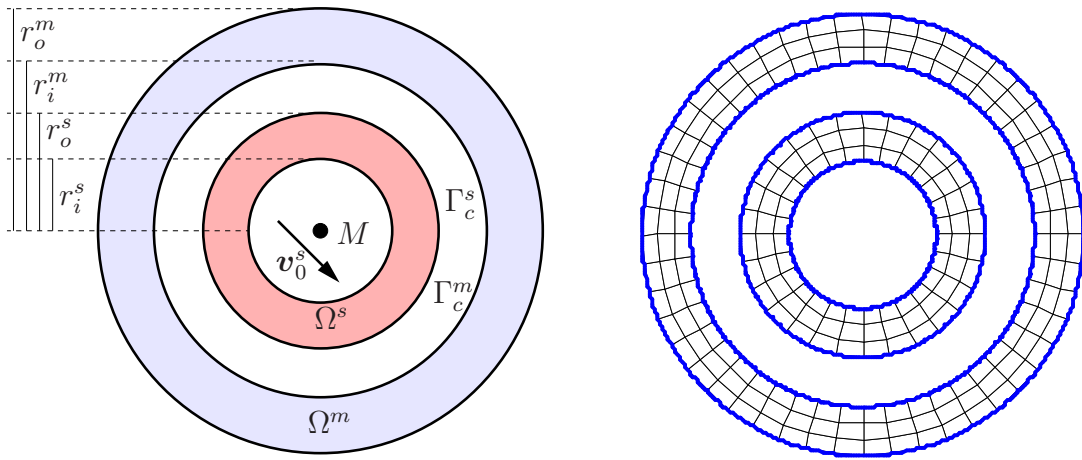


Figure 6.12.: Problem definition and initial coarse grid.

von Mises stress at different time steps for the frictionless case and Figure 6.10 shows the same time steps for Coulomb’s friction law with the coefficient of friction $\mathfrak{F} = 0.8$. In contrast to the case without friction the half-ring tilts to the right side for the case with friction. This effect arises due to the tangential frictional forces.

Figure 6.11 shows the energy evolution in time for the case with and without friction. As illustrated in the left picture in this figure, the total energy is constant in time for the case without friction, whereas the picture in the middle shows that it decreases for the frictional case. Furthermore, the right picture shows that the loss in the energy is exactly the contact work arising due to the friction. Thus, the sum of the total energy and the contact work is constant in time.

Second example

In our second we example we consider two rings with midpoint $M = (0, 0)^\top$ as illustrated in the left picture in Figure 6.12. The inner ring with initial velocity $\mathbf{v}_0^s = (10, -10)^\top$ hits upon the outer ring which rests in its initial configuration. The inner ring is assumed

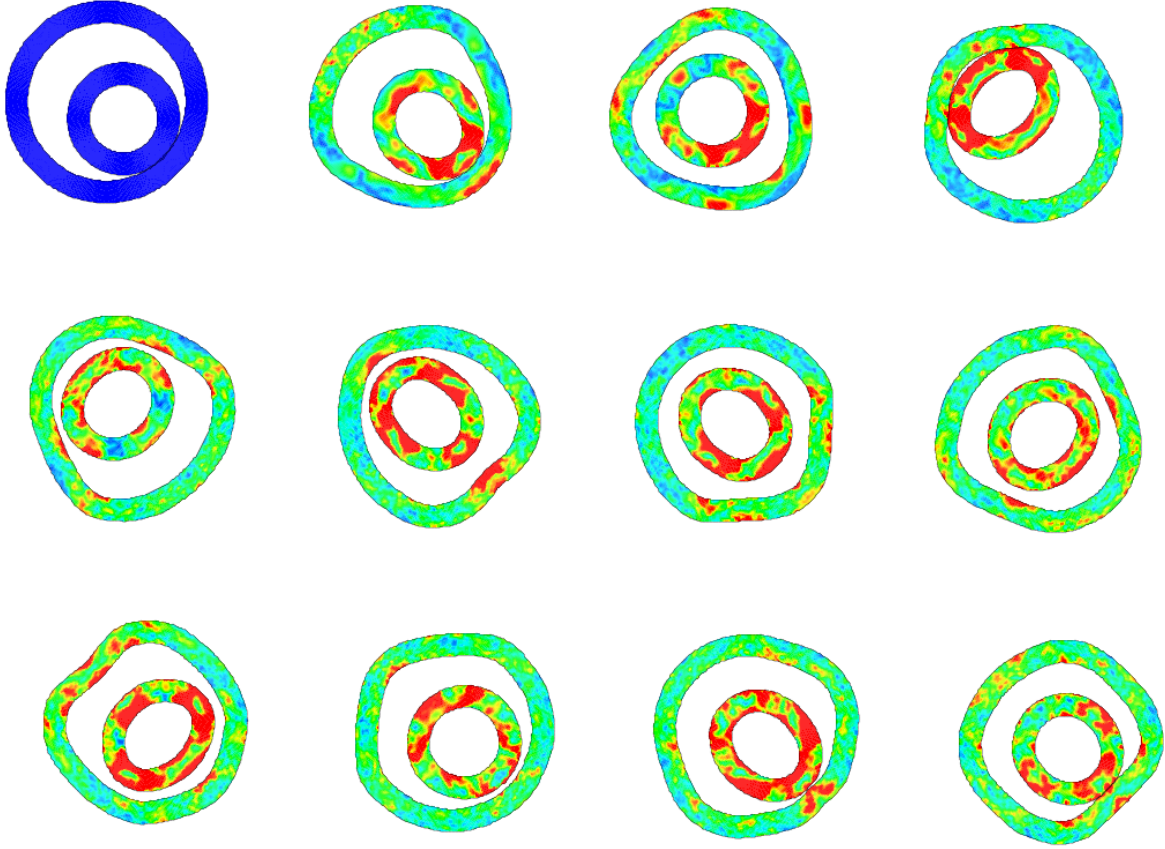


Figure 6.13.: Situation with effective von Mises stress without friction for $t^k = k\Delta t$ with $k = 15, 50, 85, 120, 155, 190, 225, 269, 295, 330, 365, 400$.

to be the slave body Ω^s and the outer ring the master body Ω^m . Therefore, Γ_c^s is the outer boundary of the inner ring and Γ_c^m the inner boundary of the outer ring. The radii indicated in Figure 6.12 are chosen as $r_i^s = 30$, $r_o^s = 50$, $r_i^m = 70$ and $r_o^m = 90$. As for the first example we use the neo-Hookean material law (1.43). As material parameters we use $E^s = 6986$, $\nu^s = 0.3$ and $\varrho^s = 0.3$ for the inner ring and $E^m = 2100$, $\nu^m = 0.3$ and $\varrho^m = 1.0$ for the outer one. We consider the time interval $(0, 40)$ with the time step size $\Delta t = 0.1$. Our computations are made on a quadrilateral mesh obtained after two uniform refinement steps of the coarse mesh shown in the right picture in Figure 6.12. The inner ring is then discretized by 672 nodes and the outer ring by 828 nodes. In our numerical algorithm we set the parameters in the nonlinear complementarity function to $c = 1000$. Figure 6.13 shows the distorted bodies with the effective von Mises stress at different time steps for the case without friction and Figure 6.14 shows the same time steps for Coulomb's friction law with the coefficient of friction $\mathfrak{F} = 0.3$. Comparing the final time steps for the two settings, we observe a completely different behavior for the case with friction than for the case without friction.

Figure 6.15 shows the energy evolution in time for the case with and without friction.

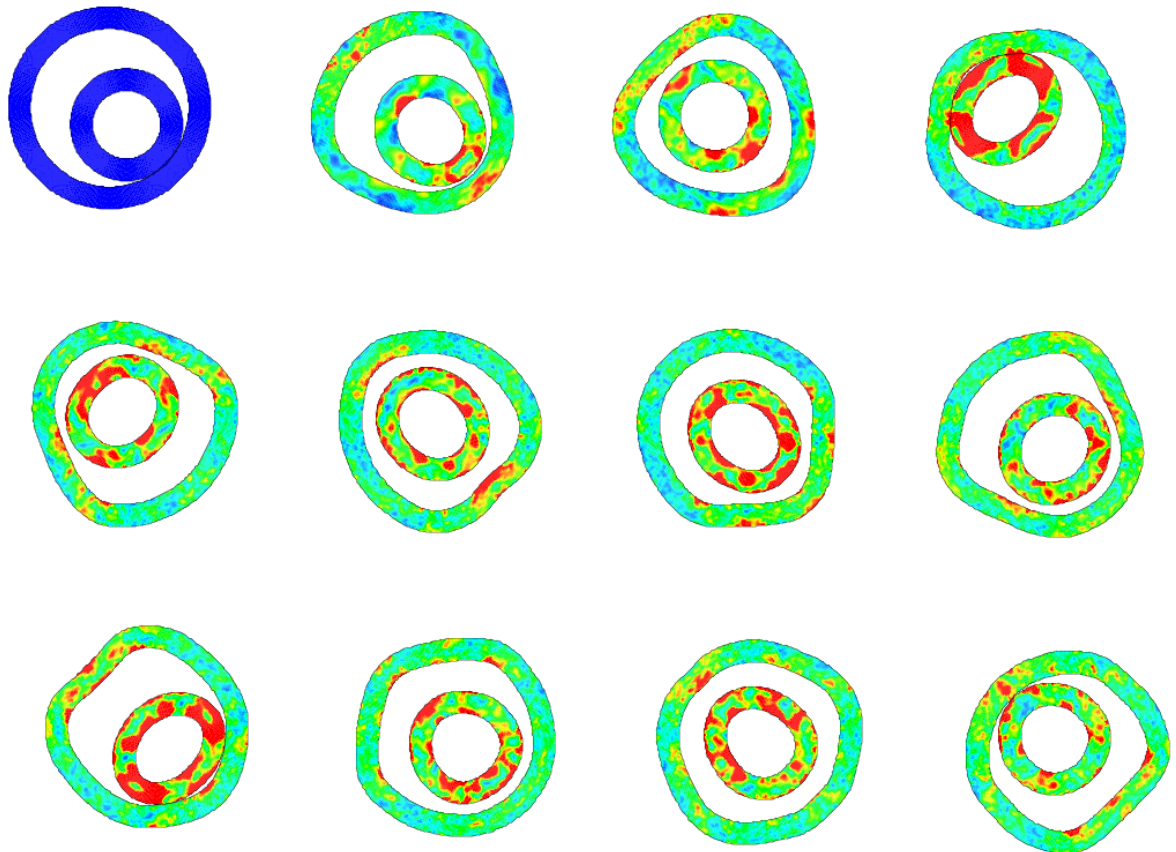


Figure 6.14.: Situation with effective von Mises stress with friction for $t^k = k\Delta t$ with $k = 15, 50, 85, 120, 155, 190, 225, 269, 295, 330, 365, 400$.

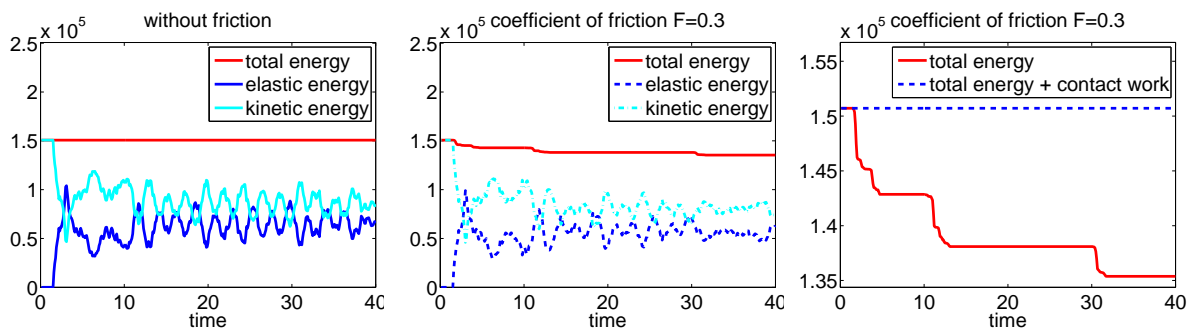


Figure 6.15.: Energy and contact work without (left) and with (middle and right) friction.

Again we observe qualitatively the same behavior as for the first example. As illustrated in the left picture in this figure, the total energy is constant in time for the case without friction, whereas the picture in the middle shows that the total energy decreases for the case with friction. Furthermore, the right shows that the loss in the energy is exactly the

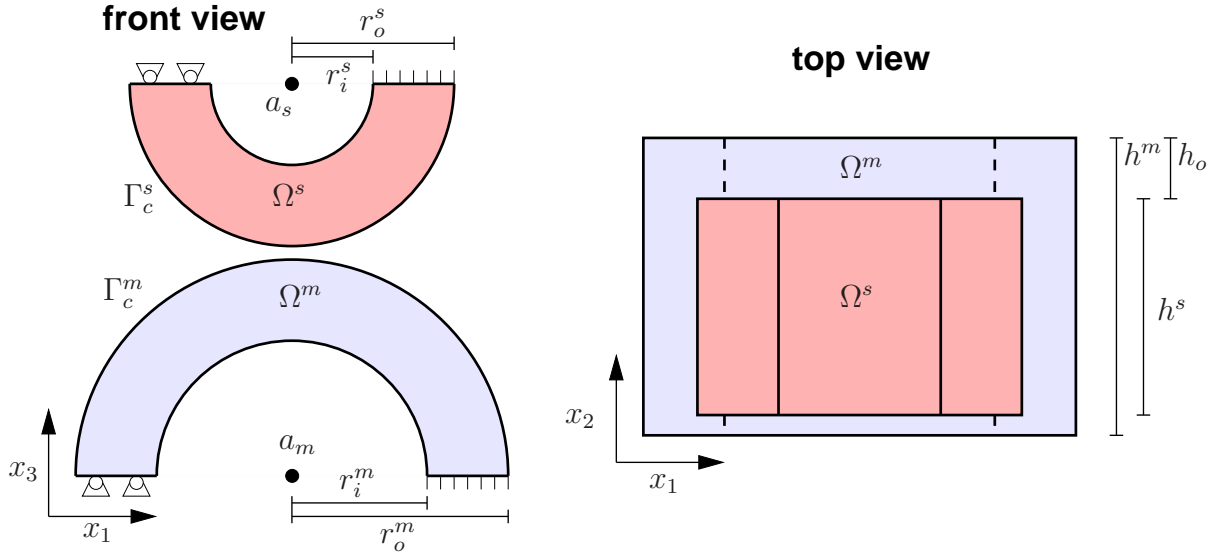


Figure 6.16.: Problem definition.

contact work arising due to the friction. Thus, again the sum of the total energy and the contact work is constant in time. During the three time intervals, in which the two rings are not in contact, the total energy is preserved.

Third example

As third example we consider two half-cylinders pressing against each other. The problem definition is illustrated in the two pictures in Figure 6.16. The axis of both half-cylinders are orthogonal to the x_1x_3 -plane. The midpoints of the two axes are given by $a_s = (0, 0.14)^\top$ and $a_m = (0, -0.17)^\top$, respectively. For the inner and outer radii of the cylinders we set $r_i^m = 0.13$, $r_o^m = 0.17$, $r_i^s = 0.09$ and $r_o^s = 0.13$. For the length of the half-cylinders we set $h^m = 0.17$ and $h^s = 0.11$. Furthermore, we set $h_o = 0.05$ and remark that the initial configuration is unsymmetric in x_2 -direction. We fix the lower half-cylinder assumed to be the master body Ω^m at its right lower surface. The left lower surface is fixed only in x_2 - and x_3 -direction. On the upper surfaces half-cylinder we apply inhomogeneous Dirichlet data. The right one is subjected to

$$\mathbf{u}_{D,r}^s = \begin{pmatrix} 0 \\ 0 \\ -0.1\frac{t}{T} \end{pmatrix},$$

whereas the left one is subjected to Dirichlet data only with respect to the x_2 - and the x_3 -direction whereas in x_1 -direction we apply homogeneous Neumann boundary condition. The boundary conditions for this surface are summarized as follows:

$$\left(\begin{array}{l} \text{free boundary condition} \\ (u_{D,l}^s)_2 = 0 \\ (u_{D,l}^s)_3 = -0.12\frac{t}{T} \end{array} \right).$$

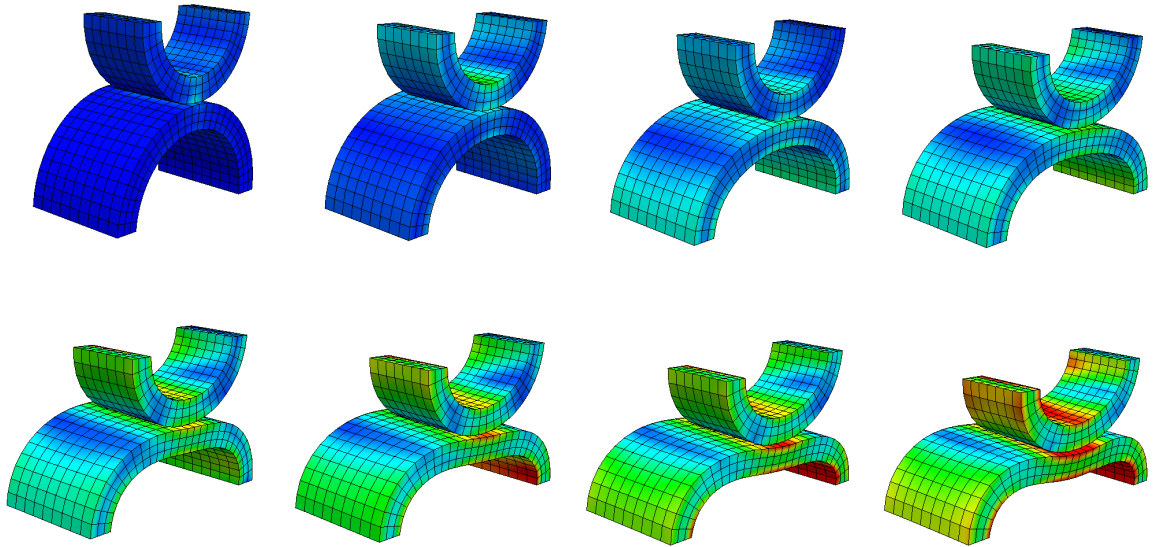


Figure 6.17.: Situation with effective von Mises stress without friction for $t^k = k\Delta t$ with $k = 5, 10, 15, 20, 25, 30, 35, 40$.

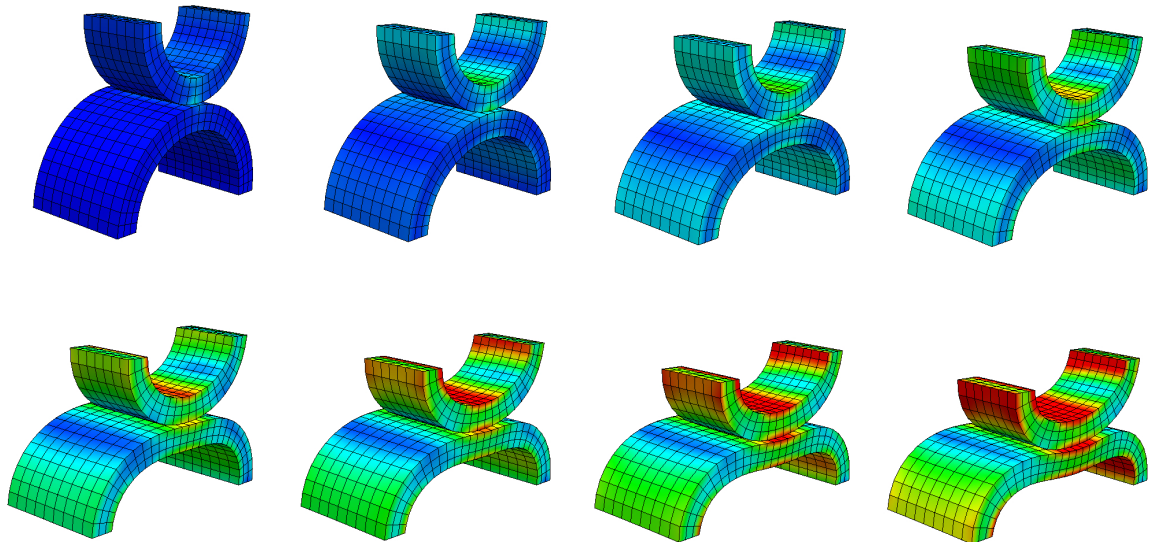


Figure 6.18.: Situation with effective von Mises stress with friction for $t^k = k\Delta t$ with $k = 5, 10, 15, 20, 25, 30, 35, 40$.

As for the other examples we use the neo-Hookean material law (1.43). As material parameters we use $E^s = 120$, $\nu^s = 0.3$ and $\varrho^s = 0.3$ for the inner ring and $E^m = 60$, $\nu^m = 0.25$ and $\varrho^m = 0.5$ for the outer one.

We consider the time interval $(0, T)$ with the final time $T = 1$ and the time step size

$\Delta t = 0.025$. Our computations are made on a hexahedral mesh. The upper half-cylinder Ω^s is discretized by 672 nodes and the lower half-cylinder Ω^m by 870 nodes. In our numerical algorithm we set the parameters in the nonlinear complementarity function to $c = 20$. Figure 6.17 shows the distorted bodies with the effective von Mises stress at different time steps for the case without friction and Figure 6.18 shows the same time steps for Coulomb's friction law with the coefficient of friction $\mathfrak{f} = 0.3$. Comparing the case without friction with the case with friction, we observe that the effective stresses are higher at the contact zone for the case with friction. This results due to fact that contact forces in tangential direction occur at the contact zone. Furthermore, we observe that the relative tangential displacement between the two bodies is much higher for the case without friction than for the case with friction. Although this effect can not be seen in detail in the presented pictures it can be observed clearly from the movie which unfortunately can not be shown here.

7. Thermo-mechanical contact problems

Due to the sliding of the bodies being in contact most of the frictional work results in generation of heat. This observation motivates the extension of the mortar method to thermo-mechanical dynamical contact problems including frictional heating and thermal softening effects at the contact interface. In addition to the displacement field, the temperature field enters as a further primal variable. Similar the thermal flux at the contact interface has to be introduced as an additional dual variable, also denoted as Lagrange multiplier. While the mechanical Lagrange multiplier takes care on the non-penetration condition and the friction law for the mechanical unknowns, also the thermal Lagrange multiplier is necessary to model the generation of heat as well as the flow condition for the thermal variables. The main focus in this chapter is on the treatment of the Robin-type thermal interface condition within the mortar framework. A straightforward application of the concept of biorthogonality to Robin-type constraints does not decouple the thermal constraints at the nodes. To benefit from the elimination of the Lagrange multiplier, we introduce a stable operator which can be interpreted as mass lumping at the interface. For the formulation of the linear thermo-elastic constitutive equations, we follow [20, 135]. A more general thermo-plasticity formulation is given in [126]. The extension to dynamical thermo-mechanical contact mechanics can be found, e.g., in [87, 106, 116] and is also considered in the textbooks [135, 142]. For the modeling of the contact heat flux, we use the linear model proposed in [116]. More general models can be found in [144]. For the considered formulation with a coefficient of friction depending on the temperature, we refer to [106, 116].

This chapter is organized as follows. We start with the problem formulation for linear thermo-elasticity in Section 7.1. The time discretization is obtained in Section 7.2 and the space discretization in terms of mortar techniques in Section 7.3. Section 7.4 deals with the algebraic system of the nonlinear problem followed by some comments on the applied numerical algorithm. Finally, Section 7.6 contains two numerical examples illustrating the discretization and the proposed numerical algorithm.

7.1. Problem formulation for linear thermo-elasticity

In addition to the displacement field $\mathbf{u}^i(\mathbf{x}, t)$ we are interested in the temperature field $\theta^i(\mathbf{x}, t)$ for $(\mathbf{x}, t) \in \Omega^i \times (0, T)$. As in Section 1.1 the local balance of momentum is given by

$$\varrho^i \ddot{\mathbf{u}}^i - \text{Div}(\mathbf{P}^i) = \mathbf{f}^i \quad \text{in } \Omega^i \times (0, T), \quad (7.1)$$

but now the first Piola–Kirchhoff stress tensor \mathbf{P}^i depends on both, the displacement and the temperature. The vector \mathbf{f}^i again describes the given body forces acting on Ω^i . In the case of linear thermo-elasticity, the stress tensor is given by

$$\mathbf{P}^i := \lambda^i \operatorname{tr}(\boldsymbol{\varepsilon}^i) \operatorname{Id}_d + 2\mu^i \boldsymbol{\varepsilon}^i - dK^i \alpha^i (\theta^i - \theta_0) \operatorname{Id}_d, \quad (7.2)$$

see [20, 135], where the linearized strain tensor is introduced in (1.39). The Lamé parameters λ^i and μ^i are obtained by formula (1.33) in terms of Young’s modulus $E^i > 0$ and the Poisson ratio $\nu^i \in (0, 0.5)$. The bulk modulus K^i is given by

$$K^i := \lambda^i + \frac{2}{d}\mu^i.$$

θ_0 is a reference temperature at which the bodies are stress free, and the factor α^i denotes the thermal expansion coefficient of the material of body Ω^i . We remark that the relation between the relative temperature $\theta^i - \theta_0$ and the stress is given by the stress-temperature tensor, which reduces to $dK^i \alpha^i \operatorname{Id}_d$, due to the assumed isotropy.

In addition, we have to consider the heat conduction equation which results from the first law of thermodynamics:

$$c_\theta^i \dot{\theta}^i = -\mathcal{H}^i - \operatorname{div}(\mathbf{q}^i) + r^i \quad \text{in } \Omega^i \times (0, T), \quad (7.3)$$

with the specific heat capacity c_θ^i of the body Ω^i . The term \mathcal{H}^i denotes the heating from the Joule effect, and the prescribed heat source term is given by r^i . Following [135], we get for linearized thermo-elasticity

$$\mathcal{H}^i := d\alpha^i K^i \theta_0 \operatorname{div}(\dot{\mathbf{u}}^i). \quad (7.4)$$

Due to the classical Fourier’s law, the heat flux is given by

$$\mathbf{q}^i = -\kappa^i \nabla \theta^i \quad (7.5)$$

with the thermal conductivity $\kappa^i > 0$. We remark that in a more general setting, κ^i is a tensor which is positive semi-definite as a consequence of the second law of thermodynamics.

To formulate the initial boundary value problem, we consider again the decomposition of the boundary in the reference configuration $\Gamma^i := \partial\Omega^i$ of the domain Ω^i into three nonoverlapping open subsets Γ_D^i , Γ_N^i and Γ_c^i with $\bar{\Gamma}_D^i \cup \bar{\Gamma}_N^i \cup \bar{\Gamma}_c^i = \Gamma^i$. In addition, we have two subsets Γ_θ^i and Γ_q^i such that $\bar{\Gamma}_\theta^i \cup \bar{\Gamma}_q^i = \bar{\Gamma}_D^i \cup \bar{\Gamma}_N^i$ and $\Gamma_\theta^i \cap \Gamma_q^i = \emptyset$. Using the linear stress tensor $\boldsymbol{\sigma}^i$ as introduced in (1.38), we summarize (7.1)-(7.5) and formulate the initial boundary value problem

$$\rho^i \ddot{\mathbf{u}}^i - \operatorname{Div}(\boldsymbol{\sigma}^i) + dK^i \alpha^i \nabla \theta^i = \mathbf{f}^i \quad \text{in } \Omega^i \times (0, T), \quad (7.6a)$$

$$c_\theta^i \dot{\theta}^i + d\alpha^i K^i \theta_0 \operatorname{div}(\dot{\mathbf{u}}^i) - \operatorname{div}(\kappa^i \nabla \theta^i) = r^i \quad \text{in } \Omega^i \times (0, T), \quad (7.6b)$$

where we assume θ_0 to be constant on $\Omega^s \cup \Omega^m$. As initial conditions, we set

$$\begin{aligned} \mathbf{u}^i(\mathbf{x}, 0) &= \mathbf{0} & \text{in } \Omega^i, \\ \dot{\mathbf{u}}^i(\mathbf{x}, 0) &= \mathbf{v}_0^i(\mathbf{x}) & \text{in } \Omega^i, \\ \theta^i(\mathbf{x}, 0) &= \theta_0^i(\mathbf{x}) & \text{in } \Omega^i, \end{aligned} \quad (7.7)$$

where $\mathbf{v}_0^i(\mathbf{x})$ denotes the initial velocity of the body Ω^i and $\theta_0^i(\mathbf{x})$ its initial temperature. To obtain a well defined system, we have to specify suitable boundary conditions for the displacement and the temperature

$$\begin{aligned} \mathbf{u}^i &= \mathbf{u}_D^i & \text{on } \Gamma_D^i \times (0, T), \\ \mathbf{P}^i \mathbf{n}_0^i &= \mathbf{t}_N^i & \text{on } \Gamma_N^i \times (0, T), \\ \theta^i &= \theta_D^i & \text{on } \Gamma_\theta^i \times (0, T), \\ \mathbf{q}^i \mathbf{n}_0^i &= \mathbf{q}_N^i & \text{on } \Gamma_q^i \times (0, T), \end{aligned} \quad (7.8)$$

where \mathbf{n}_0^i denotes the outward unit normal vector in the reference configuration on Γ^i .

The mechanical interface conditions on the contact boundary are the same as stated in Section 1.2. We only replace the coefficient of friction \mathfrak{F} in Coulomb's friction law (1.19) by a temperature dependent one. Defining the maximal temperature of the two contact interfaces

$$\bar{\theta}_c(\mathbf{x}, t) := \max\{\theta^s(\mathbf{x}, t), \theta^m(R_t(\mathbf{x}), t)\} \quad \text{for } (\mathbf{x}, t) \in \Gamma_c^s \times (0, T), \quad (7.9)$$

and Coulomb's friction law reads now as

$$\begin{cases} \|\mathbf{p}_\tau\| \leq \mathfrak{F}(\bar{\theta}_c) |p_n|, \\ \|\mathbf{p}_\tau\| < \mathfrak{F}(\bar{\theta}_c) |p_n| \Rightarrow [\dot{\mathbf{u}}]_\tau = 0, \\ \|\mathbf{p}_\tau\| = \mathfrak{F}(\bar{\theta}_c) |p_n| \Rightarrow \exists \beta : \mathbf{p}_\tau = \beta^2 [\dot{\mathbf{u}}]_\tau, \end{cases} \quad \text{on } \Gamma_c^s \times (0, T), \quad (7.10)$$

where the following temperature dependent coefficient of friction $\mathfrak{F}(\bar{\theta}_c) \geq 0$ is used:

$$\mathfrak{F}(\bar{\theta}_c) := \mathfrak{F}_0 \frac{(\bar{\theta}_c - \theta_{\text{dam}})^2}{(\theta_{\text{dam}} - \theta_{\text{ref}})^2}. \quad (7.11)$$

In this definition, \mathfrak{F}_0 is the static coefficient of friction at the given reference temperature θ_{ref} , and θ_{dam} is a damage temperature on the interface. Typically, θ_{dam} is related to the temperature at which frictional stress is no longer due to solid shearing effects but is generated by viscous shear of a molten film on the contact interface. It can be taken as the lowest melting temperature of the two bodies in contact, see [106]. Since $\bar{\theta}_c < \theta_{\text{dam}}$, we have $\mathfrak{F}'(\bar{\theta}_c) \leq 0$ and $\lim_{\bar{\theta}_c \rightarrow \theta_{\text{dam}}} \mathfrak{F}(\bar{\theta}_c) = 0$. Therefore (7.11) shows a thermal softening effect.

The conditions for the heat flux $q_c^i := \mathbf{q}^i \mathbf{n}^i$ across the possible contact interface Γ_c^i can be written as

$$q_c^i = \gamma_c^i(p_n)(\theta^i - \theta_0), \quad q_c^s + q_c^m + \mathbf{p}_\tau [\dot{\mathbf{u}}]_\tau = 0 \quad \text{on } \Gamma_c^s \times (0, T), \quad (7.12)$$

where $\gamma_c^i(\cdot)$ depends only on the normal pressure and has to satisfy $\gamma_c^i(0) = 0$, see [87, 106, 116]. This condition guarantees that there is no heat flux between the two bodies if they are not in contact. For $\gamma_c^i(\cdot)$, we employ a linear model $\gamma_c^i(p_n) := \bar{\gamma}_c^i p_n$, see [106]. Using (7.10) and (7.12), we find

$$q_c^s = \beta_c p_n [\theta] - \delta_c \mathfrak{F}(\bar{\theta}_c) p_n \|[\dot{\mathbf{u}}]_\tau\|, \quad (7.13a)$$

$$q_c^m = -\beta_c p_n [\theta] - (1 - \delta_c) \mathfrak{F}(\bar{\theta}_c) p_n \|[\dot{\mathbf{u}}]_\tau\| \quad (7.13b)$$

on $\Gamma_c^s \times (0, T)$ with the parameters

$$\beta_c := \frac{\bar{\gamma}_c^s \bar{\gamma}_c^m}{\bar{\gamma}_c^s + \bar{\gamma}_c^m} \quad \text{and} \quad \delta_c := \frac{\bar{\gamma}_c^s}{\bar{\gamma}_c^s + \bar{\gamma}_c^m}. \quad (7.14)$$

We mention that $[\theta] := \theta^s - \theta^m$ denotes the jump of the temperature over the possible contact part $\Gamma_c^s \times (0, T)$ introduced according to the definition of the jump in the displacement in (1.18). Then (7.13) yields

$$q_c^m = -q_c^s - \mathfrak{F}(\bar{\theta}_c) p_n \|[\dot{\mathbf{u}}]_\tau\|, \quad (7.15)$$

with a non-negative dissipation due to friction

$$\mathcal{D}_c := \mathcal{D}_c^{\text{mech}} + \mathcal{D}_c^{\text{therm}} = \mathfrak{F}(\bar{\theta}_c) p_n \|[\dot{\mathbf{u}}]_\tau\| + \sum_{i=s,m} \frac{\bar{\gamma}_c^i p_n}{\theta^i} (\theta^i - \theta_0)^2 \geq 0. \quad (7.16)$$

Finally, the coupled problem to be solved is given by the equilibrium conditions (7.6), the boundary conditions (7.8), the initial conditions (7.7), the mechanical contact conditions (1.17) and (7.10) and the thermal flow conditions on the contact interface (7.12).

7.2. Discretization in time

Both the hyperbolic mechanical equilibrium condition (7.6a) and the parabolic thermal one (7.6b) are discretized using the midpoint scheme which is of order two. We use the same notations as introduced in Subsection 6.3.1. Firstly, we remind the definition of $t^k := k \Delta t$, $k = 0, \dots, N_T$, where the time step size is given by $\Delta t := T/N_T$. Secondly, we denote by $\mathbf{u}^k \approx \mathbf{u}(\cdot, t^k)$ and $\theta^k \approx \theta(\cdot, t^k)$ the approximation of the displacement field and the temperature at time t^k , respectively. Setting $\Delta \mathbf{u}^k := \mathbf{u}^{k+1} - \mathbf{u}^k$, the midpoint scheme yields to the approximation given in (6.12). In the same way, the values $\Delta \theta^k$, $\theta^{k+1/2}$ and $\dot{\theta}^{k+1/2}$ for the temperature are defined. The equilibrium (7.6) stated at the midpoint $t^{k+1/2}$ of the time interval can now be written as

$$\frac{2}{\Delta t^2} \rho^i \Delta \mathbf{u}^{i,k} - \frac{1}{2} \text{Div}(\boldsymbol{\sigma}^i(\Delta \mathbf{u}^{i,k})) + dK^i \alpha^i \nabla \theta^{i,k+1/2} = \mathbf{f}_1^{i,k+1/2}, \quad (7.17a)$$

$$\frac{2}{\Delta t} c_\theta^i \theta^{i,k+1/2} + \frac{1}{\Delta t} d\alpha^i K^i \theta_0 \text{div}(\Delta \mathbf{u}^{i,k}) - \text{div}(\kappa^i \nabla \theta^{i,k+1/2}) = \mathbf{f}_2^{i,k+1/2}, \quad (7.17b)$$

with the right hand sides

$$\mathbf{f}_1^{i,k+1/2} := \mathbf{f}^i(\mathbf{x}, t^{k+1/2}) + \frac{2}{\Delta t} \rho^i \dot{\mathbf{u}}^{i,k} + \text{Div}(\boldsymbol{\sigma}^i(\mathbf{u}^{i,k})), \quad (7.18)$$

$$\mathbf{f}_2^{i,k+1/2} := \mathbf{r}^i(\mathbf{x}, t^{k+1/2}) + \frac{2}{\Delta t} c_\theta^i \theta^{i,k}. \quad (7.19)$$

As time discretization of the non-penetration condition we use as in Section 6.3.1 in each time step the linearized condition (6.16). The discrete version of the mechanical frictional contact conditions (7.10) at time $t^{k+1/2}$ can be formulated as follows:

$$\begin{cases} \|\mathbf{p}_\tau^{k+1/2}\| \leq \mathfrak{F}(\bar{\theta}_c^{k+1/2}) |p_n^{k+1/2}|, \\ \|\mathbf{p}_\tau^{k+1/2}\| < \mathfrak{F}(\bar{\theta}_c^{k+1/2}) |p_n^{k+1/2}| \Rightarrow [\Delta \mathbf{u}]_\tau^k = 0, \\ \|\mathbf{p}_\tau^{k+1/2}\| = \mathfrak{F}(\bar{\theta}_c^{k+1/2}) |p_n^{k+1/2}| \Rightarrow \exists \beta : \mathbf{p}_\tau^{k+1/2} = \beta^2 [\Delta \mathbf{u}]_\tau^k. \end{cases} \quad (7.20)$$

The time discretization of the thermal flux conditions on the contact interface given in (7.13) reads

$$q_c^{s,k+1/2} = \beta_c p_n^{k+1/2} [\theta]^{k+1/2} - \delta_c \mathfrak{F}(\bar{\theta}_c^{k+1/2}) p_n^{k+1/2} \frac{\|[\Delta \mathbf{u}]_\tau^k\|}{\Delta t}, \quad (7.21a)$$

$$q_c^{m,k+1/2} = -\beta_c p_n^{k+1/2} [\theta]^{k+1/2} - (1 - \delta_c) \mathfrak{F}(\bar{\theta}_c^{k+1/2}) p_n^{k+1/2} \frac{\|[\Delta \mathbf{u}]_\tau^k\|}{\Delta t}. \quad (7.21b)$$

Similar to (7.15), we obtain

$$q_c^{m,k+1/2} = -q_c^{s,k+1/2} - \mathfrak{F}(\bar{\theta}_c^{k+1/2}) p_n^{k+1/2} \frac{\|[\Delta \mathbf{u}]_\tau^k\|}{\Delta t}. \quad (7.22)$$

Summarizing the equilibrium condition (7.17), the mechanical contact conditions (6.16) and (7.20) and the thermal contact condition (7.21) leads to the time discretized formulation of the coupled thermodynamic contact problem. Additionally, we have to enforce the boundary conditions (7.8) in each time step $t^{k+1/2}$ as well as choose \mathbf{u}^0 , $\dot{\mathbf{u}}^0$ and θ^0 according to the initial conditions (7.7).

7.3. Space discretization and mortar formulation

In this section, the space discretized variational formulation of the time discretized thermodynamic contact problem is derived. In addition to the mechanical Lagrange multiplier for the mechanical boundary stress \mathbf{p}_c , denoted in this chapter by *bflambda_u* we introduce the thermal Lagrange multiplier λ_θ for the thermal heat flux q_c^s on the possible contact boundary, respectively. To do so, we end up with a mortar based formulation. Our main focus is on the treatment of the Robin type thermal interface conditions (7.13) which leads to a generalized saddle point formulation. A local static condensation of the thermal Lagrange multiplier can easily be obtained by a lumping technique. For the spatial discretization of the primal variables \mathbf{u} and θ , standard conforming finite elements of

lowest order are used. As overall in this thesis, the basis functions of the dual variables λ_u and λ_θ are biorthogonal to the trace of the shape functions of the primal variables. For the duality, we refer to Subsection 2.2.1.

We start with the introduction of the discrete function spaces. In addition to the function spaces introduced in Subsection 2.2 for the mechanical variable, we have to define function spaces for the thermal variable. Although for the mechanical variable the same function spaces as before are used, we recall its definitions. To simplify the notation in what follows, a discrete function is denoted by the same symbol as its continuous counterpart, omitting the usual index h (i.e. $\mathbf{u}^{k+1/2}$ instead of $\mathbf{u}_h^{k+1/2}$). We define the vector valued space $\mathbf{V}^{i,h} \subset [H^1(\Omega^i)]^d$ for the displacement field and the scalar valued space $V^{i,h} \subset H^1(\Omega^i)$ on each subdomain $i = s, m$ for the temperature by

$$\mathbf{V}^{i,h} := \left\{ \mathbf{u}^i \in [\mathcal{S}_1^i]^d : \mathbf{u}^i|_{\Gamma_D^i} = \mathbf{u}_D^i \right\}, \quad V^{i,h} := \left\{ \theta^i \in \mathcal{S}_1^i : \theta^i|_{\Gamma_\theta^i} = \theta_D^i \right\}, \quad (7.23)$$

where $\mathcal{S}_1^i = \mathcal{S}_1^i(\Omega^i, \mathcal{T}_{h,\Omega^i})$ denotes the finite elements space of standard nodal basis functions of order one associated with the triangulation \mathcal{T}_{h,Ω^i} of the subdomain Ω^i . The corresponding product spaces are given by $\mathbf{V}^h := \mathbf{V}^{s,h} \times \mathbf{V}^{m,h}$ and $V^h := V^{s,h} \times V^{m,h}$. As test spaces, we have to use spaces satisfying zero Dirichlet boundary conditions given by $\mathbf{V}_0^h := \mathbf{V}_0^{s,h} \times \mathbf{V}_0^{m,h}$ and $V_0^h := V_0^{s,h} \times V_0^{m,h}$ with

$$\mathbf{V}_0^{i,h} := \left\{ \mathbf{v}^i \in [\mathcal{S}_1^i]^d : \mathbf{v}^i|_{\Gamma_D^i} = \mathbf{0} \right\}, \quad V_0^{i,h} := \left\{ \chi^i \in \mathcal{S}_1^i : \chi^i|_{\Gamma_\theta^i} = 0 \right\}. \quad (7.24)$$

Any function $\boldsymbol{\xi} \in \mathbf{V}^h$ or $\boldsymbol{\xi} \in \mathbf{V}_0^h$ and $\xi \in V^h$ or $\xi \in V_0^h$ stand for the pair $\boldsymbol{\xi} = (\boldsymbol{\xi}^s, \boldsymbol{\xi}^m)$, $\xi = (\xi^s, \xi^m)$, respectively. We remark that the spaces \mathbf{V}^h and V^h depend on time $t^{k+1/2}$, if the Dirichlet data \mathbf{u}_D and θ_D are not constant over time. But this time index is neglected for ease of notation. Similar to the vector value spatially discrete space \mathbf{M}^h for the mechanical Lagrange multiplier λ_u we denote the spatially discrete space for the thermal Lagrange multiplier λ_θ by M^h . We remark that we use the constrained basis introduced in Subsection 2.3.1 not only for the discrete mechanical space but also for the discrete thermal space.

A function $\boldsymbol{\mu}_u \in \mathbf{M}^h$ is written as $\boldsymbol{\mu}_u = \sum_{p \in \mathcal{S}} \boldsymbol{\mu}_p \psi_p$, $\boldsymbol{\mu}_p \in \mathbb{R}^d$, where its normal and tangential parts are defined according to (2.16). Now, the discrete convex subset $\mathbf{M}^h(\lambda_u, \theta)$ of \mathbf{M}^h yields, due to the biorthogonality relation (2.12)

$$\mathbf{M}^h(\lambda_u, \theta) = \left\{ \boldsymbol{\mu}_u = \sum_{p \in \mathcal{S}} \boldsymbol{\mu}_p \psi_p \in \mathbf{M}^h : \mu_{pn} \geq 0, \quad \|\boldsymbol{\mu}_{p\tau}\| \leq \mathfrak{F}_p \lambda_{pn}, \quad p \in \mathcal{S} \right\}. \quad (7.25)$$

We mention that the only difference to the definition (2.27) is the dependence on the temperature θ which enters in the definition of the temperature dependent coefficient of friction \mathfrak{F}_p at each node p according to the continuous law (7.11). The temperature is approximated by the discrete function $\theta \in V^h$, i.e., $\theta = \sum_p \theta_p \phi_p = \sum_p \hat{\theta}_p \hat{\phi}_p$, $\theta_p, \hat{\theta}_p \in \mathbb{R}$, where θ_p are the coefficients with respect to the standard nodal basis, and $\hat{\theta}_p$ are the coefficients with respect to the new constrained basis. The coefficients are related by $\theta = \mathbf{Q}_1^\top \hat{\theta}$. Since the coefficient $\hat{\theta}_p$, $p \in \mathcal{S}$, denotes the weak jump between the master

and the slave side due to (2.25), $\theta_p - \hat{\theta}_p$ can be regarded as the value of the master side at the slave node p . Therefore we define \mathfrak{F}_p by

$$\mathfrak{F}_p := \mathfrak{F}_0 \frac{(\bar{\theta}_{cp} - \theta_{\text{dam}})^2}{(\theta_{\text{dam}} - \theta_{\text{ref}})^2}, \quad \bar{\theta}_{cp} := \max\{\theta_p, \theta_p - \hat{\theta}_p\}, \quad p \in \mathcal{S}. \quad (7.26)$$

Multiplying the semi-discrete mechanical equilibrium condition (7.17a) with a test function $\mathbf{v}^i \in \mathbf{V}_0^{i,h}$, integrating over Ω^i , applying partial integration and summation over $i = s, m$, incorporating the boundary conditions (7.8) and the fact that $\boldsymbol{\lambda}_u \in \mathbf{M}^h(\boldsymbol{\lambda}_u, \theta)$ approximates the contact stress \mathbf{p}_c , finally leads to

$$\frac{2}{\Delta t^2} m_1(\Delta \mathbf{u}^k, \mathbf{v}) + \frac{1}{2} a_{11}(\Delta \mathbf{u}^k, \mathbf{v}) + a_{12}(\theta^{k+1/2}, \mathbf{v}) + \langle [\mathbf{v}], \boldsymbol{\lambda}_u^{k+1/2} \rangle = f_1^{k+1/2}(\mathbf{v}), \quad (7.27)$$

with the bilinear forms

$$m_1(\mathbf{u}, \mathbf{v}) := \sum_{i=s,m} \int_{\Omega^i} \varrho^i \mathbf{u}^i \mathbf{v}^i \, d\mathbf{x}, \quad (7.28)$$

$$a_{11}(\mathbf{u}, \mathbf{v}) := \sum_{i=s,m} \int_{\Omega^i} \boldsymbol{\sigma}^i(\mathbf{u}^i) : \nabla \mathbf{v}^i \, d\mathbf{x}, \quad (7.29)$$

$$a_{12}(\theta, \mathbf{v}) := \sum_{i=s,m} \int_{\Omega^i} dK^i \alpha^i \nabla \theta^i \mathbf{v}^i \, d\mathbf{x} \quad (7.30)$$

and the linear form

$$\begin{aligned} f_1^{k+1/2}(\mathbf{v}) &:= \sum_{i=s,m} \int_{\Omega^i} \mathbf{f}^i(\mathbf{x}, t^{k+1/2}) \mathbf{v}^i(\mathbf{x}) \, d\mathbf{x} + \sum_{i=s,m} \int_{\Gamma_N^i} \mathbf{t}_N^i(\mathbf{x}, t^{k+1/2}) \mathbf{v}^i(\mathbf{x}) \, d\mathbf{s} \\ &+ \frac{2}{\Delta t} m_1(\dot{\mathbf{u}}^k, \mathbf{v}) - a_{11}(\mathbf{u}^k, \mathbf{v}). \end{aligned} \quad (7.31)$$

Multiplying the time discretized thermal equilibrium condition (7.17b) with a test function $\chi^i \in V_0^{i,h}$, integrating over Ω^i , applying partial integration, summation over $i = s, m$ and using the boundary conditions (7.8), we end up with

$$\frac{2}{\Delta t} m_2(\theta^{k+1/2}, \chi) + \frac{1}{\Delta t} a_{21}(\Delta \mathbf{u}^k, \chi) + a_{22}(\theta^{k+1/2}, \chi) + \sum_{i=s,m} \int_{\Gamma_c^i} q_c^i \chi^i \, d\mathbf{s} = \tilde{f}_2^{k+1/2}(\chi), \quad (7.32)$$

with the bilinear forms

$$m_2(\theta, \chi) := \sum_{i=s,m} \int_{\Omega^i} c_\theta^i \theta^i \chi^i \, d\mathbf{x}, \quad (7.33)$$

$$a_{21}(\mathbf{u}, \chi) := \sum_{i=s,m} \int_{\Omega^i} dK^i \theta_0 \alpha^i \operatorname{div}(\mathbf{u}^i) \chi^i \, d\mathbf{x}, \quad (7.34)$$

$$a_{22}(\theta, \chi) := \sum_{i=s,m} \int_{\Omega^i} \kappa^i \nabla \theta^i \nabla \chi^i \, d\mathbf{x} \quad (7.35)$$

and the linear form

$$\begin{aligned} \tilde{f}_2^{k+1/2}(\chi) &:= \sum_{i=s,m} \int_{\Omega^i} r^i(\mathbf{x}, t^{k+1/2}) \chi^i(\mathbf{x}) \, d\mathbf{x} - \sum_{i=s,m} \int_{\Gamma_q^i} q_N^i(\mathbf{x}, t^{k+1/2}) \chi^i(\mathbf{x}) \, ds \\ &\quad + \frac{2}{\Delta t} m_2(\theta^k, \chi). \end{aligned} \quad (7.36)$$

Introducing the thermal Lagrange multiplier $\lambda_\theta^{k+1/2}$ as the heat flux on the slave side $q_c^{s,k+1/2}$ and using (7.21b) to express the heat flux $q_c^{m,k+1/2}$ on the master side, we obtain from (7.32)

$$\frac{2}{\Delta t} m_2(\theta^{k+1/2}, \chi) + \frac{1}{\Delta t} a_{21}(\Delta \mathbf{u}^k, \chi) + a_{22}(\theta^{k+1/2}, \chi) + \langle [\chi], \lambda_\theta^{k+1/2} \rangle = f_{2,h}^{k+1/2}(\chi), \quad (7.37)$$

where the right hand side is defined by

$$f_{2,h}^{k+1/2}(\chi) := \tilde{f}_2^{k+1/2}(\chi) + \sum_{p \in \mathcal{S}} \mathfrak{F}_p^{k+1/2} \frac{\|\Delta \hat{\mathbf{u}}_{p\tau}^k\|}{\Delta t} \int_{\Gamma_c^s} \lambda_{pn}^{k+1/2} \psi_p(\chi^m \circ R_t) \, ds. \quad (7.38)$$

We note that (7.38) is the discretized version of the non-linear term in the thermal flux condition (7.22).

Taking into account the normal and the tangential part $\lambda_{pn}^{k+1/2}$ and $\lambda_{p\tau}^{k+1/2}$ of the nodal value $\lambda_p^{k+1/2}$ of the discrete mechanical Lagrange multiplier, we can discretize the time discrete mechanical contact conditions (6.16) and (7.20) in space and arrive similar to the continuous version (6.17b) at

$$\langle [\Delta \mathbf{u}]_n^k, \mu_{un} - \lambda_{un}^{k+1/2} \rangle + \langle [\Delta \mathbf{u}]_\tau^k, \mu_{u\tau} - \lambda_{u\tau}^{k+1/2} \rangle \leq \langle g^k, \mu_{un} - \lambda_{un}^{k+1/2} \rangle \quad (7.39)$$

for all $\mu_u \in \mathbf{M}^h(\lambda_u, \theta)$.

The thermo-mechanical contact condition (7.22) is a Robin-type interface condition relating the temperature $\theta^{k+1/2}$ with the heat fluxes $q_c^{s,k+1/2}$, $q_c^{m,k+1/2}$. Employing the definition of the thermal Lagrange multiplier $\lambda_\theta^{k+1/2}$ as the heat flux on the slave side $q_c^{s,k+1/2}$, the thermal flux condition is satisfied in the following weak sense

$$\langle w, \lambda_\theta^{k+1/2} \rangle = b_h(\theta^{k+1/2}, w) - d_h^{k+1/2}(w), \quad w \in W^h, \quad (7.40)$$

where the bilinear forms are defined as

$$b_h(\cdot, \cdot) : V^h \times W^h \rightarrow \mathbb{R}, \quad b_h(\chi, w) := \sum_{p \in \mathcal{S}} \beta_c \lambda_{pn}^{k+1/2} \hat{\chi}_p \int_{\Gamma_c^s} \phi_p w \, ds, \quad (7.41)$$

and the linear form $d_h(\cdot)$ is given by

$$d_h^{k+1/2}(w) := \sum_{p \in \mathcal{S}} \delta_c \mathfrak{F}_p^{k+1/2} \lambda_{pn}^{k+1/2} \frac{\|\Delta \hat{\mathbf{u}}_{p\tau}^{k+1/2}\|}{\Delta t} \int_{\Gamma_c^s} w_p \phi_p \, ds. \quad (7.42)$$

Similar to the definition of the second term on the right hand side of (7.38), we simplify the non-linearities in the bilinear form $b_h(\cdot, \cdot)$ and the linear form $d_h(\cdot)$ to handle the fully discrete formulation of the time discretized thermal flux condition (7.22). For simplicity, the dependence of the bilinear form $b_h(\cdot, \cdot)$ on the normal contact pressure $\lambda_{un}^{k+1/2}$ is not reflected in the notation, as well as the dependence of the linear forms $f_{2,h}^{k+1/2}(\cdot)$ and $d_h^{k+1/2}(\cdot)$ on the displacement $\Delta \hat{\mathbf{u}}^{k+1/2}$, the temperature $\theta^{k+1/2}$ and the normal contact pressure $\lambda_{un}^{k+1/2}$.

Summarizing (7.27), (7.37) and the contact conditions (7.39) and (7.40), we end up with the fully discrete weak form of the thermo-dynamic contact problem: find $(\Delta \mathbf{u}^k, \theta^{k+1/2}, \boldsymbol{\lambda}_u^{k+1/2}, \lambda_\theta^{k+1/2}) \in \mathbf{V}^h \times V^h \times \mathbf{M}^h(\boldsymbol{\lambda}_u^{k+1/2}, \theta^{k+1/2}) \times M^h$ such that for all time steps

$$\begin{aligned} \frac{2}{\Delta t^2} m_1(\Delta \mathbf{u}^k, \mathbf{v}) + \frac{1}{2} a_{11}(\Delta \mathbf{u}^k, \mathbf{v}) + a_{12}(\theta^{k+1/2}, \mathbf{v}) + b_1(\mathbf{v}, \boldsymbol{\lambda}_u^{k+1/2}) &= f_1^{k+1/2}(\mathbf{v}), \\ \frac{2}{\Delta t} m_2(\theta^{k+1/2}, \chi) + \frac{1}{\Delta t} a_{21}(\Delta \mathbf{u}^k, \chi) + a_{22}(\theta^{k+1/2}, \chi) + \langle [\chi], \lambda_\theta^{k+1/2} \rangle &= f_{2,h}^{k+1/2}(\chi), \\ \langle [\Delta \mathbf{u}]_n^k, \mu_{un} - \lambda_{un}^{k+1/2} \rangle + \langle [\Delta \mathbf{u}]_\tau^k, \boldsymbol{\mu}_{u\tau} - \boldsymbol{\lambda}_{u\tau}^{k+1/2} \rangle &\leq \langle g^k, \mu_{un} - \lambda_{un}^{k+1/2} \rangle, \\ b_h(\theta^{k+1/2}, w) - \langle w, \lambda_\theta^{k+1/2} \rangle &= d_h^{k+1/2}(w) \end{aligned} \tag{7.43}$$

holds for all $(\mathbf{v}, \chi, \boldsymbol{\mu}_u, w) \in \mathbf{V}_0^h \times V_0^h \times \mathbf{M}^h(\boldsymbol{\lambda}_u^{k+1/2}, \theta^{k+1/2}) \times W^h$, together with a suitable weak form of the initial conditions (7.7). We remark that (7.43) is non-linear. Due to the use of Coulomb friction the right hand sides $f_{2,h}^{k+1/2}(\cdot)$ and $d_h^{k+1/2}(\cdot)$ as well as $b_h(\cdot, \cdot)$ depend on the mechanical Lagrange multiplier $\boldsymbol{\lambda}_u^{k+1/2}$; further the right hand sides $f_{2,h}^{k+1/2}(\cdot)$ and $d_h^{k+1/2}(\cdot)$ also depend on the temperature $\theta^{k+1/2}$, via the temperature-dependent coefficient of friction \mathfrak{F} . The following remark concludes this section.

Remark 7.1. The Robin-type interface condition for the heat flux can also be expressed without Lagrange multiplier. Choosing $w = [\chi] \in W^h$ in the last equation in (7.43) and summing up the second and the last equations in (7.43), we obtain, due to the definition of the bilinear form $b_h(\cdot, \cdot)$ and the fact that $\lambda_{un}^{k+1/2} = p_n^{k+1/2}$,

$$\begin{aligned} \frac{2}{\Delta t} m_2(\theta^{k+1/2}, \chi) + \frac{1}{\Delta t} a_{21}(\Delta \mathbf{u}^k, \chi) \\ + a_{22}(\theta^{k+1/2}, \chi) + b_h(\theta^{k+1/2}, [\chi]) = f_{2,h}^{k+1/2}(w) + d_h([\chi]). \end{aligned} \tag{7.44}$$

7.4. Algebraic representation

To formulate the algebraic representation of the first two equations in (7.43), we introduce the mass matrices \mathbf{M}_j , $j = 1, 2$, resulting from the bilinear forms $m_j(\cdot, \cdot)$ with respect to the nodal basis. To avoid numerical oscillations in space due to the possible non-zero heat flux at the interface, we use a standard lumping technique and replace the mass matrix \mathbf{M}_2 by a diagonal matrix $\mathbf{M}_2^L[p, p] := \sum_q \mathbf{M}_2[p, q]$. We remark that using the

lumped version of the mass matrix does not deteriorate the numerical convergence rate, see [133]. The stiffness matrices according to the bilinear forms $a_{ij}(\cdot, \cdot)$, $i, j = 1, 2$, with respect to the nodal finite element basis are denoted by \mathbf{A}_{ij} . The corresponding matrices with respect to the new constrained basis are obtained by the local transformation $\hat{\mathbf{M}}_1 = \mathbf{Q}_d \mathbf{M}_1 \mathbf{Q}_d^\top$, $\hat{\mathbf{M}}_2^L = \mathbf{Q}_1 \mathbf{M}_2^L \mathbf{Q}_1^\top$, $\hat{\mathbf{A}}_{11} = \mathbf{Q}_d \mathbf{A}_{11} \mathbf{Q}_d^\top$, $\hat{\mathbf{A}}_{12} = \mathbf{Q}_d \mathbf{A}_{12} \mathbf{Q}_1^\top$, $\hat{\mathbf{A}}_{21} = \mathbf{Q}_1 \mathbf{A}_{21} \mathbf{Q}_d^\top$ and $\hat{\mathbf{A}}_{22} = \mathbf{Q}_1 \mathbf{A}_{22} \mathbf{Q}_1^\top$. With these notations, the algebraic version of the first two equations in (7.43) in the new constrained basis can be written as

$$\begin{pmatrix} \frac{2}{\Delta t^2} \hat{\mathbf{M}}_1 + \frac{1}{2} \hat{\mathbf{A}}_{11} & \hat{\mathbf{A}}_{12} \\ \frac{1}{\Delta t} \hat{\mathbf{A}}_{21} & \frac{2}{\Delta t} \hat{\mathbf{M}}_2^L + \hat{\mathbf{A}}_{22} \end{pmatrix} \begin{pmatrix} \Delta \hat{\mathbf{u}}^k \\ \hat{\theta}^{k+1/2} \end{pmatrix} + \begin{pmatrix} \tilde{\mathbf{D}}_d & \mathbf{0} \\ \mathbf{0} & \tilde{\mathbf{D}}_1 \end{pmatrix} \begin{pmatrix} \lambda_u^{k+1/2} \\ \lambda_\theta^{k+1/2} \end{pmatrix} = \begin{pmatrix} \hat{\mathbf{f}}_1^{k+1/2} \\ \hat{\mathbf{f}}_2^{k+1/2} \end{pmatrix}, \quad (7.45)$$

where we used the notation $\tilde{\mathbf{D}}_d := (\mathbf{0}, \mathbf{D}_d)^\top$. Before stating the definition of the right hand side in (7.45), we mention that the zero blocks in the coupling matrix between the finite element shape functions in the constrained basis and the Lagrange multipliers λ_u and λ_θ correspond to the nodes in the set $\mathcal{N} \cup \mathcal{M}$. Following (7.18), the right hand side for the mechanical part $\hat{\mathbf{f}}_1^{k+1/2}$ with respect to the new constrained basis is given by

$$\hat{\mathbf{f}}_1^{k+1/2} := \mathbf{Q}_d \left(\mathbf{f}_1^{k+1/2} + \frac{2}{\Delta t} \mathbf{M}_1 \dot{\mathbf{u}}^k - \mathbf{A}_{11} \mathbf{u}^k \right) = \mathbf{Q}_1 \mathbf{f}_1^{k+1/2} + \frac{2}{\Delta t} \hat{\mathbf{M}}_1 \hat{\mathbf{u}}^k - \hat{\mathbf{A}}_{11} \hat{\mathbf{u}}^k, \quad (7.46)$$

where $\mathbf{f}_1^{k+1/2}$ stands for the discrete vector of the first two terms on the right hand side in (7.31) assembled with respect to the nodal basis at time $t^{k+1/2}$. Denoting by $\tilde{\mathbf{f}}_2^{k+1/2}$ the discrete vector of the first two terms of the right hand side in (7.36) assembled with respect to the nodal basis at time $t^{k+1/2}$ and taking into account the definition of $f_{2,h}(\cdot)$, see (7.38), we obtain for the right hand side $\hat{\mathbf{f}}_2^{k+1/2}$ in (7.45) the relation

$$\hat{\mathbf{f}}_2^{k+1/2} := \mathbf{Q}_1 \mathbf{f}_2^{k+1/2} - \begin{pmatrix} \mathbf{0} \\ \mathbf{B}_d^\top \\ \mathbf{0} \end{pmatrix} \mathbf{l}^{k+1/2}, \quad \mathbf{f}_2^{k+1/2} := \tilde{\mathbf{f}}_2^{k+1/2} + \frac{2}{\Delta t} \mathbf{M}_2^L \theta^k, \quad (7.47)$$

where the entries of the vector $\mathbf{l}^{k+1/2}$ are given by

$$\mathbf{l}_p^{k+1/2} := \mathfrak{F}_p^{k+1/2} \lambda_{pn}^{k+1/2} \frac{\|\Delta \hat{\mathbf{u}}_{p\tau}^k\|}{\Delta t}, \quad p \in \mathcal{S},$$

which results from the second term on the right hand side of (7.38). Again the zero blocks refer to the nodes in the set \mathcal{N} and \mathcal{M} .

Next, we derive the algebraic form of the fully discrete weak forms of the mechanical contact conditions (7.39) and the thermal interface conditions (7.40). The algebraic version of the mechanical contact conditions (7.39) are the same as in (6.18) and (6.19). However, we have to replace in the frictional constraints (6.19) the coefficient of friction \mathfrak{F} by the temperature dependent one $\mathfrak{F}_p^{k+1/2}$. Denoting by W^h the scalar valued analogon to the vector valued space \mathbf{W}^h and using this space as test space for (7.40), the matrix associated with the bilinear form $b_h(\cdot, \cdot)$, see (7.41), will not be a diagonal one, and the

thermal contact constraints will not decouple as the mechanical ones in (6.18) and (6.19). To exploit the advantage of the dual Lagrange multiplier shape function we use

$$b_h(\theta^{k+1/2}, I^h w) - \langle w, \lambda_\theta^{k+1/2} \rangle = d_h^{k+1/2}(w), \quad w \in W^h \quad (7.48)$$

instead of (7.40), where the interpolation operator $I^h : W^h \rightarrow M^h$ is defined by

$$w := \sum_{p \in \mathcal{S}} w_p \phi_p \quad \mapsto \quad I^h w = \sum_{p \in \mathcal{S}} w_p \psi_p. \quad (7.49)$$

A rigorous theoretical analysis and optimal convergence rates for the linear framework can easily be obtained by observing the fact that I^h is defined locally, preserves constants and is stable with respect to the L^2 -norm. Moreover, the action of I^h on $b_h(\cdot, \cdot)$ can be regarded as lumping or equivalently as under-integration. Thus, to show optimality, the same techniques as in [133] can be applied. Due to the choice of the biorthogonal basis functions, (7.48) decouples for each node $p \in \mathcal{S}$ to

$$\beta_c \lambda_{pn}^{k+1/2} \hat{\theta}_p^{k+1/2} - \lambda_{\theta p}^{k+1/2} = \delta_c \mathfrak{F}_p^{k+1/2} \lambda_{pn}^{k+1/2} \frac{\|\Delta \hat{\mathbf{u}}_{p\tau}^k\|}{\Delta t}. \quad (7.50)$$

Now, we summarize our results. The algebraic version of the space discretized weak formulation (7.43) of the dynamic thermo-mechanical contact problem is given by (7.45) with the mechanical contact constraints (6.18) and (6.19) with $\mathfrak{F}_p^{k+1/2}$ instead of \mathfrak{F} and the thermo-dynamic flow condition at the contact zone (7.50). We end this section with three remarks concerning the applied space discretization.

Remark 7.2. Similar to Remark 7.1, one can show that the discretized version of the thermal part given by the second line of (7.45) and (7.50) is equivalent to

$$\begin{aligned} & \frac{2}{\Delta t} m_2(\theta^{k+1/2}, \chi) + \frac{1}{\Delta t} a_{21}(\Delta \mathbf{u}^k, \chi) \\ & + a_{22}(\theta^{k+1/2}, \chi) + b_h(\theta^{k+1/2}, I^h \pi^h[\chi]) = f_{2,h}^{k+1/2}(\chi) + d_h(\pi^h[\chi]), \end{aligned} \quad (7.51)$$

where $\pi^h : L^2(\Gamma_c^s) \rightarrow W^h$ denotes the standard mortar projection given by

$$\int_{\Gamma_c^s} \chi \mu_\theta \, d\mathbf{s} = \int_{\Gamma_c^s} (\pi^h \chi) \mu_\theta \, d\mathbf{s}, \quad \mu_\theta \in M^h. \quad (7.52)$$

The algebraic formulation of (7.51) leads to the solution if we substitute the values $\lambda_{\theta p}^{k+1/2}$ coming from (7.50) into the second line of (7.45). Here, we have to take into account that for $\chi = \sum_p \chi_p \phi_p \in V^h$ the mortar projection of the jump is given by $\pi^h[\chi] = \sum_{p \in \mathcal{S}} \hat{\chi}_p \phi_p$, where $\hat{\chi}_p$ are the coefficients with respect to the new constrained basis. Therefore both formulations are equivalent.

Remark 7.3. As already mentioned in Remark 6.1 we evaluate the contact integrals and the discrete gap on the current configuration at time t^k . Therefore the matrices \mathbf{D}_d and \mathbf{B}_d and also the basis transformation (2.22) depend on t^k , and the values for the Lagrange multipliers λ_u and λ_θ are defined on the current configuration. As in Section 6.3, we have neglected all time indices in these quantities before.

Remark 7.4. Similar to Remark 6.2 we also remove the mass from the nodes in \mathcal{S} in the mass matrix \mathbf{M}_1 to avoid the spurious oscillations in the mechanical Lagrange multiplier.

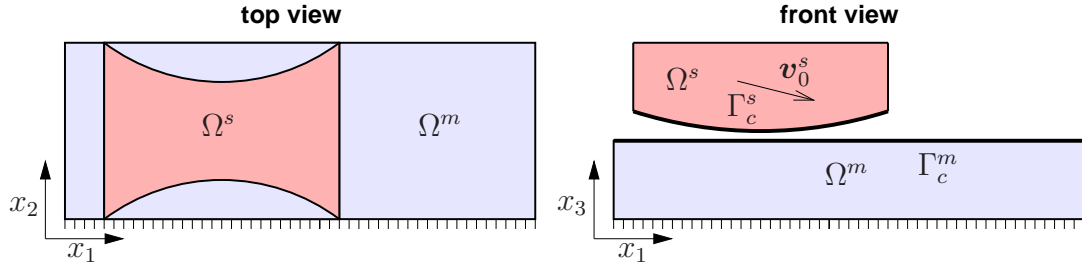


Figure 7.1.: Problem definition.

7.5. Numerical algorithm

One of the challenges in the numerical simulation of such type of problems is the design of fast and robust solvers which can handle the non-linearities in the mechanical and thermal interface constraints efficiently. For the highly non-linear mechanical condition we use the semi-smooth Newton method presented in Section 5.6. At the same time, we update the non-linearities of the thermal condition in the iteration process using a fixed point approach. Furthermore, we update the coefficient of friction as well as the non-linearities in the Robin-type thermal interface condition (7.50) and the non-linear part $\mathbf{l}_p^{k+1/2}$ in (7.47) using a fixed point strategy.

We remark that the resulting system matrix is not symmetric due to the contributions of the thermo-mechanical coupling and the asymmetry in the modifications for the sliding nodes on the contact zone. For details we refer to Chapter 5. Since the algebraic properties of the matrix are not affected, the asymmetry does not influence the convergence rates of appropriate iterative schemes such as multigrid methods.

Due to the decoupled constraints, we can also easily eliminate the degrees of freedom of the Lagrange multipliers from the global system. The constraints both for the mechanical part and for the thermal part are of Dirichlet-, Neumann- or Robin-type and have to be included into the system. Thus, only a system in the primal variables for the displacement and the temperature has to be solved. The Lagrange multipliers can efficiently be obtained by a local post-process.

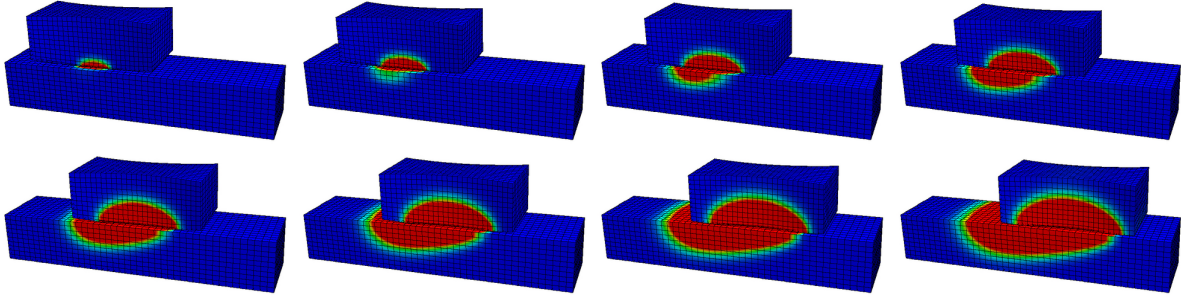
Finally, we mention that since the time discretization scheme does not expect to conserve the energy, we here do not use the discrete version of the persistency condition (6.20) as in Section 6.3 but fulfill the non-penetration condition (6.16) directly.

7.6. Numerical examples

In this section, we show numerical examples both in the three- and the two-dimensional situation for the proposed formulation and algorithm.

Table 7.1.: Material parameters.

	slave body Ω^s	master body Ω^m
mass density ϱ^i	7 856	8 154
Young's modulus E^i	2.1×10^5	8.2×10^5
Poisson ratio ν^i	0.25	0.3
thermal expansion coefficient α^i	1.5×10^{-5}	1.5×10^{-5}
specific heat capacity c_θ^i	460	520
thermal conductivity κ^i	55	65

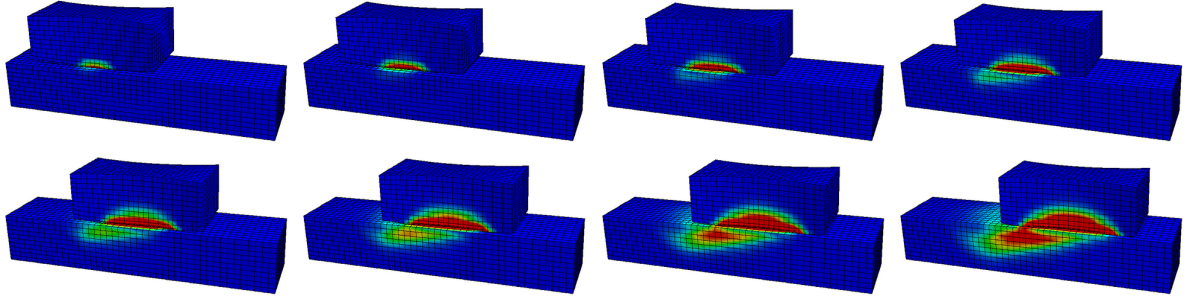
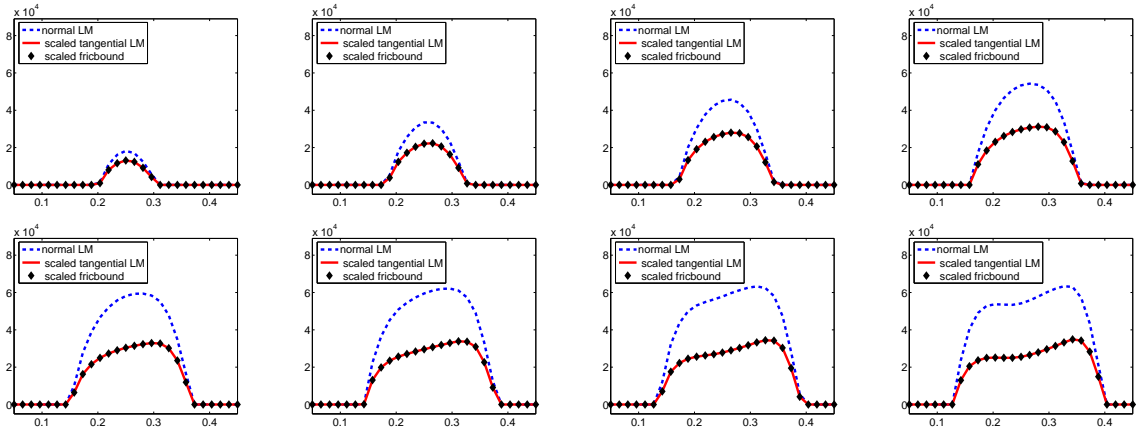
Figure 7.2.: Temperature distribution at time $t^{k-1/2}$ for $k = 8, 14, 20, 26, 32, 38, 44, 50$.

7.6.1. Three-dimensional example

In the first numerical example, we consider the three-dimensional situation sketched in Figure 7.1. The upper body Ω^s , assumed to be the slave side, impinges with the initial velocity $\mathbf{v}_0^s = (30, 0, -1.1)^\top$ on the lower body Ω^m and slides over it. The lower body Ω^m rests in the initial configuration and is clamped at its bottom surface. For all other boundary faces, we assume homogeneous surface tractions and thermal fluxes, i.e., $\mathbf{t}_N^i = \mathbf{0}$ and $q_N^i = 0$, respectively. The lower body is modeled by the cuboid $\Omega^m := [0.0, 0.85] \times [-0.1, 0.1] \times [0.15, 0.15]$, whereas Ω^s was generated from the cuboid $[0.05, 0.45] \times [-0.1, 0.1] \times [0.17, 0.31]$ by deforming the lower, front and back surface such that we get the body depicted in Figure 7.1. The lower surface of Ω^s is assumed to be the possible contact boundary Γ_c^s and the upper surface of Ω^m forms the opposite contact boundary Γ_c^m . The chosen material parameters are summarized in Table 7.1.

The initial and the reference temperature are set to $\theta_0 = 20$ for both bodies. For the reference and the damage temperature in the coefficient of friction (7.11), we use $\theta_{\text{ref}} = 20$ and $\theta_{\text{dam}} = 60$, respectively. The static coefficient of friction is assumed to be $\mathfrak{F}_0 = 0.03$. Furthermore, we use the parameters $\bar{\gamma}_c^s = \bar{\gamma}_c^m = 1$, which lead to $\beta_c = \delta_c = 0.5$ in (7.14). The considered time interval $[0, 1]$ is split into 50 time steps of size $\Delta t = 0.2$. For the space discretization, we use $45 \times 13 \times 11 = 6435$ nodes for the lower body Ω^m and $27 \times 13 \times 11 = 3861$ for the upper body Ω^s .

The numerical results are presented in Figures 7.2 to 7.7. Figure 7.2 shows the distorted bodies with the temperature distribution at different time steps. One can observe that heat is generated at the contact interface due to the sliding process and is diffusing


 Figure 7.3.: Effective stress σ_{eff} at time t^k for $k = 8, 14, 20, 26, 32, 38, 44, 50$.

 Figure 7.4.: Normal component $\lambda_{pn}^{k-1/2}$ and tangential part $\|\lambda_{p\tau}^{k-1/2}\|$ of the contact stress at the nodes $x_2 = 0$ for $k = 8, 14, 20, 26, 32, 38, 44, 50$.

into the bodies. In Figure 7.3, the distorted bodies are displayed with the effective von Mises stress σ_{eff} given by $\sigma_{\text{eff}}^2 := \sum_{i,j=1}^d |\sigma_{ij} - \delta_{ij}p|^2$, where the pressure is defined by $p := \frac{1}{d}\text{tr}(\boldsymbol{\sigma})$. Figures 7.4 to 7.7 present the behavior of the frictional interface conditions (6.19) with \mathfrak{F} replaced by $\mathfrak{F}_p^{k+1/2}$ and (7.50) at the contact nodes of the upper body Ω^s on the line $x_2 = 0$. Therefore the horizontal axis of these figures represents the x_1 -axis as indicated in Figure 7.1. In Figure 7.4, the behavior of the contact pressure in normal and tangential direction is shown, where the dots mark the friction bound $\mathfrak{F}_p|\lambda_{pn}|$. One can see that the normal part of the contact pressure and the contact zone increases with time. All contact nodes are sliding ones, and the numerical results confirm condition (6.19) with $\mathfrak{F}_p^{k+1/2}$ instead of \mathfrak{F} . The thermal flow condition (7.50) at the contact nodes is evaluated in Figure 7.5. Due to the increasing contact pressure λ_{pn} , the thermal flux λ_θ also increases with time. The curve $\beta_c \lambda_{pn}[\theta]_p = \beta_c \lambda_{pn} \hat{\theta}_p$ shows that the jump in the temperature is positive for the nodes with larger x_1 -coordinate and negative otherwise.

This behavior perfectly fits to the plots of the temperature evolution of θ^s and θ^m on both sides of the contact zone shown in Figure 7.6, where the vertical dashed lines mark the current contact zone. The series of pictures in Figure 7.7 displays the evolution of

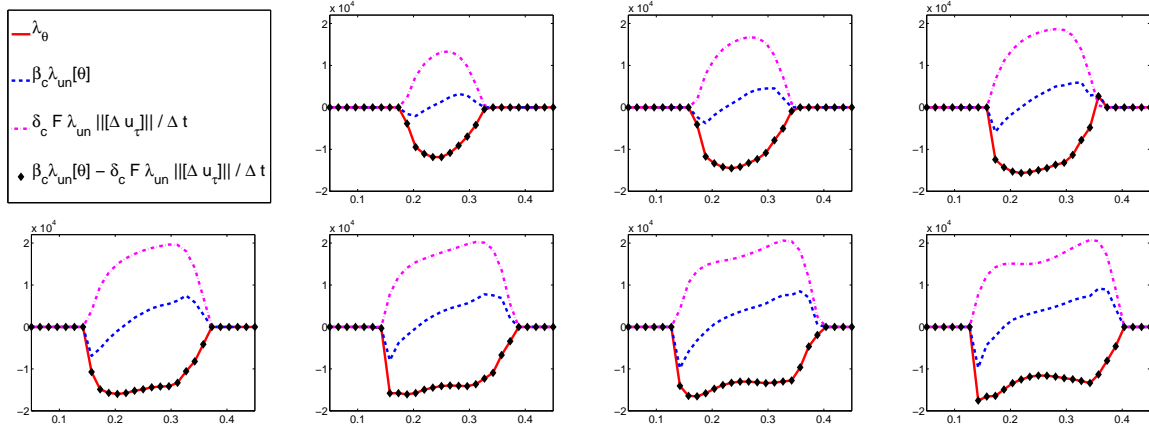


Figure 7.5.: Thermal interface condition (7.50) at the nodes $x_2 = 0$ for at time $t^{k-1/2}$ for $k = 14, 20, 26, 32, 38, 44, 50$.

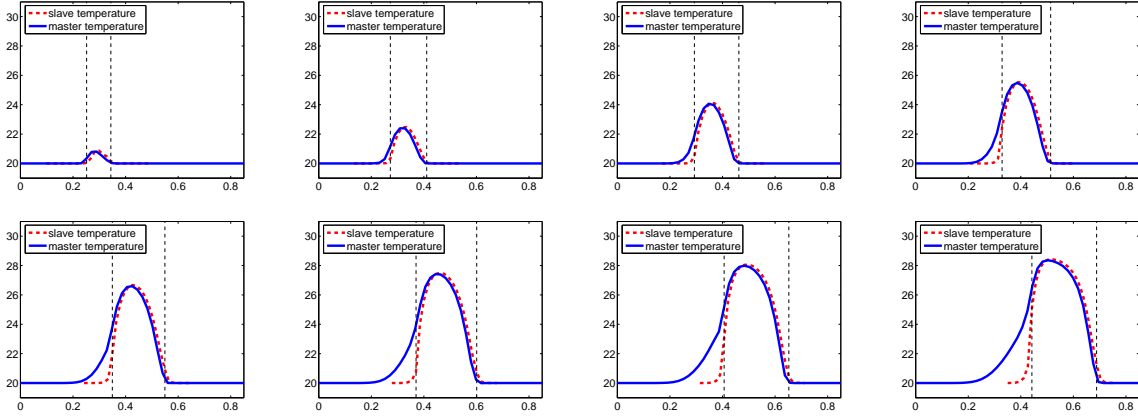


Figure 7.6.: Temperature distribution $\theta_p^{s,k-1/2}$ and $\theta_p^{m,k-1/2}$ at the nodes $x_2 = 0$ for $k = 8, 14, 20, 26, 32, 38, 44, 50$.

the temperature dependent coefficient of friction \mathfrak{F}_p at the maximal temperature $\bar{\theta}_p$ on the contact nodes. The horizontal dashed line marks the static coefficient of friction \mathfrak{F}_0 , and the two vertical lines indicate the current contact zone. One can observe that, due to the heating of the two bodies, the maximal temperature $\bar{\theta}_p$ increases over time, and therefore \mathfrak{F}_p decreases due to (7.26).

To illustrate the performance of the algorithm described in Section 7.5, Figure 7.8 depicts the relative errors

$$\frac{\|(\Delta \hat{\mathbf{u}}^k, \hat{\theta}^{k+1/2})^j - (\Delta \hat{\mathbf{u}}^k, \hat{\theta}^{k+1/2})^{j-1}\|_2}{\|(\Delta \hat{\mathbf{u}}^k, \hat{\theta}^{k+1/2})^j\|_2} \quad (7.53)$$

of the iterates for different time steps. Here, $\|\cdot\|_2$ denotes the Euclidean norm of the coefficient vector and j the iteration index. The iteration process was initialized with the

7. Thermo-mechanical contact problems

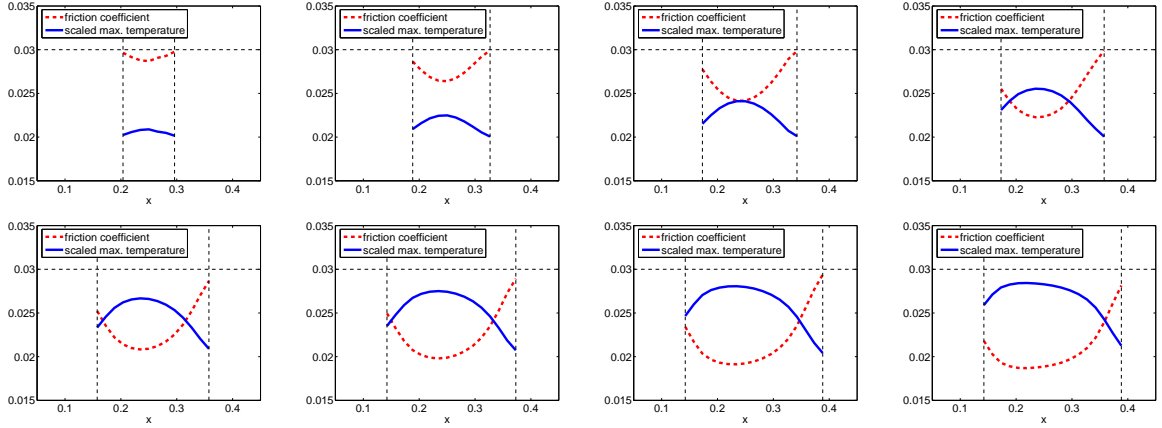


Figure 7.7.: Coefficient of friction $\mathfrak{F}_p^{k-1/2}$ and maximal temperature $\bar{\theta}_p^{k-1/2}$ at the contact nodes $x_2 = 0$ for $k = 8, 14, 20, 26, 32, 38, 44, 50$.

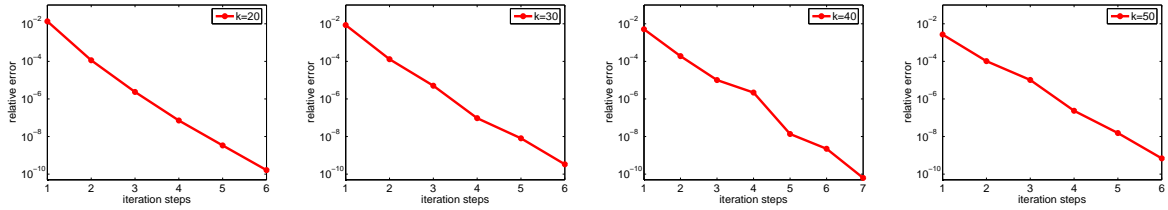


Figure 7.8.: Relative error (7.53) of the iterates for the time steps t^k with $k = 20, 30, 40, 50$.

solution from the former time step. As our algorithm is a combination of a semi-smooth Newton method and fixed point approach, we expect and numerically observe a linear convergence behavior for each time step with around 6 iteration steps being necessary to obtain a relative accuracy of 10^{-9} .

As a second example, we change the initial conditions of the temperature for the lower body Ω^m to $\theta_0^m = 10$ instead of $\theta_0^m = 20$ as before. The initial temperature of the upper body Ω^s $\theta_0^s = 20$ and the value $\theta_{\text{ref}} = 20$ is not altered, as well as other parameters. Due to the fact that the upper body is warmer compared to the lower one, there is a temperature exchange between both bodies through the contact interface in addition to the frictional heat generation. The results are presented in Figure 7.9. One can see that the temperature in the upper body Ω^s is higher and therefore the jump $[\theta]_p = \hat{\theta}_p$ is positive. Furthermore, there are contact nodes with a larger coefficient of friction \mathfrak{F}_p than the static value \mathfrak{F}_0 . This effect arises since we choose $\theta_{\text{ref}} = 20$ and the heat transfer from the warmer upper body Ω^s to the lower body Ω^m starts as soon as the bodies come into contact, resulting in $\bar{\theta}_p < \theta_{\text{ref}}$.

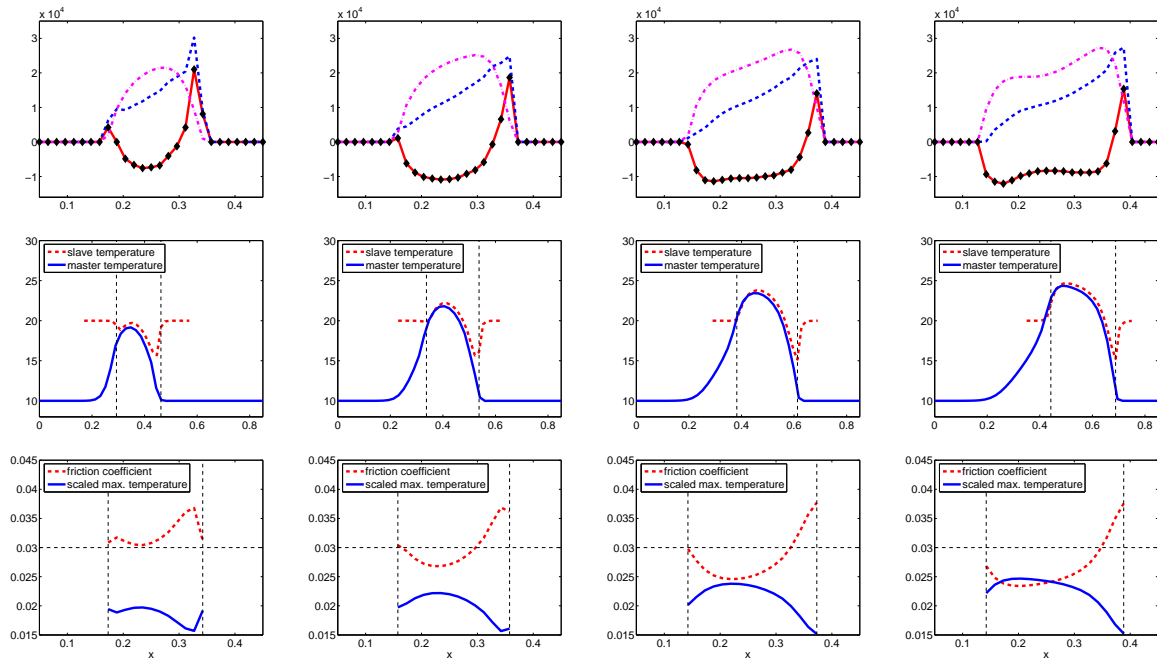


Figure 7.9.: Thermal interface condition (7.50) (first row), temperature distribution $\theta_p^{s,k-1/2}$ and $\theta_p^{m,k-1/2}$ (second row) and coefficient of friction $\mathfrak{F}_p^{k-1/2}$ and maximal temperature $\bar{\theta}_p^{k-1/2}$ (third row) at the contact nodes $x_2 = 0$ for $k = 20, 30, 40, 50$ for the second example.

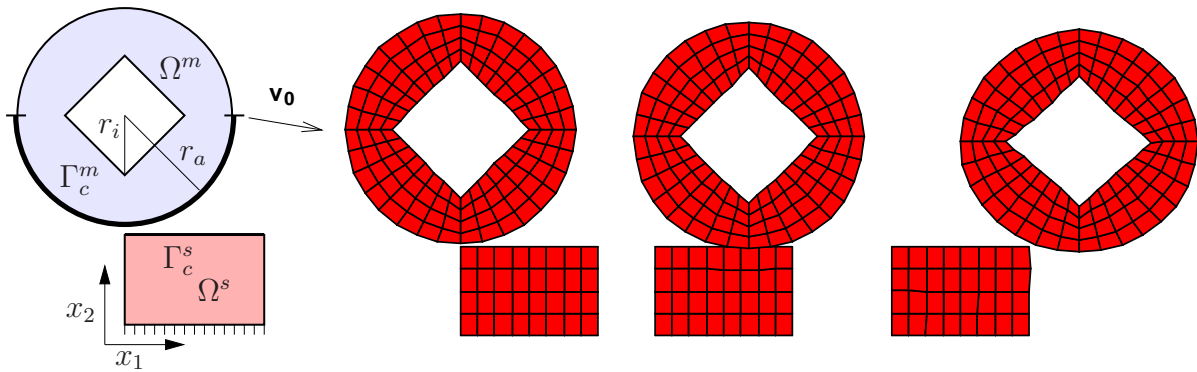


Figure 7.10.: Problem definition and grids at initial state, during and after contact on level 0.

7.6.2. Two-dimensional example

Now, we consider the two-dimensional situation sketched in Figure 7.10. The upper domain Ω^m is modeled by a disc with radius $r_a = 0.5$ and origin $(0, 0)^\top$ featuring a squared hole with a diagonal of length $2r_i = 0.6$. The body Ω^m impinges with an initial velocity $\mathbf{v}_0 = (2.4, -0.2)^\top$ the lower body $\Omega^s = [0.0, 0, 6] \times [-0.9, -0.51]$ being at rest

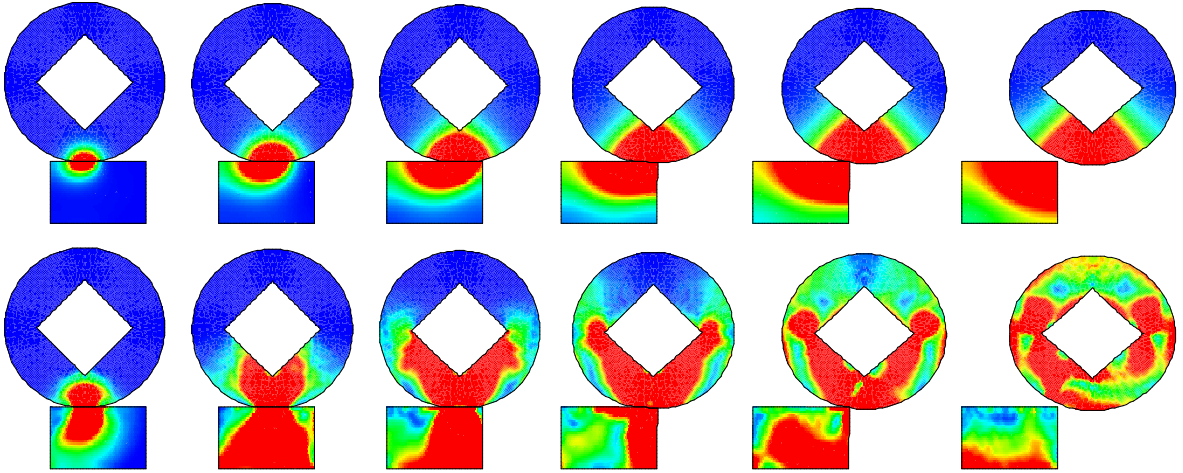


Figure 7.11.: Temperature distribution at time $t^{k-1/2}$ (upper) and effective stress σ_{eff} at time t^k (lower) for $k = 90, 140, 190, 240, 290, 340$.

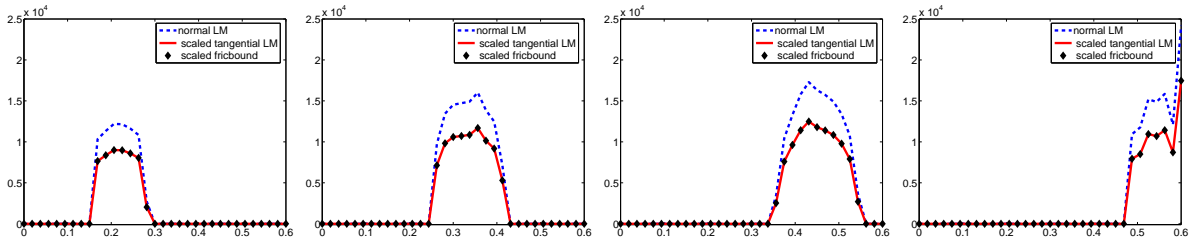


Figure 7.12.: Normal component $\lambda_{pn}^{k-1/2}$ and tangential part $\|\lambda_{p\tau}^{k-1/2}\|$ of the contact stress on Γ_c^s for $k = 90, 140, 190, 240$.

in the initial configuration and clamped on its lower side. For all other boundary faces, we assume homogeneous surface tractions and thermal fluxes, i.e., $\mathbf{t}_N^i = \mathbf{0}$ and $q_N^i = 0$, respectively. As indicated in Figure 7.10, the upper part of Ω^s is assumed to be the possible contact boundary Γ_c^s and the lower part of Ω^m models the opposite contact boundary Γ_c^m . For the material parameters, we use again the ones stated in Table 7.1 but vice versa, i.e., Ω^s has now the parameters given in Table 7.1 for Ω^m and Ω^m the ones for Ω^s . The initial temperature is chosen as $\theta_0 = 20$ for both bodies, while the reference and the damage temperature in the coefficient of friction (7.11) is assumed to be $\theta_{\text{ref}} = 20$ and $\theta_{\text{dam}} = 60$, respectively, with the static coefficient of friction $\mathfrak{f}_0 = 0.003$. Furthermore, we set the parameters $\bar{\gamma}_c^s = \bar{\gamma}_c^m = 1$, which leads to $\beta_c = \delta_c = 0.5$ in (7.14).

The mesh used in the computation is obtained by applying two uniform refinement steps to the grid presented in Figure 7.10, and consists of 2737 nodes, 561 for Ω^s and 2176 for Ω^m . The time discretization consists of 340 time steps of size $\Delta t = 10^{-3}$. The two bodies come into contact at $t^k = 50 \Delta t$ and disconnect at $t^k = 306 \Delta t$. The numerical results for this example are presented in Figures 7.11 to 7.15. The distorted bodies with the temperature distribution at different time steps are shown in the upper

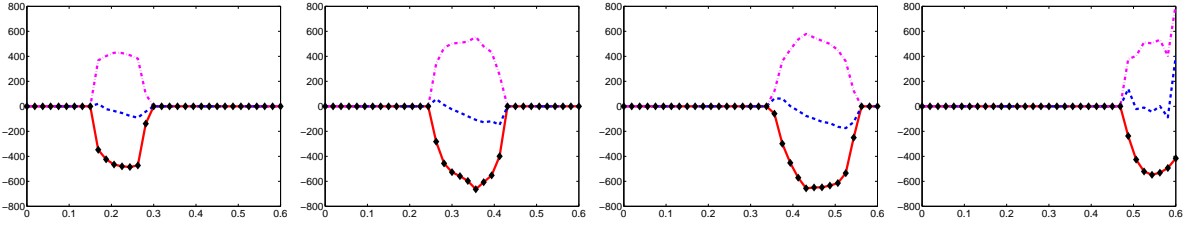


Figure 7.13.: Thermal interface condition (7.50) on Γ_c^s at time $t^{k-1/2}$ for $k = 90, 140, 190, 240$.

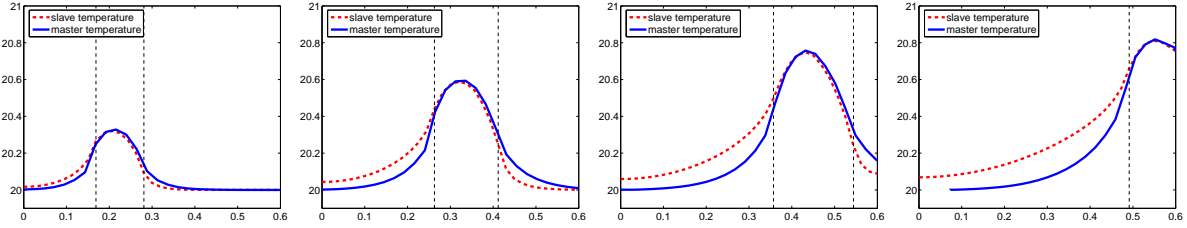


Figure 7.14.: Temperature distribution $\theta_p^{s,k-1/2}$ and $\theta_p^{m,k-1/2}$ on Γ_c^s for $k = 90, 140, 190, 240$.

row of Figure 7.11, whereas the bottom row of Figure 7.11 depicts the effective von Mises stress σ_{eff} .

The behavior of the frictional interface conditions (6.19) with \mathfrak{F} replaced by $\mathfrak{F}_p^{k+1/2}$ and (7.50) at the contact nodes of the lower body Ω^s are illustrated in Figures 7.12 to 7.15. The first one shows the behavior of the contact pressure in normal and tangential direction with respect to time, the dots are indicating the friction bound $\mathfrak{F}_p|\lambda_{pn}|$. One can observe that the normal part of the contact pressure and the contact zone increases with time. As in the previous examples all contact nodes are sliding ones, and the numerical results fulfill condition (6.19) with $\mathfrak{F}_p^{k+1/2}$ instead of \mathfrak{F} . The thermal flow condition (7.50) at the contact nodes is presented in Figure 7.13. Due to the increasing contact pressure λ_{pn} the thermal flux λ_θ also increases over time. For the legend of the curves we refer to Figure 7.5. The curve $\beta_c \lambda_{pn} [\theta]_p = \beta_c \lambda_{pn} \hat{\theta}_p$ shows that the jump in the temperature is negative for the nodes with larger x_1 -coordinate and positive for the other ones. This behavior perfectly fits with the plots of the temperature evolution of θ^s and θ^m on both sides of the contact zone shown in Figure 7.14, where the vertical dashed lines mark the current contact zone. Finally, Figure 7.15 displays the evolution of the temperature dependent coefficient of friction \mathfrak{F}_p and the maximal temperature $\bar{\theta}_p$ on the contact nodes on Γ_c^s . The horizontal dashed line marks the static coefficient of friction \mathfrak{F}_0 and the two vertical lines indicate the current contact zone. One can see that due to the heating of the two bodies, the maximal temperature $\bar{\theta}_p$ increases over time and therefore the coefficient of friction \mathfrak{F}_p decreases due to (7.26).

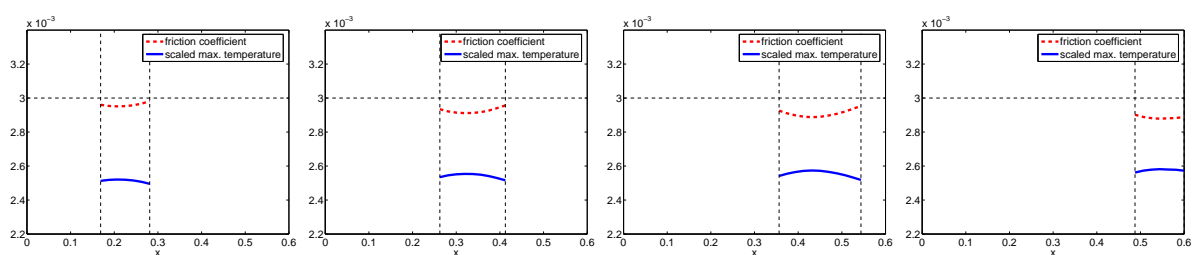


Figure 7.15.: Coefficient of friction $\mathfrak{F}_p^{k-1/2}$ and maximal temperature $\bar{\theta}_p^{k-1/2}$ on Γ_c^s for $k = 90, 140, 190, 240$.

8. Concluding remarks

This thesis is devoted to the mathematical formulation of nonlinear contact problems, its discretization and the development of efficient numerical solution algorithms. In order to handle the typical situation of nonconforming finite element meshes at the contact interface, the mortar method with dual basis functions for the Lagrange multiplier has been employed. This choice allows a rigorous mathematical analysis and optimal a priori estimates for the discretization error. Furthermore, it provides an excellent starting point for the construction of efficient numerical solution algorithms based on semi-smooth Newton methods. A large number of numerical examples has been provided in order to confirm the theoretical results and to show the flexibility, the robustness and the efficiency of the proposed algorithms.

After introducing the strict mathematical formulation of contact problems, the first topic of the thesis has been dedicated to the mortar formulation for nonlinear contact problems. Furthermore, its discretization by using dual basis functions for the Lagrange multiplier and the resulting algebraic representation of the discrete variational inequality have been presented. Optimal a priori error estimates for the discretization error of the mortar formulation have been obtained under suitable regularity assumptions on the exact solution.

The main part of the thesis has been devoted to the development and the numerical investigation of semi-smooth Newton methods to solve the arising nonlinear equations. Due to the employment of dual basis functions for the Lagrange multiplier, a point-wise decoupling of the contact constraints at the contact interface has been derived. Moreover, the introduction of a basis transformation of the finite element basis has allowed for transforming a two-body contact problem to the same structure as a one-body contact problem. This transformation has turned out to be a simple local algebraic modification of the system matrix and the right hand side. Due to this, efficient semi-smooth Newton methods have been developed and an equivalent reformulation in terms of a primal-dual active set strategy has been given for the case without friction. Even in the frictional case with Coulomb's friction law, a full semi-smooth Newton method has been presented which exhibits a superlinear convergence behavior. Moreover, it has been shown that combining these approaches with linear multigrid methods for solving the arising linear systems in each step, inexact strategies can be applied, such that the total effort for solving the nonlinear contact problem is almost the same as for solving a linear problem.

In the last part of this thesis, extensions of the discretization method and the numerical algorithm to more general contact problems have been considered. Firstly, its application to contact dynamics including large deformations with nonlinear material laws in the framework of energy-conserving time integration schemes has been investigated. Secondly, thermo-mechanical contact problems have been considered. A discrete variational

formulation in terms of mortar techniques by using dual basis functions both for the mechanical and the thermal Lagrange multiplier has been derived and an extension of the numerical algorithm to this highly nonlinear system has been introduced.

Summarizing the results, we conclude that the proposed discretization techniques and the numerical algorithms provides a powerful and efficient tool for the simulation of frictional contact problems. Due to their comparatively simple structure and their quite simple adaptability to existing finite element codes for structural mechanics the proposed methods are a promising approach not only for the simulation of frictional contact problems but also for the wide range of simulation processes based on the discretization and numerical solution of variational inequalities.

Bibliography

- [1] R. Adams. *Sobolev Spaces*. Academic Press, New York, 1975. 19
- [2] P. Alart and A. Curnier. A generalized Newton method for contact problems with friction. *J. Méc. Théor. Appl.*, 7(suppl. 1):67–82, 1988. 65, 95
- [3] P. Alart and A. Curnier. A mixed formulation for frictional contact problems prone to Newton like solution methods. *Comput. Methods Appl. Mech. Engrg.*, 92(3):353–375, 1991. 65, 67, 81, 87
- [4] K. Andersen, E. Christiansen, A. Conn, and M. Overton. An efficient primal-dual interior-point method for minimizing a sum of Euclidean norms. *SIAM J. Sci. Comput.*, 22(1):243–262, 2000. 86
- [5] P. Bastian, K. Birken, K. Johannsen, S. Lang, N. Neuß, H. Rentz–Reichert, and C. Wieners. UG – a flexible software toolbox for solving partial differential equations. *Comput. Vis. Sci.*, 1(1):27–40, 1997. viii
- [6] G. Bayada, J. Sabil, and T. Sassi. Algorithme de Neumann-Dirichlet pour des problèmes de contact unilatéral: résultat de convergence. *C. R. Math. Acad. Sci. Paris*, 335(4):381–386, 2002. 65
- [7] Z. Belhachmi and F. Ben Belgacem. Quadratic finite element approximation of the Signorini problem. *Math. Comp.*, 72(241):83–104, 2003. 35
- [8] F. Ben Belgacem. Numerical simulation of some variational inequalities arisen from unilateral contact problems by the finite element methods. *SIAM J. Numer. Anal.*, 37(4):1198–1216, 2000. 35
- [9] F. Ben Belgacem, P. Hild, and P. Laborde. Extension of the mortar finite element method to a variational inequality modeling unilateral contact. *Math. Models Methods Appl. Sci.*, 9(2):287–303, 1999. 17, 35
- [10] F. Ben Belgacem and Y. Renard. Hybrid finite element methods for the Signorini problem. *Math. Comp.*, 72(243):1117–1145 (electronic), 2003. 17, 35
- [11] C. Bernardi, Y. Maday, and A. Patera. A new nonconforming approach to domain decomposition: the mortar element method. In *Nonlinear partial differential equations and their applications. Collège de France Seminar, Vol. XI (Paris, 1989–1991)*, volume 299 of *Pitman Res. Notes Math. Ser.*, pages 13–51. Longman Sci. Tech., Harlow, 1994. 17

- [12] C. Bernardi, Y. Maday, and A. T. Patera. Domain decomposition by the mortar element method. In *Asymptotic and numerical methods for partial differential equations with critical parameters (Beaune, 1992)*, volume 384 of *NATO Adv. Sci. Inst. Ser. C Math. Phys. Sci.*, pages 269–286. Kluwer Acad. Publ., Dordrecht, 1993. 17
- [13] P. Betsch and C. Hesch. Energy-momentum conserving schemes for frictionless contact problem. Part I: NTS method. In P. Wriggers and U. Nackenhorst, editors, *Computational Methods in Contact Mechanics*, volume 3 of *IUTAM Bookseries*, pages 77–96. Springer, 2007. 113
- [14] P. Boieri, F. Gastaldi, and D. Kinderlehrer. Existence, uniqueness, and regularity results for the two-body contact problem. *Applied Mathematics and Optimization*, 15(1):251–277, 1987. 22
- [15] A. Borrelli, C. O. Horgan, and M. C. Patria. Saint-Venant’s principle for antiplane shear deformations of linear piezoelectric materials. *SIAM J. Appl. Math.*, 62(6):2027–2044 (electronic), 2002. 56
- [16] D. Braess. *Finite Elements*. Cambridge University Press, 1997. 42
- [17] S. Brenner and L. Scott. *The Mathematical Theory of Finite Element Methods*. Springer-Verlag, New York, 1994. 19
- [18] F. Brezzi, W. W. Hager, and P.-A. Raviart. Error estimates for the finite element solution of variational inequalities. *Numer. Math.*, 28(4):431–443, 1977. 35
- [19] S. Brunßen, S. Hieber, and B. I. Wohlmuth. Contact Dynamics with Lagrange Multipliers. In P. Wriggers and U. Nackenhorst, editors, *Computational Methods in Contact Mechanics*, volume 3 of *IUTAM Bookseries*, pages 17–32. Springer, 2007. 121
- [20] D. Carlson. Linear thermoelasticity. In S. Fluegge, editor, *Handbuch der Physik*, volume VIa, pages 297–346. Springer, Berlin, 1972. 135, 136
- [21] C. Carstensen, O. Scherf, and P. Wriggers. Adaptive finite elements for elastic bodies in contact. *SIAM J. Sci. Comput.*, 20(5):1605–1626, 1999. 47
- [22] T. Chan, G. Golub, and P. Mulet. A nonlinear primal-dual method for total variation-based image restoration. *SIAM J. Sci. Comput.*, 20(6):1964–1977, 1999. 86
- [23] V. Chawla and T. A. Laursen. Energy consistent algorithms for frictional contact problems. *Internat. J. Numer. Methods Engrg.*, 42(5):799–827, 1998. 122, 124
- [24] X. Chen, Z. Nashed, and L. Qi. Smoothing methods and semismooth methods for nondifferentiable operator equations. *SIAM J. Numer. Anal.*, 38(4):1200–1216 (electronic), 2000. 66

-
- [25] Z. Chen. On the augmented Lagrangian approach to Signorini elastic contact problem. *Numer. Math.*, 88(4):641–659, 2001. 17
- [26] P. Christensen. A semi-smooth Newton method for elasto-plastic contact problems. *Internat. J. Solids Structures*, 39:2323–2341, 2002. 65
- [27] P. Christensen, A. Klarbring, J. Pang, and N. Strömberg. Formulation and comparison of algorithms for frictional contact problems. *Internat. J. Numer. Methods Engrg.*, 42(1):145–173, 1998. 65, 81, 87, 104
- [28] P. Christensen and J. Pang. Frictional contact algorithms based on semismooth Newton methods. In *Reformulation: nonsmooth, piecewise smooth, semismooth and smoothing methods*, volume 22 of *Appl. Optim.*, pages 81–116. Kluwer Acad. Publ., Dordrecht, 1999. 65, 81, 87, 104
- [29] P. W. Christensen. A nonsmooth Newton method for elastoplastic problems. *Comput. Methods Appl. Mech. Engrg.*, 191(11-12):1189–1219, 2002. 65
- [30] J. Chung and G. M. Hulbert. A time integration algorithm for structural dynamics with improved numerical dissipation: the generalized- α method. *Trans. ASME J. Appl. Mech.*, 60(2):371–375, 1993. 113, 121
- [31] P. Ciarlet. *Mathematical Elasticity*, volume I. North Holland, Amsterdam, 1998. 3, 5
- [32] F. Clarke. *Optimization and Nonsmooth Analysis*. Wiley, New York, 1983. 66
- [33] P. Coorevits, P. Hild, K. Lhalouani, and T. Sassi. Mixed finite element methods for unilateral problems: convergence analysis and numerical studies. *Math. Comp.*, 71(237):1–25, 2001. 17, 35
- [34] P. Deuffhard. *Newton Methods for Nonlinear Problems*. Number 35 in Springer Series in Computational Mathematics. Springer, Berlin Heidelberg New York, 2004. 113
- [35] P. Deuffhard, R. Krause, and S. Ertel. A contact-stabilized newmark method for dynamical contact problems. *International Journal for Numerical Methods in Engineering*, 73(9):1274 – 1290, August 2007. 124
- [36] Z. Dostál, A. Friedlander, and S. A. Santos. Solution of coercive and semicoercive contact problems by FETI domain decomposition. In *Domain decomposition methods, 10 (Boulder, CO, 1997)*, volume 218 of *Contemp. Math.*, pages 82–93. Amer. Math. Soc., Providence, RI, 1998. 65
- [37] Z. Dostál, F. Gomes Neto, and S. Santos. Solution of contact problems by FETI domain decomposition with natural coarse space projections. *Computer Methods in Applied Mechanics and Engineering*, 190(13), 2000. 65

- [38] Z. Dostál and D. Horák. Scalability and FETI based algorithm for large discretized variational inequalities. *Math. Comput. Simulation*, 61(3-6):347–357, 2003. MOD-ELLING 2001 (Pilsen). 65
- [39] Z. Dostál, D. Horák, R. Kučera, V. Vondrák, J. Haslinger, J. Dobiáš, and S. Pták. FETI based algorithms for contact problems: scalability, large displacements and 3D Coulomb friction. *Comput. Methods Appl. Mech. Engrg.*, 194(2-5):395–409, 2005. 81
- [40] G. Duvout and J.-L. Lions. *Inequalities in Mechanics and Physics*. Springer, Berlin, 1976. 6, 22
- [41] P. Eberhard, S. Hüeber, Y. Jiang, and B. I. Wohlmuth. Multilevel numerical algorithms and experiments for contact dynamics. In R. Helmig, A. Mielke, and B. Wohlmuth, editors, *Multifield problems in solid and fluid mechanics*, volume 28 of *Lecture notes in applied and computational mechanics*, pages 272–319. Springer, 2006. 121
- [42] C. Eck, J. Jarušek, and M. Krbec. *Unilateral Contact Problems. Variational Methods and Existence Theorems*. Chapman & Hall/CRC, Boca Raton, Fl., 2005. 3, 37
- [43] C. Eck and B. Wohlmuth. Convergence of a contact-Neumann iteration for the solution of two-body contact problems. *Math. Models Methods Appl. Sci.*, 13(8):1103–1118, 2003. 65
- [44] I. Ekeland and R. Temam. *Convex analysis and variational problems (Studies in mathematics and its applications; 1)*. North-Holland Publ. Comp., 1976. 22
- [45] N. El-Abbasi and K.-J. Bathe. Stability and patch test performance of contact discretizations and a new solution algorithm. *Comput. & Structures*, 79(16):1473–1486, 2001. 17
- [46] K. Fackeldey and R. H. Krause. Solving frictional contact problems with multigrid efficiency. In *Domain decomposition methods in Science and Engineering XVI*, volume 55 of *Lecture Notes Comput. Sci. Engrg.*, pages 547–554. Springer, 2007. 81
- [47] R. S. Falk. Error estimates for the approximation of a class of variational inequalities. *Math. Comput.*, 28:963–971, 1974. 35
- [48] K. Fischer and P. Wriggers. Frictionless 2d Contact formulations for finite deformations based on the mortar method. *Comput. Mech.*, 36(3):226–244, 2005. 17
- [49] K. A. Fischer and P. Wriggers. Mortar based frictional contact formulation for higher order interpolations using the moving friction cone. *Comput. Methods Appl. Mech. Engrg.*, 195(37-40):5020–5036, 2006. 17

-
- [50] B. Flemisch. *Non-matching Triangulations of Curvilinear Interfaces Applied to Electro-Mechanics and Elasto-Acoustics*. PhD thesis, Universität Stuttgart, Shaker Verlag, Aachen, 2007. 17
- [51] B. Flemisch and B. I. Wohlmuth. Stable Lagrange multipliers for quadrilateral meshes of curved interfaces in 3D. *Comput. Methods Appl. Mech. Engrg.*, 196(8):1589–1602, 2007. 25
- [52] C. Geiger and C. Kanzow. *Theorie und Numerik restringierter Optimierungsaufgaben*. Springer, Berlin Heidelberg New York, 2002. 22
- [53] R. Glowinski. *Numerical methods for nonlinear variational problems*. Springer, 1984. 22, 35
- [54] R. Glowinski, J.-L. Lions, and R. Tremolières. *Numerical analysis of variational problems*. North-HW03olland, 1981. 22
- [55] O. Gonzales. Exact energy momentum conserving algorithms for general models in nonlinear elasticity. *Comput. Methods Appl. Mech. Engrg.*, 190(13-14):1763–1783, 2000. 113, 121, 122
- [56] C. Hager, S. Hübner, and B. I. Wohlmuth. A stable energy-conserving approach for frictional contact problems based on quadrature formulas. *Internat. J. Numer. Methods Engrg.*, 73(2):205–225, 2008. 19, 121, 124
- [57] C. Hager and B. I. Wohlmuth. Analysis of a modified mass lumping method for the stabilization of frictional contact problems. Technical report, Universität Stuttgart, 2007. IANS Preprint 2007/003. 124
- [58] W. Han and M. Sofonea. *Quasistatic contact problems in viscoelasticity and viscoplasticity*. Studies in Advanced Mathematics. American Mathematical Society, International Press, 2002. 6
- [59] S. Hartmann. *Kontaktanalyse dünnwandiger Strukturen bei großen Deformationen*. PhD thesis, Universität Stuttgart, 2007. 113
- [60] J. Haslinger and I. Hlaváček. Contact between elastic bodies. I. Continuous problems. *Apl. Mat.*, 25(5):324–347, 1980. With a loose Russian summary. 22
- [61] J. Haslinger and I. Hlaváček. Contact between elastic bodies. II. Finite element analysis. *Apl. Mat.*, 26(4):263–290, 1981. With a loose Russian summary. 35
- [62] J. Haslinger, I. Hlaváček, and J. Nečas. Numerical methods for unilateral problems in solid mechanics. In P. Ciarlet and J.-L. Lions, editors, *Handbook of Numerical Analysis*, volume IV, pages 313–485. North-Holland, Amsterdam, 1996. 35, 37
- [63] J. Haslinger, I. Hlaváček, J. Nečas, and J. Lovíšek. *Solution of Variatioanl Inequalities in Mechanics*. Springer, 1988. 22

- [64] J. Haslinger, R. Kučera, and Z. Dostál. An algorithm for the numerical realization of 3D contact problems with Coulomb friction. In *Proceedings of the 10th International Congress on Computational and Applied Mathematics (ICCAM-2002)*, volume 164/165, pages 387–408, 2004. 81
- [65] P. Hauret and P. Le Tallec. A stabilized discontinuous mortar formulation for elastostatics and elastodynamics. Part I: Formulation and analysis. Technical Report 553, Ecole Polytechnique CMAP, 2004. 113
- [66] P. Hauret and P. Le Tallec. A stabilized discontinuous mortar formulation for elastostatics and elastodynamics. Part II: Discontinuous Lagrange multipliers. Technical Report 554, Ecole Polytechnique CMAP, 2004. 113
- [67] P. Hauret and P. Le Tallec. Energy-controlling time integration methods for nonlinear elastodynamics and low-velocity impact. *Comput. Methods Appl. Mech. Engrg.*, 195(37-40):4890–4916, 2006. 113, 121
- [68] P. Heintz and P. Hansbo. Stabilized Lagrange multiplier methods for bilateral elastic contact with friction. *Comput. Methods Appl. Mech. Engrg.*, 195(33-36):4323–4333, 2006. 17
- [69] H. Hertz. Über die Berührung fester elastischer Körper. *J. Reine Angew. Math.*, 92:156–171, 1882. 47
- [70] C. Hesch. *Mechanische Integratoren für Kontaktvorgänge deformierbarer Körper unter großen Verzerrungen*. PhD thesis, Universität Siegen, 2004. 113
- [71] H. Hilber, T. Hughes, and R. Taylor. Improved numerical dissipation for time integration algorithms in structural dynamics. *Earthquake Eng. Struct. Dyn.*, 5(3):283–292, 1977. 113
- [72] P. Hild. Numerical implementation of two nonconforming finite element methods for unilateral contact. *Comput. Methods Appl. Mech. Engrg.*, 184(1):99–123, 2000. 17, 35
- [73] P. Hild and P. Laborde. Quadratic finite element methods for unilateral contact problems. *Appl. Numer. Math.*, 41(3):401–421, 2002. 17, 35, 37, 39, 45
- [74] P. Hild and Y. Renard. An error estimate for the Signorini problem with Coulomb friction approximated by finite elements. *SIAM J. Numer. Anal.*, 45(5):2012–2031 (electronic), 2007. 35
- [75] M. Hintermüller, K. Ito, and K. Kunisch. The primal-dual active set strategy as a semi-smooth Newton method. *SIAM J. Optim.*, 13(3):865–888, 2003. 65, 66, 67, 83

-
- [76] M. Hintermüller, V. Kovtunenکو, and K. Kunisch. Semismooth Newton methods for a class of unilaterally constrained variational problems. *Adv. Math. Sci. Appl.*, 14(2):513–535, 2004. 65
- [77] M. Hintermüller and G. Stadler. An infeasible primal-dual algorithm for total variation-based inf-convolution-type image restoration. *SIAM J. Sci. Comput.*, 28(1):1–23, 2006. 86
- [78] C. O. Horgan. Anti-plane shear deformations in linear and nonlinear solid mechanics. *SIAM Rev.*, 37(1):53–81, 1995. 56
- [79] S. Hübner, M. Mair, and B. I. Wohlmuth. A priori error estimates and an inexact primal-dual active set strategy for linear and quadratic finite elements applied to multibody contact problems. *Appl. Numer. Math.*, 54(3-4):555–576, 2005. 35, 52, 53, 65, 73, 78
- [80] S. Hübner, A. Matei, and B. I. Wohlmuth. A mixed variational formulation and an optimal a priori error estimate for a frictional contact problem in elasto-piezoelectricity. *Bull. Math. Soc. Sc. Math. Roumanie*, 48(2):209–232, 2005. 35
- [81] S. Hübner, A. Matei, and B. I. Wohlmuth. Efficient algorithms for problems with friction. *SIAM J. Sci. Comput.*, 29(1):70–92, 2007. 19, 35, 56
- [82] S. Hübner, G. Stadler, and B. I. Wohlmuth. A primal-dual active set algorithm for three-dimensional contact problems with Coulomb friction. *SIAM J. Sci. Comput.*, 30(2):572–596, 2008. 81, 95
- [83] S. Hübner and B. I. Wohlmuth. An optimal a priori error estimate for nonlinear multibody contact problems. *SIAM J. Numer. Anal.*, 43(1):156–173 (electronic), 2005. 35, 36
- [84] S. Hübner and B. I. Wohlmuth. A primal-dual active set strategy for nonlinear multibody contact problems. *Comput. Methods Appl. Mech. Engrg.*, 194(27-29):3147–3166, 2005. 18, 19, 65, 72, 73
- [85] S. Hübner and B. I. Wohlmuth. Mortar methods for contact problems. In P. Wriggers and U. Nackenhorst, editors, *Analysis and Simulation of Contact Problems*, volume 27 of *Lecture Notes in Applied and Computational Mechanics*, pages 39–47. Springer, 2006. 100, 101
- [86] K. Ito and K. Kunisch. Semi-smooth Newton methods for variational inequalities of the first kind. *M2AN Math. Model. Numer. Anal.*, 37(1):41–62, 2003. 65, 67
- [87] L. Johansson and A. Klarbring. Thermoelastic frictional contact problems: Modelling, finite element approximation and numerical realization. *Comput. Methods Appl. Mech. Eng.*, 105(2):181–210, 1993. 135, 138
- [88] K. Johnson. *Contact Mechanics*. Cambridge University Press, 1985. 47

- [89] M. Jung and U. Langer. *Methode der finiten Elemente für Ingenieure*. Teubner, 2001. 101
- [90] H. B. Khenous, P. Laborde, and Y. Renard. Comparison of two approaches for the discretization of elastodynamic contact problems. *C. R. Math. Acad. Sci. Paris*, 342(10):791–796, 2006. 124
- [91] N. Kikuchi and J. Oden. *Contact Problems in Elasticity: A Study of Variational Inequalities and Finite Element Methods*. SIAM Studies in Applied Mathematics 8, Philadelphia, 1988. 3, 9, 17, 22, 47, 95
- [92] N. Kikuchi and Y. J. Song. Penalty/finite-element approximations of a class of unilateral problems in linear elasticity. *Quart. Appl. Math.*, 39(1):1–22, 1981/82. 17, 95
- [93] R. Kornhuber and R. Krause. Adaptive multigrid methods for Signorini’s problem in linear elasticity. *Comput. Vis. Sci.*, 4(1):9–20, 2001. 65, 81
- [94] R. Kornhuber, R. H. Krause, O. Sander, P. Deuffhard, and S. Ertel. A monotone multigrid solver for two body contact problems in biomechanics. *Computing and Visualization in Science*, 11(1):3–15, 1 2006. 65
- [95] T. Koziara and N. Bićanić. Semismooth Newton method for frictional contact between pseudo-rigid bodies. *Comput. Methods Appl. Mech. Engrg.*, 197(33-40):2763–2777, 2008. 113
- [96] R. H. Krause. *Monotone Multigrid Methods for Signorini’s Problem with Friction*. PhD thesis, Freie Universität Berlin, 2001. 65
- [97] R. H. Krause. From inexact active set strategies to nonlinear multigrid methods. In P. Wriggers and U. Nackenhorst, editors, *Analysis and Simulation of Contact Problems*, volume 27 of *Lecture Notes in Applied and Computational Mechanics*, pages 13–21. Springer, 2006. 71
- [98] R. H. Krause and B. I. Wohlmuth. A Dirichlet-Neumann type algorithm for contact problems with friction. *Comput. Vis. Sci.*, 5(3):139–148, 2002. 18, 47, 65
- [99] R. Kučera. Minimizing quadratic functions with separable quadratic constraints. *Optim. Methods Softw.*, 22(3):453–467, 2007. 81
- [100] R. Kučera, J. Haslinger, and Z. Dostál. A new FETI-based algorithm for solving 3D contact problems with Coulomb friction. In *Domain decomposition methods in Science and Engineering XVI*, volume 55 of *Lecture Notes Comput. Sci. Engrg.*, pages 643–650. Springer, 2007. 81
- [101] D. Kuhl and M. A. Crisfield. Energy-conserving and decaying algorithms in nonlinear structural dynamics. *Internat. J. Numer. Methods Engrg.*, 45(5):569–599, 1999. 113

-
- [102] D. Kuhl and E. Ramm. Constraint energy momentum algorithm and its application to non-linear dynamics of shells. *Comput. Methods Appl. Mech. Engrg.*, 136(3-4):293–315, 1996. 113
- [103] D. Kuhl and E. Ramm. Generalized energy-momentum method for non-linear adaptive shell dynamics. *Comput. Methods Appl. Mech. Engrg.*, 178(3-4):343–366, 1999. 113
- [104] K. Kunisch and G. Stadler. Generalized Newton methods for the 2D-Signorini contact problem with friction in function space. *M2AN Math. Model. Numer. Anal.*, 39(4):827–854, 2005. 65, 67
- [105] B. P. Lamichhane and B. I. Wohlmuth. Higher order dual Lagrange multiplier spaces for mortar finite element discretizations. *Calcolo*, 39(4):219–237, 2002. 52
- [106] T. A. Laursen. *Computational Contact and Impact Mechanics*. Springer, Berlin Heidelberg, 2002. 3, 8, 17, 95, 124, 135, 137, 138
- [107] T. A. Laursen and V. Chawla. Design of energy conserving algorithms for frictionless dynamic contact problems. *Internat. J. Numer. Methods Engrg.*, 40(5):863–886, 1997. 122, 124
- [108] T. A. Laursen and G. R. Love. Improved implicit integrators for transient impact problems—geometric admissibility within the conserving framework. *Internat. J. Numer. Methods Engrg.*, 53(2):245–274, 2002. 122
- [109] T. A. Laursen and X. N. Meng. A new solution procedure for application of energy-conserving algorithms to general constitutive models in nonlinear elastodynamics. *Comput. Methods Appl. Mech. Engrg.*, 190(46-47):6309–6322, 2001. 122
- [110] T. A. Laursen and J. C. Simo. Algorithmic symmetrization of Coulomb frictional problems using augmented Lagrangians. *Comput. Methods Appl. Mech. Engrg.*, 108(1-2):133–146, 1993. 17
- [111] K. Lhalouani and T. Sassi. Nonconforming mixed variational formulation and domain decomposition for unilateral problems. *East-West J. Numer. Math.*, 7(1):23–30, 1999. 35
- [112] A. Matei, V. V. Motreanu, and M. Sofonea. A quasistatic antiplane contact problem with slip dependent friction. *Adv. Nonlinear Var. Inequal.*, 4(2):1–21, 2001. 56
- [113] T. McDevitt and T. A. Laursen. A mortar-finite element formulation for frictional contact problems. *Internat. J. Numer. Methods Engrg.*, 48(10):1525–1547, 2000. 17
- [114] W. McLean. *Strongly Elliptic Systems and Boundary Integral Equations*. Cambridge University Press, 2000. 19

- [115] J. Nečas, J. Jarušek, and J. Haslinger. On the solution of the variational inequality to the Signorini problem with small friction. *Boll. Un. Mat. Ital. B (5)*, 17(2):796–811, 1980. 95
- [116] V. Oancea and T. A. Laursen. A finite element formulation of thermomechanical rate-dependent frictional sliding. *Int. J. Numer. Methods Eng.*, 40(23):4275–4311, 1997. 135, 138
- [117] R. Ogden. *Non-Linear Elastic Deformations*. Dover, Mineola, New York, 1984. 3, 10
- [118] P. Papadopoulos and R. Taylor. A mixed formulation for the finite element solution of contact problems. *Comput. Methods Appl. Mech. Engrg.*, 94(3):373–389, 1992. 17
- [119] M. A. Puso and T. A. Laursen. A mortar segment-to-segment contact method for large deformation solid mechanics. *Comput. Methods Appl. Mech. Engrg.*, 193(6-8):601–629, 2004. 17
- [120] M. A. Puso and T. A. Laursen. A mortar segment-to-segment frictional contact method for large deformations. *Comput. Methods Appl. Mech. Engrg.*, 193(45-47):4891–4913, 2004. 17
- [121] L. Qi. Convergence analysis of some algorithms for solving nonsmooth equations. *Math. Oper. Res.*, 18(1):227–244, 1993. 66
- [122] L. Qi and J. Sun. A nonsmooth version of Newton’s method. *Math. Programming*, 58(3, Ser. A):353–367, 1993. 66, 83
- [123] O. Schenk and K. Gärtner. Solving unsymmetric sparse systems of linear equations with PARDISO. *Journal of Future Generation Computer Systems*, 20(3):475–487, 2004. viii, 104
- [124] O. Schenk and K. Gärtner. On fast factorization pivoting methods for sparse symmetric indefinite systems. *Elec. Trans. Numer. Anal.*, 23:158–179, 2006. viii, 104
- [125] J. Schöberl. NETGEN: An advancing front 2D/3D-mesh generator based on abstract rules. *Comput. Vis. Sci.*, 1(1):41–52, 1997. viii
- [126] J. Simo and C. Miehe. Associative coupled thermoplasticity at finite strains: Formulation, numerical analysis and implementation. *Comput. Methods Appl. Mech. Eng.*, 98(1):41–104, 1992. 135
- [127] J. Simo and N. Tarnow. The discrete energy-momentum method. Conserving algorithms for nonlinear elastodynamics. *Z. Angew. Math. Phys.*, 43(5):757–792, 1992. 113, 122

-
- [128] J. C. Simo and T. A. Laursen. An augmented Lagrangian treatment of contact problems involving friction. *Comput. & Structures*, 42(1):97–116, 1992. 17
- [129] G. Stadler. *Finite-Dimensional Semi-Smooth Newton and Augmented Lagrangian Methods for Friction and Contact Problems in Elasticity*. PhD thesis, TU Graz, 2004. 65
- [130] G. Stadler. Semismooth Newton and augmented Lagrangian methods for a simplified friction problem. *SIAM J. Optim.*, 15(1):39–62 (electronic), 2004. 65
- [131] E. Stein and M. Rüter. Finite Element Methods for Elasticity with Error-controlled Discretization and Model Adaptivity. In E. Stein, R. de Borst, and T. Hughes, editors, *Encyclopedia of Computational Mechanics*, volume 2: Solids and Structures, pages 5–58. Wiley, 2004. 3, 10
- [132] R. L. Taylor and P. Papadopoulos. On a finite element method for dynamic contact/impact problems. *Internat. J. Numer. Methods Engrg.*, 36(12):2123–2140, 1993. 113
- [133] V. Thomée. *Galerkin Finite Element Methods for Parabolic Problems*. Springer-Verlag, New York, 1997. 144, 145
- [134] A. Weiss and B. I. Wohlmuth. Multigrid methods for unresolved Dirichlet boundaries. Technical Report 11, Universität Stuttgart, IANS Preprint, 2005. 71
- [135] K. Willner. *Kontinuums- und Kontaktmechanik*. Springer, Berlin Heidelberg, 2003. 3, 17, 135, 136
- [136] B. I. Wohlmuth. A mortar finite element method using dual spaces for the Lagrange multiplier. *SIAM J. Numer. Anal.*, 38(3):989–1012 (electronic), 2000. 18, 24, 28, 52
- [137] B. I. Wohlmuth. *Discretization Methods and Iterative Solvers Based on Domain Decomposition*. Springer, 2001. 37, 38, 39, 50
- [138] B. I. Wohlmuth. A comparison of dual Lagrange multiplier spaces for mortar finite element discretizations. *M2AN Math. Model. Numer. Anal.*, 36(6):995–1012 (2003), 2002. 43, 48
- [139] B. I. Wohlmuth. A \mathcal{V} -cycle multigrid approach for mortar finite elements. *SIAM J. Numer. Anal.*, 42(6):2476–2495 (electronic), 2005. 71
- [140] B. I. Wohlmuth and R. H. Krause. A multigrid method based on the unconstrained product space for mortar finite element discretizations. *SIAM J. Numer. Anal.*, 39(1):192–213 (electronic), 2001. 18, 25, 71
- [141] B. I. Wohlmuth and R. H. Krause. Monotone multigrid methods on nonmatching grids for nonlinear multibody contact problems. *SIAM J. Sci. Comput.*, 25(1):324–347 (electronic), 2003. 18, 71

- [142] P. Wriggers. *Nichtlineare Finite-Element-Methoden*. Springer, Berlin Heidelberg New York, 2001. 3, 10, 11, 135
- [143] P. Wriggers. *Computational Contact Mechanics*. J. Wiley & Sons Ltd, Chichester, 2002. 3, 17, 95
- [144] P. Wriggers and C. Miehe. Contact constraints within coupled thermomechanical analysis—a finite element model. *Comput. Methods Appl. Mech. Engrg.*, 113(3-4):301–319, 1994. 135
- [145] B. Yang, T. A. Laursen, and X. Meng. Two dimensional mortar contact methods for large deformation frictional sliding. *Internat. J. Numer. Methods Engrg.*, 62(9):1183–1225, 2005. 17, 26, 123